

**THEORY AND EXPERIMENTAL EVALUATION OF A
CONSISTENT STEADY-STATE KINETIC MODEL FOR
2-D CONDUCTIVE STRUCTURES IN IONOSPHERIC
PLASMAS WITH APPLICATION TO BARE
ELECTRODYNAMIC TETHERS IN SPACE**

by

Éric Choinière

A dissertation submitted in partial fulfillment
of the requirements for the degree of
Doctor of Philosophy
(Electrical Engineering)
in The University of Michigan
2004

Doctoral Committee:

Professor Brian E. Gilchrist, Chair
Assistant Professor Sven G. Bilén
Professor Iain Boyd
Professor Alec D. Gallimore
Professor Kamal Sarabandi

© Éric Choinière 2004
All Rights Reserved

À mon amour, Isabelle, pour sa patience et son support,
et à la mémoire de ma grand-mère Bernadette.

ACKNOWLEDGMENTS

First, I would like to thank my research advisor and committee chair, Professor Brian Gilchrist, for allowing me on board in September of 1999 when I first stepped foot in his office, for making so many great opportunities happen during my years in Ann Arbor, and for all of his support throughout this exciting, difficult, and rewarding journey. I really appreciate the freedom and trust you have given me throughout the years, as well as the friendly atmosphere that you have fostered within the SETS group. I look forward to collaboration in the future.

I would also like to thank the other members of my thesis committee, Prof. Sven Bilén, Prof. Iain Boyd, Prof. Alec Gallimore and Prof. Sarabandi, for accepting to judge this work and for their guidance. Special thanks go to Prof. Bilén for teaching me the ropes of experimental work while he was working as a Postdoc at Michigan, as well as for his guidance with the English language throughout several co-authored papers and this thesis. I would like to thank Prof. Gallimore for his essential support of our experimental work in the Large Vacuum Test Facility, and for having given a second life to this outstanding vacuum test facility.

I would like to thank my colleagues of the Space Electrodynamics and Tether Systems (SETS) group for their assistance and guidance throughout the years, for all the insightful discussions, for the entertaining and politically-charged debates, and for their friendship. Thanks to Dave Morris, Chris Davis, Boon Lim, Brent West, Hannah Goldberg, Chris

Deline, and Keith Fuhrhop. Special thanks to Keith for all his help preparing and analyzing laboratory tests.

I am grateful for scholarship support provided by a 2-year Postgraduate Scholarship from the Natural Sciences and Engineering Research Council of Canada, two Fessenden Graduate Awards from the Communications Research Centre and Industry Canada, a 1-year Departmental Fellowship from the Electrical Engineering and Computer Science department, and a 1-year Rackham Predoctoral Fellowship from the Horace H. Rackham School of Graduate Studies. These fellowships not only allowed me to join the Ph.D. program within such a great institution as the University of Michigan, they also gave me the liberty to take risks in undertaking the development of a new computational plasma model, which would probably not have been possible through other types of funding resources.

I would like to acknowledge the support of NASA for part of the experimental portion of this work through the STEP-Airseds project. I would also like to acknowledge the support of Tethers Unlimited, Inc. with special thanks to Rob Hoyt, Bryan Minor and Nestor Voronka. Thank you for providing new and exciting opportunities for the application of the KiPS models to the remediation of radiation belts. I look forward to future collaboration on this and other exciting space projects.

From the Plasmadynamics and Electric Propulsion Laboratory, I would like to thank, in addition to Professor Alec Gallimore, all of the students and staff members who have assisted and guided in one way or another myself and other members of the Space Electrodynamic and Tether Systems group during several electrodynamic tether sample testing sessions. Thanks to Tim Smith, Dan Hermann, Mitchell Walker, Brian Beal, Jon Van Noord, and Travis Patrick.

Several fellow members of the Radiation Laboratory have provided their technical assistance, guidance or friendship during my stay at Michigan. I would like to thank in

particular Stéphane Legault, Hanh Pham, Mark Casciato, Lee Harle, Brian Hornbuckle, Valdis Liepa and Nadib Nashashibi.

Special thanks go to several researchers in the space plasma community with whom I have had some very insightful exchanges and discussions: Prof. James Laframboise, Dr. Ira Katz, Prof. Juan Sanmartín, Prof. Manual Martínez-Sánchez, Dr. Tatsuo Onishi, and Dr. Dave Cook.

Several staff members have indirectly contributed to this thesis by making things run smoother for me as a graduate student. In the Space Physics Research Laboratory, I would like to thank Charles Navarre (“Chuck”) for his help in the machine shop, Clinton Lee for putting up with all my special backup needs, and Melissa Lee, our outstanding secretary. For their flawless administrative support, I would like to thank Susan Charnley, Mary Eyler and Karen Kirchener from the Radiation Laboratory and Beth Stalnaker from EECS.

The highly computational nature of the present work relies on the existence and availability of large parallel computing resources. I would like to thank Mark Giuffrida, director of the *Computer Aided Engineering Network*, for his collaboration and flexibility in the deployment and operation of a powerful opportunistic computing platform for plasma simulations on the CAEN network.

Authors of free software provide an invaluable contribution to the scientific community. I would like to specifically acknowledge Frédéric Hecht, the author of the *Bidimensional Anisotropic Mesh Generator* (BAMG), and all the authors of the *Parallel Virtual Machine* (PVM) at Oak Ridge National Laboratory. I am also grateful to Leslie Lamport, the author of the most essential thesis writing tool, L^AT_EX.

I would like to thank my friends from up in Québec for their support and continuous friendship despite the 12-hour drive that separated us during almost five years. Merci pour votre amitié.

I acknowledge my family as well as my wife's family for their support and patience throughout the past years spent in the United States. I would especially like to thank my parents for encouraging me to reach for my dreams. Chère soeur, I have not forgotten your promise to read my thesis once completed ! I only wish my grandmother Bernadette had lived to see this work completed.

Last, but not least, I wish to thank my wife Isabelle for her love, companionship and endurance throughout the past 5 years. You have largely contributed to the success of this journey. Merci mon amour!

Éric Choinière
September 24, 2004

ABSTRACT

THEORY AND EXPERIMENTAL EVALUATION OF A CONSISTENT STEADY-STATE KINETIC MODEL FOR 2-D CONDUCTIVE STRUCTURES IN IONOSPHERIC PLASMAS WITH APPLICATION TO BARE ELECTRODYNAMIC TETHERS IN SPACE

by
Éric Choinière

Chair: Brian E. Gilchrist

A steady-state kinetic computational model is developed, allowing for self-consistent simulations of collisionless, unmagnetized flowing plasmas in a vast region surrounding any two-dimensional conductive object. An optimization approach is devised based on a stable, noise-robust Tikhonov-regularized Newton method. Dynamic, adaptive, unstructured meshing allows arbitrary geometries and adequate resolution of plasma sheath features. A 1-D cylindrical solver (KiPS-1D) and a full 2-D solver (KiPS-2D) were developed, the latter using coarse-grained parallelism.

This technique is applied to investigate various applications of special and fundamental importance, principally for space plasmas, although not limited as such. This thesis addresses new simulations and experiments relevant to space borne electrodynamic tethers for propellantless propulsion and for the remediation of radiation belts through charge precipitation, as well as to Langmuir probes for plasma diagnostic in flowing plasmas.

Here, the existing set of plasma sheath profiles and current collection characteristics for round cylinders in stationary plasmas is extended to large bias potentials. Interfer-

ence effects between two parallel cylinders are shown to exist for spacings upward of 20 times the single-cylinder sheath radius, and an optimal spacing equal to the single-cylinder sheath radius maximizes the sheath area, a finding qualitatively supported by our new experimental data on electron-collecting thin slotted tapes. Also, a thin conductive solid tape is shown to have an equal-capacitance circular radius of about 0.29 times its width. Its predicted collected current characteristic as a function of width approximately agrees with experimental measurements. Further, it has a lower current collection capability than the equal-capacitance circular cylinder.

For ion-attracting cylinders, ionospheric plasma representative of an altitude of 1500 km with a flow energy on the order of the thermal energy is shown to cause significant sheath asymmetries, reducing the sheath radius and current collection by about 30%. For electron-attracting cylinders, a mesosonic flow is experimentally shown to significantly enhance electron collection. This cannot be predicted by a collisionless model and may be due to an elongation of the ram-side pre-sheath into a collisional zone for electrons.

TABLE OF CONTENTS

DEDICATION	ii	
ACKNOWLEDGMENTS	iii	
ABSTRACT	vii	
LIST OF TABLES	xiv	
LIST OF FIGURES	xv	
LIST OF ALGORITHMS	xxiii	
LIST OF APPENDICES	xxiv	
CHAPTERS		
1	Introduction, Background and Previous Research	1
1.1	Motivation and Definition of the Problem	1
1.1.1	Bare Electrodynamic Tethers for Space Propulsion	2
1.1.2	Bare Electrodynamic Tethers for Ionospheric High-Energy Charge Precipitation (“Electrostatic” Tethers)	5
1.1.3	Plasma Diagnostics Probes	6
1.1.4	Other Applications	7
1.1.5	Description of the Problem & Regimes of interest	8
1.2	Cylindrical Plasma Probes: Background and Literature Review .	11
1.2.1	Stationary plasmas	12
1.2.1.1	Thin Sheath Limit	13
1.2.1.2	Orbital-Motion Limit (“Thick” Sheath Limit) .	14
1.2.1.3	Numerical Approaches for Arbitrary Probe Sizes	16
1.2.2	Flowing Plasmas	17
1.2.2.1	Treatments Based on a Symmetric Potential Profile Assumption	17
1.2.2.2	Consistent Numerical Treatments	18
1.2.2.2.1	Steady-State Kinetic Treatments .	18
1.2.2.2.2	Particle-in-Cell Treatment	19
1.3	Summary of Research Contributions	19

1.3.1	A Self-Consistent Steady-State Kinetic Model for Arbitrary 2-D Conductive Structures in Flowing Plasmas	20
1.3.2	New Simulation Results	21
1.3.3	New Experimental Results	22
1.4	Dissertation Overview	23
2	Steady-State Poisson–Vlasov Model: Theory and Implementation	25
2.1	Basic Assumptions	27
2.2	Poisson–Vlasov Representation of Collisionless Plasmas	33
2.3	Finite-Element Poisson Solver	36
2.3.1	1-D Cylindrical Implementation	37
2.3.2	2-D Implementation	41
2.3.2.1	Poisson Boundary Conditions	41
2.3.2.2	Finite-Element Formulation	43
2.3.2.2.1	Formulation of the Outer Boundary Condition	43
2.3.2.2.2	Formulation of the Internal Finite Elements	46
2.4	Steady-State Vlasov Solver	50
2.4.1	1-D Cylindrical Implementation	51
2.4.1.1	Approximating the Vlasov Functional f_V in 1-D .	52
2.4.1.2	Linearizing the 1-D Vlasov Solver	55
2.4.2	Full 2-D Implementation	56
2.4.2.1	Orbit Tracking and Analysis	56
2.4.2.1.1	A Note on Segment-bound Trajectories	62
2.4.2.2	Sampling the Velocity Distribution Function . .	62
2.4.2.3	Velocity Space Integration	65
2.4.2.3.1	Defining “Directional-Energy” Space .	65
2.4.2.3.2	Numerical Integration in “Directional-Energy” Space	66
2.4.2.4	Linearizing the 2-D Vlasov Solver	70
2.5	Regularized Newton Iterative Poisson–Vlasov Scheme	70
2.5.1	Top-level Iterative Scheme	71
2.5.2	Conditioning and Quadrature Noise Issues	73
2.5.3	Diagonal Preconditioning	75
2.5.4	Tikhonov “Progressive” Regularization	76
2.5.5	Discrepancy Principle as Stopping Criteria	81
2.5.6	Dynamic Step Size Control	82
2.5.7	Dynamic Adaptive Quadrature Tolerance	85
2.6	Dynamic Adaptive Mesh Refinement	86
2.6.1	KiPS Cylindrical 1-D Implementation	86
2.6.2	KiPS 2-D Implementation	88
2.6.2.1	Meshing Software	88
2.6.2.2	Mesh Symmetry Axes	88

2.6.2.3	Mesh Refinement: Strategy & Metrics	89
2.6.2.4	Examples of Mesh Geometries Under Consideration	91
2.6.2.4.1	Single Round Cylinder	91
2.6.2.4.2	Tape Cylinder	92
2.6.2.4.3	Two Round Cylinders	93
2.7	Computer Implementation	94
2.7.1	General Philosophy	94
2.7.2	Optimizing & Parallelizing the Vlasov Solver	95
2.7.3	Present Parallel Computing Platform	96
2.7.4	Alternative Parallel Computing Platforms	96
3	Experimental Investigation of Electron-Collecting Tether Samples in a Mesosonic Xenon Plasma	98
3.1	Background	98
3.2	Design and Assembly of Solid and Slotted Tape Tether Guarded Samples	99
3.3	Vacuum Chamber Setup and Plasma Source Characteristics	105
3.4	Plasma Parameter Measurements Using Negatively-Biased Langmuir Probes	108
3.5	Experimental Results & Analysis	110
3.5.1	Reference Cylinder	111
3.5.2	Solid Tapes	112
3.5.3	Slotted Tapes	114
3.5.4	Comparison of the Solid and Slotted Tapes	116
3.6	Present Status and Conclusions	120
4	Simulation Results and Validation	122
4.1	Definition of Normalized Physical Quantities	122
4.2	Single Round Cylinder in Stationary Plasma	126
4.2.1	Validation of Potential & Density Profiles at Low Bias Voltages	126
4.2.2	Validation of Collected Current at Low Bias Voltages	130
4.2.3	Assessment of Collected Current at High Bias Voltages	131
4.2.4	Plasma Profiles at High Voltages	133
4.2.4.1	Typical Plasma Profile from KiPS-1D	134
4.2.4.2	Typical Two-Dimensional Plasma Structure from KiPS-2D	137
4.2.4.3	Profile dependence on Bias Potential and Cylinder Radius	137
4.2.4.4	Variation of the Ion Velocity Distribution Throughout the Sheath	143
4.2.5	Sheath Radius at High Voltages	146
4.3	Interference of Parallel Round Cylinders in a Stationary Plasma	149
4.3.1	Treatment of Repelled Electrons	150

4.3.2	Orbits of the Attracted Ions	150
4.3.2.1	Criteria for Trapped Orbits	151
4.3.2.2	Examples of Ion Orbits	152
4.3.3	Inspection of the 2-D Sheath Structure	154
4.3.4	Definition of an <i>Effective Sheath Area</i> Concept	170
4.3.5	Determination of the Effective Sheath Area of the Two-Cylinder Configuration	171
4.3.6	Parametric Analysis of the Sheath Structure	181
4.3.7	Interference Effect on Collected Current	186
4.4	Solid Tape Cylinder in Stationary Plasma: Current Collection	189
4.4.1	Equivalent Cylinder Radius and Collected Current: Theoretical Comparisons	189
4.4.2	Collected Current: Comparisons with Experimental Results	192
4.5	Flow Effects on Ion-Attracting Round Cylinder	196
4.5.1	Criteria for Trapped Orbits	198
4.5.2	Treatment of Electrons	199
4.5.3	Validation with Existing Simulation Results	200
4.5.3.1	Ion Density Profile Validations	200
4.5.3.2	Ion Current Collection Validations	203
4.5.4	Ionospheric Flow Effects at High Altitudes ($H=1500$ km)	206
4.5.4.1	Flow Energy at Altitude of Interest	206
4.5.4.2	Inspection of the Sheath Structure	207
4.5.4.3	Plasma Flow Effects on Sheath Structure and Dimensions	223
4.5.4.4	Plasma Flow Effect on Ion Current Collection	226
4.6	Flow Effects on Electron-Attracting Round Cylinder	227
4.6.1	Potential and Density Profiles	228
4.6.2	Electron Current Collection	237
4.7	Outline of Simulation Resource Requirements	242
4.7.1	1-D Cylindrical Implementation (KiPS-1D)	242
4.7.2	2-D Cylindrical Implementation (KiPS-2D)	244
4.7.2.1	Processing Time	244
4.7.2.2	Random-Access Memory Requirements	247
5	Conclusions and Recommendations for Future Research	248
5.1	Summary and Conclusions of Research	248
5.1.1	Self-Consistent Steady-State Kinetic Model	248
5.1.2	Experimental Investigation of Electron-Collecting Tether Samples	250
5.1.3	Important Simulation and Experimental Results	251
5.1.3.1	Ion-Attracting High-Voltage Single Cylinder in Stationary Plasma	251
5.1.3.2	Interference Effects of Parallel Cylinders	251
5.1.3.3	Geometry Effects of the Solid Tape Cylinder	252
5.1.3.4	Plasma Flow Effects on Ion-Attracting Cylinder	252

5.1.3.5	Plasma Flow Effects on Electron-Attracting Cylinder	253
5.2	Recommendations for Future Research	253
5.2.1	Computational Modeling	254
5.2.2	Experimental Testing	256
APPENDICES	258
BIBLIOGRAPHY	281

LIST OF TABLES

Table

1.1	Approximate plasma parameters for the main applications of interest.	11
2.1	Decay rates of the radial electric field $E_{rn} = -\frac{\partial V_{xn}}{\partial r}$ for various circular harmonic modes.	42
2.2	Functional operators and corresponding numerical solvers.	71
3.1	Effective diameter of the reference cylinder and effective widths of the three solid tapes.	101
3.2	Effective center-to-center line spacing as a function of sample porosity. . .	101
3.3	Operating parameters of the plasma source (P5 Hall thruster).	107
3.4	Variation of the measured plasma parameters as a function of distance from the Hall thruster.	108

LIST OF FIGURES

Figure

1.1	Example of an application of the electrodynamic space tether concept for use as a station keeping device for the <i>International Space Station</i>	3
1.2	Geometry of the interaction of the electrodynamic tether and the radiation belt.	5
1.3	Four examples of the cylinder geometries under consideration.	10
1.4	Normalized current characteristics in the thin sheath limit and orbital motion limit.	16
2.1	Example of the semi-analytical particle tracking process through the potential mesh on a grid with normalized coordinates.	59
2.2	Poisson–Vlasov operator comprised of both the Poisson and Vlasov solvers.	71
2.3	Tikhonov-regularized Newton iterative Poisson–Vlasov procedure.	72
2.4	Sequence of refined meshes obtained for a single one-Debye-length-radius round cylinder.	92
2.5	Sequence of refined meshes obtained for a tape cylinder.	93
2.6	Sequence of refined meshes for 2 parallel one-Debye-length-radius cylinders.	94
3.1	Drawing and description of the six guarded tether samples shown before assembly.	100
3.2	Assemblies of the reference cylinder and tape guarded tether samples. . . .	102
3.3	Example of the ceramic attachment used on all solid and slotted tape samples.	103
3.4	Pictures of three typical tether samples.	104

3.5	Experimental setup in the Large Vacuum Test Facility (LVTF) at the Plasmadynamics and Electric Propulsion Laboratory (PEPL).	106
3.6	Picture of the guarded sample support structure and the P5 Hall thruster used as a high-speed plasma source.	107
3.7	Schematic of the computer-controlled high-voltage test equipment setup. . .	109
3.8	Normalized I–V characteristics of parallel and perpendicular solid tapes. .	113
3.9	Normalized I–V characteristics of parallel and perpendicular slotted tapes. .	115
3.10	Comparison of the I–V characteristics of solid and slotted tapes at 75 cm. .	117
3.11	Comparison of the I–V characteristics of solid and slotted tapes at 160 cm. .	118
3.12	Comparison of the I–V characteristics of solid and slotted tapes at 300 cm. .	119
4.1	Normalized ion and electron charge densities as a function of normalized distance from the surface of a round cylindrical probe.	127
4.2	Normalized net charge density as a function of normalized distance from the surface of a round cylindrical probe.	128
4.3	Normalized electric potential as a function of normalized distance from the surface of a round cylindrical probe.	129
4.4	Normalized collected ion current I/I_{th} to a round conductive cylinder as a function of normalized bias potential $\phi_0 = (V_0 - V_p)/T_e$	131
4.5	Current ratio I/I_{oml} (“current collection efficiency”) as a function of the radius of a round conductive cylinder.	132
4.6	Typical high-voltage cylindrical sheath structure.	134
4.7	Poisson–Vlasov consistent KiPS-2D solution for a single cylinder configuration.	138
4.8	Poisson–Vlasov consistent electron and ion density distributions for a single-cylinder configuration.	139
4.9	Family of electron and ion density profiles for a round conductive cylinder with radius $r_0 = \lambda_{\text{De}}$	140
4.10	Family of electron and ion density profiles for a round conductive cylinder with radius $r_0 = 0.001\lambda_{\text{De}}$	141

4.11 Family of potential profiles for a round conductive cylinder with radius $r_0 = \lambda_{De}$	142
4.12 Family of potential profiles for a round conductive cylinder with radius $r_0 = 0.001\lambda_{De}$	142
4.13 Ion “directional-energy” distributions in the high-voltage cylindrical sheath.	144
4.14 Equivalent sheath radius as a function of normalized bias potential and nor- malized line charge for an ion-attracting round conductive cylinder	147
4.15 Examples of some typical ion orbits within the self-consistent potential structure of a two-cylinder system.	153
4.16 Poisson–Vlasov consistent solution for a two-cylinder configuration with $\Delta x = 2\lambda_{De}$	155
4.17 Poisson–Vlasov consistent electron and ion density distributions for a two- cylinder configuration with $\Delta x = 2\lambda_{De}$	156
4.18 Poisson–Vlasov consistent solution for a two-cylinder configuration with $\Delta x = 10\lambda_{De}$	158
4.19 Poisson–Vlasov consistent electron and ion density distributions for a two- cylinder configuration with $\Delta x = 10\lambda_{De}$	159
4.20 Poisson–Vlasov consistent solution for a two-cylinder configuration with $\Delta x = 20\lambda_{De}$	160
4.21 Poisson–Vlasov consistent electron and ion density distributions for a two- cylinder configuration with $\Delta x = 20\lambda_{De}$	161
4.22 Poisson–Vlasov consistent solution for a two-cylinder configuration with $\Delta x = 40\lambda_{De}$	163
4.23 Poisson–Vlasov consistent electron and ion density distributions for a two- cylinder configuration with $\Delta x = 40\lambda_{De}$	164
4.24 Poisson–Vlasov consistent solution for a two-cylinder configuration with $\Delta x = 80\lambda_{De}$	165
4.25 Poisson–Vlasov consistent electron and ion density distributions for a two- cylinder configuration with $\Delta x = 80\lambda_{De}$	166
4.26 Poisson–Vlasov consistent solution for a two-cylinder configuration with $\Delta x = 160\lambda_{De}$	168

4.27 Poisson–Vlasov consistent electron and ion density distributions for a two-cylinder configuration with $\Delta x = 160\lambda_{De}$	169
4.28 Potential contour levels along with a plot of the contour level as a function of the area enclosed by a given contour, for a two-cylinder configuration with $\Delta x = 2\lambda_{De}$	172
4.29 Potential contour levels along with a plot of the contour level as a function of the area enclosed by a given contour, for a two-cylinder configuration with $\Delta x = 10\lambda_{De}$	173
4.30 Potential contour levels along with a plot of the contour level as a function of the area enclosed by a given contour, for a two-cylinder configuration with $\Delta x = 20\lambda_{De}$	174
4.31 Potential contour levels along with a plot of the contour level as a function of the area enclosed by a given contour, for a two-cylinder configuration with $\Delta x = 40\lambda_{De}$	175
4.32 Potential contour levels along with a plot of the contour level as a function of the area enclosed by a given contour, for a two-cylinder configuration with $\Delta x = 80\lambda_{De}$	176
4.33 Potential contour levels along with a plot of the contour level as a function of the area enclosed by a given contour, for a two-cylinder configuration with $\Delta x = 160\lambda_{De}$	177
4.34 Effective sheath area ratio R_{As} as a function of the center-to-center spacing of two parallel cylinders.	181
4.35 Ratio of the outward sheath radius to the single independent cylinder sheath radius $r_{s,1}$ as a function of the center-to-center spacing of two parallel cylinders.	183
4.36 Ratio of the total surface charge on both cylinders to the surface charge held by a single independent cylinder.	184
4.37 Equivalent bias potential of a single cylinder as a function of the center-to-center spacing of two parallel cylinders.	185
4.38 Equivalent radius of a single cylinder as a function of the center-to-center spacing of two parallel cylinders.	186
4.39 Current ratio as a function of center-to-center spacing for the two-cylinder configuration.	187

4.40	Illustration of the convex envelope surrounding both cylinders.	188
4.41	Equivalent circular probe radius as a function of width for a solid tape electron collector biased at $\phi_0 = \frac{V_0 - V_p}{T_e} = 300$.	191
4.42	Current ratio I/I_{oml} as a function of tape width for a solid tape biased at $\phi_0 = \frac{V_0 - V_p}{T_e} = 300$.	192
4.43	Simulated current ratio I/I_{oml} as a function of tape width for a solid tape biased at $\phi_0 = \frac{V_0 - V_p}{T_e} = 100$, along with experimental data.	193
4.44	Normalized current characteristics of solid tapes: comparison of simulation results with experimental data obtained at 75 cm.	196
4.45	Normalized current characteristics of solid tapes: comparison of simulation results with experimental data obtained at 160 cm.	197
4.46	Normalized current characteristics of solid tapes: comparison of simulation results with experimental data obtained at 300 cm.	197
4.47	Ion normalized density profile along the central axis of a round conductive cylinder ($r_0 = \lambda_{\text{De}}$) biased at a potential of $-25T_e$ and immersed in a plasma flowing at speed ratios $S_d = 0.5$ and $S_d = 1$.	201
4.48	Ion normalized density profile along the central axis of a round conductive cylinder ($r_0 = \lambda_{\text{De}}$) biased at a potential of $-25T_e$ and immersed in a plasma flowing at speed ratios $S_d = 3$ and $S_d = 6$.	202
4.49	Collected ion current as a function of the ion speed ratio S_d , for a round conductive cylinder with probe radii $r_0 = 0.2\lambda_{\text{De}}$ and $r_0 = \lambda_{\text{De}}$, immersed in a flowing plasma with $T_i = T_e$.	204
4.50	Collected ion current as a function of the ion speed ratio S_d , for a round conductive cylinder with probe radii $r_0 = 5\lambda_{\text{De}}$ and $r_0 = 10\lambda_{\text{De}}$, immersed in a flowing plasma with $T_i = T_e$.	205
4.51	Poisson–Vlasov consistent solution for an ion-attracting cylinder ($r_0 = \lambda_{\text{De}}$) biased at $\phi_0 = -5$ and immersed in a flowing plasma with flow energy $U_{\text{ev}} = 0.66T_e$.	209
4.52	Poisson–Vlasov consistent electron and ion density distributions for an ion-attracting cylinder ($r_0 = \lambda_{\text{De}}$) biased at $\phi_0 = -5$ and immersed in a flowing plasma with flow energy $U_{\text{ev}} = 0.66T_e$.	210

4.53 Poisson–Vlasov consistent solution for an ion-attracting cylinder ($r_0 = \lambda_{De}$) biased at $\phi_0 = -10$ and immersed in a flowing plasma with flow energy $U_{ev} = 0.66T_e$.	211
4.54 Poisson–Vlasov consistent electron and ion density distributions for an ion-attracting cylinder ($r_0 = \lambda_{De}$) biased at $\phi_0 = -10$ and immersed in a flowing plasma with flow energy $U_{ev} = 0.66T_e$.	212
4.55 Poisson–Vlasov consistent solution for an ion-attracting cylinder ($r_0 = \lambda_{De}$) biased at $\phi_0 = -20$ and immersed in a flowing plasma with flow energy $U_{ev} = 0.66T_e$.	213
4.56 Poisson–Vlasov consistent electron and ion density distributions for an ion-attracting cylinder ($r_0 = \lambda_{De}$) biased at $\phi_0 = -20$ and immersed in a flowing plasma with flow energy $U_{ev} = 0.66T_e$.	214
4.57 Poisson–Vlasov consistent solution for an ion-attracting cylinder ($r_0 = \lambda_{De}$) biased at $\phi_0 = -50$ and immersed in a flowing plasma with flow energy $U_{ev} = 0.66T_e$.	215
4.58 Poisson–Vlasov consistent electron and ion density distributions for an ion-attracting cylinder ($r_0 = \lambda_{De}$) biased at $\phi_0 = -50$ and immersed in a flowing plasma with flow energy $U_{ev} = 0.66T_e$.	216
4.59 Poisson–Vlasov consistent solution for an ion-attracting cylinder ($r_0 = \lambda_{De}$) biased at $\phi_0 = -100$ and immersed in a flowing plasma with flow energy $U_{ev} = 0.66T_e$.	217
4.60 Poisson–Vlasov consistent electron and ion density distributions for an ion-attracting cylinder ($r_0 = \lambda_{De}$) biased at $\phi_0 = -100$ and immersed in a flowing plasma with flow energy $U_{ev} = 0.66T_e$.	218
4.61 Poisson–Vlasov consistent solution for an ion-attracting cylinder ($r_0 = \lambda_{De}$) biased at $\phi_0 = -200$ and immersed in a flowing plasma with flow energy $U_{ev} = 0.66T_e$.	219
4.62 Poisson–Vlasov consistent electron and ion density distributions for an ion-attracting cylinder ($r_0 = \lambda_{De}$) biased at $\phi_0 = -200$ and immersed in a flowing plasma with flow energy $U_{ev} = 0.66T_e$.	220
4.63 Poisson–Vlasov consistent solution for an ion-attracting cylinder ($r_0 = \lambda_{De}$) biased at $\phi_0 = -300$ and immersed in a flowing plasma with flow energy $U_{ev} = 0.66T_e$.	221

4.64 Poisson–Vlasov consistent electron and ion density distributions for an ion-attracting cylinder ($r_0 = \lambda_{De}$) biased at $\phi_0 = -300$ and immersed in a flowing plasma with flow energy $U_{ev} = 0.66T_e$	222
4.65 Set of curves of the axial potential profiles corresponding to various bias potentials for a one-Debye-length-radius round cylinder immersed in a flowing plasma with flow energy $U_{ev} = 0.66T_e$	223
4.66 Set of curves of the electron and ion axial density profiles corresponding to various bias potentials for a one-Debye-length-radius round cylinder immersed in a flowing plasma with flow energy $U_{ev} = 0.66T_e$	224
4.67 Effective sheath area ratio R_{A_s} as a function of normalized bias potential for an ion-attracting single round cylinder immersed in a flowing plasma with flow energy $U_{ev} = 0.66T_e$	225
4.68 Ratio of surface charge to the “stationary” surface charge as a function of normalized bias potential, for an ion-attracting single round cylinder immersed in a flowing plasma with flow energy $U_{ev} = 0.66T_e$	226
4.69 Current ratio as a function of normalized bias potential for an ion-attracting single round cylinder immersed in a flowing plasma with flow energy $U_{ev} = 0.66T_e$	227
4.70 Poisson–Vlasov consistent solution for an electron-attracting cylinder ($r_0 = \lambda_{De}$) biased at $\phi_0 = 20$ and immersed in a flowing plasma with flow energy $U_{ev} = 0.2 T_e$	229
4.71 Poisson–Vlasov consistent electron and ion density distributions for an electron-attracting cylinder ($r_0 = \lambda_{De}$) biased at $\phi_0 = 20$ and immersed in a flowing plasma with flow energy $U_{ev} = 0.2 T_e$	230
4.72 Poisson–Vlasov consistent solution for an electron-attracting cylinder ($r_0 = \lambda_{De}$) biased at $\phi_0 = 20$ and immersed in a flowing plasma with flow energy $U_{ev} = 0.5 T_e$	231
4.73 Poisson–Vlasov consistent electron and ion density distributions for an electron-attracting cylinder ($r_0 = \lambda_{De}$) biased at $\phi_0 = 20$ and immersed in a flowing plasma with flow energy $U_{ev} = 0.5 T_e$	232
4.74 Poisson–Vlasov consistent solution for an electron-attracting cylinder ($r_0 = \lambda_{De}$) biased at $\phi_0 = 20$ and immersed in a flowing plasma with flow energy $U_{ev} = T_e$	233

4.75 Poisson–Vlasov consistent electron and ion density distributions for an electron-attracting cylinder ($r_0 = \lambda_{De}$) biased at $\phi_0 = 20$ and immersed in a flowing plasma with flow energy $U_{ev} = T_e$.	234
4.76 Poisson–Vlasov consistent solution for an electron-attracting cylinder ($r_0 = \lambda_{De}$) biased at $\phi_0 = 20$ and immersed in a flowing plasma with flow energy $U_{ev} = 1.5 T_e$.	235
4.77 Poisson–Vlasov consistent electron and ion density distributions for an electron-attracting cylinder ($r_0 = \lambda_{De}$) biased at $\phi_0 = 20$ and immersed in a flowing plasma with flow energy $U_{ev} = 1.5 T_e$.	236
4.78 Collected Electron Current Ratio I_e/I_{oml} as a function of the normalized flow energy U_{ev}/T_e ($\phi_0 = 20$, $r_0 = \lambda_{De}$).	238
4.79 Number of iterations required for convergence and CPU time as a function of the number of unknowns in KiPS-1D simulations involving a cylinder radius of $r_0 = \lambda_{De}$. The number of unknowns was modulated by changing the bias potential, since higher potentials demand a larger number of grid samples.	243
4.80 CPU time as a function of the number of iterations required for convergence in KiPS-1D simulations involving a cylinder of radius $r_0 = \lambda_{De}$. The number of unknowns was modulated by changing the bias potential, since higher potentials demand a larger number of grid samples.	244
4.81 Simulation time required as a function of the magnitude of the normalized bias ϕ_0 , for the KiPS-2D simulations shown in Section 4.5.4, with $r_0 = \lambda_{De}$, $U_{ev} = 0.66 T_e$, and one mesh refinement.	245
F.1 Best fit of the I_i^2 -vs.- V data in the ion saturation regime.	274
F.2 Best fits in the electron retardation regime of a transverse-flow Langmuir probe.	278
F.3 Theoretical “blurring” of the current collection to probes in the <i>thin sheath</i> and <i>OML</i> limits.	279

LIST OF ALGORITHMS

Algorithm

1	Algorithm used to compute the elements of the density Jacobian $\frac{\partial \vec{n}}{\partial \vec{V}}$ (1-D cylindrical implementation)	57
2	Numerically stable evaluation of quadratic root	61
3	Dynamic step size control	84
4	Relaxation of relative quadrature tolerance	86
5	General mesh refinement strategy	87

LIST OF APPENDICES

APPENDIX

A	Nomenclature	259
B	Acronyms	264
C	2-D Poisson Solver: Detailed Expression of the Loading Matrix Elements .	265
D	Adaptive Integration Using Trapezoidal Quadrature	267
E	Linearization of the 2-D Vlasov Solver	268
F	Langmuir Probe Analysis for the Experimental Assessment of Density, Temperature, and Flow Speed	273

CHAPTER 1

Introduction, Background and Previous Research

1.1 Motivation and Definition of the Problem

Long conductive structures immersed in flowing plasmas have several applications in science and engineering. Among them are propellantless in-orbit spacecraft propulsion [1, 2] and high-energy charge precipitation from the Earth’s radiation belts [3–5], also known as remediation of radiation belts. Another common application is the Langmuir probe, a device that is widely used for laboratory and in-space plasma diagnostics [6, 7].

Unfortunately, the existing models commonly used as design tools for these applications are limited in terms of one or more of the following:

- the cross-sectional geometries they can address;
- the regimes of operation they can support (e.g. voltage bias, plasma flow speed);
- the validity and accuracy of their treatment (self-consistency of the fields and space charge).

As it turns out, the design parameters of some of the applications of present interest, namely propellantless propulsion and high-energy charge precipitation, simply fall outside of the scope of existing models, as will be explained later.

In the following paragraphs, the engineering applications that have motivated this research will be described in more detail, and a generic problem will be defined along with the regimes of interest applicable to these applications. This will demonstrate the need for a more capable model of the plasma sheath structure and current collection properties of conductive structures in ionospheric plasmas. For the moment however, let us outline the scientific contributions provided by this thesis in order to address the need for such a model:

1. definition and validation of an accurate 2-D steady-state plasma model based on a fully kinetic description of the plasma species, applicable to cylinders of various cross-section geometries immersed in stationary or flowing unmagnetized plasmas;
2. elaboration of a 1-D cylindrical version of the model useful for determining plasma sheath dimensions for round cylindrical conductors in stationary plasmas; this model expands the domain of applicability of a similar existing 1-D model [8] to very large voltages ($\sim 10,000$ times the electron temperature);
3. acquisition and analysis of new experimental vacuum chamber simulation data pertaining to simulated tether samples in high-speed plasmas, in support of the 2-D model.

The need for these new capabilities will become obvious in the following descriptions of the engineering applications of interest.

1.1.1 Bare Electrodynamic Tethers for Space Propulsion

Space electrodynamic tethers offer the opportunity for propellantless propulsion of spacecraft in orbit around any planet with a magnetic field and plasmasphere, based on the conversion of the geomagnetic force on an electric current along a conducting tether

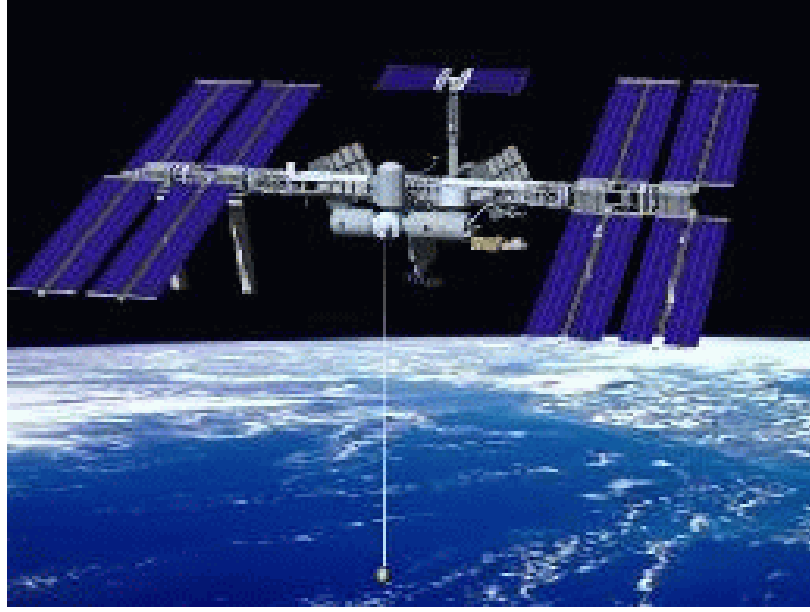


Figure 1.1: Example of an application of the electrodynamic space tether concept for use as a station keeping device for the *International Space Station*. This image is a courtesy of NASA.

into a propulsive force [2, 9]. The electric current flow along the tether is generated through either one of these mechanisms:

- the motional electromotive force (emf) experienced by the tether-bound charge carriers as they move at orbital speed through the Earth’s magnetic field;
- an on-board voltage source, which can either add to the motional emf or counter it.

The motional emf and the on-board voltage source can be used to drive current in either direction, resulting in an increase or decrease of the orbital energy. Figure 1.1 shows an example of the use of the propulsive force of an electrodynamic tether for station keeping purposes on the *International Space Station (ISS)*. The accelerating thrust provided by the electrodynamic tether could be used to counter the atmospheric drag on the space station, without the need for propellant that presently must be hauled periodically to the *ISS* by the Space Shuttle [10]. One of the key parameters affecting thrust is the amount of electrical current flowing through the tether, which in turn is limited by the amount of electron current

collected from the ionosphere.

Some authors have proposed the use of bare conductive tethers as an alternative to configurations using an insulated tether combined with an end collector [1, 2]. Bare tethers are believed to be efficient electron collectors provided that electrons are collected in a quasi orbital-motion-limited (OML) regime. In a stationary unmagnetized plasma, the electron collection process can reach the orbital motion limit, provided that the cylindrical collector is sufficiently thin [11, 12] with respect to a Debye length, the characteristic shielding distance in a plasma. However, space tethers are moving through the ionosphere at orbital velocities, effectively adding a flow component to the surrounding plasma. It is desirable to assess how the electron collection capability of a cylindrical bare tether immersed in a flowing plasma departs from that predicted by the orbital motion limit.

Past bare tether designs used a small, closely packed cross-section of wires or even a single wire as the anode [13]. In future designs, addressing concerns such as survivability from collisions with micro-meteoroids and space debris will require the use of distributed or sparse tether cross-section geometries, which could span tens of Debye lengths, depending on plasma density [14]. Since the merits of bare tethers are closely related to the efficiency of the orbital-motion-limited regime, one needs to consider how these new distributed or sparse geometries will perform in terms of current collection, as compared to thin cylinders.

To summarize, a better understanding of the effects of plasma flow and collector geometry on electron collection is necessary in order to enable efficient design techniques for future propulsive space tether designs.

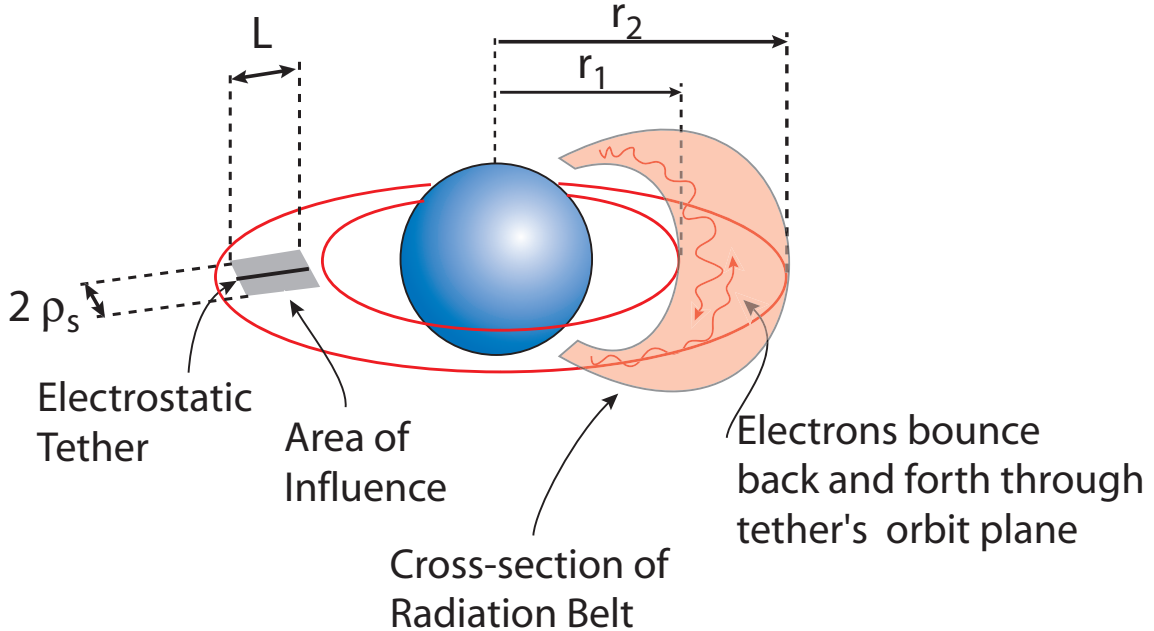


Figure 1.2: Geometry of the interaction of the electrodynamic tether and the radiation belt. Figure reproduced with permission [15]. The term “electrostatic tether”, used in this figure, is often used to refer to the specific application of particle precipitation using electrodynamic tethers and distinguish it from their original use for spacecraft propulsion.

1.1.2 Bare Electrodynamic Tethers for Ionospheric High-Energy Charge Precipitation (“Electrostatic” Tethers)

Another emerging application for bare electrodynamic tethers is the ionospheric high-energy charge precipitation.¹ Sometimes called *space remediation*, its aim is to provide a means to precipitate high-energy (MeV) electrons from the Earth’s radiation belts [3–5, 15]. Such high-energy particles could be born out of a single low-yield (10–20 kilotons), high-altitude (125–300 km) nuclear explosion and could potentially “*disable — in weeks to months — all low-Earth-orbit satellites not specifically hardened to withstand radiation*” [16]. Figure 1.2 illustrates the interaction between a bare tether used as a scattering device (the “electrostatic” tether) and a trapped population of high-energy electrons that are bouncing back and forth along the Earth’s magnetic field lines. A large sheath forming

¹The expression “Electrostatic Tether” is sometimes used to distinguish the use of electrodynamic tethers for charge precipitation applications from their use as space propulsion devices.

around this high-voltage tether is meant to act as a scattering structure for the high-energy electrons, causing some of them to fall prematurely into the *loss cone* of an Earth-bound “leaky magnetic bottle” [4]. In this application, the bare tether is biased negatively, creating an ion-attracting, electron-repelling plasma sheath around it. This allows for the scattering of high-energy electrons by the electric field, while minimizing the amount of collected current, due to the heavy mass of the collected ions as compared to electrons.

In the present application, the collected current is directly linked to the power expenditure necessary for maintaining the plasma sheath, and one therefore seeks to minimize current collection. Interestingly, this goal of minimizing current collection is the opposite of that demanded of bare tethers in the propulsive electrodynamic systems, in which the propulsive force is proportional to the amount of current flowing on the tether. The two quantities of interest are thus:

- the sheath dimension, which determine the “cross-section” of the particle scatterer;
- the collected ion current, which is an undesired secondary effect that translates into expended power.

Designers of charge-precipitation tether systems will need to consider various tether cross-section geometries in order to maximize sheath dimensions, while minimizing current collection. In addition, the ionospheric flow plays a role in the determination of the plasma sheath dimensions and current collection. Both the flow and geometry effects thus need to be assessed in order to provide the tools necessary for the development of this emerging technology.

1.1.3 Plasma Diagnostics Probes

Langmuir probes are widely used as plasma diagnostic devices, both in vacuum chamber experiments and in on-board spacecraft instruments [6, 7]. They allow for the determi-

nation of plasma parameters such as the electron temperature, extracted from the electron retardation regime, and the ion and electron densities, extracted from the ion and electron saturation regimes. Analytical expressions for current characteristics to conductive cylinders only exist for the two extreme geometrical cases, that is, for probes with very large radii (hundreds of Debye lengths) or small radii (one Debye length or less). In order to minimize perturbations and optimize the spatial resolution of the measurement, however, small probes are usually preferred, in which case the analytical expression for the orbital-motion-limited current can be used for both electron and ion collection. The orbital-motion-limited result only applies in stationary plasmas, but is still widely used for plasma diagnostics of flowing plasmas, which may lead to errors in the extracted plasma densities, especially when the electron saturation data are used for density extraction.

A new model that accounts for the effects of the plasma flow on current collection is needed to allow for the development of improved plasma-parameter extraction algorithms for use in the analysis of the current characteristics of Langmuir probes in flowing plasmas.

1.1.4 Other Applications

Although the applications outlined above define our requirements for the 2-D steady-state plasma model developed here, a multitude of other potential applications exist. For instance, this model could be adapted for the analysis of the interaction of a spacecraft with the surrounding ionospheric plasma, including spacecraft charging effects. Other possible applications include plasma processing, plasma screens, plasma-based thrusters for space propulsion, charge transport in solid-state materials (e.g., semiconductors), and space charge effects in solid or fluid dielectrics.

1.1.5 Description of the Problem & Regimes of interest

The three applications described above (propellantless propulsion, charge precipitation, and plasma diagnostics using Langmuir probes) require a detailed model of the plasma kinetics in order to allow for the accurate prediction of sheath structures and current collection.

For the propellantless propulsion application, electron current collection is the most important parameter of interest because it relates directly to the amount of thrust available to the system; electrodynamic tether designers are thus interested in maximizing current collection.

For the charge precipitation application, sheath size is of primary concern since it relates directly to the overall cross-section of the system and, therefore, its scattering efficiency. Ion current collection, however, must be minimized because it translates directly into expended power.

In addition, both of these applications will require designs that are survivable to collisions with small orbiting debris. This may involve multi-wire or similar concepts spreading the tether structure over several parallel elements.

The geometries encountered in those applications are somewhat similar, allowing for the definition of a generic problem applicable to all three technologies. The basic geometry under consideration is an arbitrarily-shaped 2-dimensional conductive object, i.e., a cylinder of arbitrary cross-section geometry and infinite length. Figure 1.3 illustrates some examples of geometries that are considered in this thesis either through the use of the proposed kinetic model or via experimental measurements. We describe them below.

Single Round Circular Cylinder The round cylinder is the most standard geometry for tethers as well as for Langmuir probes; we investigate it here using both simulations and experiments. We will use results for this geometry in order to validate our mod-

eling approach with existing results at low voltages, which are available for both the stationary [8] and flowing [17] cases.

Two Parallel Circular Cylinders Using multiple parallel wires as a tether structure is of interest both from the standpoint of collision survivability, applicable to both propulsion and charge precipitation, and from the standpoint of reducing the collected ion current in the electrostatic tether application.

The first logical step in the analysis of the multi-wire geometry is to seek an understanding of the physics involved in the two-wire geometry, which we develop using our kinetic model. We assess the scaling of the sheath around the two wires, as well as study interference effects involved in current collection. Results are validated against an existing model for wire interference [18] and qualitative comparisons are made with some of our experimental results involving slotted tapes, which basically were equivalent to 4 parallel wires.

Thin Tape Cylinder The thin tape cylinder is another fairly simple geometry that is an example of the geometries that could be considered for improved survivability from collisions. We are primarily interested in determining the effect of the tape width and plasma flow on collected electron current. Simulation results will be compared against our own experimental data and against existing models for tapes in stationary plasmas [11].

Slotted tape This geometry was investigated experimentally. It consists of a flat tape out of which slots were cut out, and is equivalent to a set of four parallel narrow tapes, as seen on Figure 1.3(d). The experimental results will help our understanding of sheath interference effects on current collection.

Even though we consider only a limited set of geometries as part of this thesis, our kinetic

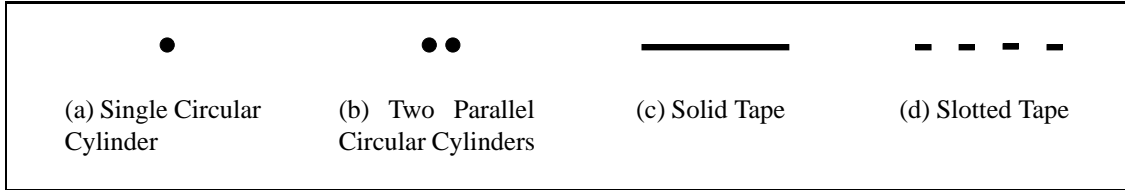


Figure 1.3: Four examples of the cylinder geometries under consideration.

model was developed for problems involving conductive cylinders with arbitrary cross-section geometries (i.e., any 2-D conductive object), as will become obvious in Chapter 2.

For each of the conductive cylinder geometries under consideration, the 2-D object is immersed in a 2-species, unmagnetized plasma (flowing or stationary), and biased at a specified potential $V_0 - V_p$ with respect to the background plasma potential V_p . When considering a flowing plasma, the flow will always be directed along the x axis.

Table 1.1 lists some estimated representative values for the parameters of interest corresponding to the propulsion and charge precipitation applications, along with corresponding estimates for the vacuum chamber experiment described in Chapter 3 and used in comparison with our kinetic model. It is seen that all forms of collisions play a very minor role in these plasmas, so that they can safely be modeled as *collisionless* plasmas (more detail on our assumptions can be found in Section 2.1). Another common feature among the three sets of parameters is that the effective plasma flow is much lower than the electron thermal velocity ($U \ll v_{the}$), which allows some simplifications for the treatment of the electron species. Such simplifications are not possible for ions, because the ion thermal velocity is seen to take on values that are alternatively smaller, larger, or on the order of the flow velocity. The implications of the Larmor gyroradius are discussed in Section 2.1.

	Vac. Chamber Experiments	Propellantless Propulsion	Charge Precipitation
Main Plasma Parameters			
Altitude (km)	–	300 km	1500 km
Dominant ion species	Xe ⁺	O ⁺	H ⁺
Ion mass (kg)	2.18×10^{-25}	2.7×10^{-26}	1.7×10^{-27}
Plasma density n_0 (m ⁻³)	5×10^{14} – 5×10^{15}	10^{11}	1.8×10^{10}
Electron/ion temperature (eV)	1.5–1.8	0.1	0.4
Ion thermal velocity (m/s)	1049–1194	644	6136
Electron thermal velocity (m/s)	$5.1\text{--}5.6 \times 10^5$	1.3×10^5	2.7×10^5
Orbital or flow velocity (m/s)	6000	7700	7100
Ion flow energy (eV)	25	5	0.27
Electron Debye length (m)	$1.3\text{--}4.5 \times 10^{-4}$	7.4×10^{-3}	3.5×10^{-2}
Collision MFP (m)			
Electron-neutral (elastic)	8.5	$10^3\text{--}10^4$	$10^4\text{--}10^5$
Ion–neutral (elastic)	28	3×10^3	10^8
Ion–neutral charge-exchange	2.5		
Electron–electron	5–32.6	10^6	10^7
Electron–ion	4.9–31.9	10^6	10^7
Ion–ion	3.3–23.5	10^6	10^7
Ion–electron	7.5–64.3	10^3	10^5
Ion Larmor gyroradius (m)	26–28.5	5	7.4
Electron Larmor gyroradius (m)	0.53–0.58	0.03	0.09

Table 1.1: Approximate plasma parameters for the main applications of interest [19–24] and for our vacuum chamber experiments described in Chapter 3. MFP is an acronym for *Mean Free Paths*.

1.2 Cylindrical Plasma Probes: Background and Literature Review

In the following we summarize the present state of research for the modeling of cylindrical conductive cylinders immersed in plasmas. Existing theories are described for the current collection and sheath structure that are applicable to a limited range of bias potentials, geometries and flow regimes.

1.2.1 Stationary plasmas

When considering the problem of a round cylindrical probe immersed in a stationary plasma, there are two key parameters for the applications of interest:

- *Current Collection* (electron or ion current) is of concern in all three applications. For propellantless propulsion, the tether bias potential is primarily positive, and we seek to maximize electron current collection because it translates directly into available thrust. For charge precipitation, the tether is biased negatively, and we seek to minimize the amount of ion current collected, because it translates into expended power. In plasma diagnostics using Langmuir probes, expected current characteristics as a function of plasma parameters must be precisely known in order to allow for parameter extraction;
- *Plasma sheath size* and structure is a determining factor in the charge precipitation application of electrostatic tethers. It determines the effective dimensions of the particle scatterer and thus its efficiency at precipitating high-energy electrons into the loss cone [4].

The sheath structure and dimensions are closely linked to the particle kinetics, and cannot be obtained by direct calculation for small and moderate-sized probes, even in the most simple case of a round cylindrical probe in a stationary plasma. The Child Law sheath [25] analytical expression, for example, is only applicable to probes with large dimensions as a function of the Debye length, i.e., it is only valid in the thin-sheath limit, which is outside of our regimes of interest.

Whereas sheath sizes cannot be computed directly for any probe size, exact analytical expressions have been derived for the collected current to an attracting round conductive cylinder immersed in a stationary, Maxwellian plasma. These expressions are only appli-

cable to two extreme regimes: the *thin-sheath* (infinite cylinder radius) and *orbital-motion* (vanishing cylinder radius) limits. In the following, we provide a derivation of these limits.

1.2.1.1 Thin Sheath Limit

When the cylinder radius becomes sufficiently large, the current density collected to the cylinder approaches that which would be collected on an infinite plate: this is the thin-sheath limit.

Let us assume that an infinite plate, normal to the x axis, is the rightmost bound of a 2-species Maxwellian plasma, with the velocity distribution functions of either plasma species given by

$$f_{e,i}(v_x, v_y) = \frac{n_0 m_{e,i}}{2\pi e T_{e,i}} \exp \left\{ -\frac{m_{e,i}}{2eT_{e,i}} (v_x^2 + v_y^2) \right\}, \quad (1.1)$$

where n_0 is the background plasma number density in m^{-3} , $m_{e,i}$ is the electron or ion mass in kg, $T_{e,i}$ is the electron or ion temperature in eV, and the velocity components v_x and v_y are in m/s. First, note that the background density n_0 is recovered by simply integrating over velocity space:

$$n_{e,i} = \int_{v_x=-\infty}^{+\infty} \int_{v_y=-\infty}^{+\infty} f_{e,i}(v_x, v_y) dv_x dv_y = n_0. \quad (1.2)$$

Now, let us assume that the infinite plate is biased at a potential V_0 with respect to the plasma potential (i.e., $V_{\text{plate}} - V_{\text{plasma}} = V_0$). For either population (electrons and ions), the current density collected on the infinite plate can be obtained by integrating the accelerated or decelerated particle flux over all rightward-directed velocities on the plate's left-side surface, i.e.

$$\begin{aligned} J_{e,i} &= q_{e,i} \Gamma_{e,i} \\ &= q_{e,i} \frac{n_0 m_{e,i}}{2\pi e T_{e,i}} \times \int_{v_x=\sqrt{\max(0, -\frac{2q_{e,i}V_0}{m_{e,i}})}}^{+\infty} \int_{v_y=-\infty}^{v_y=+\infty} v_x \exp \left\{ -\frac{m_{e,i}}{2eT_{e,i}} \left[\left(v_x^2 + \frac{2q_{e,i}V_0}{m_{e,i}} \right) + v_y^2 \right] \right\} dv_x dv_y. \end{aligned} \quad (1.3)$$

Performing the integral over v_y , we get

$$J_{e,i} = q_{e,i} n_0 \sqrt{\frac{m_{e,i}}{2\pi e T_{e,i}}} \int_{v_x = \sqrt{\max(0, -\frac{2q_{e,i}V_0}{m_{e,i}})}}^{+\infty} v_x \exp \left\{ -\frac{m_{e,i}}{2eT_{e,i}} \left(v_x^2 + \frac{2q_{e,i}V_0}{m_{e,i}} \right) \right\} dv_x. \quad (1.4)$$

Finally, we integrate over v_x and obtain

$$J_{e,i} = \underbrace{q_{e,i} n_0 \sqrt{\frac{e T_{e,i}}{2\pi m_{e,i}}}}_{J_{\text{th}}} \times \begin{cases} 1 & q_{e,i} V_0 \leq 0, \\ \exp \left\{ -\frac{q_{e,i} V_0}{e T_{e,i}} \right\} & q_{e,i} V_0 > 0. \end{cases} \quad (1.5)$$

In Equation (1.5), J_{th} is simply the *thermal current density*, i.e., the average random current density one finds at any location within the background plasma. This result shows that the current density varies exponentially under a repelling bias and saturates to a constant value, the thermal current J_{th} , for an attracting bias. The reason why the current density is limited to the thermal current is that the sheath only extends in a single dimension, which precludes any particle focusing.

1.2.1.2 Orbital-Motion Limit (“Thick” Sheath Limit)

We now consider the opposite limit, corresponding to a vanishing cylinder radius. In practice, this limit is achieved when the cylinder radius falls below the Debye length. An analytical expression for the OML current was first derived by *Mott-Smith and Langmuir* [26], based on conservation of energy and angular momentum in a central force field. The orbital-motion-limit (OML) regime is attained when the cylinder radius is small enough that all particle trajectories terminated on the cylinder’s surface are connected to the background plasma, regardless of their angular momentum (i.e., none are connected to another location on the probe’s surface). Since, in a collisionless plasma, the distribution function is conserved along particle orbits, having all “directions of arrival” populated corresponds to an upper limit on the collected current. In the following, we derive the OML current based on the precedent argument, similar to the approach used by *Laframboise* [6].

Using the alternative, but equivalent representation of velocity space in the form of kinetic energy $\kappa = \frac{m_{e,i}(v_x^2 + v_y^2)}{2eT_{e,i}}$ in units of electron-volts and angular direction α in units of radians, the energy distribution function of any given species at the surface of the probe may be written:

$$g_{e,i}(\kappa, \alpha) = \begin{cases} \frac{n_0}{2\pi T_{e,i}} \exp\left\{-\frac{e\kappa + q_{e,i}V}{eT_{e,i}}\right\} & \kappa > \max(0, -\frac{q_{e,i}V}{e}), \\ 0 & \kappa \leq \max(0, -\frac{q_{e,i}V}{e}), \end{cases} \quad (1.6)$$

where V is the local electric potential. The number density $n_{e,i}$ at the probe's surface is recovered by simply integrating over all of kinetic energy space and half of the angular directions (since the probe blocks half of velocity space):

$$\begin{aligned} n_{e,i} &= \int_{\kappa=0}^{+\infty} \int_{\alpha=\alpha'+\pi/2}^{\alpha=\alpha'+\frac{3\pi}{2}} g_{e,i}(\kappa, \alpha) d\kappa d\alpha \\ &= \frac{1}{2} n_0 \begin{cases} \exp\left(-\frac{q_{e,i}V}{eT_{e,i}}\right), & q_{e,i}V \leq 0, \\ 1, & q_{e,i}V > 0, \end{cases} \end{aligned} \quad (1.7)$$

where α' is the angle between the outward surface normal and the x axis. Likewise, the OML current density can be obtained by integrating the normal flux to the surface:

$$\begin{aligned} J_{e,i} &= q_{e,i} \Gamma_{e,i} \\ &= q_{e,i} \int_{\kappa=0}^{+\infty} \int_{\alpha=\alpha'+\pi/2}^{\alpha=\alpha'+\frac{3\pi}{2}} \underbrace{\sqrt{\frac{2e\kappa}{m_{e,i}}} \cos(\alpha - \alpha') f_{e,i}(\kappa, \alpha)}_{v_\perp} d\kappa d\alpha \\ &= q_{e,i} n_0 \underbrace{\sqrt{\frac{eT_{e,i}}{2\pi m_{e,i}}}}_{J_{th,e,i}} \begin{cases} \frac{2}{\sqrt{\pi}} \sqrt{-\frac{q_{e,i}V}{eT_{e,i}}} + \exp\left(-\frac{q_{e,i}V}{eT_{e,i}}\right) \operatorname{erfc}\left(\sqrt{-\frac{q_{e,i}V}{eT_{e,i}}}\right), & q_{e,i}V \leq 0 \\ \exp\left(-\frac{q_{e,i}V}{eT_{e,i}}\right), & q_{e,i}V > 0 \end{cases}. \end{aligned} \quad (1.8)$$

J_{th} is the thermal current density and the complementary error function $\operatorname{erfc}(x)$ is given by $\operatorname{erfc}(x) = \frac{2}{\sqrt{\pi}} \int_x^\infty e^{-t^2} dt$. The repelled-species current is the same in the thin sheath and OML limits, as can be seen by comparing (1.5) and (1.8) — this is called the retardation region of the current characteristic and is valid in all regimes. The attracted-species current is constant and equal to the thermal current in the thin-sheath limit, whereas in the OML

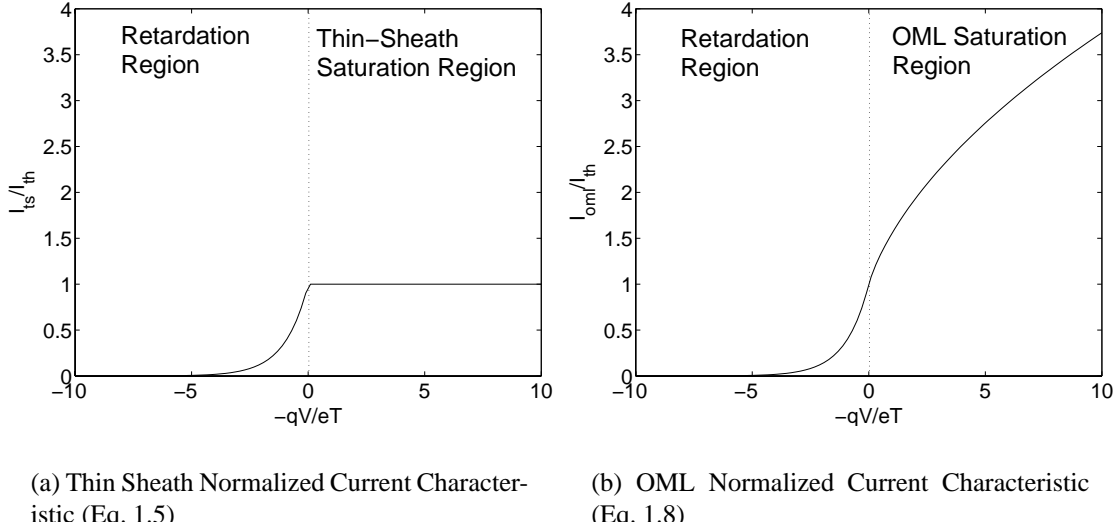


Figure 1.4: Normalized current characteristics in the thin sheath limit and orbital motion limit.

regime, it grows without limit with the effective applied bias potential $\frac{q_{e,i}V}{eT_{e,i}}$; this region is called the saturation region of the current characteristic. Figure 1.4 depicts the limits obtained in (1.5) and (1.8) for both the retardation (repelled particles) and saturation (attracted particles) regimes.

1.2.1.3 Numerical Approaches for Arbitrary Probe Sizes

To address cases other than the thin-sheath and OML limits, a consistent solution to the problem of the stationary ion-attracting round cylindrical probe was first provided by *Bernstein and Rabinowitz* [27], who developed a Poisson–Vlasov consistent, cylindrical 1-D model based on approximations of mono-energetic ions and negligible electron current. The computations consisted of numerically integrating an ordinary differential equation of one variable. *Laframboise* [8] later developed a consistent iterative numerical scheme that allowed for Maxwellian distributions (far from the probe) for both the attracted and repelled species. This theory involves the iterative resolution of a nonlinear system of integral equations, and is applicable to all temperatures, probe sizes with respect to the

Debye length and potential values, although results were only given for relatively small bias potentials.

In addition to providing results for the current collected to round cylindrical probes of arbitrary sizes, these numerical schemes were the first to provide self-consistent results for the density profiles of the attracted and repelled species.

1.2.2 Flowing Plasmas

1.2.2.1 Treatments Based on a Symmetric Potential Profile Assumption

Several authors have addressed, in a first-order sense, the problem of *ion collection* by a round cylindrical probe immersed in a flowing plasma, using the crucial assumption of a radially symmetric potential profile unaffected by any flow effects. *Mott-Smith and Langmuir* [26] derived an asymptotic formula valid in the limit of large speed ratios (relative to the ion thermal velocity) for the current characteristic in the large-sheath limit (orbital motion limit). *Kanal* [28] derived similar expressions valid in the limit of small speed ratios. *Hoegy and Wharton* [29] generalized those results by providing expressions valid for all speed ratios, for the limiting cases of thin-sheath, large-sheath (orbital-motion-limit), and retarding regimes.

Godard and Laframboise [30] went further by developing a numerical model that allowed for all probe radii to be considered in the flowing case by using the 1-D cylindrically symmetric potential profiles obtained by *Laframboise* [8] as the assumed electric potential.

In the case of the mesosonic regime, where the velocity of the flow is much larger than the ion thermal velocity but much smaller than the electron thermal velocity, only ion collection can be addressed by an approximate solution based on an assumed symmetric potential profile. Such an approximation would show virtually no departure from the stationary results in the case of electron collection, due to their large thermal velocity as compared to the speed of the flow for the regimes of interest here. The effects of the flow

on the collection of the light species — the electrons— are thus only indirect. That is, these effects only occur due to the asymmetries in the potential profile around the probe that are induced by the heavier ion species. However indirect, these effects can be significant, as will be seen in Chapter 4.

Even for the ion-attracting case, the assumption of a symmetric profile could fail to provide a correct answer at least in cases showing one or more of these two conditions [30]:

- the probe radius is not small with respect to the Debye length, implying a non negligible and likely asymmetric ion space-charge distribution near the collector;
- the ratio of flow energy to bias potential is neither very small (a small flow could only cause small asymmetries) nor very large (in which case the bias potential could not significantly affect the flow).

1.2.2.2 Consistent Numerical Treatments

A few numerical treatments have been performed to consistently model flow effects on the sheath structure (i.e., asymmetries) and current collection to a round cylinder. In the following we discuss some of the work that has been done using steady-state kinetic approaches or particle-in-cell implementations.

1.2.2.2.1 Steady-State Kinetic Treatments *Xu* [17] and *McMahon* [22] have worked on consistent steady-state kinetic models to address the problem of ion collection to a round cylinder in a flowing plasma. The main difference between their approaches is that Xu uses an *inside-out* trajectory tracking procedure whereas McMahon uses an *outside-in* strategy.

The *outside-in* steady-state method used by *McMahon* [22] bears some similarity with the popular particle-in-cell plasma modeling techniques [25], in part due to the manner in which the discrete charges are assigned to a fixed set of grid nodes. This approach is

intrinsically more efficient computationally, at the expense of some added numerical noise associated with the charge assignment.

The *inside-out* approach used by Xu [17] and in the present work, although not as efficient computationally, is based on a direct sampling of the velocity distribution function at the nodes of a mesh.

1.2.2.2 Particle-in-Cell Treatment *Onishi* [31] has performed simulations of a single electron-attracting cylinder immersed in a flowing unmagnetized plasma using a particle-in-cell approach. His findings indicate that a population of trapped electrons, upstream of the cylinder, is necessary for the plasma to reach a steady state. This requirement is attributed to the fact that the local increase of the ion density on the ram side of the cylinder, beyond the ambient density, must be matched by an increased electron density to satisfy the quasi-neutrality condition. Limitations on the computational zone size may be in part responsible for this computational requirement, and it is not clear whether or not this is a physical requirement.

1.3 Summary of Research Contributions

The general aim of the research that has led to this thesis was to improve the understanding of the steady-state perturbations caused in a two-species plasma (flowing or stationary) by the introduction of a long conductive cylinder (e.g., an electrodynamic tether) of arbitrary cross-section geometry, biased at a specified potential. Specifically, our main interests were to determine

- the structure of the plasma sheath/pre-sheath, and
- the amount of collected current

as a function of cylinder geometry, bias potential, and plasma flow speed. These objectives have required both the development of a new computer model capable of accurately simulating the general problem of interest, and an experimental investigation using a vacuum chamber. Consequently, the contributions of the research presented in this thesis fall in one of three major categories:

1. a computational model for the self-consistent modeling of arbitrary 2-D conductive structures immersed in flowing plasmas;
2. new computer simulation results for regimes (combination of biases, geometries, and plasma flow) not addressed in previous research;
3. new experimental results pertaining to the effects of plasma flow and geometry on electron collection.

We describe these contributions in more detail in the following three sub-sections corresponding to the three major categories outlined above.

1.3.1 A Self-Consistent Steady-State Kinetic Model for Arbitrary 2-D Conductive Structures in Flowing Plasmas

A new computational model was created for the self-consistent kinetic modeling of the charge-imbalance structure forming around arbitrary two-dimensional conductive objects immersed in stationary and flowing two-species plasmas. The following are some new contributions brought about by this new model.

1. A *dynamic, adaptive, unstructured meshing strategy* that allows support for arbitrary 2-D geometries and can accurately resolve features with widely disparate scales, such as very small probes together with very large sheath structures. Another typical plasma feature that requires this dynamic resolution capability is the narrow surge

of the net charge density found at the sheath edge (a location not known *a priori*) in the case of high-voltage biases, which is attributed to the combination of the density profiles of the counter-streaming attracted and repelled species.

2. A new approach based on a *Tikhonov-regularized Newton method* for the efficient minimization of the nonlinear least-squares problem, which provides a numerical approximation for the fixed point of the Poisson–Vlasov operator. This approach is robust to numerical instabilities and numerical noise as well as very versatile, in that it can successfully solve a wide class of 2-D problems without the need for empirical tuning of parameters such as is required by overrelaxation techniques [17].
3. Support for the *kinetic treatment of both ions and electrons*, even in the case of a flowing plasma. Previous treatments of the flowing plasma case, applied for ion collection only, have assumed “Boltzmann” electrons [17, 22].
4. A *parallel implementation* of the 2-D Vlasov solver based on the PVM library [32], which enables a very accurate representation of plasmas extending over large domains within reasonable computing times. The parallel code is a coarse-grained MPMD (Multiple Processors, Multiple Data) implementation that runs efficiently on a dynamically-configured scattered network of workstations, using their idle computing time. The code was developed and tested on scattered networks of SunTM and Linux workstations, and also has been tested successfully on a standard Linux cluster.

1.3.2 New Simulation Results

Using this new steady-state kinetic model, a collection of new results applicable to the problems of interest have been obtained via computer simulation. These new results

provide:

1. an *extension of the operating regimes* covered by *Laframboise* [8], *Xu* [17] and *McMahon* [22] to a wider range of bias potentials. Bias potentials from an arbitrary small fraction of the plasma temperature T up to $10,000T$ have been successfully covered by the cylindrical 1-D model. The full 2-D model has reached $640T_e$.
2. an *assessment of wire interference effects* on sheath structure and current collection based on two parallel round cylinders with various center-to-center spacings in a stationary plasma.
3. an *assessment of the sheath structure and current collection for the case of a *thin tape cylinder**.
4. an *assessment of plasma flow effects* on sheath structure and current collection for both ion- and electron-attracting round cylinders. The electron-collecting case has not been previously successfully analyzed in an unmagnetized plasma.² As for the ion-collecting case, it has previously been addressed by *Xu* [17] and *McMahon* [22] using a Boltzmann approximation for the electrons. The present research contains the first results of simulations using a non-PIC fully kinetic treatment for both species in a flowing plasma.

To the author's knowledge, items 2 and 3 constitute the first fully self-consistent kinetic simulation results for cylinder geometries other than circular cylinders.

1.3.3 New Experimental Results

Experimental testing of electron collection to tether samples of various geometries in a mesosonic xenon plasma were performed using the *Large Vacuum Test Facility* at the

²Onishi [31] has reported that his particle-in-cell code could not reach a steady state when simulating a flowing, collisionless, unmagnetized plasma.

University of Michigan’s Plasmadynamics and Electric Propulsion Laboratory. New experimental results were obtained pertaining to

- the effect of plasma flow on the electron collection to round cylinders (a significant enhancement was observed); and
- a comparison of electron current collection efficiencies of solid and slotted tape tether samples, oriented parallel and perpendicular to plasma flow.

The geometry effects observed during these experiments are in general agreement with those predicted by our kinetic model. As for the electron current enhancement associated with the mesosonic plasma flow, it cannot be predicted by our collisionless plasma model. However, the sheath structures obtained via simulation give some indication as to how pre-sheath collisions may have caused the observed enhancement.

1.4 Dissertation Overview

The five chapters of this dissertation are structured as follows:

Chapter 1 provides motivation, defines the problem of interest, reviews previous relevant research, and summarizes research contributions.

Chapter 2 develops the theory and describes the computer implementation of a steady-state Poisson–Vlasov self-consistent computational model based on kinetic theory. The model is applicable to a wide range of 2-D objects immersed in stationary and flowing plasmas. Both a 1-D cylindrical implementation and a full 2-D implementation are presented side-by-side.

Chapter 3 describes the experimental testing of electron-collecting tether samples in a mesosonic flowing plasma. The sample geometries tested include a round cylinder, thin solid tapes, and thin slotted tapes.

Chapter 4 presents and discusses the results and analyses of the kinetic simulations performed using the computer model defined in Chapter 2. Comparisons with our experimental results are also shown.

Chapter 5 discusses the conclusions of this dissertation and provides suggestions for future research.

CHAPTER 2

Steady-State Poisson–Vlasov Model: Theory and Implementation

We present the theory and software implementation of a consistent, steady-state, electrodynamic plasma model based on kinetic theory. The solver presented here is best classified as a Vlasov code based on a kinetic description of plasmas [33]. It differs from particle-in-cell methods in that the Vlasov equation is solved directly instead of resorting to a set of discrete macro-particles. It is also distinct from Eulerian Vlasov implementations [34], owing primarily to the fact that a steady-state “non time-varying” solution is sought directly, without resorting to incremental time stepping. The steady-state solver presented here bears some similarity with previous work addressing other geometries [35–37], and may be regarded as a 2-D extension of the 1-D cylindrical model developed by *Laframboise* [8].

The general aim of this model is to numerically solve, in a self-consistent manner, the Poisson and Vlasov equations in a steady state over a large computational region around an arbitrarily-shaped 2-D conductive body in a collisionless, unmagnetized, flowing 2-species plasma. The implementation of the 2-D solver, called KiPS-2D (Kinetic Plasma Solver, 2-dimensional) consists of successive linearizations of the nonlinear Poisson–Vlasov operator, within a Tikhonov-regularized Newton iterative process. Following are listed the main features of the proposed model and solver:

- it allows for the representation of the complete, arbitrary velocity distribution of both plasma species at all sampled locations in the computational domain;
- it can model plasma cross flow in all speed regimes with respect to the ion thermal velocity;
- it includes a finite-element-based Poisson solver incorporating a background plasma boundary condition based on asymptotic analytical results [27];
- it provides a dynamic, adaptive, unstructured meshing strategy, allowing for the resolution of sheath asymmetries induced by the plasma flow and the support of conductive objects with arbitrary 2-D geometries;
- it allows for the simulation of very large computational domains in order to accommodate the pronounced pre-sheath elongation along the direction of plasma flow. The variable grid size is tailored locally to efficiently accommodate potential variations. Numerical instabilities resulting from large grid sizes are handled using a Tikhonov regularization process;
- its steady-state Vlasov solver features a parallel implementation based on the PVM library [32], allowing it to run on either a single host, a parallel architecture, or a scattered network of workstations based on a MPMD (Multiple Processors, Multiple Data) scheme.

Although the primary purpose of this work was to provide a 2-D solver, a 1-D cylindrical implementation of this model, called KiPS-1D, was also developed. This 1-D code has been validated against results from *Laframboise* [8], and extends the covered range of probe bias potentials from $25T_e$ to $10,000T_e$. In addition, it serves as a validation tool for the 2-D implementation of the code. In the following sections, the general formulation will

be described consistent with the 2-D implementation. However, where necessary, specific derivations will be presented pertaining to the 1-D and 2-D implementations of each component. Note that the main symbols used throughout this chapter and others are listed in Appendix A for convenience.

2.1 Basic Assumptions

The aim of the steady-state, consistent kinetic plasma model presented in this thesis is to provide an *accurate* representation of the *dominant* physical mechanisms involved in the formation of a steady-state sheath as well as in current collection to 2-D conductive bodies. In setting up the basic physics underlying the model, we make the following assumptions regarding the physical mechanisms involved in the sheath–plasma system:

- the plasma is collisionless;
- a steady state exists;
- the plasma is unmagnetized;
- the background plasma is a drifting Maxwellian;
- end effects are negligible; and
- trapped orbits are unpopulated.

Let us now describe in more detail each of these assumptions.

The Plasma is Collisionless Several types of collisions can be considered. Based on the very long mean free paths given in Table 1.1, we can certainly neglect the elastic ion–neutral and electron–neutral collisions for all three cases (vacuum chamber experiment, electrodynamic tethers, and electrostatic tethers), because they are much larger than the typical sheath sizes we are interested in.

Coulomb collisions are also neglected, i.e., we assume that the forces experienced by any of the charged particles forming the plasma are entirely due to the collective effect of the charge density contributed by all particles, not to their individual effect. This assumption is accurate for sufficiently low plasma densities (such as space plasmas), in which any given particle very rarely “meets” another particle in a close encounter. In other words, the number of particles contained within the “sphere of influence” (Debye sphere) of a given particle is so large that the overall forces are overwhelmingly attributable to the bulk of the plasma.

A Steady State Exists We assume that there exists a steady state of the plasma density and potential distributions in the frame of reference of the moving tether or probe. By “steady state” we imply a state in which there are no time variations of the plasma density or electric potential anywhere in the frame of reference of the moving object. Our definition of the steady state allows for a steady flow of plasma particles in any directions where applicable, including a net drift component of the plasma bulk due to the orbital motion of the tether. This implies that time variations may be perceived as seen from other frames of reference.

The existence of a steady state will be proved *a posteriori* by showing that we can find a self-consistent, steady-state solution satisfying both the steady-state Vlasov and Poisson equations. Proving the existence of a steady state is not, however, a guarantee that no time variations can exist even in the absence of transients and external excitations. Nonetheless, the steady-state solution that we provide here can be regarded as a lowest energy state that the electrodynamic forces will seek to attain in order to minimize the system energy.

The Plasma is Unmagnetized We assume that the effect of the magnetic field on the so-

lution is negligible, and therefore choose to neglect the magnetic field force in our computational model. To qualify this approximation, let us consider the effect of the magnetic field for the main applications of interest. This effect can be gauged by comparing the typical gyroradius of the *attracted species* within the computational domain to the size of the computational zone, which is typically on the order of the sheath dimensions. The effect of the magnetic field on the repelled species' density is unimportant as long as the said species does not have a sizable drift component as compared to its thermal distribution, because then the local densities are solely determined by the local potential for all practical purposes. This applies to the electrons when using a negative bias potential, since their drift velocity is negligible in the regimes of interest.

For charge precipitation, the magnetic field effect on the repelled electrons is therefore negligible for the reason just mentioned. As for the attracted ions, Table 1.1 lists for their gyroradius in the background plasma a value of 7.4 m, which is admittedly smaller than the typical sheath diameters of interest for tether bias potentials in the vicinity of 100,000 volts. However, this relatively small value of the Larmor gyroradius should be put into perspective, because it only applies in the background plasma where particle velocities are on the order of the thermal velocity. Within the accelerating potential of the sheath structure however, the attracted particles are accelerated to velocities that can be up to a few hundred times the thermal velocities, for tether bias potentials of a few tens of thousands of volts. The gyroradius r_G is proportional to the ratio of the particle velocity to the magnetic field intensity [38],

$$r_G = \frac{m_i v}{eB}, \quad (2.1)$$

where the magnetic field B is in units of Tesla and v is the local ion velocity. Inside the sheath the accelerated species' gyroradius scales proportional to particle velocities,

to values much larger than the corresponding sheath size. For example, consider a one-Debye-length-radius ion-attracting tether, used for charge precipitation, biased at 100,000 volts. Scaling the ion Larmor gyroradius proportional to the ratio of in-sheath velocity to the thermal velocity, the ion gyroradius close to the probe is given by

$$r_G \approx \sqrt{\frac{100000\text{eV}}{0.4\text{eV}}} r_{GL} \Big|_{r_{GL}=7.4 \text{ m}} = \sqrt{250000} \times 7.4 \text{ m} = 3700 \text{ m}. \quad (2.2)$$

This result is significantly larger than any practical sheath size, and emphasizes the fact that the magnetic field should not play a significant role in this application. For this specific bias potential and a tether radius of one Debye length, the sheath diameter is about 92 meters according to the asymptotic expressions derived in Chapter 4.

For propellantless propulsion applications, the electrons are the attracted species. Their relatively small Larmor gyroradius of 3 cm would be scaled up, within a sheath created by a typical 1 kV-biased tether, to a value of

$$r_G \approx \sqrt{\frac{1000}{0.1}} r_{GL} \Big|_{r_{GL}=0.03 \text{ m}} = \sqrt{10000} \times 0.03 \text{ m} = 3 \text{ m}, \quad (2.3)$$

which is also significantly larger than the approximate sheath diameter of 0.5 m.

In general, we can therefore say that attracted species can be expected to have large gyroradii for most of the sheath as compared to the sheath's dimensions. This means that the magnetic field is playing a relatively minor role in the sheath formation and current collection processes, and may thus be safely ignored for these purposes, especially for the charge precipitation application where bias voltages are typically larger than in the propulsion application. A similar reasoning can be made based on a comparison of the magnitudes of the electrostatic and magnetic forces acting on the particles: the electrostatic field forces can be as much as a few orders of magnitude larger than the magnetic field forces.

Our kinetic model therefore assumes that no magnetic fields are present, resulting in a purely electrostatic solution of the plasma sheath.

The Background Plasma is a Drifting Maxwellian Although no assumptions are made with regards to the velocity distributions *within* the computational domain, the source of the plasma entering the computational domain must be known and is defined as a boundary condition. The computational domain must be made sufficiently large to include all of the major perturbations on the plasma caused by the presence of a conductive object. The velocity distribution of the incoming plasma particles entering the simulation domain is thus assumed to closely correspond to the ambient velocity distribution that exists in the background (undisturbed) plasma. In a stationary plasma, the 2-D velocity distribution is assumed to be Maxwellian (see equation 1.1). For a moving plasma, the background velocity distribution function for both electron and ion species becomes

$$f_{e,i}(v_x, v_y) = \frac{n_0 m_{e,i}}{2\pi e T_{e,i}} \exp \left\{ -\frac{m_{e,i}}{2eT_{e,i}} [(v_x - U)^2 + v_y^2] \right\}, \quad (2.4)$$

where we assume that the plasma is moving along the direction of the x axis with velocity U . Note that the v_z dependence of the 3-D velocity distribution function has been integrated out into a constant in front of equations (1.1) and (2.4) since we only consider 2-D structures in unmagnetized plasma, which implies that the v_z Maxwellian dependence of the plasma is unchanged throughout the computational domain. Section 2.4.2.2 provides more detail regarding the method used to account for the small perturbations to this distribution function that occur between the background plasma (at $r \rightarrow \infty$) and the outer boundary of the computational domain.

End Effects are Negligible Probe end effects are neglected in this treatment. This is hardly an approximation in the case of bare, space borne electrodynamic tethers,

which are typically several kilometers long, corresponding to lengths of tens of thousands of Debye lengths and beyond. In the case of laboratory probes of more modest lengths, the end effect can be neglected provided that the cylinder is of sufficient length. The typical probes considered here are several hundred to a few thousand Debye lengths long. In addition, it has been shown, at least for ion-attracting probes, that end effects are negligible provided that the probe is oriented perpendicular to the direction of plasma flow. [39]

Trapped Orbits are Unpopulated In our analysis, we assume that trapped particle orbits are unpopulated, which is consistent with the treatments described by *Laframboise* [8] and *Xu* [17] (more detail is given in Section 2.4). This assumption follows from the previous “collisionless” and “steady-state” assumptions. When both of these assumptions hold, all particles present anywhere in the vicinity of the 2-D object can be traced back to the background plasma (the “source”) on collisionless orbits. Therefore closed orbits cannot be populated because they have no source.

Collisions, when they occur, may be regarded as scattering events that can displace a particle from one “collisionless orbit” to another. The present assumption, based on a “conservation of orbits” argument, is appropriate for the plasmas of interest (see Table 1.1), because they feature very few collisions, implying that the “paths” connecting two points in the background plasma or connecting the background plasma to the tether can be traversed by a particle with virtually no collision events. Time variations, which could be induced by external perturbations such as variations in the plasma environment, can also be regarded as scattering events, similar to collisions. The present treatment does not account for any “filling” of the trapped orbits that could result from such time variations. The impact of collisional and time-varying effects on the level of filling of trapped orbits will be assessed as part of future re-

search. Some authors have provided indications as to how this may be done [40, 41].

As pointed out by Prof.Laframboise³ in recent discussions, trapped orbits could also potentially be filled by some of the particles entering through the ends of the cylindrical sheath of a tether, since some of the so-called “trapped” collisionless orbits may actually be connected to the background plasma through the hemispherical end caps of the long, but finite, cylindrical sheath enclosing the tether. The level of “steady-state filling” of trapped orbits attained through this mechanism should be assessed as part of future research but is beyond the scope of the present work.

2.2 Poisson–Vlasov Representation of Collisionless Plasmas

Obtaining a simultaneous solution in two dimensions for the asymmetric steady-state electric potential distribution and charge density distributions of both plasma species (ions and electrons) requires the ability to solve, self-consistently, Vlasov’s equation for each species and Poisson’s equation for the electric potential and charges, while satisfying appropriate boundary conditions.

Both the electric potential and charge densities are sampled on a piecewise-triangular mesh, which is generated using the Bidimensional Anisotropic Mesh Generator (*BAMG*) developed at INRIA, France [42]. An adaptive process was implemented whereby the *BAMG* mesher is used to periodically refine the mesh based on the best available approximation of the net charge density and potential distributions.

In charged media such as a plasma, the steady state of the potential distribution and net charge distribution obeys Poisson’s equation [43],

$$\nabla^2 V(x, y) = -\frac{\rho(x, y)}{\epsilon_0}, \quad (2.5)$$

³Prof. James G. Laframboise, York University, Ontario, Canada.

at any point within the plasma. In addition, each species comprising the plasma, that is, electrons and ions, is composed of particles with a distribution of velocities at any point in space $f_{3d}(x, y, z, v_x, v_y, v_z)$. In an unmagnetized electrostatic plasma bounded with 2-dimensional boundaries, the distribution of velocities along the third dimension is independent of position, such that we only need to keep track of the 2-dimensional velocity distribution function obtained by integrating along v_z

$$f_{2d}(x, y, v_x, v_y) = \int_{v_z=-\infty}^{v_z=+\infty} dv_z f_{3d}(x, y, v_x, v_y, v_z), \quad (2.6)$$

where the z variable was dropped because the 2-D boundary conditions preclude any dependence on z . The number density of each species is obtained by integrating the velocity distribution function over all velocity space,

$$n_{e,i} = \int \int f_{e,i}(x, y, v_x, v_y) dv_x dv_y, \quad (2.7)$$

where the indices e and i refer to electrons and ions, respectively. The net charge density results from

$$\rho(x, y) = q_i n_i(x, y) + q_e n_e(x, y), \quad (2.8)$$

where q_e and q_i are the electron and ion particle charge.

In a collisionless, unmagnetized plasma at the steady state, the velocity distribution functions $f(x, y, v_x, v_y)$ of each species is conserved along particle orbits. This is stated by Vlasov's equation in the steady state ($\frac{\partial f}{\partial t} = 0$) [25],

$$\frac{df_{e,i}}{dt} = v_x \frac{\partial f_{e,i}}{\partial x} + v_y \frac{\partial f_{e,i}}{\partial y} - \frac{q_{e,i}}{m_{e,i}} \frac{\partial V}{\partial x} \frac{\partial f_{e,i}}{\partial v_x} - \frac{q_{e,i}}{m_{e,i}} \frac{\partial V}{\partial y} \frac{\partial f_{e,i}}{\partial v_y} = 0, \quad (2.9)$$

where we substituted the electric field components with the gradient of the electric potential, i.e., $\vec{E} = -\nabla V$. Given a known potential distribution and a boundary condition for the incoming particles at the outer boundary of the computational domain, the method of characteristics can be used to solve (2.9) for the velocity distributions $f_{e,i}(x, y, v_x, v_y)$ of both the electrons and ions, at all positions and for all velocities.

The use of the method of characteristics for the resolution of Vlasov's equation in plasma problems was reported early on [36], and was referred to as the *inside-out* procedure. It consists of tracking a particle's trajectory back in time until it intersects the “source boundary” (which in our case is the outer boundary) of computational space, where the velocity distribution function is sampled. Any trajectory not originating from the outer shell is deemed unpopulated [8]. Such is the case for trajectories originating from the tether itself, which we assume does not emit charged particles, as well as trapped trajectories, which have no sources in the collisionless case.

The steady-state of the plasma must simultaneously satisfy Poisson's equation (2.5) and Vlasov's equation (2.9), subject to boundary conditions on the potential and the incoming particles. To find the steady-state solution, both a Poisson and a Vlasov operator are needed:

- the Poisson operator solves for the potential distribution $V(x, y)$, given a net charge distribution $\rho(x, y)$ together with boundary conditions on the potential distribution, consistent with Poisson's equation (2.5);
- the Vlasov operator solves for the charge distribution $\rho(x, y)$, given a potential distribution $V(x, y)$, consistent with Vlasov's equation equation (2.9) as well as equations (2.7) and (2.8).

Let the Poisson operator be defined by the functional

$$f_P : V(x, y) = f_P \{ \rho_{\text{in}}(x, y) \}, \quad (2.10)$$

and the Vlasov operator be defined by the functional

$$f_V : \rho_{\text{out}}(x, y) = f_V \{ V(x, y) \}. \quad (2.11)$$

Then the solution of the problem lies at the fixed point of the Poisson–Vlasov functional,

defined as a composition of the Poisson and Vlasov functionals:

$$f_{PV} : \rho_{\text{out}}(x, y) = f_{PV} \{ \rho_{\text{in}}(x, y) \} = f_V \{ f_P \{ \rho_{\text{in}}(x, y) \} \}. \quad (2.12)$$

That is, the solution for the net charge distribution $\rho(x, y)$ is that which, when given at the input of the Poisson–Vlasov operator, yields an identical output ($\rho_{\text{out}}(x, y) = \rho_{\text{in}}(x, y)$). A Vlasov-Poisson operator could also be considered that would have $V(x, y)$ as its input and output. The Poisson–Vlasov operator was chosen because of a stability advantage inherent to the regularization process discussed later.

In the following, we present the specific Poisson and Vlasov solvers used in both our 1-D and 2-D implementations. We then proceed to define an algorithm for finding a best approximation to the fixed point of the Poisson–Vlasov operator, i.e., the steady state of the plasma.

2.3 Finite-Element Poisson Solver

Here we derive the Poisson solver, a numerical approximation for the Poisson operator defined above by the functional f_P . The Poisson solver will provide the capability to obtain a numerical approximation for the potential distribution satisfying Poisson’s equation and boundary conditions for a given net charge density distribution. We have chosen to use the finite-element method to implement our Poisson solver, due to its relative simplicity and mathematical compactness. In addition, it does not present any of the numerical issues associated with the poles generated with techniques such as the method of moments.

The approximate character of the Poisson solver is due to the finite discretization employed to solve Poisson’s differential equation (2.5). Both the potential and charge distributions are assumed piecewise-linear, and the accuracy of this representation improves as the mesh density increases.

In the following, we show two separate derivations for the 1-D cylindrical Poisson

Solver, used in KiPS-1D, and for the full 2-D Poisson Solver, used in KiPS-2D.

2.3.1 1-D Cylindrical Implementation

In the absence of any azimuthal variation of either the charge distribution or boundary conditions on the potential, Poisson's equation (2.5) simplifies to

$$\frac{1}{r} \frac{d}{dr} \left(r \frac{dV}{dr} \right) = -\frac{1}{\epsilon_0} \rho(r). \quad (2.13)$$

Finding a unique solution for this differential equation requires boundary conditions on $V(r)$. At the surface of the probe, located at $r = r_0$, we require that the potential be equal to the applied bias voltage, i.e., $V(r = r_0) = V_0$. Now, our computational domain is finite and terminates at a large radius $r = r_M$. We have found that the most suitable boundary condition to represent an open-ended plasma domain is a floating boundary condition based on the asymptotic potential profile $V(r) \propto 1/r$ derived by *Bernstein and Rabinowitz* [27] and also used by *Laframboise* [8]. This asymptotic behavior, together with the bias potential, results in the following boundary conditions for the potential:

$$V(r = r_0) = V_0, \quad (2.14)$$

$$\left. \frac{dV}{dr} \right|_{r=r_M} = -\left. \frac{V}{r} \right|_{r=r_M}. \quad (2.15)$$

According to variational principles [44, 45], which are the foundation of the finite-element method, the solution of (2.13), subject to boundary conditions defined in (2.14)–(2.15), is equivalent to the stationary point (or minimum energy point) of the following functional:

$$\Pi = \int_{r_0}^{r_M} dr \left[\frac{1}{2} r V'^2(r) - \frac{r \rho(r) V(r)}{\epsilon_0} \right] + \left. \frac{V^2}{2} \right|_{r=r_M}. \quad (2.16)$$

This can be verified by deriving the variation of Π [45],

$$\delta\Pi = - \int_{r_0}^{r_M} dr \left[\frac{r\rho(r)}{\epsilon_0} + \frac{d(rV')}{dr} \right] + rV' \delta V \Big|_{r_0}^{r_M} + V \delta V \Big|_{r=r_M} = 0 \quad (2.17)$$

$$\delta\Pi = - \int_{r_0}^{r_M} dr \left[\frac{r\rho(r)}{\epsilon_0} + \frac{d(rV')}{dr} \right] + \{rV' + V\} \delta V \Big|_{r=r_M} - rV' \delta V \Big|_{r_0} = 0, \quad (2.18)$$

and finding the stationary point corresponding to $\delta\Pi = 0$. The physical solution thus corresponds to the minimum energy state for Π . Since all 3 terms in (2.18) are independent of each other, each must vanish independently. Setting the integrand of the first term equal to 0 yields Poisson's equation (2.13), while setting the second term equal to 0 yields the outer boundary condition given in (2.15). The third term vanishes simply because $\delta V \Big|_{r=r_0} = 0$, i.e., there is no variation of the potential at $r = r_0$, since it is forced to a fixed value, namely V_0 .

Thus, our Poisson solver must minimize Π as given by (2.16). To accomplish this, we first approximate (2.16) by discretizing the potential $V(r)$ and the charge distribution $\rho(r)$ and assuming a linear variation between the samples. The resulting piecewise representations of $V(r)$ and $\rho(r)$ can be used to write the following approximate equation for Π :

$$\begin{aligned} \Pi_{\text{discrete}} = & \frac{V_N^2}{2} + \sum_{i=1}^{N-1} \frac{1}{(r_{i+1} - r_i)^2} \times \left[\frac{(r_{i+1}^2 - r_i^2)}{4} (V_{i+1} - V_i)^2 \right. \\ & - \frac{(r_{i+1}^2 - r_i^2)}{2\epsilon_0} (r_{i+1}\rho_i - r_i\rho_{i+1}) (r_{i+1}V_i - r_iV_{i+1}) \\ & - \frac{(r_{i+1}^3 - r_i^3)}{3\epsilon_0} [V_i(r_i\rho_{i+1} - 2r_{i+1}\rho_i + r_{i+1}\rho_{i+1}) \\ & + V_{i+1}(r_{i+1}\rho_i - 2r_i\rho_{i+1} + r_i\rho_i)] \\ & \left. - \frac{(r_{i+1}^4 - r_i^4)}{4\epsilon_0} (\rho_{i+1} - \rho_i) (V_{i+1} - V_i) \right], \end{aligned} \quad (2.19)$$

where r_i , $i = 1, \dots, N$ are appropriately chosen sample locations in the interval $r \in [r_0, r_M]$, and the potential and charge density samples correspond to $V_i = V(r = r_i)$ and $\rho_i = \rho(r =$

r_i). The equivalent matrix-form expression is:

$$\Pi \approx \Pi_{\text{discrete}} = \frac{1}{2} \vec{V}^T \mathbf{K}_{N \times N} \vec{V} - \frac{1}{\epsilon_0} \vec{V}^T \mathbf{Q}_{N \times N} \vec{\rho}, \quad (2.20)$$

where \mathbf{K} and \mathbf{Q} are $N \times N$ matrices, and the elements of the vectors \vec{V} and $\vec{\rho}$ correspond to the potential and charge density samples V_i and ρ_i for $i \in [1, N]$. The non-zero elements of matrix \mathbf{K} are given by

$$\begin{aligned} \text{1}^{\text{st}} \text{ row: } \mathbf{K}_{1,1} &= \frac{r_2^2 - r_1^2}{2(r_2 - r_1)^2}, & \mathbf{K}_{1,2} &= -\frac{r_2^2 - r_1^2}{2(r_2 - r_1)^2} \\ \text{i}^{\text{th}} \text{ row: } \mathbf{K}_{i,i-1} &= \frac{r_{i-1}^2 - r_i^2}{2(r_i - r_{i-1})^2}, & \mathbf{K}_{i,i} &= \frac{r_i^2 - r_{i-1}^2}{2(r_i - r_{i-1})^2} + \frac{r_{i+1}^2 - r_i^2}{2(r_{i+1} - r_i)^2} \\ \text{and } \mathbf{K}_{i,i+1} &= \frac{r_i^2 - r_{i+1}^2}{2(r_{i+1} - r_i)^2}, & i &\in [2, N-1] \\ \text{N}^{\text{th}} \text{ row: } \mathbf{K}_{N,N-1} &= -\frac{r_N^2 - r_{N-1}^2}{2(r_N - r_{N-1})^2}, & \mathbf{K}_{N,N} &= 1 + \frac{r_N^2 - r_{N-1}^2}{2(r_N - r_{N-1})^2}. \end{aligned} \quad (2.21)$$

With regards to matrix \mathbf{Q} , the non-zero elements of its first row are given by

$$\begin{aligned} \mathbf{Q}_{1,1} &= \frac{1}{(r_2 - r_1)^2} \left[\frac{1}{2} r_2^2 (r_2^2 - r_1^2) - \frac{2}{3} r_2 (r_2^3 - r_1^3) + \frac{1}{4} (r_2^4 - r_1^4) \right] \text{ and} \\ \mathbf{Q}_{1,2} &= \frac{1}{(r_2 - r_1)^2} \left[-\frac{1}{2} r_1 r_2 (r_2^2 - r_1^2) + \frac{1}{3} (r_1 + r_2) (r_2^3 - r_1^3) - \frac{1}{4} (r_2^4 - r_1^4) \right], \end{aligned} \quad (2.22)$$

the non-zero elements of rows 2 through $N-1$ are given by

$$\begin{aligned} \mathbf{Q}_{i,i-1} &= \frac{1}{(r_i - r_{i-1})^2} \left[-\frac{1}{2} r_{i-1} r_i (r_i^2 - r_{i-1}^2) + \frac{1}{3} (r_{i-1} + r_i) (r_i^3 - r_{i-1}^3) - \frac{1}{4} (r_i^4 - r_{i-1}^4) \right], \\ \mathbf{Q}_{i,i} &= \frac{1}{(r_i - r_{i-1})^2} \left[\frac{1}{2} r_{i-1}^2 (r_i^2 - r_{i-1}^2) - \frac{2}{3} r_{i-1} (r_i^3 - r_{i-1}^3) + \frac{1}{4} (r_i^4 - r_{i-1}^4) \right] \\ &\quad + \frac{1}{(r_{i+1} - r_i)^2} \left[\frac{1}{2} r_{i+1}^2 (r_{i+1}^2 - r_i^2) - \frac{2}{3} r_{i+1} (r_{i+1}^3 - r_i^3) + \frac{1}{4} (r_{i+1}^4 - r_i^4) \right], \text{ and} \\ \mathbf{Q}_{i,i+1} &= \frac{1}{(r_{i+1} - r_i)^2} \left[-\frac{1}{2} r_i r_{i+1} (r_{i+1}^2 - r_i^2) + \frac{1}{3} (r_i + r_{i+1}) (r_{i+1}^3 - r_i^3) - \frac{1}{4} (r_{i+1}^4 - r_i^4) \right], \end{aligned} \quad (2.23)$$

and the non-zero elements of its N^{th} row are given by

$$\begin{aligned}\mathbf{Q}_{N,N-1} &= \frac{1}{(r_N - r_{N-1})^2} \left[-\frac{1}{2} r_{N-1} r_N (r_N^2 - r_{N-1}^2) + \frac{1}{3} (r_{N-1} + r_N) (r_N^3 - r_{N-1}^3) \right. \\ &\quad \left. - \frac{1}{4} (r_N^4 - r_{N-1}^4) \right] \text{ and} \\ \mathbf{Q}_{N,N} &= \frac{1}{(r_N - r_{N-1})^2} \left[\frac{1}{2} r_{N-1}^2 (r_N^2 - r_{N-1}^2) - \frac{2}{3} r_{N-1} (r_N^3 - r_{N-1}^3) + \frac{1}{4} (r_N^4 - r_{N-1}^4) \right],\end{aligned}\tag{2.24}$$

with all the unspecified matrix elements equal to zero.

Now, the best approximation to the physical solution, i.e., the stationary point of Π , which is also the root of $\delta\Pi$ as specified in (2.18), is obtained by setting to zero the partial derivatives of Π_{discrete} with respect to the *unknown* potential samples $V_i, i = 2, \dots, N$. This operation yields the following linear system of equations:

$$\mathbf{K}_{2:N,2:N} \vec{V}_{2:N} = \frac{1}{\epsilon_0} \mathbf{Q}_{2:N,1:N} \vec{\rho} - V_0 \mathbf{K}_{2:N,1}.\tag{2.25}$$

This system is then solved for the unknown potential samples $V_i, i \in [2, N]$:

$$\vec{V}_{2:N} = \underbrace{\left[\frac{1}{\epsilon_0} (\mathbf{K}_{2:N,2:N})^{-1} \mathbf{Q}_{2:N,1:N} \right]}_{\mathbf{J}_P'_{N-1 \times N}} \vec{\rho} - \underbrace{V_0 (\mathbf{K}_{2:N,2:N})^{-1} \mathbf{K}_{2:N,1}}_{\vec{V}^{\text{cst}'}}\tag{2.26}$$

where we have defined an $(N - 1) \times N$ matrix \mathbf{J}_P' and a vector $\vec{V}^{\text{cst}'}$ with $(N - 1)$ elements. Based on this result and the potential boundary condition at $r = r_0$, we can form the complete Poisson solver as follows:

$$\vec{V} = \mathbf{J}_P \vec{\rho} + \vec{V}^{\text{cst}},\tag{2.27}$$

with

$$\mathbf{J}_{P2:N,1:N} = \mathbf{J}_P',\tag{2.28}$$

$$\mathbf{J}_{P1,1:N} = \vec{0},\tag{2.29}$$

$$\vec{V}_{2:N}^{\text{cst}} = \vec{V}^{\text{cst}'}, \quad \text{and}\tag{2.30}$$

$$V_1^{\text{cst}} = V_0.\tag{2.31}$$

The expression given by (2.27) is the final compact form of our finite element-based cylindrical 1-D Poisson solver. It is obviously a linear operator, and only needs to be computed once upon generating a new grid.

2.3.2 2-D Implementation

For the 2-D implementation of our Poisson solver, we wish to approximately solve, in two dimensions, Poisson's equation (2.5), with appropriate boundary conditions. We will first focus on the boundary conditions, and then proceed to derive the finite element solver itself.

2.3.2.1 Poisson Boundary Conditions

At the surface of the conductive object(s) (e.g., probe), we simply enforce a fixed bias potential $V = V_0$, with the potential V being measured from infinity.

The question of the outer boundary condition is significantly more difficult to address. Since the computational domain must be finite, an appropriate outer boundary condition should be selected that will help keep the required extent of the computational domain at a reasonable size. In its undisturbed state, the plasma is neutral, and it therefore acts to shield any perturbations in the electric potential caused by a biased conductive object inserted within that plasma. For that reason, we can make the argument that the potential profile, beyond the circular outer edge of the computational domain, must fall off faster than it would in free space.

In free space, we drop the space charge term $\rho(x, y)$ on the right-hand side of Poisson's equation (eq. (2.5)), and recover Laplace's equation. In 2-D cylindrical coordinates, Laplace's equation can be written as

$$\nabla^2 V = \frac{1}{r} \frac{\partial}{\partial r} \left(r \frac{\partial V}{\partial r} \right) + \frac{1}{r^2} \frac{\partial^2 V}{\partial \theta^2} = 0 \quad (2.32)$$

mode #	Free Space $E_{rn} \propto$	Plasma $E_{rn} \propto$
0	$1/r$	$1/r^2$ [27]
1	$1/r^2$	$1/r^3$
2	$1/r^3$	$1/r^4$
\vdots	\vdots	\vdots
n	$1/r^{n+1}$	$1/r^{n+2}$

Table 2.1: Decay rates of the radial electric field $E_{rn} = -\frac{\partial V_{xn}}{\partial r}$ for various circular harmonic modes. The exact rates are given for free space [46], while in a plasma only the 0th order mode has an asymptotic rate. The rates in bold are assumed, based on a qualitative argument.

and can be solved by separation of variables. The solutions are circular harmonics of the form [46]

$$V_{x0} = C_0 \ln r + D_0, \quad (2.33)$$

$$V_{xn} = (A_n \cos n\theta + B_n \sin n\theta) (\underbrace{C_n}_{=0} r^n + D_n r^{-n}), \quad n = 1, 2, 3, \dots \quad (2.34)$$

Since we are looking for solutions that vanish as $r \rightarrow \infty$, we must set $C_n = 0$. It is thus seen that the potential for the circular harmonics decays as $1/r^n$ for $n \geq 1$. Table 2.1 lists the decay rates of the *radial electric field* $E_{rn} = -\frac{\partial V_{xn}}{\partial r}$ for each circular harmonic mode in free space, along with the corresponding assumed decay rates in a plasma. Following the asymptotic result derived for the 1-D cylindrical case [27], we assume that the 0th order mode decays as $E_{rn} \propto 1/r^2$ ($V_{xn} \propto 1/r$) in a plasma, a faster decay rate than that obtained in free space. Without further demonstration, we generalize the shielding effect of the plasma observed in the 0th order mode to higher-order modes by assuming a decay rate of $E_{rn} \propto 1/r^{n+2}$, or $V_{xn} \propto 1/r^{n+1}$.

Furthermore, we will assume these decay rates to be appropriate in flowing plasmas as well. Future work should focus on seeking asymptotic analytical expressions for these modes in stationary as well as flowing plasma; such results would very likely contribute

to reducing the computational domain size requirements in the flowing plasma case, in a similar fashion as the improvement obtained in the 1-D cylindrical case upon replacing the hard outer boundary condition $V = 0$ with a boundary condition based on the asymptotic behavior $V \propto 1/r$.

The decay rates for each mode were not hard-coded into the program. Instead, those rates are given as an input parameter by the user, such that one may provide the best-suited decay rates for the application of interest.

2.3.2.2 Finite-Element Formulation

We proceed by fully discretizing Poisson's equation in two dimensions (2.5) using a piecewise-bilinear representation of the potential and charge density distributions. The 2-D domain is subdivided into triangular elements.⁴ The formulation of the linear Poisson solver is based on that found in chapter 2 of Tong's finite-element textbook [44]. Analogous to (2.16), we choose the functional for which the stationary point corresponds to the solution of (2.5), subject to the boundary conditions defined in Section 2.3.2.1. This functional is given by

$$\Pi = \underbrace{\frac{1}{2} \iint_A dA (\nabla V)^2}_{\Pi_1} + \underbrace{\frac{1}{2} \iint_{A_\infty} dA_\infty [(\nabla V)^2 + (\nabla^2 V) V]}_{\Pi_2} - \underbrace{\frac{1}{\epsilon_0} \iint_A dA \rho(x, y) V}_{\Pi_3}, \quad (2.35)$$

where $(\nabla V)^2 \equiv (\nabla V) \cdot (\nabla V)$, the area A refers to the full area of the computational domain, and A_∞ represents the area extending beyond the computational domain, all the way to infinity ($r \geq r_M$).

2.3.2.2.1 Formulation of the Outer Boundary Condition We hereby derive an approximation for Π_2 , the energy outside of the computational domain, in terms of the samples of the potential profile at the outer boundary $r = r_M$ of the computational domain, to

⁴Section 2.6 describes the mesh construction process.

serve as an outer boundary condition, consistent with the assumptions on the decay rates of circular harmonics described in Section 2.3.2.1.

Using Green's 1st formula [47], the second term of (2.35) can be re-written as a contour integral on the outer circular boundary at $r = r_M$:

$$\Pi_2 = -\frac{1}{2} \int_{\theta=0}^{2\pi} V \frac{\partial V}{\partial r} r_M d\theta. \quad (2.36)$$

Outside of the computational domain ($r \geq r_M$), an expansion of the 2-D potential profile in circular harmonics yields, for the potential and its first radial derivative:

$$V(\theta, r) = A_0 \frac{r_M}{r} + \sum_{n=1}^{N_{\text{modes}}} \left(\frac{r_M}{r} \right)^{\gamma(n)} (A_n \cos n\theta + B_n \sin n\theta) \quad (2.37)$$

$$-\frac{\partial V}{\partial r} = A_0 \frac{r_M}{r^2} + \sum_{n=1}^{N_{\text{modes}}} \gamma(n) \left(\frac{r_M^{\gamma(n)}}{r^{\gamma(n)+1}} \right) (A_n \cos n\theta + B_n \sin n\theta), \quad (2.38)$$

where $\gamma(n)$ is the specified decay rate for the n^{th} circular harmonic of the potential and is usually set to $\gamma(n) = n + 1$, consistent with the arguments given in Section 2.3.2.1. The Fourier series coefficients are given by Euler formulas [47]:

$$A_0 = \frac{1}{2\pi} \int_0^{2\pi} d\theta V(r_M, \theta) \quad (2.39)$$

$$A_n = \frac{1}{\pi} \int_0^{2\pi} d\theta V(r_M, \theta) \cos n\theta, \quad n = 1, 2, \dots \quad (2.40)$$

$$B_n = \frac{1}{\pi} \int_0^{2\pi} d\theta V(r_M, \theta) \sin n\theta, \quad n = 1, 2, \dots \quad (2.41)$$

where the potential is integrated over the outer circular boundary. These formulas are discretized based on a bilinear variation of the edge potential between its samples $V(r_M, \theta_i)$:

$$A_0 \approx \frac{1}{2\pi} \sum_{i=1}^{N_{\text{ob}}} a_{0i} V(r_M, \theta_i) \quad (2.42)$$

$$A_n \approx \frac{1}{\pi} \sum_{i=1}^{N_{\text{ob}}} a_{ni} V(r_M, \theta_i) \quad n = 1, 2, \dots \quad (2.43)$$

$$B_n \approx \frac{1}{\pi} \sum_{i=1}^{N_{\text{ob}}} b_{ni} V(r_M, \theta_i) \quad n = 1, 2, \dots \quad (2.44)$$

where N_{ob} is the number of potential samples on the outer boundary. The coefficients a_{0i} , a_{ni} and b_{ni} are obtained by integrating the piecewise-linear representation of the boundary potential profile along with either 1, $\cos n\theta$, or $\sin n\theta$ over each sub-interval defined by the outer boundary sample locations, yielding:

$$a_{0i} = \frac{1}{2} [\text{mod}(\theta_{i+1} - \theta_i, 2\pi) + \text{mod}(\theta_i - \theta_{i-1}, 2\pi)] \quad (2.45)$$

$$a_{ni} = \frac{(\cos n\theta_i - \cos n\theta_{i-1})}{n^2 \text{mod}(\theta_i - \theta_{i-1}, 2\pi)} - \frac{(\cos n\theta_{i+1} - \cos n\theta_i)}{n^2 \text{mod}(\theta_{i+1} - \theta_i, 2\pi)}, \quad (2.46)$$

$$b_{ni} = \frac{(\sin n\theta_i - \sin n\theta_{i-1})}{n^2 \text{mod}(\theta_i - \theta_{i-1}, 2\pi)} - \frac{(\sin n\theta_{i+1} - \sin n\theta_i)}{n^2 \text{mod}(\theta_{i+1} - \theta_i, 2\pi)} \quad (2.47)$$

where $\text{mod}()$ is the modulo function, and the θ_i samples are assumed to be ordered in counter-clockwise (increasing) order. These coefficients are computed for modes $n = 0, 1, 2, \dots, N_{\text{modes}}$, where N_{modes} is chosen sufficiently large to accurately represent the azimuthal modes that the outer boundary sampling can support. Typically, N_{modes} is chosen as a few times (10 times, for example) the approximate Nyquist limit, i.e.,

$$N_{\text{modes}} = \text{ceil} \left(10 \frac{\pi}{\min |\text{mod}(\theta_{i+1} - \theta_i, 2\pi)|} \right). \quad (2.48)$$

where the function $\text{ceil}(\cdot)$ rounds its argument up to the next integer. In contrast with the discrete Fourier transform, which gives rise to aliasing when the Nyquist limit is exceeded, there is no concern for aliasing here, since we have defined the coefficients a_{0i} , a_{ni} and b_{ni} based on the continuous Fourier transform of a piecewise-linear boundary potential, as opposed to having discretized the Fourier integrands, as is done in the discrete Fourier transform.

We may now put the pieces together to obtain a discrete representation of Π_2 . Inserting (2.37)–(2.38) into (2.36), we obtain for Π_2 :

$$\Pi_2 = \pi \left\{ A_0^2 + \frac{1}{2} \sum_{n=1}^{N_{\text{modes}}} \gamma(n) (A_n^2 + B_n^2) \right\}. \quad (2.49)$$

Using (2.45)–(2.47), we insert (2.42)–(2.44) into (2.49), and re-write the resulting expression in vector form,

$$\Pi_2 = \frac{1}{2} \vec{V}_b^T \underbrace{\left[\frac{1}{2\pi} \vec{a}_0 \vec{a}_0^T + \frac{1}{\pi} \sum_{n=1}^{N_{\text{modes}}} \gamma(n) (\vec{a}_n \vec{a}_n^T + \vec{b}_n \vec{b}_n^T) \right]}_{\mathbf{K}'_2} \vec{V}_b, \quad (2.50)$$

where \vec{V}_b is a vector containing the potential samples at the outer boundary, $(\vec{V}_b)_i = V(r_M, \theta_i)$, and the vectors \vec{a}_0 , \vec{a}_n , and \vec{b}_n are made up of the elements given by (2.45)–(2.47). The matrix \mathbf{K}'_2 is a stiffness matrix that constitutes the outer boundary condition and will contribute to the global stiffness matrix defined in what follows.

2.3.2.2.2 Formulation of the Internal Finite Elements Analogous to the 1-D cylindrical case given by (2.19), both surface integrals in the energy contributions Π_1 and Π_3 in (2.35) are approximated by sums of sub-functionals π_{n1} and π_{n3} ($n = 1, 2, \dots, N_t$) that each operate on a sub-domain defined by triangle n :

$$\Pi = \underbrace{\sum_{n=1}^{N_t} \pi_{n1}}_{\Pi_1} + \Pi_2 + \underbrace{\sum_{n=1}^{N_t} \pi_{n3}}_{\Pi_3} \quad (2.51)$$

with

$$\pi_{n1} = \frac{1}{2} \iint_{A_n} \left[\left(\frac{\partial V}{\partial x} \right)^2 + \left(\frac{\partial V}{\partial y} \right)^2 \right] dx dy \quad \text{and} \quad \pi_{n3} = -\frac{1}{\epsilon_0} \iint_{A_n} \rho(x, y) V(x, y) dx dy, \quad (2.52)$$

where N_t is the number of triangles, and A_n defines the surface of the n^{th} triangle.

The potential and charge density distributions are assumed piecewise-bilinear over the set of triangular elements. Within triangle n , the potential and charge density profiles are given by

$$V(x, y) = V_{i(n,1)} f_1(x, y) + V_{i(n,2)} f_2(x, y) + V_{i(n,3)} f_3(x, y) \quad \text{and} \quad (2.53)$$

$$\rho(x, y) = \rho_{i(n,1)} f_1(x, y) + \rho_{i(n,2)} f_2(x, y) + \rho_{i(n,3)} f_3(x, y), \quad (2.54)$$

where the V_i 's and ρ_i 's are samples of the potential and charge density distributions, and $i(n,:)$ is a lookup table mapping each of the 3 vertices of triangle n to the corresponding indices within the vectors of samples \vec{V} and $\vec{\rho}$. The f_i 's are bilinear interpolation functions given by

$$f_i(x, y) = \frac{(a_i + b_i x + c_i y)}{2\Delta}, \quad i = 1, 2, 3, \quad (2.55)$$

with coefficients [44]

$$\begin{aligned} \Delta &= \frac{1}{2} |x_2 y_3 - x_3 y_2 + x_3 y_1 - x_1 y_3 + x_1 y_2 - x_2 y_1|, \\ a_1 &= x_2 y_3 - x_3 y_2, \quad b_1 = y_2 - y_3, \quad c_1 = x_3 - x_2, \\ a_2 &= x_3 y_1 - x_1 y_3, \quad b_2 = y_3 - y_1, \quad c_2 = x_1 - x_3, \\ a_3 &= x_1 y_2 - x_2 y_1, \quad b_3 = y_1 - y_2, \quad c_3 = x_2 - x_1, \end{aligned} \quad (2.56)$$

where the x_i 's and y_i 's are the coordinates of the 3 vertices for triangle n and Δ is the triangle area. Based on the piecewise-linear description of the potential and charge density distributions specified by (2.53)–(2.56), approximations for π_{n1} and π_{n3} can be written in matrix form as

$$\pi_{n1} \approx \frac{1}{2} \vec{V}_{i(n,1:3)}^T \mathbf{k}_{n1} \vec{V}_{i(n,1:3)} \quad \text{and} \quad \pi_{n3} \approx -\frac{1}{\epsilon_0} \vec{V}_{i(n,1:3)}^T \mathbf{Q}_n \vec{\rho}_{i(n,1:3)}, \quad (2.57)$$

where \mathbf{k}_{n1} , and \mathbf{Q}_n are both 3×3 matrices. The elements of \mathbf{k}_{n1} are obtained from [44]

$$\begin{aligned} (k_{n1})_{ij} &= \int_{A_n} \left(\frac{\partial f_i}{\partial x} \frac{\partial f_j}{\partial x} + \frac{\partial f_i}{\partial y} \frac{\partial f_j}{\partial y} \right) dx dy \\ &= \frac{1}{4\Delta} (b_i b_j + c_i c_j), \end{aligned} \quad (2.58)$$

where Δ , the b_i 's, and the c_i 's are defined by (2.56) for triangle n .

Now, finding an expression for the elements of the 3×3 loading matrix \mathbf{Q}_n is a bit more involved. The following expression is consistent with π_{n3} in (2.52), (2.54), and (2.57):

$$(\mathbf{Q}_n)_{ij} = \frac{1}{4\Delta^2} \int_{A_n} (a_j + b_j x + c_j y) (a_i + b_i x + c_i y) dx dy, \quad (2.59)$$

where the a_i 's and b_i 's are given by (2.56) for triangle n . Using Green's theorem [47], we can substitute this surface integral, performed over triangle n 's area A_n , with a counter-clockwise contour integral over the triangle's three edges:

$$(\mathbf{Q}_n)_{ij} = \frac{1}{4\Delta^2} \oint_{C_n} F_1(x, y) dx + F_2(x, y) dy \quad (2.60)$$

$$\text{with } F_1(x, y) = -\frac{1}{2} \int dy (a_j + b_j x + c_j y) (a_i + b_i x + c_i y) \quad (2.61)$$

$$\text{and } F_2(x, y) = +\frac{1}{2} \int dx (a_j + b_j x + c_j y) (a_i + b_i x + c_i y). \quad (2.62)$$

Now, the contour integral is based on 3 line integrals over the edges of triangle n . This requires parameterizing F_1 and F_2 over each edge: $\begin{Bmatrix} x \\ y \end{Bmatrix} = \begin{Bmatrix} x_0 \\ y_0 \end{Bmatrix} + s \begin{Bmatrix} x_1 - x_0 \\ y_1 - y_0 \end{Bmatrix}$, where the coordinates (x_0, y_0) and (x_1, y_1) represent the coordinates of the starting and ending vertices for each edge, respectively. Using this parametrization yields

$$\begin{aligned} (\mathbf{Q}_n)_{ij} &= \pm \frac{1}{4\Delta^2} \sum_{i_e=1}^3 \int_{s=0}^1 \left\{ F_1(s) \frac{dx}{ds} + F_2(s) \frac{dy}{ds} \right\} ds \\ &= \pm \sum_{i_e=1}^3 \underbrace{\frac{1}{4\Delta^2} \left[(x_1 - x_0) \int_{s=0}^1 F_1(s) ds + (y_1 - y_0) \int_{s=0}^1 F_2(s) ds \right]}_{((\mathbf{Q}_n)_{ij})_{i_e}}, \end{aligned} \quad (2.63)$$

where the plus or minus sign is used depending upon whether the three edges are ordered in counter-clockwise or clockwise order, respectively. The indefinite integrals given by (2.61) and (2.62), as well as the definite integral given in (2.63) can all be performed analytically. Equation (C.1) in appendix C gives a detailed analytical expression for $((\mathbf{Q}_n)_{ij})_{i_e}$, which can be used directly to compute the elements of matrix \mathbf{Q}_b , without resorting to numerical integration.

The approximate expressions for the energies π_{n1} and π_{n3} given by (2.57) can be combined to form approximate expressions for the energy contributions Π_1 and Π_3 in (2.51):

$$\Pi_1 \approx \frac{1}{2} \vec{V}^T \underbrace{\mathbf{K}_1}_{N \times N} \vec{V} \quad \text{and} \quad \Pi_3 \approx -\frac{1}{\epsilon_0} \vec{V}^T \underbrace{\mathbf{Q}}_{N \times N} \vec{\rho}, \quad (2.64)$$

where N is the total number of samples (vertices) in the computational domain, and the $N \times N$ matrices \mathbf{K}_1 and \mathbf{Q} are obtained by combining the contributions of the \mathbf{k}_{n1} 's and \mathbf{Q}_n 's given by (2.58) and (C.1). The “decay rates” outer boundary condition, embedded in Π_2 and defined in (2.50), can now be added to (2.64) to obtain the complete approximation for the functional Π :

$$\Pi \approx \Pi_{\text{discrete}} = \underbrace{\frac{1}{2} \vec{V}^T \underbrace{\mathbf{K}_1 + \mathbf{K}_2}_{\mathbf{K}} \vec{V}}_{\Pi_1 + \Pi_2} - \underbrace{\frac{1}{\epsilon_0} \vec{V}^T \mathbf{Q} \vec{\rho}}_{\Pi_3}, \quad (2.65)$$

where the $N \times N$ matrix \mathbf{K}_2 is built by filling some of its entries with elements from the $N_b \times N_b$ matrix \mathbf{K}'_2 , with N the total number of vertices and N_b the number of outer boundary vertices. This is done according to $\mathbf{K}_2(\vec{i}_b, \vec{i}_b) = \mathbf{K}'_2$, where \vec{i}_b is an index vector listing the indices of the vertices located on the outer boundary, sorted in a counter-clockwise order.

The stationary point of (2.65), corresponding to the minimum energy state of the system and providing an approximation to Poisson's equation in two dimensions, is obtained by equating to zero the gradient of the approximate energy Π_{discrete} with respect to the unknown potential samples. This process, similar to that which lead to (2.25), results in the following linear system of equations:

$$\mathbf{K}_{\vec{u}, \vec{u}} \vec{V}_{\vec{u}} = \frac{1}{\epsilon_0} \mathbf{Q}_{\vec{u}, :} \vec{\rho} - V_0 \mathbf{K}_{\vec{u}, \vec{k}} \vec{1}, \quad (2.66)$$

where $\vec{1}$ represents a vector with all elements equal to 1, and where we introduced the following subsets of potential sample indices:

- the subset \vec{k} designates all sample indices located on the conductor surface, for which the value is *known* (this is the bias potential);
- the subset \vec{u} designates all sample indices not located on the conductor surface, for which the value is *unknown*;

- the use of the colon “:” as a matrix index designates the complete set of potential samples (same notation as in the *Matlab*TM scripting language).

We can then solve for the unknown potential samples, analogous to (2.26):

$$\vec{V}_{\vec{u}} = \underbrace{\left[\frac{1}{\epsilon_0} (\mathbf{K}_{\vec{u}, \vec{u}})^{-1} \mathbf{Q}_{\vec{u}, :} \right] \vec{\rho}}_{\mathbf{J}_P'_{N_u \times N}} \underbrace{-V_0 (\mathbf{K}_{\vec{u}, \vec{u}})^{-1} \mathbf{K}_{\vec{u}, \vec{k}} \vec{1}}_{\vec{V}^{\text{cst}'}}, \quad (2.67)$$

where N_u is the number of unknown samples (i.e., the length of \vec{u}), and $\vec{V}^{\text{cst}'}$ has N_u elements. Finally, we combine this resulting operator with the known potential samples to form the complete 2-D Poisson solver as follows:

$$\vec{V} = \mathbf{J}_P \vec{\rho} + \vec{V}^{\text{cst}}, \quad (2.68)$$

with

$$\mathbf{J}_{P\vec{u}, :} = \mathbf{J}_P', \quad (2.69)$$

$$\mathbf{J}_{P\vec{k}, :} = [0]_{N_k \times N}, \quad (2.70)$$

$$\vec{V}_{\vec{u}}^{\text{cst}} = \vec{V}^{\text{cst}'}, \quad \text{and} \quad (2.71)$$

$$\vec{V}_{\vec{k}}^{\text{cst}} = V_0 \vec{1}, \quad (2.72)$$

where $[0]_{N_k \times N}$ is an $N_k \times N$ zero matrix. (2.68) gives the final compact form of our finite element-based 2-D Poisson solver. Just like its 1-D counterpart, it is a linear operator and only needs to be computed once upon generating a new triangular mesh.

2.4 Steady-State Vlasov Solver

We now derive the Vlasov solver, that is, a numerical approximation for the Vlasov operator defined above by the functional f_V . The Vlasov solver will provide the capability to find a numerical approximation for the net charge density distribution satisfying Vlasov's equation and boundary conditions for the inbound particles.

The Vlasov solver described here allows each species to express the full kinetic nature of its 2-D velocity distribution. This feature allows for the realistic and accurate modeling of non-thermal plasmas, that is, plasmas that are not at thermal equilibrium due to large electric fields and high velocity flows. It accounts for the largest part of the computational complexity of the technique presented in this work.

The approximate character of the Vlasov solver is due to the following:

- the finite discretization of the potential mesh: the potential distribution is approximated by a piecewise-bilinear representation, which limits the accuracy of the trajectory tracking procedure (2-D implementation only);
- the finite precision of the quadrature technique employed to integrate over velocity space (both 1-D and 2-D implementations).

The Vlasov functional f_V , and therefore the Vlasov solver, are nonlinear operators. In this section, we will derive, in addition to the Vlasov nonlinear operator itself, a technique for the extraction of the linearized behavior of the Vlasov operator about a given “operating point” corresponding to a potential profile. The resulting linearized Vlasov operator will be required in Section 2.5 when we formulate our regularized Newton iterative scheme for the resolution of the nonlinear fixed point problem involving the Poisson–Vlasov functional f_{PV} , defined in (2.12).

Following are two separate derivations: one for the 1-D cylindrical Vlasov solver, used in KiPS-1D, and one for the full 2-D Vlasov solver, used in KiPS-2D.

2.4.1 1-D Cylindrical Implementation

Our 1-D formulation of the Vlasov solver is based on equations provided by Sanmartín [11], and is equivalent to the procedure used by Laframboise [8].

2.4.1.1 Approximating the Vlasov Functional f_V in 1-D

The potential profile is symmetric about the center of the round cylindrical probe. Since the only force present is that due to the electrostatic field, we have a central force field. Because there are no azimuthal forces, the angular momentum $L = mrv_\theta$ of any particle is conserved along its trajectory. In addition, the transverse energy of a particle, $E = \frac{m_{e,i}}{2} (v_r^2 + v_\theta^2)$, is conserved⁵:

$$\frac{m_{e,i}}{2} (v_r^2 + v_\theta^2) + qV \equiv E, \quad (2.73)$$

where V is the electric potential, and m and q are the mass and charge of the particle. In this 1-D formulation, the cylindrical symmetry of the electric field and particle distributions only allows us to consider the “stationary plasma” case. Both the ion and electron populations are assumed to have Maxwellian velocity distributions far from the probe, as $r \rightarrow \infty$:

$$f_{e,i}(r \rightarrow \infty, E, L) = \frac{n_0 m_{e,i}}{2\pi e T_{e,i}} \exp\left(-\frac{E}{eT_{e,i}}\right), \quad (2.74)$$

where we use the invariants E and L as the independent variables for simplicity and to be consistent with Sanmartín.⁶ At any given location in space, the velocity distribution is equal to that given by (2.74) for all energy and angular momentum values (E, L) corresponding to a trajectory that is connected to infinity, and is assumed unpopulated otherwise. Let us define $L_r^2(E) \equiv 2m_{e,i}r^2 [E - q_{e,i}V(r)]$ and recognize that $L_r^2(E) = L^2 + m_{e,i}^2 r^2 v_r^2$. We repeat here, for completeness, the criteria given in [11] for a trajectory to be connected to infinity:

- owing to conservation of energy, only particles with a total energy sufficient to overcome any electric potential barriers, i.e., particles with an energy

$$E \geq E_{\min} = \max(0, \max\{qV(r'); r \leq r' < \infty\}), \quad (2.75)$$

⁵ v_∞ is the particle’s velocity when it is far removed from the probe, i.e., as $r \rightarrow \infty$.

⁶In this text, the variable L is used for angular momentum, whereas Sanmartín [11] uses the notation J .

are connected to infinity;

- an incoming particle can only reach r if its angular momentum L is sufficiently small to allow v_r^2 to have stayed positive from $r' = \infty$ to $r' = r$. This specifies an allowed range that the angular momentum of an incoming particle can have at r :

$$0 < L < L_r^*(E) = \min \{L_{r'}(E); r \leq r' < \infty\}. \quad (2.76)$$

Particles with a larger angular momentum $L > L_r^*(E)$ are thus “reflected” by what is sometimes described as an effective potential barrier;

- for outgoing particles there is, in addition to an upper bound $L_r^*(E)$ on the angular momentum, a lower bound $L_{r_0}^*(E) = \min \{L_{r'}(E); r_0 \leq r' < \infty\}$. Particles having a lower angular momentum are collected on the probe at $r = r_0$ and thus do not return.

Based on these bounds for the angular momentum, the velocity distribution is given by:

$$f_{e,i}(r, E, L) = \begin{cases} f_{e,i}(r \rightarrow \infty, E, L) & \text{if } v_r < 0 \text{ and } 0 < L < L_r^*(E) \\ f_{e,i}(r \rightarrow \infty, E, L) & \text{if } v_r > 0 \text{ and } L_{r_0}^*(E) < L < L_r^*(E) \\ 0 & \text{otherwise.} \end{cases} \quad (2.77)$$

The number density is then obtained by integrating the velocity distribution function over velocity space, or alternatively, over the 2-D space defined by E and L . The change of variables $(v_r, v_\theta) \rightarrow (E, L)$ implies the following Jacobian:

$$\frac{\partial(v_r, v_\theta)}{\partial(E, L)} = \begin{vmatrix} \frac{\partial v_r}{\partial E} & \frac{\partial v_r}{\partial L} \\ \frac{\partial v_\theta}{\partial E} & \frac{\partial v_\theta}{\partial L} \end{vmatrix} = \frac{1}{m\sqrt{L_r^2(E) - L^2}}. \quad (2.78)$$

Using this Jacobian and accounting for both positive and negative values of the angular momentum L , we obtain

$$\begin{aligned}
n_{e,i}(r) &= \frac{n_0}{\pi e T_{e,i}} \int_{E=E_{\min}}^{\infty} dE \exp\left(-\frac{E}{eT_{e,i}}\right) \left[\underbrace{\int_{L=0}^{L_r^*(E)} \frac{dL}{\sqrt{L_r^2(E)-L^2}}}_{v_r<0} + \underbrace{\int_{L=L_{r_0}^*(E)}^{L=L_r^*(E)} \frac{dL}{\sqrt{L_r^2(E)-L^2}}}_{v_r>0} \right] \\
&= \frac{n_0}{\pi e T_{e,i}} \int_{E=E_{\min}}^{\infty} dE \exp\left(-\frac{E}{eT_{e,i}}\right) \left[\underbrace{\sin^{-1}\left(\frac{L}{L_r(E)}\right)\Big|_0^{L_r^*(E)}}_{v_r<0} + \underbrace{\sin^{-1}\left(\frac{L}{L_r(E)}\right)\Big|_{L_{r_0}^*(E)}^{L_r^*(E)}}_{v_r>0} \right] \\
&= \frac{n_0}{\pi e T_{e,i}} \int_{E=E_{\min}}^{\infty} dE \exp\left(-\frac{E}{eT_{e,i}}\right) \left[2\sin^{-1}\frac{L_r^*(E)}{L_r(E)} - \sin^{-1}\frac{L_{r_0}^*(E)}{L_r(E)} \right], \tag{2.79}
\end{aligned}$$

with E_{\min} as defined in (2.75), and $L_r^*(E)$ as defined in (2.76). The integral in (2.79) cannot, in general, be performed analytically, because of the dependence of $L_r^*(E)$ and $L_{r_0}^*(E)$ on part or all of the potential profile through (2.76). This is true even in the case of the orbital motion limit, a regime in which all trajectories hitting the probe surface at $r = r_0$ are connected to infinity, except for $n(r = r_0)$. In the case of OML, $L_{r_0}^*(E) = L_r(E)$ applies, so that the bracketed expression in (2.79) goes to $\pi/2$, resulting in $n(r_0) = n_0/2$. However, even in OML, $L_r^*(E) < L_r(E)$ for some positions r , which means that, at several positions, especially further out from the probe, the integral cannot be performed analytically to obtain the number density.

In general, it suffices to integrate the exponentially-decaying integrand up to a finite energy value $E = \kappa_{\text{range}} e T_{e,i}$, with a sufficiently large value for κ_{range} , to obtain an acceptable accuracy on the integral. A value of $\kappa_{\text{range}} = 5$ is typically chosen, corresponding to an integrand $\exp\left(-\frac{E}{eT_{e,i}}\right)\Big|_{E=5eT_{e,i}} = 0.0067$, and yielding integration accuracies on the order of 1%. Our 1-D Vlasov solver computes an approximation for this integral to a given relative

accuracy ε_r using a numerical integration technique. We have implemented an adaptive scheme using the trapezoidal quadrature rule [48] to that effect, which is discussed in Appendix D. This adaptive quadrature scheme selects a set of abscissa $E_k, k = 1, 2, \dots, N_k$, where the integrand is evaluated, along with associated weights, resulting in the following approximation for the density profile at locations $r = r_j, j = 1, 2, \dots, N$:

$$n_{e,i}(r_j) \approx (n_{e,i})_j = \frac{n_0}{\pi e T_{e,i}} \sum_{k=1}^{N_k} w_k \exp\left(-\frac{E_k}{eT_{e,i}}\right) \left[2 \sin^{-1} \frac{L_{r_j}^*(E_k)}{L_{r_j}(E_k)} - \sin^{-1} \frac{L_{r_1}^*(E_k)}{L_{r_j}(E_k)} \right]$$

with $E_1 < E_2 < \dots < E_k < \dots < E_{N-1} < E_N$,

$$E_1 = \max(0, \max\{q_{e,i}V_{j'}, j' \leq j' \leq N\}),$$

$$L_{r_j}(E_k) = \begin{cases} \sqrt{2m_{e,i}r_j^2 [E_k - q_{e,i}V_j]} & E_k \geq q_{e,i}V_j \\ 0 & E_k < q_{e,i}V_j \end{cases}, \quad \text{and}$$

$$L_{r_j}^*(E_k) = \min\{L_{r_{j'}}, j' \leq j' \leq N\}.$$
(2.80)

The complete 1-D Vlasov solver computes both density profiles $n_e(r)$ and $n_i(r)$ by numerically evaluating (2.80) at a set of radial positions in computational space within the range $r_0 < r < r_M$. It then combines both results to obtain the “output” net charge density at all sampled locations $r_j, j = 1, 2, \dots, N$:

$$\rho(r_j) \approx (\vec{\rho}_{\text{out}})_j = q_e(n_e)_j + q_i(n_i)_j, \quad (2.81)$$

where q_e and q_i are the electron and ion charge, respectively. The term “output” is used here to designate the output of the Vlasov solver.

2.4.1.2 Linearizing the 1-D Vlasov Solver

We now proceed to find expressions for the linearized behavior of the discrete Vlasov operator specified by (2.81) and (2.80), with respect to the samples of the potential profile. Let us define $\frac{\partial \vec{\rho}}{\partial \vec{V}}$, an $N \times N$ matrix, as the Jacobian of the Vlasov solver, i.e., a matrix containing the linearized behavior of each net charge density sample as a function of all the

potential samples:

$$\left(\frac{\partial \vec{\rho}}{\partial \vec{V}} \right)_{jk} \equiv \frac{\partial \rho_j}{\partial V_k}, \quad j, k = 1, 2, \dots, N. \quad (2.82)$$

Based on (2.81) we can define $\frac{\partial \vec{n}_i}{\partial \vec{V}}$ and $\frac{\partial \vec{n}_e}{\partial \vec{V}}$ such that $\frac{\partial \vec{\rho}}{\partial \vec{V}} = q_e \frac{\partial \vec{n}_e}{\partial \vec{V}} + q_i \frac{\partial \vec{n}_i}{\partial \vec{V}}$ as follows:

$$\left(\frac{\partial \vec{n}_e}{\partial \vec{V}} \right)_{j,k} \equiv \frac{\partial (n_e)_j}{\partial V_k}, \quad j, k = 1, 2, \dots, N, \quad \text{and} \quad (2.83)$$

$$\left(\frac{\partial \vec{n}_i}{\partial \vec{V}} \right)_{j,k} \equiv \frac{\partial (n_i)_j}{\partial V_k}, \quad j, k = 1, 2, \dots, N. \quad (2.84)$$

Analytical expressions for the elements of these two $N \times N$ matrices are fairly complicated and therefore difficult to write in compact form. However, they can be written in a fairly compact form as an algorithm used to fill the elements, which is done in Algorithm 1, consistent with (2.80). It should be noted that the E_k 's are samples of the independent variable (the energy), and therefore have no dependence on the potential.

Finally, considering a Vlasov “input” potential profile \vec{V}_{in} , a Vlasov “output” net charge profile $\vec{\rho}_{\text{out}}$, and the Jacobian expression $\mathbf{J}_V = \frac{\partial \vec{\rho}}{\partial \vec{V}}$, the linearized behavior of the Vlasov solver can be described as

$$\vec{\rho} \cong \vec{\rho}_{\text{out}} + \frac{\partial \vec{\rho}}{\partial \vec{V}} (\vec{V} - \vec{V}_{\text{in}}) \quad (2.85)$$

for any input potential profile \vec{V} in the vicinity of \vec{V}_{in} . This linearized behavior will be used in Section 2.5 for the implementation of the regularized Newton iterative scheme used for the resolution of the nonlinear fixed point Poisson–Vlasov problem.

2.4.2 Full 2-D Implementation

2.4.2.1 Orbit Tracking and Analysis

The crucial difference between the 1-D Vlasov solver and its 2-D counterpart is that the latter requires explicit tracking of particle trajectories in order to sample the velocity distribution function in 2-D velocity space. This requirement is born out of the fact that, generally speaking, the 2-D potential profile is not rotationally symmetric, i.e., there are

Algorithm 1 Algorithm used to compute the elements of the density Jacobian $\frac{\partial \vec{n}}{\partial \vec{V}}$ (1-D cylindrical implementation)

```

Initialize Jacobian:  $\frac{\partial \vec{n}}{\partial \vec{V}} = [0]_{N \times N}$ 
for  $k = 1$  to  $N$  do
    if  $k \neq k^*$  and  $L_{r_k}^*(E_k) > 0$  then
         $\left( \frac{\partial \vec{n}}{\partial \vec{V}} \right)_{k,k} = \left( \frac{\partial \vec{n}}{\partial \vec{V}} \right)_{k,k} + \frac{q_{e,i} n_0}{\pi e T_{e,i}} w_k \exp \left( -\frac{E_k}{e T_{e,i}} \right) \gamma \frac{\sqrt{u}}{(E_k - qV_k) \sqrt{1 - \gamma^2 u}},$ 
         $\left( \frac{\partial \vec{n}}{\partial \vec{V}} \right)_{k,k^*} = \left( \frac{\partial \vec{n}}{\partial \vec{V}} \right)_{k,k^*} - \frac{q_{e,i} n_0}{\pi e T_{e,i}} w_k \exp \left( -\frac{E_k}{e T_{e,i}} \right) \gamma \frac{1}{(E_k - qV_k) \sqrt{u(1 - \gamma^2 u)}},$ 
        with  $\gamma = \frac{r_k^*}{r_k}$  and  $u = 1 + q \frac{V_k - V_k^*}{E_k - qV_k}$ .
    end if
    if  $k \neq 1^*$  and  $L_{r_1}^*(E_k) > 0$  then
         $\left( \frac{\partial \vec{n}}{\partial \vec{V}} \right)_{k,1^*} = \left( \frac{\partial \vec{n}}{\partial \vec{V}} \right)_{k,1^*} + \frac{q_{e,i} n_0}{2\pi e T_{e,i}} w_k \exp \left( -\frac{E_k}{e T_{e,i}} \right) \gamma' \frac{\sqrt{u'}}{(E_k - qV_k) \sqrt{1 - \gamma'^2 u'}},$ 
         $\left( \frac{\partial \vec{n}}{\partial \vec{V}} \right)_{k,1^*} = \left( \frac{\partial \vec{n}}{\partial \vec{V}} \right)_{k,1^*} - \frac{q_{e,i} n_0}{2\pi e T_{e,i}} w_k \exp \left( -\frac{E_k}{e T_{e,i}} \right) \gamma' \frac{1}{(E_k - qV_k) \sqrt{u'(1 - \gamma'^2 u')}},$ 
        with  $\gamma' = \frac{r_1^*}{r_k}$  and  $u' = 1 + q \frac{V_k - V_1^*}{E_k - qV_k}$ .
    end if
end for

```

where k^* , r_k^* and 1^* , r_1^* are such that:

$$L_{r_k}^*(E_k) \equiv L_{r_k^*}(E_k) \equiv L_{r_{k^*}}(E_k) = \min \{L_{r_{k'}}(E_k) : k \leq k' \leq N\}$$

$$L_{r_1}^*(E_k) \equiv L_{r_1^*}(E_k) \equiv L_{r_{1^*}}(E_k) = \min \{L_{r_{k'}}(E_k) : 1 \leq k' \leq N\}$$

azimuthal variations of the potential and net charge density distributions. Any particle trajectory belongs to one of three states:

plasma-bounded trajectories are trajectories originating from the background plasma;

conductor-bounded trajectories are trajectories originating from the surface of a conductor, such as a probe;

trapped trajectories are trajectories of indefinite length, which typically orbit around the probe.

In our basic implementation, only *plasma-bounded* trajectories are populated. *Conductor-bounded* trajectories are left empty, consistent with our assumption of non-emitting conductors; accounting for thermionic emission would require populating those trajectories. *Trapped* trajectories are deemed unpopulated because of the absence of collisions to scatter bounded particles into trapped states.⁷

In the 1-D cylindrical case, conservation of angular momentum L allows for the direct determination of the state of a particle’s trajectory based solely on its energy E and angular momentum L , as described in Section 2.4.1. However, since the angular momentum L is not conserved in the more general 2-D case, an “inside-out” [36] trajectory tracking procedure is employed in order to determine the origin of each trajectory and therefore its state.

Figure 2.1 illustrates the particle tracking process, which is similar to that used by Xu [17]. The trajectories are tracked analytically backward in time from one edge of the mesh to another, assuming a constant electric field within any given triangle of the mesh; this is consistent with the assumption of a piecewise-bilinear potential distribution. Every sub-trajectory is resolved by computing the intersection of a quadratic parametric curve with a segment on the mesh.

Within a given triangle of the mesh, a particle’s trajectory is described by

$$x = x_i + v_{ix}t + \frac{1}{2}a_x t^2 \quad \text{and} \quad (2.86)$$

$$y = y_i + v_{iy}t + \frac{1}{2}a_y t^2, \quad (2.87)$$

where (x_i, y_i) and (v_{ix}, v_{iy}) are the initial position and velocity of the particle upon entering the triangle, $t < 0$ is the negative time-of-flight⁸ from the triangle entry, and the constant

⁷Under certain conditions, however, even very low collision rates can lead to substantial accumulation of particles in trapped states [41].

⁸The time-of-flight is negative since we are tracking trajectories backward in time.

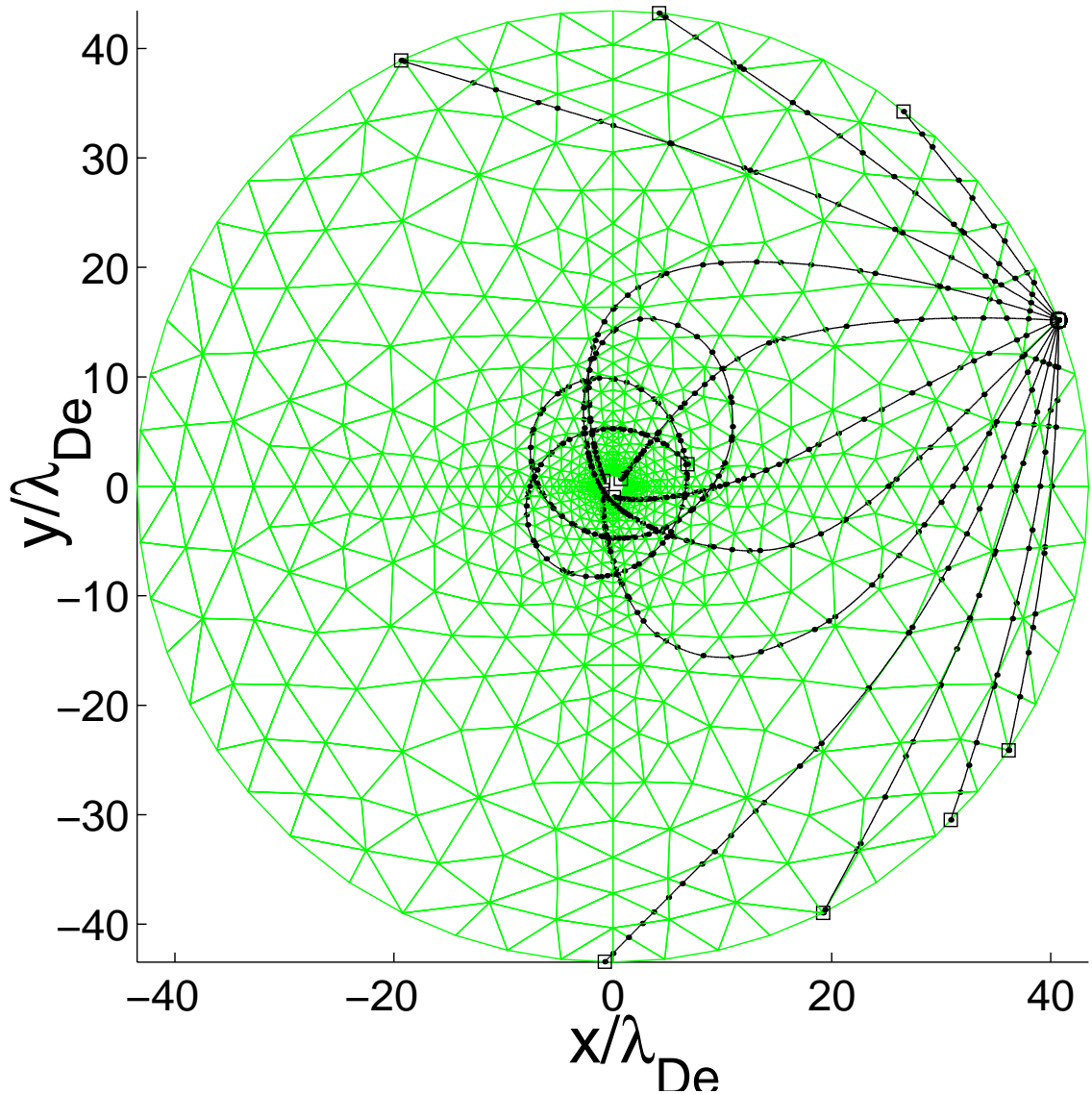


Figure 2.1: Example of the semi-analytical particle tracking process through the potential mesh on a grid with normalized coordinates. The normalized coordinates of the density interrogation point for the case shown are (40.7, 15.2).

acceleration $\vec{a} = \begin{Bmatrix} a_x \\ a_y \end{Bmatrix}$ is obtained from the potential samples at the triangle's vertices using

$$\begin{aligned}\vec{a} &= \frac{q}{m} \vec{E} = -\frac{q}{m} \nabla V \\ &= -\frac{q}{m} \frac{[(V_1 b_1 + V_2 b_2 + V_3 b_3) \hat{x} + (V_1 c_1 + V_2 c_2 + V_3 c_3) \hat{y}]}{2\Delta},\end{aligned}\quad (2.88)$$

where V_1 , V_2 , and V_3 are the potential samples at the three vertices of the triangle under consideration and the b_i , c_i , and Δ constants are given by (2.56) as a function of the triangle vertex coordinates. This trajectory is intersected with each of the three segments, and the intersection resulting in the shortest time-of-flight is selected as the origin of this subtrajectory. Each triangle's segment can be represented in one of two forms:

$$z(x, y) = s(y - px - q) = 0 \quad (2.89)$$

for segments oriented within 45 degrees of the x axis, and

$$z'(x, y) = s(x - p'y - q') = 0 \quad (2.90)$$

for other segments. In both (2.89) and (2.90), s is chosen as either +1 or -1, such that $z(x, y)$ or $z'(x, y)$ is made positive inside the triangle and negative outside. Inserting (2.86) and (2.87) into either (2.89) or (2.90), we obtain

$$z(t) = \underbrace{\frac{s}{2}(a_y - pa_x)t^2}_{z_A} + \underbrace{s(v_{iy} - pv_{ix})t}_{z_B} + \underbrace{s(y_i - px_i - q)}_{z_C} = 0 \quad (2.91)$$

or

$$z(t) = \underbrace{\frac{s}{2}(a_x - p'a_y)t^2}_{z_A} + \underbrace{s(v_{ix} - p'v_{iy})t}_{z_B} + \underbrace{s(x_i - p'y_i - q')}_{z_C} = 0, \quad (2.92)$$

respectively. Only one of the two roots of $z(t)$, which we define as $z(t) = z_A t^2 + z_B t + z_C$ in either cases, corresponds to an intersection where the particle is *entering* the triangle. This “entering” intersection must satisfy $\frac{dz}{dt} > 0$, since $z(t) < 0$ outside the triangle and $z(t) < 0$ inside the triangle. The unique solution that is both a root of $z(t)$ and satisfies $\frac{dz}{dt} > 0$ can

Algorithm 2 Numerically stable evaluation of quadratic root

if $z_B^2 - 4z_Az_C < 0$ **then**

No real root: trajectory does not intersect segment

else if $z_B \leq 0$ and $z_A \geq 0$ **then**

No past “entering” root for $t < 0$

else if $z_B \leq 0$ and $z_A < 0$ **then**

$$t \leftarrow \frac{-z_B + \sqrt{z_B^2 - 4z_Az_C}}{2z_A}$$

else if $z_B > 0$ **then**

$$t \leftarrow \frac{-2z_C}{z_B + \sqrt{z_B^2 - 4z_Az_C}}$$

end if

be written in two equivalent forms. For numerical stability [48], the roots are evaluated according to Algorithm 2.

Although both expressions for t in Algorithm 2 are mathematically equivalent, either one can become numerically unstable, and we must therefore choose the most stable expression on every evaluation. Our condition on $\frac{dz}{dt}$ is easily verified for both expressions: $\frac{dz}{dt} = 2z_A t + z_B = \sqrt{z_B^2 - 4z_Az_C} > 0$. The first expression is numerically unstable when $z_B > 0$, especially when z_A is small, due to near cancellation of the two terms in the numerator; a pathological example is that when $z_A = 0$, which leads to $t \leftarrow \frac{-z_B + z_B}{0} = \frac{0}{0}$, an indeterminate state, while the second expression yields the correct result, $t = -\frac{z_C}{z_B}$. The second expression is numerically unstable when $z_B \leq 0$, especially when z_C is small, due to near cancellation of the two terms in the denominator; a pathological example is that when $z_C = 0$, leading to the indeterminate state $t \leftarrow \frac{0}{z_B - z_B} = \frac{0}{0}$.

This semi-analytical trajectory-tracking technique is much more efficient than using a fixed time step particle pusher, since the number of computations necessary for each trajectory depends on the number of edges being crossed rather than the number of time steps necessary to reach a boundary. This is a highly desirable feature, in light of the fact that our typical applications (small probes at high voltage) require multi-scale resolution.

In addition, given the assumption of a piecewise-bilinear potential distribution, it provides exact (*nearly* exact if we account for roundoff errors) conservation of energy along orbits, which contributes to the accuracy of the overall approach.

2.4.2.1.1 A Note on Segment-bound Trajectories Under certain conditions of the accelerating electric fields in the two triangles surrounding a given mesh segment, some trajectories become bound to that segment, which can give rise to a large number of intersections with the segment due to tiny oscillations of the trajectory from one side of the segment to the other. Because this large number of intersections can significantly slow down computations, this case is treated as an exception. When such infinitesimal oscillations are detected, the oscillating portion of the trajectory is resolved using only the tangential velocity and acceleration along the segment. This process does not reduce the accuracy of the trajectory tracking in any way.

2.4.2.2 Sampling the Velocity Distribution Function

In collisionless plasmas, the velocity distribution function $f(x, y, v_x, v_y)$ is conserved along particle orbits [25], which allows one to infer the value of $f(x_f, y_f, v_{xf}, v_{yf})$ at a final position (x_f, y_f) and velocity (v_{xf}, v_{yf}) , based on its initial value $f(x_i, y_i, v_{xi}, v_{yi})$ at the origin of the particle's trajectory, at a position (x_i, y_i) and velocity (v_{xi}, v_{yi}) .

Using the semi-analytical trajectory-tracking procedure just described, we may determine the origin of a given particle trajectory, and thus sample the velocity distribution function. This is typically referred to as the *inside-out* technique [36] in plasma modeling and, more generally, as the method of characteristics [49] for solving partial differential equations (here, the collisionless Vlasov equation).

For *plasma-bounded* trajectories, the reverse-time tracking procedure eventually gets to the outer boundary of the computational domain (its origin), at a position (x_i, y_i) with

an “initial” velocity (v_{xi}, v_{yi}) . The velocity distribution at the “final” position (x_f, y_f) and velocity (v_{xf}, v_{yf}) can therefore be sampled based on the known velocity distribution on the outer boundary. The fact that the potential is floating on the outer boundary implies that the velocity distribution function at that location, $f_i(v_{xi}, v_{yi}) = f(x_i, y_i, v_{xi}, v_{yi})$, is different than the velocity distribution function $f_\infty(v_{x\infty}, v_{y\infty})$ at infinity. Since the electric fields are not modeled from $r = \infty$ to the outer boundary of the computational domain, an approximation must be made to infer f_i from f_∞ .

For this purpose, we use the “*straight-line approximation*”. This approximation consists of assuming straight-line trajectories from infinity to the outer boundary of the computational domain. Particles in the drifting Maxwellian population at $r = \infty$ are assumed to be accelerated along straight lines in the direction pointed to by their initial velocity, all the way to the point where they intersect the outer boundary of the computational domain. Based on this assumption, a drifting Maxwellian at infinity, given by

$$f_\infty(v_{x\infty}, v_{y\infty}) = \frac{n_0 m_{e,i}}{2\pi e T_{e,i}} \exp \left\{ -\frac{m_{e,i}}{2eT_{e,i}} \left((v_{x\infty} - U)^2 + v_{y\infty}^2 \right) \right\}, \quad (2.93)$$

where U is the flow speed of the background plasma, would be mapped to the following distribution on the outer boundary of the computational domain:

$$f_i(x_i, y_i, v_{xi}, v_{yi}) = \frac{n_0 m_{e,i}}{2\pi e T_{e,i}} \exp \left\{ -\frac{m_{e,i}}{2eT_{e,i}} \left(2 \frac{q_{e,i}}{m_{e,i}} V_{\text{edge}} + v_{xi}^2 + v_{yi}^2 + U^2 - 2U v_{xi} \sqrt{\frac{v_{xi}^2 + v_{yi}^2 + 2 \frac{q_{e,i}}{m_{e,i}} V_{\text{edge}}}{v_{xi}^2 + v_{yi}^2}} \right) \right\}, \quad (2.94)$$

where V_{edge} is the potential at the entry point on the outer boundary of the computational domain. This method was used for the calculations performed by *Godard and Laframboise* [30]. Its main advantage is that it provides a smooth transition to the stationary case where $U = 0$, in which case we simply recover the exact accelerated Maxwellian distribution. The expression given by (2.94) is no longer an approximation when $U = 0$ because,

in this case, the velocity distribution function samples do not depends on trajectories, they simply depend on total energy, just like in the 1-D model.

The reverse-time tracking procedure eventually traces the origin of *conductor-bounded* trajectories back to the surface of the probe or other conducting surfaces. Since the conductors are not emitting particles, we assume that these trajectories are unpopulated and set $f_{e,i}(x_f, y_f, v_{xf}, v_{yf}) = 0$.

Trapped trajectories, defined earlier in this section, are deemed unpopulated just like *conductor-bounded* trajectories. Thus, the velocity distribution function sample for trajectories identified as trapped is set to zero. The main difficulty with these trajectories, however, resides in the determination of the trapped state. Since, by definition, trapped trajectories orbit indefinitely, a set of criteria must be used to determine whether a trajectory being followed is actually trapped:

Maximum angular displacement The angular displacement of the particle is integrated over time, i.e.,

$$\theta_{\text{var}} = \int_{t=t_i}^{t_f} \left| \frac{d\theta(t)}{dt} \right| dt. \quad (2.95)$$

When this quantity goes beyond $2\pi M_{\text{orb}}$, the trajectory is deemed trapped. Typically, M_{orb} is set to 3, which, for a trajectory orbiting in a constant orientation along θ , corresponds to 3 full orbits about the origin.

Maximum number of radial oscillations Beyond a given number M_{rosc} of significant oscillations of the particle's radial coordinate r , the trajectory is assumed trapped. Typically, M_{rosc} is set to 5. This parameter is discussed in more detail in Section 4.3.2.1.

Maximum number of intersections of any single edge When the trajectory intersects a given edge, within the mesh, more than a given number M_{segcross} of times, the trajectory is assumed trapped. Typically, M_{segcross} is set to 100.

2.4.2.3 Velocity Space Integration

Having defined a mechanism for sampling the velocity distribution function, we now turn to the method used to compute the particle number density at any given point in computational space. This requires integrating $f(x, y, v_x, v_y)$ over all of velocity space.

2.4.2.3.1 Defining “Directional-Energy” Space For convenience, we map all of the 2-D velocity space onto *directional-energy* space, a 2-D space defined as follows:

$$E_v = \frac{q_{e,i}}{e} V(x, y) + \frac{m_{e,i}}{2e} (v_x^2 + v_y^2), \quad (2.96)$$

$$\cos \alpha = \frac{v_x}{\sqrt{v_x^2 + v_y^2}}, \quad (2.97)$$

$$\sin \alpha = \frac{v_y}{\sqrt{v_x^2 + v_y^2}}, \quad (2.98)$$

where the total (kinetic+potential) particle energy E_v is in units of electron-volts. Using the (E_v, α) domain of integration instead of the velocity domain of integration, i.e. (v_x, v_y) , simplifies the integration process and facilitates the graphical representation, in cylindrical coordinates, of velocity distributions. In this new domain, the density integral (2.7) becomes:

$$n_{e,i}(x, y) = \int \int g_{e,i}(x, y, E_v, \alpha) dE_v d\alpha, \quad (2.99)$$

where $g_{e,i}(x, y, E_v, \alpha)$ is the directional-energy distribution function defined as

$$g_{e,i}(x, y, E_v, \alpha) = \frac{e}{m_{e,i}} f_{e,i} \left(x, y, \sqrt{\frac{2e}{m_{e,i}} \left(E_v - \frac{q_{e,i}}{e} V \right)} \cos(\alpha), \sqrt{\frac{2e}{m_{e,i}} \left(E_v - \frac{q_{e,i}}{e} V \right)} \sin(\alpha) \right). \quad (2.100)$$

In this domain, the drifting Maxwellian velocity distribution becomes:

$$\begin{aligned} g_{e,i}(x, y, E_v, \alpha) &= g_{e,i}(x_i, y_i, E_v, \alpha_i) \\ &= \frac{n_0}{2\pi T_{e,i}} \exp \left\{ -\frac{1}{T_{e,i}} \left(E_v - U \sqrt{\frac{2m_{e,i} E_v}{e}} \cos \alpha_i + \frac{m_{e,i} U^2}{2e} \right) \right\}, \end{aligned} \quad (2.101)$$

where the index i refers to the entry (or “initial”) point of the particle at the outer boundary of computational space, and the total energy E_v is conserved all along the trajectory from (x_i, y_i) to (x, y) .

To limit the computational task, we restrict the domain of integration to a finite annular region within directional-energy space, outside of which $g_{e,i}(x, y, E_v, \alpha)$ is known to be very low:

$$E_{v,\min} = \max \left(\frac{q_{e,i}}{e} V(x, y), \left(\sqrt{\frac{m_{e,i}}{2e}} U - \sqrt{\kappa_{\text{range}} T_{e,i}} \right)^2 \right) \quad (2.102)$$

$$E_{v,\max} = \left(\sqrt{\frac{m_{e,i}}{2e}} U + \sqrt{\kappa_{\text{range}} T_{e,i}} \right)^2. \quad (2.103)$$

Outside of those bounds for the energy E_v , the exponential factor in (2.101) is guaranteed to be lower than $\exp\{-\kappa_{\text{range}}\}$. We typically choose $\kappa_{\text{range}} = 5$, corresponding to $\exp\{-\kappa_{\text{range}}\}|_{\kappa_{\text{range}}=5} = 0.0067$. This means that we are neglecting the integrand wherever its value goes below 0.67% of its maximum value (see discussion on page 54).

2.4.2.3.2 Numerical Integration in “Directional-Energy” Space Based on the new directional-energy space defined above, we numerically integrate $g_{e,i}(x, y, E_v, \alpha)$ within the rectangular domain given by:

$$E_{v,\min} \leq E_v \leq E_{v,\max} \quad (2.104)$$

$$0 \leq \alpha \leq 2\pi. \quad (2.105)$$

Several numerical quadrature schemes were considered, such as an adaptive cubature of triangular elements [50, 51]. As it turns out, however, this technique, as well as other high-order automatic quadrature routines available, are most suitable for smooth integrands.

Even though (2.101) does appear to be a smooth function, the directional-energy domain defined above is only partly covered with plasma-bounded trajectories. Some sub-

domains are populated with conductor-bounded and trapped trajectories, for which the distribution function $g_{e,i}(x, y, E_v, \alpha)$ is set to zero. This creates major discontinuities in the integrand, which are best represented and integrated using simple first-order polynomials.

Consistent with those findings, a low-order numerical scheme was implemented using a 2-D iterated integral, based on a single-variable adaptive trapezoidal quadrature [48]. The outer integral is performed along the direction α :

$$n(x, y) = \int_{\alpha=0}^{2\pi} I_1(x, y, \alpha) d\alpha \approx \sum_{k_\alpha=1}^{N_\alpha} w_{k_\alpha} I_1(x, y, \alpha_{k_\alpha}) \equiv n_{\text{est}}(x, y), \quad (2.106)$$

with the integrand $I_1(x, y, \alpha_{k_\alpha})$ obtained by integrating along the energy E_v (inner integrand),

$$\int_{E_v=E_{v,\min}}^{E_{v,\max}} g_{e,i}(x, y, E_v, \alpha_{k_\alpha}) dE_v \approx \sum_{k_E=1}^{N_E(k_\alpha)} w_{k_\alpha, k_E} g_{e,i}(x, y, E_{k_\alpha, k_E}, \alpha_{k_\alpha}) = I_1(x, y, \alpha_{k_\alpha}), \quad (2.107)$$

where we have explicitly indicated the dependence of the inner quadrature coefficients w_{k_α, k_E} , the energy samples $E_{k_\alpha, k_E} = E_v(k_\alpha, k_E)$ and the number of energy samples $N_E(k_\alpha)$ on the azimuthal sample number k_α .

For each one-dimensional quadrature, the domain of integration is sub-divided into a set number of sub-intervals, typically 25 along E_v and 45 along α . The integral over each sub-interval is then initially performed using both 2-point and 3-point trapezoidal rules [48]. The difference between the 2-point and 3-point quadratures is used as an estimate of the quadrature error. The sub-integrals are then refined by increasing the number of points used with the trapezoidal rule, providing improved sub-integrals and error estimates. This refinement is performed on the sub-integrals in decreasing order of quadrature error, until the total estimated error δn_{est} over the collection of sub-intervals is small enough that $\delta n_{\text{est}} \leq \tau_{\text{rel}} n_{\text{est}}$, where δn_{est} is the estimated error on n_{est} , and τ_{rel} is a relative tolerance on the integration error.

Let us consider the outer quadrature given by (2.106). In addition to the error caused by this quadrature approximation, there is a second error term caused by the error $\delta I_1(x, y, \alpha_{k_\alpha})$ on the integrand $I_1(x, y, \alpha_{k_\alpha})$, which stems from the error generated by the inner quadrature given by (2.107). However, if we assume that the errors $\delta I_1(x, y, \alpha_{k_\alpha})$, $k_\alpha = 1, \dots, N_\alpha$ are not correlated and use the same relative error τ_{rel} for the inner quadrature as we do for the outer quadrature, then the total error term contributed by those integrand errors can be considered small as compared to the quadrature error $\delta n_{\text{est}} = \tau_{\text{rel}} n_{\text{est}}$ on the outer quadrature:

$$\sum_{k_\alpha=1}^{N_\alpha} w_{k_\alpha} \delta I_1(x, y, \alpha_{k_\alpha}) = \sum_{k_\alpha=1}^{N_\alpha} w_{k_\alpha} p_{k_\alpha} \tau_{\text{rel}} I_1(x, y, \alpha_{k_\alpha}) << \tau_{\text{rel}} n_{\text{est}}, \quad (2.108)$$

where $p_{k_\alpha} = \pm 1$ is a random phase factor. This justifies using the same relative tolerance for both the inner and outer quadratures.

In addition to the use of a relative error tolerance, an absolute error tolerance is also used, in order to prevent excessive refinements of the inner quadrature. For some values of k_α , the integrand $I_1(x, y, \alpha_{k_\alpha})$ can take on relatively small values, contributing very little to n_{est} , and therefore need not be computed with an accuracy as good as that specified by the relative tolerance. Let us assume that we can tolerate an additional error term to n_{est} , on the same order of magnitude as $\delta n_{\text{est}} = \tau_{\text{rel}} n_{\text{est}}$, which, if we spread it out over the integrand $I_1(x, y, \alpha)$, determines an absolute tolerance on the values computed for $I_1(x, y, \alpha_{k_\alpha})$:

$$\tau_{\text{abs}, E} = \frac{\tau_{\text{rel}} n_{\text{est}}}{2\pi}. \quad (2.109)$$

Since the value for $\tau_{\text{abs}, E}$ is required in advance, i.e., before having computed a value for n_{est} , we use our best available estimate for n_{est} to compute $\tau_{\text{abs}, E}$, that is, the value obtained at the previous iteration of the iterative process (see Section 2.5). Finally, for the same reasons mentioned earlier, the non-correlated addition of the error terms caused by the use of this absolute error tolerance actually contributes much less than the outer-integral quadrature error $\delta n_{\text{est}} = \tau_{\text{rel}} n_{\text{est}}$. Therefore, for all practical purposes, we need not account

for this error term within δn_{est} .

We hereby summarize the complete quadrature process:

- The inner quadrature dynamically selects, using adaptive trapezoidal rules on a set of sub-intervals, the energy samples E_{k_α, k_E} , $k_E = 1, \dots, N_E(k_\alpha)$ and corresponding weights w_{k_α, k_E} that are required in order to compute $I_1(x, y, \alpha_{k_\alpha})$ with a relative accuracy τ_{rel} such that

$$\delta I_1(x, y, \alpha_{k_\alpha}) \leq \tau_{\text{rel}} I_1(x, y, \alpha_{k_\alpha}) + \tau_{\text{rel}} \frac{n_{\text{est,prev}}}{2\pi} \quad (2.110)$$

with $n_{\text{est,prev}}$ an estimate for the density based on the previous iteration.

- The outer quadrature dynamically selects, using adaptive trapezoidal rules on a set of sub-intervals, the direction samples α_{k_α} , $k_\alpha = 1, \dots, N_\alpha$ and corresponding weights w_{k_α} that are required in order to compute the estimate $n_{\text{est}}(x, y)$ for the density $n(x, y)$ with an accuracy

$$\delta n_{\text{est}} \leq \tau_{\text{rel}} n_{\text{est}}. \quad (2.111)$$

- The net result of those two embedded quadratures is an approximate number density

$$n_j \equiv n(x_j, y_j) = \sum_{k_\alpha=1}^{N_\alpha} w_{k_\alpha} \sum_{k_E=1}^{N_E(k_\alpha)} w_{k_\alpha, k_E} g_{e,i}(x, y, E_{k_\alpha, k_E}, \alpha_{k_\alpha}), \quad (2.112)$$

where w_{k_α} and α_{k_α} are selected by the α -quadrature, while w_{k_α, k_E} and E_{k_α, k_E} are selected by the E -quadrature. Finally, both the electron and ion number density estimates at all node locations are combined into the net charge density $\vec{\rho}$ through the expression

$$\rho(x_j, y_j) = (\vec{\rho}_{\text{out}})_j = q_e(n_e)_j + q_i(n_i)_j. \quad (2.113)$$

2.4.2.4 Linearizing the 2-D Vlasov Solver

The linearization of the 2-D Vlasov operator is similar to that of the 1-D Vlasov operator. It provides a Jacobian matrix $\mathbf{J}_V = \frac{\partial \vec{f}_V}{\partial \vec{V}} = \frac{\partial \vec{\rho}_{\text{out}}}{\partial \vec{V}}$ that describes the linear dependence of the output charge distribution onto the potential distribution.

Appendix E details the linearization process used for the 2-D Vlasov solver. It describes two different techniques that are used alternatively for stationary and flowing problems, respectively, along with sources of error in the calculation of the Jacobian.

2.5 Regularized Newton Iterative Poisson–Vlasov Scheme

Using the Poisson and Vlasov solvers, we now seek to find a solution for the potential and charge distributions that satisfies both the Poisson and Vlasov equations. We have seen that this task is equivalent to finding the fixed point of the Poisson–Vlasov functional defined in (2.12) and illustrated in Figure 2.2. In Sections 2.3 and 2.4, we have defined Poisson and Vlasov solvers that are numerical approximations of the Poisson (2.10) and Vlasov (2.11) operators, respectively. In Table 2.2, we show the correspondence between the functional and associated numerical solver for the Poisson, Vlasov, and Poisson–Vlasov operators. As can be seen in that table, we distinguish the functionals from their corresponding numerical solvers by putting an arrow on top of the symbols used for the operators, which were defined in Section 2.2. The newly defined functions \vec{f}_P , \vec{f}_V and \vec{f}_{PV} are thus all multi-valued functions of multiple variables.

There are known difficulties arising in finding the fixed point of a multivalued, multivariate function [8]. Simple iteration of the fixed point operator does not in general yield convergence, since it is a non-contractive mapping [52]. Laframboise [8], Xu [17], and McMahon [22] use a method consisting of mixing consecutive iterates using empirically-determined mixing functions. Because of the breadth of regimes sought as part of this

Operator	Functional	Numerical Solver
Poisson	$V(x,y) = f_P \{\rho(x,y)\}$	$\vec{V} = \vec{f}_P \{\vec{\rho}_{\text{in}}\}$
Vlasov	$\rho(x,y) = f_V \{V(x,y)\}$	$\vec{\rho}_{\text{out}} = \vec{f}_V \{\vec{V}\}$
Poisson–Vlasov	$\rho_{\text{out}}(x,y) = f_{PV} \{\rho_{\text{in}}(x,y)\}$	$\vec{\rho}_{\text{out}} = \vec{f}_{PV} \{\vec{\rho}_{\text{in}}\}$

Table 2.2: Functional operators and corresponding numerical solvers. The Poisson–Vlasov functional is defined as a composition of the Poisson and Vlasov functionals, so that $\vec{f}_{PV} \{\cdot\} = \vec{f}_V \{\vec{f}_P \{\cdot\}\}$.

research (low and high voltages, arbitrary geometries, plasma flow), we found that the iterate mixing method could not provide a repeatable and reliable automated technique for finding accurate approximations to the fixed point of the Poisson–Vlasov operator in a reasonable number of iterations. This is especially true when modeling two kinetic species and in regimes comprising high voltages and various probe geometries.

2.5.1 Top-level Iterative Scheme

To address these difficulties, we have chosen to implement a procedure based on Newton’s method for nonlinear systems of equations [53]. This technique, which we designate as the *Progressive Tikhonov-regularized Newton iterative Poisson–Vlasov procedure*, is depicted in Figure 2.3. It consists of progressively improving a solution vector $\vec{\rho}_{\text{in}}$, i.e., reducing the residual norm $\|\vec{\rho}_{\text{in}} - \vec{\rho}_{\text{out}}\|$, by successively linearizing the Poisson–Vlasov

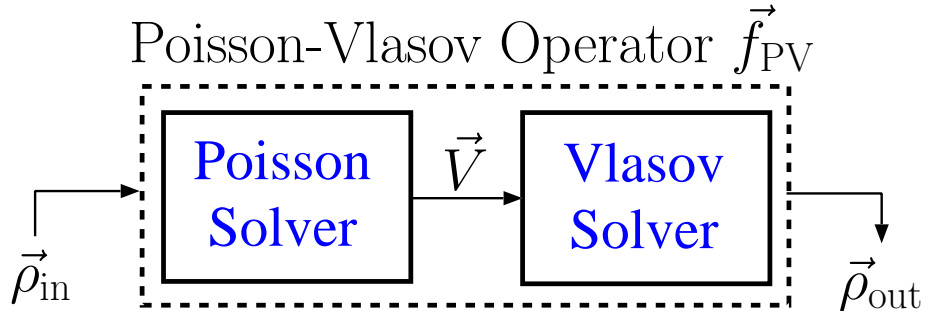


Figure 2.2: Poisson–Vlasov operator comprised of both the Poisson and Vlasov solvers. This operator is an approximation of the Poisson–Vlasov functional defined in (2.12).

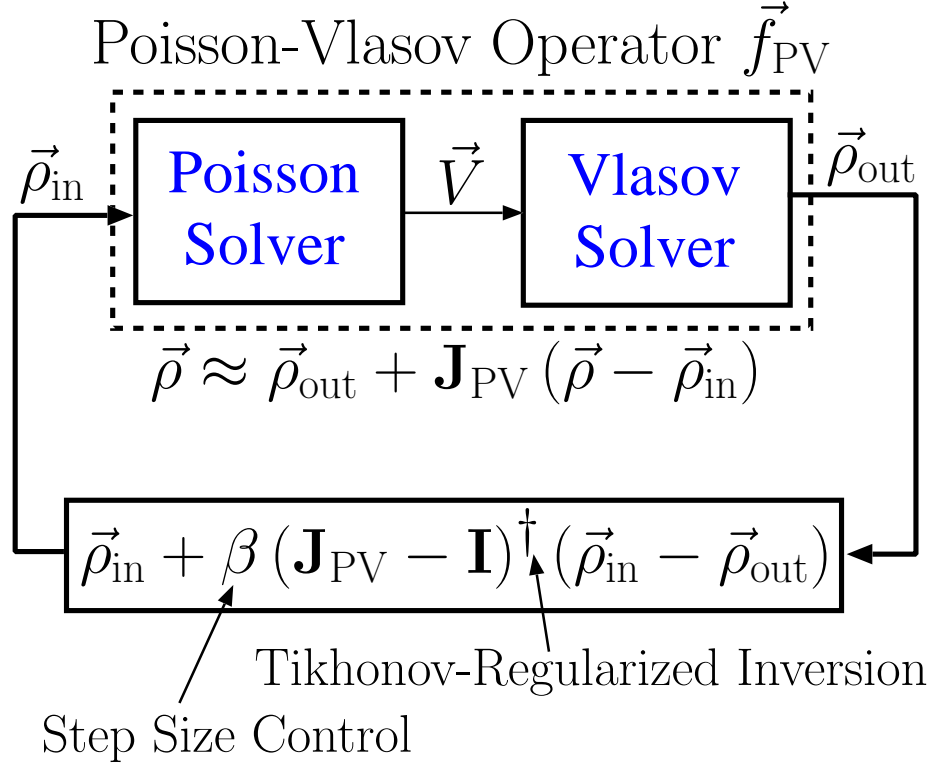


Figure 2.3: Tikhonov-regularized Newton iterative Poisson–Vlasov procedure.

operator and finding a regularized solution for the resulting linearized system of equations. This process relaxes the solution vector $\vec{\rho}_{in}$ and has the global effect of reducing the Euclidean distance between $\vec{\rho}_{in}$ and $\vec{\rho}_{out}$. The iterative process continues until the solution can no longer be improved with the specified quadrature accuracy used in the Vlasov solver. In practice, a suitable quadrature accuracy is chosen that allows the iterates to reach a reasonably low residual norm $\|\vec{\rho}_{in} - \vec{\rho}_{out}\|_\infty$, on the order of one percent of the background plasma density.

This iterative procedure requires the $N \times N$ Jacobian matrix \mathbf{J}_{PV} of the Poisson–Vlasov operator, which is defined as

$$\mathbf{J}_{PV} = \left. \frac{\partial \vec{f}_{PV}}{\partial \vec{\rho}} \right|_{\vec{\rho}=\vec{\rho}_{in}} \quad (2.114)$$

and can be obtained, using the chain rule, as a combination of the Jacobian matrices of the

Poisson and Vlasov operators, following

$$\mathbf{J}_{PV} = \frac{\partial \vec{f}_V}{\partial \vec{V}} \times \frac{\partial \vec{f}_P}{\partial \vec{\rho}} \Big|_{\vec{\rho}=\vec{\rho}_{in}} = \underbrace{\frac{\partial \vec{\rho}_{out}}{\partial \vec{V}}}_{\mathbf{J}_V} \underbrace{\frac{\partial \vec{V}}{\partial \vec{\rho}_{in}}}_{\mathbf{J}_P} = \mathbf{J}_V \mathbf{J}_P, \quad (2.115)$$

where the Jacobian of the Poisson operator was simply recognized as the matrix in the linear Poisson operator, as obtained for KiPS-1D in (2.27) and for KiPS-2D in (2.68). The Jacobian of the Vlasov solver, \mathbf{J}_V , was derived in Sections 2.4.1.2 and 2.4.2.4, where we discussed the linearization of the Vlasov operator in the 1-D and 2-D solvers, respectively.

In its simplest form, the Newton method [53] attempts to use the linearized behavior of a multivalued function of several variables to solve a nonlinear system of equations. In the present case, we are looking for the fixed point of the Poisson–Vlasov operator or, put differently, we are looking for the vectorial root of the vectorial equation

$$\vec{g}(\vec{\rho}) = \vec{f}_{PV}(\vec{\rho}) - \vec{\rho} = 0, \quad (2.116)$$

which, upon approximating \vec{f}_{PV} by its first-order Taylor expansion

$$\vec{f}_{PV}(\vec{\rho}) \approx \vec{\rho}_{out} + \mathbf{J}_{PV}(\vec{\rho} - \vec{\rho}_{in}), \quad (2.117)$$

yields a linear system of N equations in N variables,

$$[\mathbf{J}_{PV} - \mathbf{I}] (\vec{\rho} - \vec{\rho}_{in}) = \vec{\rho}_{in} - \vec{\rho}_{out}, \quad (2.118)$$

where the unknown vector $\vec{\rho} - \vec{\rho}_{in}$ is an incremental improvement that will be added to the present guess $\vec{\rho}_{in}$ of the charge density distribution, and \mathbf{I} is the $N \times N$ identity matrix.

2.5.2 Conditioning and Quadrature Noise Issues

One is first tempted to simply invert the system matrix and compute the corrected charge density distribution according to

$$\vec{\rho}_{in} \leftarrow \vec{\rho}_{in} + [\mathbf{J}_{PV} - \mathbf{I}]^{-1} (\vec{\rho}_{in} - \vec{\rho}_{out}), \quad (2.119)$$

which can be performed using standard linear algebra algorithms such as the LU decomposition [54]. Such an attempt, however, is in general met with wild, non-physical variations in the charge density distribution $\vec{\rho}_{\text{in}}$ at some point during the iterative process, and almost never leads to a convergence of the result to a low $\|\vec{\rho}_{\text{in}} - \vec{\rho}_{\text{out}}\|_{\infty}$ error state. This diverging behavior is generally due to the ill-conditioning of the system matrix $[\mathbf{J}_{PV} - \mathbf{I}]$ for some iterates, which can greatly amplify any quadrature noise present in the error vector $(\vec{\rho}_{\text{in}} - \vec{\rho}_{\text{out}})$. The ill-conditioning of the system matrix can be due to a combination of several causes, some of which we identify here.

Ill-conditioning of the Vlasov operator, which can be due to the weak or nonexistent dependence of most particle trajectories upon some samples of the potential, at various “operating points” of the potential solution vector \vec{V} (near or far from the physical solution).

Ill-conditioning of the Poisson operator due to a high mesh density in some locations that creates very similar dependences to some of the densely packed charge samples, thereby causing highly similar lines in the Poisson matrix \mathbf{J}_P , defined in Section 2.3.

Incomplete entries in the Vlasov Jacobian \mathbf{J}_V due to the fact that some components of the linearized dependence upon the potential samples \vec{V} could not be fully accounted for by the approximate gradient calculation (this only applies to the 2-D version — see Section 2.4.2.4).

Because of the ill-posedness of this problem, the standard Newton method turns out to be impractical for the resolution of this nonlinear system of equations. In the following, we will describe a diagonal scaling technique and a nonlinear regularization method to address this conditioning issue.

Even though our nonlinear system (2.116) does not contain any noisy data per se, the right-hand side of the linearized system (2.118) is noisy due to the finite precision used in calculating the output charge profile $\vec{\rho}_{\text{out}} = \vec{f}_{PV}(\vec{\rho}_{\text{in}})$, which we emphasize here:

$$[\mathbf{J}_{PV} - \mathbf{I}] (\vec{\rho} - \vec{\rho}_{\text{in}}) = \vec{\rho}_{\text{in}} - \underbrace{\vec{\rho}_{\text{out}}}_{\vec{\rho}_{\text{out}} + \delta\vec{\rho}_{\text{out}}} , \quad (2.120)$$

where $\delta\vec{\rho}_{\text{out}}$ is the quadrature noise term. Recall that the output charge profile $\vec{\rho}_{\text{out}}$ is computed based on subtracting the electron and ion charge profiles,

$$\vec{\rho}_{\text{out}} = e (\vec{n}_i - \vec{n}_e) , \quad (2.121)$$

which implies that any numerical quadrature error in the calculation of the density profiles \vec{n}_i and \vec{n}_e can lead to a large relative error $\frac{\|\delta\vec{\rho}_{\text{out}}\|}{\|\vec{\rho}_{\text{out}}\|}$ wherever the electron and ion densities are very similar, leading to a subtraction of like terms. This situation arises close to the outer boundary of the computational domain, which is typically sized large enough to enclose all of the significant charge imbalance, that is, all of the sheath and some of the pre-sheath.

2.5.3 Diagonal Preconditioning

One of the simplest measures that can be taken in order to mitigate the propagation of the quadrature errors present on the RHS of (2.120) to the incremental solution $\vec{\rho} - \vec{\rho}_{\text{in}}$ is to perform a diagonal preconditioning of the linear system, in an effort to reduce the condition number of the system matrix. Let us first re-cast the linearized system of interest (2.120) into the following standard form:

$$\mathbf{A}\vec{x} = \vec{b} = \vec{b} + \delta\vec{b} , \quad (2.122)$$

where $\mathbf{A} \equiv [\mathbf{J}_{PV} - \mathbf{I}]$, $\vec{b} \equiv \vec{\rho}_{\text{in}} - \vec{\rho}_{\text{out}}$, $\vec{x} \equiv (\vec{\rho} - \vec{\rho}_{\text{in}})$ and the quadrature noise is given by $\delta\vec{b} \equiv -\delta\vec{\rho}_{\text{out}}$. The vector \vec{x} thus constitutes an increment to the present state of the charge profile $\vec{\rho}_{\text{in}}$. We choose to use a diagonal right preconditioner [54] \mathbf{D}_p that must approximate

\mathbf{A}^{-1} as best as possible without actually inverting \mathbf{A} , in such a manner as to make the product \mathbf{AD}_p closer to the identity matrix. Inserting $\mathbf{D}_p\mathbf{D}_p^{-1}$ into (2.122), we write:

$$\underbrace{\mathbf{AD}_p}_{\mathbf{A}'} \underbrace{(\mathbf{D}_p^{-1}\vec{x})}_{\vec{x}'} = \vec{b}. \quad (2.123)$$

To solve (2.122), we will therefore first solve $\mathbf{A}'\vec{x}' = \vec{b}$, and then compute \vec{x} using $\vec{x} = \mathbf{D}_p\vec{x}'$.

For the class of problems at hand, it was found that setting the entries of the diagonal matrix \mathbf{D}_p equal to the inverse of the norm of the corresponding column vectors of \mathbf{A} yielded the best results:

$$\mathbf{D}_p : \begin{cases} i = j & (\mathbf{D}_p)_{ij} = \frac{1}{\|\mathbf{A}_{:,i}\|_2} \\ i \neq j & (\mathbf{D}_p)_{ij} = 0, \end{cases} \quad (2.124)$$

where $\|\mathbf{A}_{:,i}\|_2$ is the Euclidean norm of the i^{th} column of the system matrix \mathbf{A} . Using this preconditioner, the scaled solution vector \vec{x}' has its elements scaled proportional to the level of dependence of the system matrix \mathbf{A} on each element of \vec{x} , thereby improving the signal-to-noise ratio on the elements of \vec{x} upon which the system is most dependent.

Even though preconditioning is essential and improves the condition of the linearized system, it is simply not sufficient to fully prevent quadrature noise from entering the solution vector. The regularization process described below will complete the required set of tools for an accurate resolution of the nonlinear systems at hand.

2.5.4 Tikhonov “Progressive” Regularization

In this section we will describe the complete regularization procedure, which we represent as a “Tikhonov-regularized inversion” in Figure 2.3.

The topic of regularization of linear systems of equations has attained a very good maturity level [55–60] and is extensively used for inverse linear problems involving noisy data in applications such as ionospheric characterizations [61]. A typical linear inverse problem involving noisy data is of the form $A\vec{x} = \vec{y} = \vec{y}_0 + \vec{\delta}$, where \vec{y} contains some noisy

data and \vec{x} is a set of unknown parameters.

Nonlinear inversion has also seen significant progress [62–66]. It consists of looking for a solution \vec{x} to a nonlinear system of equations of the form

$$\vec{F}(\vec{x}) = \vec{y} = \vec{y}_0 + \vec{\delta}, \quad (2.125)$$

where \vec{F} is a nonlinear multivalued function of several variables, \vec{y} contains noisy data, and \vec{x} is the set of unknown parameters.

Our problem of interest is different from nonlinear inversion in that we are not trying to “invert” a nonlinear function given a specified noisy data set. Instead, we are looking for the fixed point of a nonlinear function $\vec{f}_{PV}(\vec{\rho})$, i.e., the root of the nonlinear function $\vec{g}(\vec{\rho})$ as specified by (2.116). This is equivalent to solving a nonlinear system of the form given by (2.125) with $\vec{y} = 0$.

We therefore seek a method to limit the amount of quadrature noise entering the solution vector $\vec{\rho}_{\text{in}}$ at every iteration, while still allowing a significant improvement of the solution. Instead of directly solving the preconditioned linear system of equations (2.123), we seek a compromise between the reduction of the error $\|\mathbf{A}'\vec{x}' - \vec{b}\|$ and the amount of noise “creeping into” the solution. A useful compromise is one that would prevent any significant magnification of the noise present in \vec{b} by the inversion of the ill-conditioned system matrix \mathbf{A}' , while still significantly reducing the error $\|\mathbf{A}'\vec{x}' - \vec{b}\|$. This can be accomplished by solving only for the “modes” in \vec{x}' upon which the preconditioned system matrix \mathbf{A}' is most dependent, effectively filtering out the more independent, higher-order “modes” that are very sensitive to any noise in \vec{b} .

The “modes” we refer to here correspond to the set of singular values of the preconditioned system matrix \mathbf{A}' . Using the singular value decomposition [54], the $N \times N$ matrix

\mathbf{A}' can be factorized to the form:

$$\mathbf{A}' = \mathbf{U} \operatorname{diag}(\vec{\sigma}) \mathbf{V}^T, \quad (2.126)$$

where $\operatorname{diag}(\vec{\sigma})$ is a diagonal matrix whose diagonal is formed by the N elements of the vector $\vec{\sigma}$, which are the singular values of \mathbf{A}' numbered in descending order, $\sigma_1 \geq \sigma_2 \geq \dots \geq \sigma_n \geq 0$. \mathbf{U} and \mathbf{V} are both $N \times N$ unitary matrices. Recasting the system equation (2.123) based on this transformation yields:

$$\operatorname{diag}(\vec{\sigma}) \mathbf{V}^T \vec{x}' = \mathbf{U}^T \vec{b} \quad (2.127)$$

or

$$\operatorname{diag}(\vec{\sigma}) \tilde{x} = \tilde{b}, \quad (2.128)$$

with

$$\tilde{x} = \mathbf{V}^T \vec{x}' \quad \text{and} \quad \tilde{b} = \mathbf{U}^T \vec{b}. \quad (2.129)$$

The linearized system has been re-written in a vector space corresponding to the singular values of the system matrix \mathbf{A} , yielding a set of uncoupled linear relationships between the corresponding components of \tilde{x} and \tilde{b} :

$$\begin{aligned} \sigma_1 \tilde{x}_1 &= \tilde{b}_1 \\ \sigma_2 \tilde{x}_2 &= \tilde{b}_2 \\ &\vdots \\ \sigma_N \tilde{x}_N &= \tilde{b}_N. \end{aligned} \quad (2.130)$$

In this transformed vector space, a direct inversion of the linearized system is performed by simply solving each mode separately using

$$\tilde{x}_i = \frac{\tilde{b}_i}{\sigma_i}. \quad (2.131)$$

Now, an ill-conditioned matrix \mathbf{A} has some extremely small singular values σ_i for large i , potentially resulting in extremely large amplitudes for some of the \tilde{x}_i 's, along with significant amplification of the noise present in the corresponding \tilde{b}_i 's.

Setting an appropriate “low-pass” filter to allow the lowest-order modes corresponding to the largest singular values of σ_i while blocking the high-order modes corresponding to the smallest singular values of σ_i would accomplish our goal of somewhat improving upon the current guess $\vec{\rho}_{\text{in}}$ while limiting the amount of noise creeping into the solution. The Tikhonov regularization [56, 58] implements such a continuous “low-pass” filter. Instead of directly solving for \tilde{x} using (2.131), the Tikhonov-regularized inversion is implemented as

$$\tilde{x}_i = \frac{\sigma_i}{\sigma_i^2 + \lambda^2} \tilde{b}_i, \quad (2.132)$$

effectively shutting down the high-order modes corresponding to small singular values for which $\sigma_i < \lambda$. A mathematically equivalent form of the Tikhonov regularization exists in the non-transformed domain, as a replacement for the simple inversion $\vec{x}' = [\mathbf{A}']^{-1} \vec{b}$:

$$\vec{x}' = [\mathbf{A}'^T \mathbf{A}' + \lambda^2 \mathbf{I}]^{-1} \mathbf{A}'^T \vec{b}. \quad (2.133)$$

For our application, the Tikhonov-regularization parameter λ is tuned according to the following criteria: the targeted error is to be equal to half of the present error, in order to achieve some progress while limiting the amount of noise creeping into the solution. This prudent requirement constitutes the basis of the proposed *progressive* Tikhonov regularization. It has been shown in practice to prevent divergence due to the ill-conditioning of the system matrix, while allowing for significant reduction of the present error $\|\vec{\rho}_{\text{in}} - \vec{\rho}_{\text{out}}\|_2$.

This criteria can be written as

$$\|\vec{b} - \mathbf{A}' \vec{x}'_\lambda\|_2 = 0.5 \|\vec{b}\|_2 \quad (2.134)$$

or, using the original notation,

$$\|(\vec{\rho}_{\text{in}} - \vec{\rho}_{\text{out}}) - [\mathbf{J}_{PV} - \mathbf{I}] \vec{x}_\lambda\|_2 = 0.5 \|\vec{\rho}_{\text{in}} - \vec{\rho}_{\text{out}}\|_2. \quad (2.135)$$

In these two expressions, \vec{x}'_λ and \vec{x}_λ both correspond to the result from (2.133) for a given

value of the regularization parameter λ , and are related through $\vec{x}_\lambda = \mathbf{D}_p \vec{x}'_\lambda$. At each iteration, an optimal value for λ must be determined that satisfies the equivalent expressions (2.134) and (2.135). This is done in one of two ways:

- If the dimension of the system matrix, N , is not too large (say $N < 1000$), \mathbf{A}' is first factored into a set of singular values and corresponding unitary matrices \mathbf{U} and \mathbf{V} , consistent with (2.126), using the singular value decomposition algorithm [54]. (2.134) is then solved by numerically solving for λ the equivalent expression

$$\sum_{i=1}^N \frac{\lambda^4}{(\sigma_i^2 + \lambda^2)^2} \tilde{b}_i^2 = \frac{1}{4} \sum_{i=1}^N \tilde{b}_i^2, \quad (2.136)$$

using an appropriate numerical root-finding algorithm (we use the function *fminnbd()* provided as part of the *Matlab*TM software package).

- If the dimension of the system matrix N is too large ($N > 1000$) for the singular value decomposition to be performed quickly, then equations (2.134) and (2.133) are used to numerically solve for λ with reasonable accuracy. This method is more computationally economical than the previous one since, by using the optimal value of λ obtained at the previous iteration, as few as 10 trials are typically necessary to re-optimize for λ . For large N , 10 linear system resolutions of an $N \times N$ system as performed in (2.133) are done much faster than one singular value decomposition (e.g., for $N = 1000$, it takes about 65 times longer to perform a singular value decomposition than to perform an LU decomposition.⁹)

This progressive regularization strategy enables the iterative refinement procedure to safely get through the highly singular iterates, that is, the iterates for which the system matrix $\mathbf{A} = [\mathbf{J}_{PV} - \mathbf{I}]$ is quasi-singular, without diverging. The net effect of the progressive

⁹Based on a benchmark performed on a Linux-based MatlabTM 6.0 engine.

Tikhonov regularization is that the incremental correction of the solution vector dominates over the addition of quadrature noise, resulting in a net improvement of the solution.

The combination of the diagonal preconditioner, described in Section 2.5.3 and the regularized inversion described in this section constitute the “Tikhonov-regularized inversion” and are represented using the symbol \dagger in Figure 2.3. The complete Tikhonov-regularized inversion referred to in Figure 2.3 can thus be written as

$$\Delta\vec{\rho}_{\text{in}} = \beta (\mathbf{J}_{PV} - \mathbf{I})^\dagger (\vec{\rho}_{\text{in}} - \vec{\rho}_{\text{out}}) \equiv \beta \mathbf{D}_p \left[(\mathbf{A}\mathbf{D}_p)^T \mathbf{A}\mathbf{D}_p + \lambda^2 \mathbf{I} \right]^{-1} (\mathbf{A}\mathbf{D}_p)^T (\vec{\rho}_{\text{in}} - \vec{\rho}_{\text{out}}), \quad (2.137)$$

where $\mathbf{A} = (\mathbf{J}_{PV} - \mathbf{I})$, λ is determined according to (2.135), \mathbf{D}_p is the diagonal preconditioner described in Section 2.5.3, and β is the step length determined by the step size control procedure described in Section 2.5.6.

2.5.5 Discrepancy Principle as Stopping Criteria

As the algorithm approaches the solution, the error $\vec{b} = \vec{\rho}_{\text{in}} - \vec{\rho}_{\text{out}}$ goes down significantly while the quadrature error $\delta\vec{b} = -\delta\vec{\rho}_{\text{out}}$ on the RHS of (2.122) and (2.123) increases due to the fact that the densities for both species have reached similar values close to the outer computational boundary, that is, in the pre-sheath (see discussion in Section 2.5.2).

For a given quadrature accuracy, there is a point at which the magnitude of the quadrature error will become comparable to that of the residual norm of the solution, i.e., $\|\vec{b}\|_2 \approx \|\delta\vec{b}\|_2$. According to the *discrepancy principle* [57], [67, §26], [64], this corresponds to the ideal level of regularization, an optimal compromise between the minimization of the residual norm $\|\vec{\rho}_{\text{in}} - \vec{\rho}_{\text{out}}\|_2$ and the penetration of quadrature noise in the solution $\vec{\rho}_{\text{in}}$.

We therefore set as a stopping criteria that the iterations must stop when the ratio of quadrature noise over residual norm goes beyond unity:

$$\text{Stopping Criteria: } \frac{\|\delta\vec{b}\|_2}{\|\vec{b}\|_2} = \frac{\|\delta\vec{\rho}_{\text{out}}\|_2}{\|\vec{\rho}_{\text{in}} - \vec{\rho}_{\text{out}}\|_2} \geq 1. \quad (2.138)$$

Continuing the iterations further would “oversolve” the problem (or under-regularize) and stopping any earlier would “undersolve” the problem (or over-regularize). Of course, this stopping criteria is dependent upon computing a sufficiently accurate estimate of the quadrature error as part of the quadrature algorithms for KiPS-1D and KiPS-2D, presented in Sections 2.4.1.1 and 2.4.2.3 respectively.

The quadrature accuracy estimates used as part of this work are conservative, i.e., they tend to overestimate the quadrature error, which means that most of the time we may be somewhat “undersolving” (or over-regularizing) the solution. The only consequence of this is that a better quadrature accuracy may be required in order to reduce the residual norm to a given desired level as compared to the ideal situation where one has an infinitely accurate evaluation of the quadrature error. We choose to stay on the “safe” side and risk undersolving the problem rather than to risk letting any quadrature noise degrade the quality of the solution and possibly generate a nonphysical solution.

2.5.6 Dynamic Step Size Control

We hereby describe the step size control procedure represented by the constant β in Figure 2.3. The standard Newton method simply uses $\beta = 1$. This is not suitable, in general, for our problems of interest, for several reasons:

- For some iterates, the local curvature of the “solution path” in N -dimensional space is sufficiently pronounced that the local linearization of the Poisson–Vlasov operator \vec{f}_{PV} , represented by the Jacobian \mathbf{J}_{PV} , cannot be trusted to represent \vec{f}_{PV} for a full unit step.
- Even though the analytical Poisson–Vlasov functional f_{PV} (see Table 2.2) has a fixed point corresponding to the physical solution, its approximate numerical representation \vec{f}_{PV} may not actually have an exact fixed point due to the discrete representation

of the numerical solver. Therefore, the Poisson–Vlasov operator \vec{f}_{PV} can be singular at the optimum solution point, i.e., the linearized system can be ill-conditioned near the optimum solution. The optimal solution in this case corresponds to a least-squares solution.

- The Jacobian can in some cases be incomplete for some N-dimensional space directions, as mentioned in Section 2.5.2.

In order to ensure a fault-tolerant step size control algorithm (i.e., tolerant to an incomplete Jacobian), we cannot use any implicit step size formula that would be based on the Jacobian. In addition, we cannot afford to perform an explicit line search that would involve evaluating the Poisson–Vlasov operator along the search direction. Instead, we seek to control the progress of the iterations by enforcing a specified “angle” α_c between successive search directions, as defined by

$$\cos(\alpha_c)_k = \left[\frac{(\Delta\vec{\rho}_{in})_k}{\|(\Delta\vec{\rho}_{in})_k\|} \right]^T \left[\frac{(\Delta\vec{\rho}_{in})_{k-1}}{\|(\Delta\vec{\rho}_{in})_{k-1}\|} \right], \quad (2.139)$$

where $\frac{(\Delta\vec{\rho}_{in})_k}{\|(\Delta\vec{\rho}_{in})_k\|}$ is the present search direction (iteration k) and $\frac{(\Delta\vec{\rho}_{in})_{k-1}}{\|(\Delta\vec{\rho}_{in})_{k-1}\|}$ is the previous iteration’s search direction (iteration $k - 1$).

The *guarded tangent control* algorithm that we present here seeks to control the step size β in such a way as to stabilize the change in successive directions to a target value $\alpha_c = \alpha_c^t$. Let us first define an *a posteriori* formula that applies a correction to the present step length β based on the present value of α_c and the target value α_c^t ,

$$\beta_k^{\text{desired}} = \beta_{k-1} \times \min \left\{ \frac{1}{2}, \frac{1 + \cos(\alpha_c)_k}{1 + \cos \alpha_c^t} \right\}, \quad (2.140)$$

where we enforce a minimum step size compression of $\frac{1}{2}$ to improve the stability of the algorithm. This correction formula provides a simple correction based on two successive search directions. However, using it directly may cause the step size to oscillate as a function of the iteration number k . For additional stability, controls are included that mix the

Algorithm 3 Dynamic step size control

Initialize step size: set $\beta = 1$;
Initialize mixing factor: set $\mu_{\text{mix}} = 0.1$;
Initialize iteration number: set $k = 0$;
while Solution has not converged **do**
 $k \leftarrow k + 1$;
 Compute search direction;
 if Not first iteration **then**
 Compute angle $(\alpha_c)_k$ between $(k - 1)^{\text{th}}$ and k^{th} search directions using (2.139);
 Compute desired step size β^{desired} based on present step size β and α_c using (2.140);
 if $(\alpha_c)_k$ is below a threshold value α_c^{max} **then**
 Mix the present step size with the desired step size using the mixing factor μ_{mix} :
 $\beta \leftarrow \beta + \mu_{\text{mix}} (\beta^{\text{desired}} - \beta)$
 Enforce maximum step size (a prudent value is $\beta_{\text{max}} = 1$): $\beta \leftarrow \min(\beta_{\text{max}}, \beta)$;
 if the step size has changed in the opposite direction from the previous iteration
 then
 Decrease the mixing factor (within bounds)
 $\mu_{\text{mix}} \leftarrow \max(0.01, 0.5 \mu_{\text{mix}})$
 else
 Increase the mixing factor (within bounds)
 $\mu_{\text{mix}} \leftarrow \min(1.0, 1.1 \mu_{\text{mix}})$
 end if
 else
 Use the desired step size directly: set $\beta_k = \beta_k^{\text{desired}}$;
 Resume the previous solution vector : set $(\vec{\rho}_{\text{in}})_k = (\vec{\rho}_{\text{in}})_{k-1}$;
 end if
 end if
 end while

previous step size β_{k-1} with the “desired” step size β_k^{desired} , and dynamically adjust the mixing factor in order to stabilize the step size. This is shown in Algorithm 3. Note that the stabilizing effect comes from the contrast between the increasing (1.1) and decreasing (0.5) multipliers used to modify the mixing factor μ_{mix} : the mixing factor drops sharply to dampen any detected oscillations, and then slowly ramps up as long as no oscillations are detected. In addition to attempting to maintain α_c near a target value α_c^t , the algorithm features a “guard” value α_c^{max} that it is not allowed to exceed. Whenever successive search directions differ so much that α_c^{max} is exceeded, the previous incremental adjustment to the solution vector $\vec{\rho}_{\text{in}}$ is canceled and the iterations resume starting with the previous guess for

$\vec{\rho}_{\text{in}}$ and an appropriately reduced step size. This adds some stability to the whole procedure by guarding against excessive step sizes that would bring the solution vector too far off from the linearized behavior of the Poisson–Vlasov operator.

2.5.7 Dynamic Adaptive Quadrature Tolerance

In Section 2.5.5, we have seen that the iterative process is allowed to continue as long as the quadrature error is smaller than the residual norm (see (2.138)). On the other hand, for the early iterates the residual norm is so large that it would be acceptable to use a larger quadrature tolerance for these iterates. Setting the quadrature tolerance in a dynamic fashion at every iteration allows great savings on computing time. In order to include margin with the stopping criteria, however, our dynamic adaptive quadrature tolerance strategy is based on the requirement

$$\frac{\|\Delta\vec{\rho}_{\text{out}}\|_2}{\|\vec{\rho}_{\text{in}} - \vec{\rho}_{\text{out}}\|_2} \leq 0.5, \quad (2.141)$$

which is equal to half of the level set for the stopping criteria defined in (2.138).

Now, the output charge density profile is computed from $\vec{\rho}_{\text{out}} = e(\vec{n}_i - \vec{n}_e)$, where e is the magnitude of the electron and ion charge, and \vec{n}_i, \vec{n}_e are the ion and electron number density profiles. Thus, the error on the net output charge density profile relates to the relative quadrature tolerance on densities τ_{rel} through

$$\Delta\vec{\rho}_{\text{out}} = e \tau_{\text{rel}} (\vec{n}_i + \vec{n}_e). \quad (2.142)$$

Combining the requirement given by (2.141) with (2.142), the relative quadrature tolerance τ_{rel} for a given iteration can be set based on the previous iteration’s residual norm using

$$\tau_{\text{rel}}^{\text{goal}} = \frac{1}{2} \frac{\|\vec{\rho}_{\text{in}} - \vec{\rho}_{\text{out}}\|_2}{e \|(\vec{n}_i + \vec{n}_e)\|_2}. \quad (2.143)$$

Now, in order to prevent oscillations of the tolerance from one iterate to another, we introduce asymmetric mixing factors that favor a reduction rather than an increase of the

tolerance. The actual tolerance is computed based on the present tolerance and the “goal” tolerance given by (2.143) following Algorithm 4.

Algorithm 4 Relaxation of relative quadrature tolerance

```

if  $\tau_{\text{rel}}^{\text{goal}} \leq \tau_{\text{rel}}$  then
     $\tau_{\text{rel}} \Leftarrow \tau_{\text{rel}}^{\text{goal}}$ 
else
     $\tau_{\text{rel}} \Leftarrow \tau_{\text{rel}} + 0.1 (\tau_{\text{rel}}^{\text{goal}} - \tau_{\text{rel}})$ 
end if

```

2.6 Dynamic Adaptive Mesh Refinement

For both the 1-D and 2-D implementations, a dynamic adaptive grid refinement strategy is necessary in order to efficiently resolve not only the geometrical features of the conductive structure (in the 2-D case), but also the natural features of the density and net charge density profile. For example, in the case of high-voltage probes a sharply-defined ring forms in the net charge density profile, as a result of the combinations of the density drops of both the electron and ion species. The location of this sharp peak is not known *a priori*, which is why mesh refinements are necessary to accurately resolve this important feature.

The general mesh refinement strategy used in both KiPS-1D and KiPS-2D is shown in Algorithm 5. The mesh is refined a set number of times, typically anywhere from 3 to 5 times, which we have found sufficient to capture all of the important features of the plasma for the cases of interest, based on observing the convergence of the plasma profiles.

In the following we describe the particular details of the mesh refinement strategies pertaining to both the 1-D and 2-D implementations of KiPS.

2.6.1 KiPS Cylindrical 1-D Implementation

The grid used in the 1-D implementation is fairly simple. We start with an initial set of samples spaced logarithmically along the radial direction between the round cylinder and

an outer boundary located at a specified radius R_{\max} , which is typically set to be about three times the expected sheath size. This has been found to be more than sufficient to capture all of the important features of the density profiles that cannot be accurately accounted for by the floating outer boundary condition used for the Poisson solver and specified in (2.14)–(2.15).

The grid refinement is implemented as follows using *Matlab*TM. For a given absolute tolerance $\tau_{\text{mesh,abs}}$ specifying the acceptable errors on the electron, ion, and net charge density profiles, we first compute the desired local grid spacings $h_{\text{goal}}(r_i)$ based on their local second derivatives,

$$h_{\text{goal}}(r_i) = \sqrt{\frac{\tau_{\text{mesh,abs}}}{\max\left(\frac{1}{n_0} \frac{d^2 n_e}{dr^2}\Big|_{r=r_i}, \frac{1}{n_0} \frac{d^2 n_i}{dr^2}\Big|_{r=r_i}, \frac{1}{en_0} \frac{d^2 \rho}{dr^2}\Big|_{r=r_i}\right)}}, \quad (2.144)$$

for all radial samples $r = r_i$, with the second derivatives approximated using finite differences. This relationship is based on assuming a piecewise linear variation for all three quantities, which is consistent with a local error given by $\delta n(r_i) \approx h(r_i) \frac{d^2 n}{dr^2}\Big|_{r=r_i}$.

The dynamic grid refinement simply consists of sub-dividing the intervals for which the desired local grid spacing is smaller than the present local grid spacing, i.e., for which $h_{\text{goal}}(r_i) < h(r_i)$. Those said intervals are divided into a number of sub-intervals given by $N_{\text{div}} = \text{ceil}\left(\frac{h(r_i)}{h_{\text{goal}}(r_i)}\right)$.

Algorithm 5 General mesh refinement strategy

Generate initial mesh from given geometry.

Initialize the solution vector with some “guessed” charge distribution (typically we assume zero net charge everywhere, i.e., no disturbance of the plasma);

for a pre-determined number of refinement steps N_r **do**

- Refine the present mesh based on the present best estimate of the solution and a given set of criteria pertaining to the electron density distribution, ion density distribution, net charge distribution, and potential distribution;

- Improve the solution using the regularized Newton iterative Poisson–Vlasov scheme until convergence;

end for

In the 1-D implementation, the grid intervals are always refined, never coarsened. A more efficient mesh refinement procedure would both refine and coarsen as needed. Chapter 4 shows some KiPS-1D simulation results that illustrate the result of the grid refinement described here.

2.6.2 KiPS 2-D Implementation

The 2-D implementation was designed to allow the analysis of any 2-D geometry immersed in a flowing plasma. As mentioned in Section 2.3.2.2, the 2-D implementation of the finite-element formulation is performed over a set of triangular elements filling the complete 2-D domain occupied by the plasma.

2.6.2.1 Meshing Software

In order to generate the meshes for arbitrarily-defined geometries, we use an unstructured mesh generator, a freely available copyrighted software called the *Bidimensional Anisotropic Mesh Generator* (BAMG) developed at the INRIA (France). The BAMG manual [68] describes the software in detail, and related publications [69, 70] provide its theoretical basis.

The mesh generation and refinement process is performed based on a file-based interface. KiPS-2D generates the initial geometry input file required by BAMG, and calls to BAMG are made to both generate the initial mesh and perform mesh refinements.

2.6.2.2 Mesh Symmetry Axes

KiPS-2D implements 2 optional symmetry axes that can be used wherever applicable. Horizontal ($y = 0$) and vertical ($x = 0$) symmetry axes can be defined that apply to both the electrostatic fields (Poisson solver) and kinetic plasma flow (Vlasov solver). These allow for major savings in terms of computational effort and memory requirements. The

following are the typical cases where savings can be made based on using symmetry axes:

1. In a stationary plasma, for any structure that has 2 symmetry axes ($x = 0$ and $y = 0$), we generate a “single quadrant” mesh and perform the kinetic simulation in this quadrant only. This results in a reduction of the Vlasov computational effort by a factor 4, and a reduction of the Poisson computational effort by a factor $4^{2.64} \approx 39$, an estimate based on the measured computational work for the LU decomposition, which scales as $N^{2.64}$. The Poisson savings becomes significant when the number of samples N is on the order of 2000 and beyond;
2. In a flowing plasma with an x -directed flow, for any structure having at least a horizontal symmetry axis, we generate a “two-quadrant” mesh and perform the kinetic simulation in those two quadrants. In this case, we must simulate two quadrants even with structures having two symmetry axes, because of the asymmetry introduced by the horizontal flow.

A minor modification was made to the metric construction routine within the BAMG software to allow for the correct mesh refinement near the computational zones bounded by one of the symmetry axes. Whereas the original version of the code assumes vanishing second derivatives on all boundaries for the quantity being refined, with our modification it accounts for non-zero second derivatives consistent with a “mirroring” of the quantity being refined at the boundary.

2.6.2.3 Mesh Refinement: Strategy & Metrics

Mesh refinement is driven by the state of the best-available consistent simulation results at any of the refinement stages as shown in Algorithm 5. The mesh refinement is performed based on the criteria of the equidistribution of error [68] for several quantities of interest (single-species number density, charge density, and potential distributions). Several metrics

are used in conjunction to determine the best set of anisometric triangles that should be used based on the best-known consistent plasma solution. Using several calls to BAMG's metric construction routine, a single anisometric metric is generated that seeks to satisfy all of the following set criteria:

- the absolute error on the electric potential distribution $V(r, \theta)$ must be no larger than $\min \{(\Delta V)_{\max}, \tau_{\text{mesh},V} \times [\max \{V(r, \theta)\} - \min \{V(r, \theta)\}]\}$, where $(\Delta V)_{\max}$ and $\tau_{\text{mesh},V}$ are absolute and relative tolerances, respectively;
- the absolute error on the net charge density distribution $\rho(r, \theta)$ must be no higher than a set fraction $\tau_{\text{mesh},\rho}$ of the full range of the charge density distribution $\Delta\rho = \max \{\rho(r, \theta)\} - \min \{\rho(r, \theta)\}$, i.e., $\delta\rho \leq \tau_{\text{mesh},\rho}\Delta\rho$;
- the absolute error on each single-species number density distribution $n_e(r, \theta)$ and $n_i(r, \theta)$ must be no higher than a set fraction $\tau_{\text{mesh},n}$ of the full range of each of the number density distributions $\Delta n_{e,i} = \max \{n_{e,i}(r, \theta)\} - \min \{n_{e,i}(r, \theta)\}$, i.e., $\delta n_{e,i} \leq \tau_{\text{mesh},n}\Delta n_{e,i}$.

The resulting metric satisfying all these criteria specifies the desired 2-D dimensions and orientations of the triangle elements. The metric is then fed into the mesh refinement routine from BAMG to construct a refined mesh. Typical values used for the tolerances defined above are as follows:

Tolerance Parameter	Typical Value
$(\Delta V)_{\max}$	2.0
$\tau_{\text{mesh},V}$	0.025 – 0.05
$\tau_{\text{mesh},\rho}$	0.025 – 0.05
$\tau_{\text{mesh},n}$	0.025 – 0.05

These values were chosen based on a reasonable compromise between the accuracy of the results and the required computational effort. Since these specified tolerances apply to normalized quantities (as opposed to physical ones), they are not application-dependent. It is

generally recognized in the finite-element community that using several different redundant tolerance criteria based on the physical quantities of interest, as we have done here, improves the accuracy of the macroscopic results.

2.6.2.4 Examples of Mesh Geometries Under Consideration

The 2-D implementation of our solver generally supports any 2-D conductor geometry. Three basic geometries have been tested as part of this thesis and are described in this section. Support for additional geometries can be implemented through the addition of a fairly simple geometry-construction routine along with an associated routine for the interpretation of collected currents.

The three geometries shown here all use two symmetry axes, such that their meshes were computed for a single quadrant and then replicated in the 3 other quadrants. In addition, since all three of these cases correspond to stationary situations, the symmetry of the plasma and electric fields is conserved; therefore, the actual simulations were all performed within a single quadrant only. However, four-quadrant meshes are shown to illustrate more clearly the actual geometries under consideration. Note that an independent mesh refinement for all four quadrants is also possible for cases not featuring either symmetry axes.

2.6.2.4.1 Single Round Cylinder The simplest geometry of interest is the single round cylinder, which is a case that can be compared directly against the KiPS-1D simulation results (see Chapter 4 for detailed comparisons). Figure 2.4 shows the evolution of the mesh structure from the initial mesh to the fourth refinement step for a typical single one-Debye-length-radius round cylinder simulation. It is seen that the fourth and fifth mesh are quite similar, which is an indication that a sufficient number of refinements have been performed. It is seen that a strong mesh density is required near the sheath edge (which is well within the computational domain) to satisfy all of the metric requirements outlined in

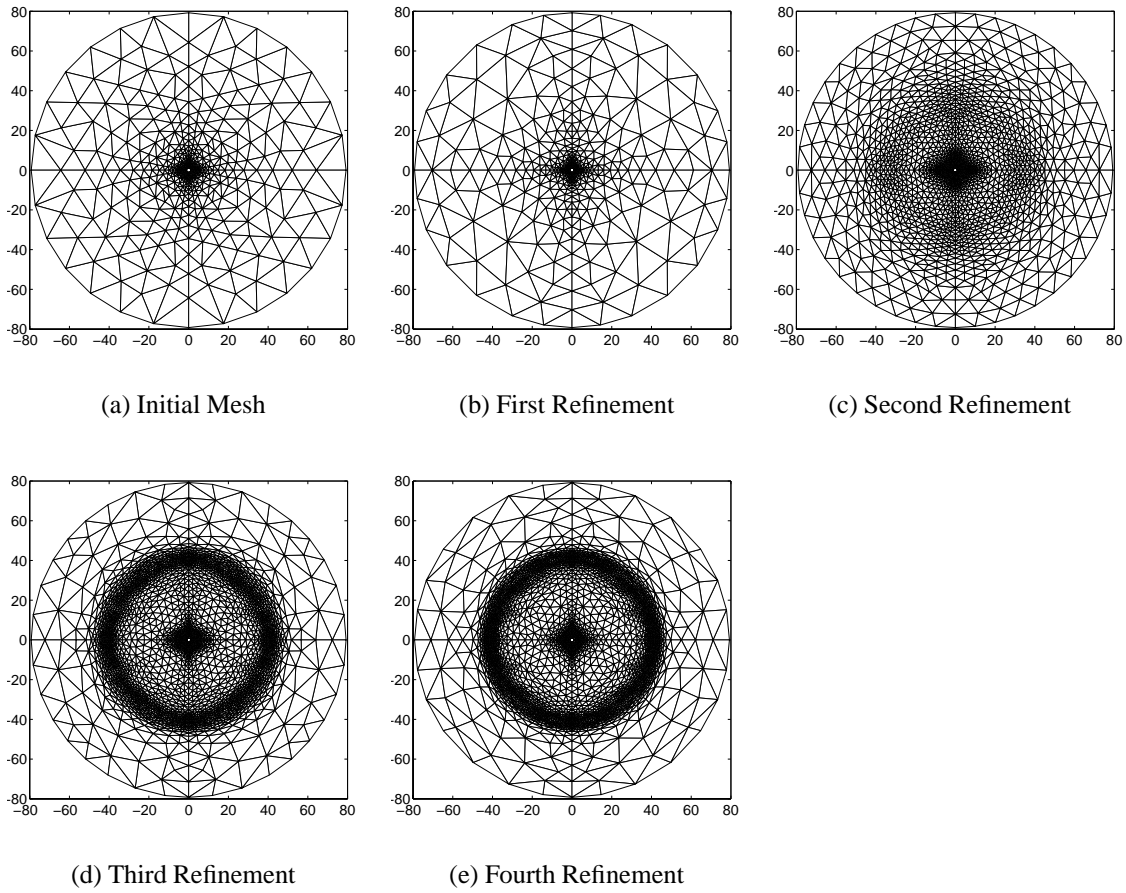


Figure 2.4: Initial mesh shown together with a set of four refined meshes obtained for a single one-Debye-length-radius round cylinder biased negatively at a voltage of $-640T_e$ and immersed in a stationary plasma. Two symmetry axes were used in this simulation. Scales represent the x and y coordinates in units of the Debye length.

Section 2.6.2.3.

2.6.2.4.2 Tape Cylinder In Figure 2.5 we show a sequence of five meshes obtained for the simulation of a thin tape cylinder of dimensions $20.4\lambda_{\text{De}} \times 0.7\lambda_{\text{De}}$, biased at a positive potential of $180T_e$. Again, we observe a convergence of the mesh structure, which emphasizes the concentration of charge on the circular sheath edge that is well contained within the simulation domain. Note that the tape geometry of the cylinder is filtered out by the Laplacian fields within the sheath. This occurs with sufficiently large biases for which the space charge in the vicinity of the tape is negligible as compared to the amount of surface

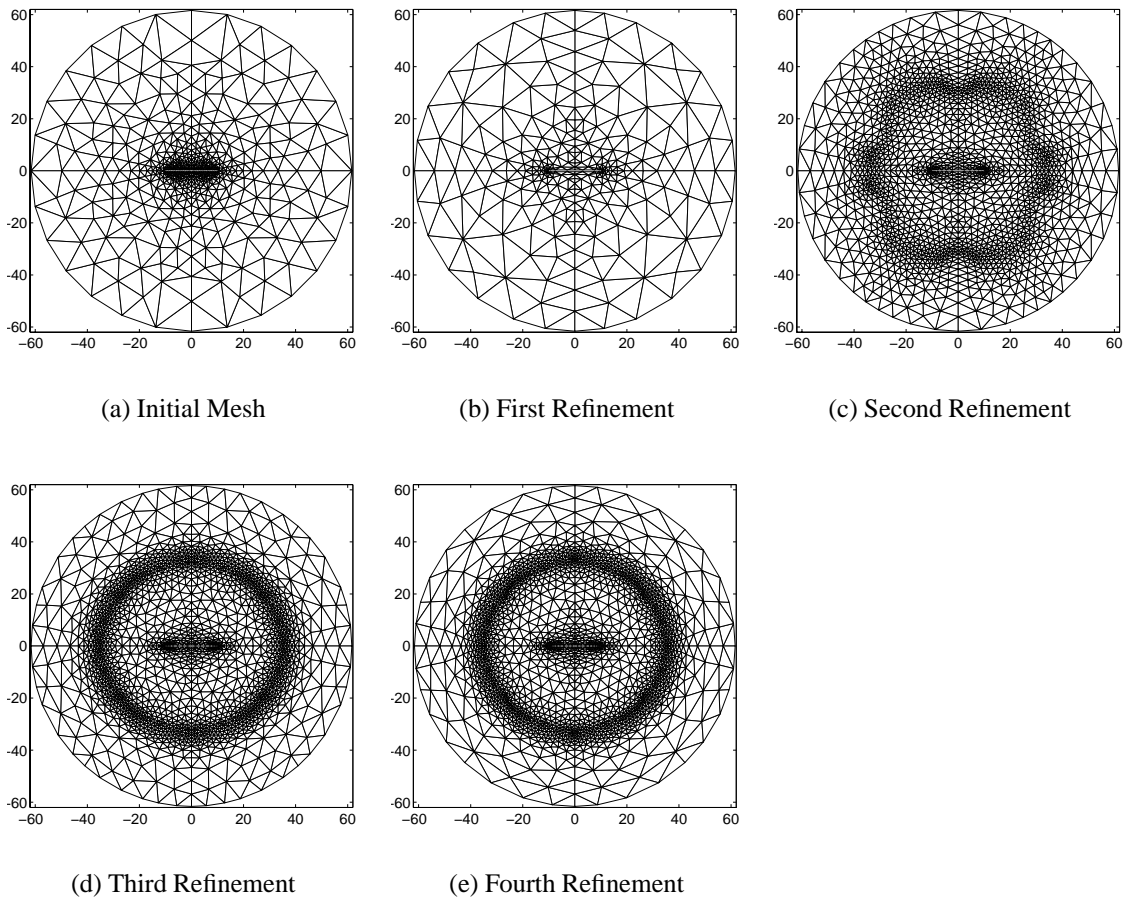


Figure 2.5: Initial mesh shown together with a set of four refined meshes obtained for a tape cylinder with a width of $20.4\lambda_{De}$ and a thickness of $0.7\lambda_{De}$. The tape was biased at a positive voltage of $180T_e$ and immersed in a stationary plasma. Two symmetry axes were used in this simulation. Scales represent the x and y coordinates in units of the Debye length.

charge on the conducting tape itself.

2.6.2.4.3 Two Round Cylinders In Figure 2.6 we show a sequence of five meshes pertaining to the 2-wire configuration. Two parallel one-Debye-length-radius round cylinders are spaced $10\lambda_{De}$ apart (center-to-center distance) and are both biased at a negative voltage of $-320T_e$. Here again, mesh convergence is observed after the fifth refinement step. Despite the asymmetric geometry of the structure, a circular charge-rich sheath structure still forms on a circle of radius $\sim 30\lambda_{De}$ and is resolved by the mesh refinement procedure.

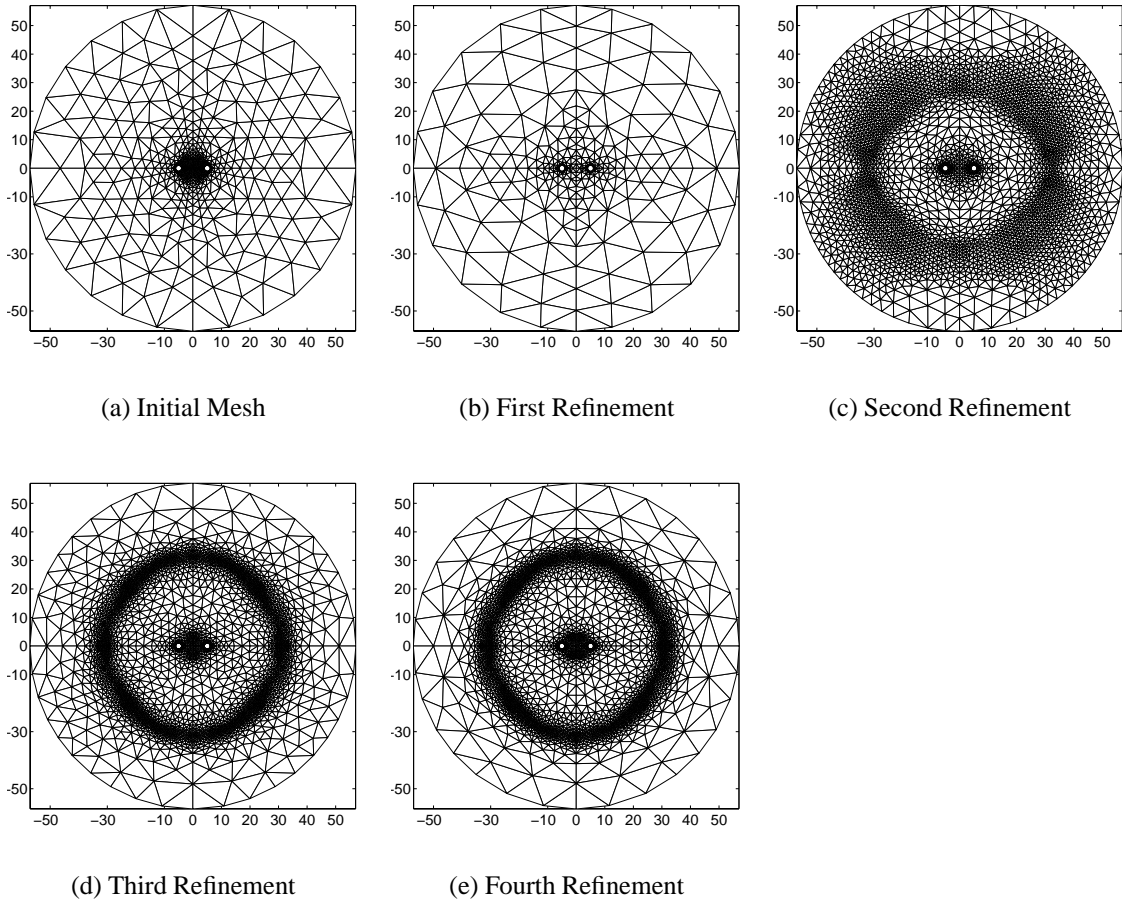


Figure 2.6: Initial mesh shown together with a set of four refined meshes obtained for 2 parallel one-Debye-length-radius cylinders with a center-to-center spacing of $10\lambda_{De}$. Both cylinders were biased at a negative voltage of $-320T_e$ and immersed in a stationary plasma. Two symmetry axes were used in this simulation. Scales represent the x and y coordinates in units of the Debye length.

2.7 Computer Implementation

In the following we explain the general approach used for implementing the algorithms described in this chapter, for both the cylindrical 1-D and full 2-D cases.

2.7.1 General Philosophy

Our general scientific programming philosophy is to use a high-level scripting language wherever possible (*Matlab*TM scripts were implemented for that purpose, which could be

easily ported to functionally similar platforms such as *Scilab* or *Octave*), because it speeds up development time and is less error prone. Where necessary, specific routines can then be optimized through a different implementation using a lower-level language such as Fortran 90, a very standard platform in the scientific computing community. Appropriate interfaces must then be used to dynamically link the Fortran 90 routines with *Matlab*TM at run time when called from high-level *Matlab*TM scripts. Building *Matlab*TM EXecutable (MEX) files using Fortran routines allows such interfacing.

2.7.2 Optimizing & Parallelizing the Vlasov Solver

At the early stages of development, it soon became apparent that the Vlasov solvers (both 1-D and 2-D versions) were so computationally demanding that they required optimization for any practical use.

The numerous numerical integrations performed in the 1-D Vlasov solver can actually be performed from within *Matlab*TM, but it is much more efficient to implement the numerical quadrature in Fortran 90.

In the case of the 2-D Vlasov solver, the computational requirements are much more severe for the following three reasons in decreasing order of importance:

1. in KiPS-2D, each sample of the velocity distribution function that is being integrated as part of the quadrature integration involves tracking a particle trajectory through the potential structure, whereas in the case of KiPS-1D no particle tracking is required;
2. in KiPS-2D, the numerical quadrature integrations need to be performed in 2-D velocity space, whereas in KiPS-1D one of the integrals is performed analytically, which means that only a single-variable quadrature is required;
3. in KiPS-2D, the number of density samples that need to be computed, using numerical quadrature, is an order of magnitude larger than that which is required in the 1-D

implementation ($\sim N^2$ as compared to N).

For these reasons, implementing a Vlasov solver that would be both efficient and accurate mandated the use of parallel computing resources. To accomplish this, the 2-D version of the Vlasov solver was thus implemented in Fortran 90 using an MPMD¹⁰ parallel processing scheme based on the *Parallel Virtual Machine* library [32]. Since the Vlasov solver consists of computing a fixed number (say M) of plasma density samples throughout the computational domain based on a given potential profile, it can be divided easily into M independent sub-tasks. These sub-tasks can be distributed to the slave nodes on a parallel platform in what constitutes a *coarse-grained* parallel algorithm.

2.7.3 Present Parallel Computing Platform

The primary computing platform that we have used for this purpose consists of:

- A Linux-based master node,¹¹ running the top-level *Matlab*TM scripts, the *Matlab*TM-based Poisson solver, and the top-level part of the Fortran 90-based Vlasov solver that distributes sub-tasks to slave nodes.
- A dynamically-configured pool of about 150 Sun Blade 1000/1500 workstations, each running a Fortran 90-based slave node and forming part of the Vlasov solver. A total of 250 workstations are being used on an opportunistic basis, being swapped in and out of the 150-workstation slave node pool according to their availability.¹²

2.7.4 Alternative Parallel Computing Platforms

Other parallel computing platforms were used as part of this project:

¹⁰Multiple Program, Multiple Data.

¹¹Dual-CPU Intel-based system running at a clock speed of 2.4 GHz with 4 GB of random-access memory.

¹²A workstation is removed from the slave node pool when a console user logs in, and only moved back in when no console users are logged in.

- An opportunistic pool of around 10 to 20 Linux workstations (based on 3.0-GHz CPU's) was used. Although the computing power of these nodes surpassed that of the Sun Blade workstations, the number of Linux nodes accessible on campus could not rival the sheer number of existing Sun workstations;
- Dedicated Linux clusters, such as those operated by the University of Michigan's *Computer Aided Engineering Network* (CAEN) as part of the *National Partnership for Advanced Computer Infrastructure* (NPACI), were used and shown to provide very efficient computing power due to a better interconnection speed between the slave and master nodes. However, the number of nodes and level of availability of these queue-managed systems could not compare to that provided by the opportunistic pooling of workstations for purposes of developing the code. Future production runs requiring less user interaction and changes may be more suited for this kind of platform.

Ultimately, the ideal computing platform is a dedicated Linux cluster comprised of about 20 dual-CPU nodes. This would provide simulation times on par with our present pool of 150 Sun workstations with a much higher degree of availability than pooled parallel computing resources.

CHAPTER 3

Experimental Investigation of Electron-Collecting Tether Samples in a Mesosonic Xenon Plasma

3.1 Background

In this chapter, we present the results of an experimental investigation of the electron current collection to tether samples of various cross-section geometries: round cylinder, solid tape and slotted tape. These results were submitted for publication [71]. A comparison of some of these results with kinetic simulation results obtained using KiPS-2D are performed in Chapter 4 as part of the kinetic model validation.

The orbital-motion limit will be used as a baseline to compare the current collection results for the various sample geometries and sizes. Recall that the OML electron current collected by a thin cylinder is given by (1.8), which we re-write here for clarity:

$$I = \underbrace{A_p n_e e \sqrt{\frac{e T_e}{2\pi m_e}}}_{I_{the}} \left\{ \frac{2}{\sqrt{\pi}} \sqrt{\frac{V_0 - V_p}{T_e}} + \exp\left(\frac{V_0 - V_p}{T_e}\right) \operatorname{erfc}\left(\sqrt{\frac{V_0 - V_p}{T_e}}\right) \right\}, \quad (3.1)$$

with $\operatorname{erfc}(x) = \frac{2}{\sqrt{\pi}} \int_x^\infty e^{-t^2} dt$. (3.1) is approximated, for $V_0 - V_p > 2T_e$, by

$$I = \underbrace{A_p n_e e \sqrt{\frac{e T_e}{2\pi m_e}}}_{I_{the}} \frac{2}{\sqrt{\pi}} \sqrt{1 + \frac{V_0 - V_p}{T_e}}, \quad (3.2)$$

where V_0 is the applied voltage, V_p is the plasma potential, T_e is the electron temperature in eV, A_p is the cylinder area, and I_{the} is the electron thermal current given as a function of the

electron number density n_e (in m^{-3}), electron mass m_e , and electron charge magnitude e . In an effort to facilitate comparisons with OML theory, results are presented in a normalized format, showing the normalized current $I_n = I/I_{the}$ as a function of the normalized voltage $\phi_0 = (V_0 - V_p)/T_e$, which in the case of OML yields the simple equation:

$$I_n = \frac{2}{\sqrt{\pi}} \sqrt{\phi_0} + \exp(\phi_0) \operatorname{erfc}\left(\sqrt{\phi_0}\right) \approx \frac{2}{\sqrt{\pi}} \sqrt{1 + \phi_0}. \quad (3.3)$$

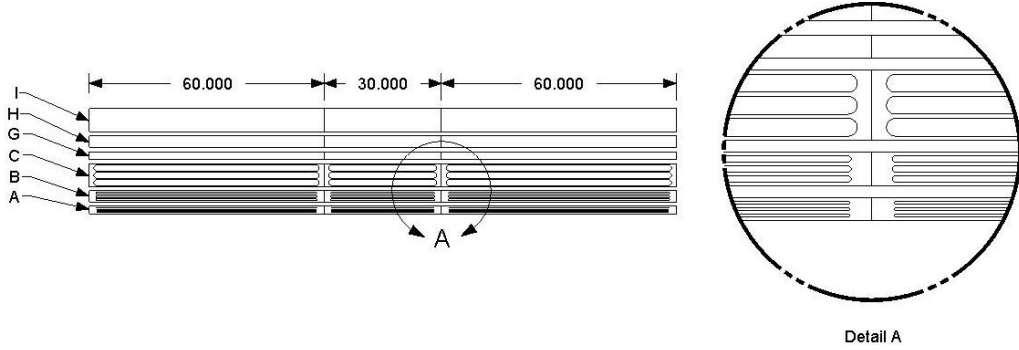
For large voltages, (3.3) is independent of the temperature T_e , since both the right-hand side and left-hand side are then proportional to $1/\sqrt{T_e}$. This normalization allows us to directly compare the OML theory, which only applies to thin cylinders in *stationary* plasmas, with our experimental results involving a flowing plasma and various tether geometries.

In a previous investigation [72], it was concluded that tape tethers with widths up to 10 Debye lengths would perform close to an equal-area reference cylinder and that the perpendicular tape orientation, with respect to plasma flow, would consistently outperform the parallel orientation in terms of collected current.

In this chapter, we describe the results of a new set of chamber tests that were intended to address questions of end effects and plasma source current limitations discussed by *Gilchrist et al* [72], in addition to testing a larger breadth of “solid tape” widths and a new “slotted tape” geometry with various porosities. The issue of end effects was addressed by adding guards to the tether samples, which are described below. The question of possible plasma source current limitations, raised by *Gilchrist et al* [72], was resolved by modifying the plasma source parameters, as discussed in Section 3.3.

3.2 Design and Assembly of Solid and Slotted Tape Tether Guarded Samples

The tether samples tested here, in addition to a thin cylindrical reference sample, included solid tape samples in three different widths, and slotted samples of equivalent widths



Sample	Description	Width (mm)	Feature Description
A	4 lines, 3 slots, 28% porosity	1.95	Slot gap: 0.20 mm Line width: 0.34 mm
B	4 lines, 3 slots, 50% porosity	2.89	Slot gap: 0.51 mm Line width: 0.34 mm
C	4 lines, 3 slots, 75% porosity	5.95	Slot gap: 1.53 mm Line width: 0.34 mm
G	Narrow Solid Tape	1.95	N/A
H	Medium Solid Tape	2.89	N/A
I	Wide Solid Tape	5.95	N/A

Figure 3.1: Drawing and description of the six guarded tether samples shown before assembly. The lengths indicated in the drawing are in mm (30-mm probe, 60-mm guards)

and corresponding to three different porosity levels. The details of these designs, as well as a drawing of the samples and their characteristic sizes, are shown in Figure 3.1. Each of the 6 solid and slotted tapes were tested in two different orientations, parallel and perpendicular to the plasma flow, and, along with the reference sample, at three different distances from the plasma source. Tungsten metal was used for all samples to ensure that they would endure the expected high temperatures that are caused by the collection of high-energy electrons to the samples' surfaces. Nonetheless, a low duty cycle pulsing of the applied voltages was necessary to allow the samples to cool off, thus preventing melting; details of this procedure are reported by *Gilchrist et al* [72].

The effective diameter of the reference cylinder and effective widths of the three tape samples, for the plasma densities tested here, are given in Table 3.1 in terms of the Lang-

Pos.	Ref. Cyl.	Solid Tape		
		Narrow	Medium	Wide
75 cm	2.0	13.7	20.4	41.9
160 cm	1.1	7.4	11.0	22.6
300 cm	0.7	4.9	7.2	14.9

Table 3.1: Effective diameter of the reference cylinder and effective widths of the three solid tapes at all three locations, in terms of the local Debye length.

muir probe-measured local Debye length for the three chamber positions that were used in these tests. The reference cylinder's diameter, spanning from 0.7 to 2.0 Debye lengths depending on position, is sufficiently thin to collect electron current under conditions close to that of the OML regime in a stationary plasma. The effective solid tape widths spanned from 4.9 to 41.9 Debye lengths, which extends the previous range of tested widths [72].

As for the three slotted samples, they were designed with the same overall widths as their solid counterparts; this strategy allowed us to compare solid and porous samples spanning equivalent widths. In addition, the design is such that each of the four lines on every slotted sample has the same perimeter as the reference cylinder, allowing one to consider the effects and measure the extent of sheath interactions. The effective center-to-center spacings of the slotted samples are given in Table 3.2.

Since our primary interest is very long electrodynamic tethers, a technique was sought to mitigate any probe end effects. For this purpose, guards were included in all of our tether sample assemblies. Each guard is essentially identical to the center section and is biased at the same potential. The guards, which are each 6 cm in length while the center probe itself

Position	Slotted Tapes by Porosity		
	28%	50%	75%
75 cm	3.8	6.0	13.2
160 cm	2.1	3.2	7.1
300 cm	1.4	2.1	4.7

Table 3.2: Effective center-to-center line spacing as a function of sample porosity at all three locations, in terms of the local Debye length.

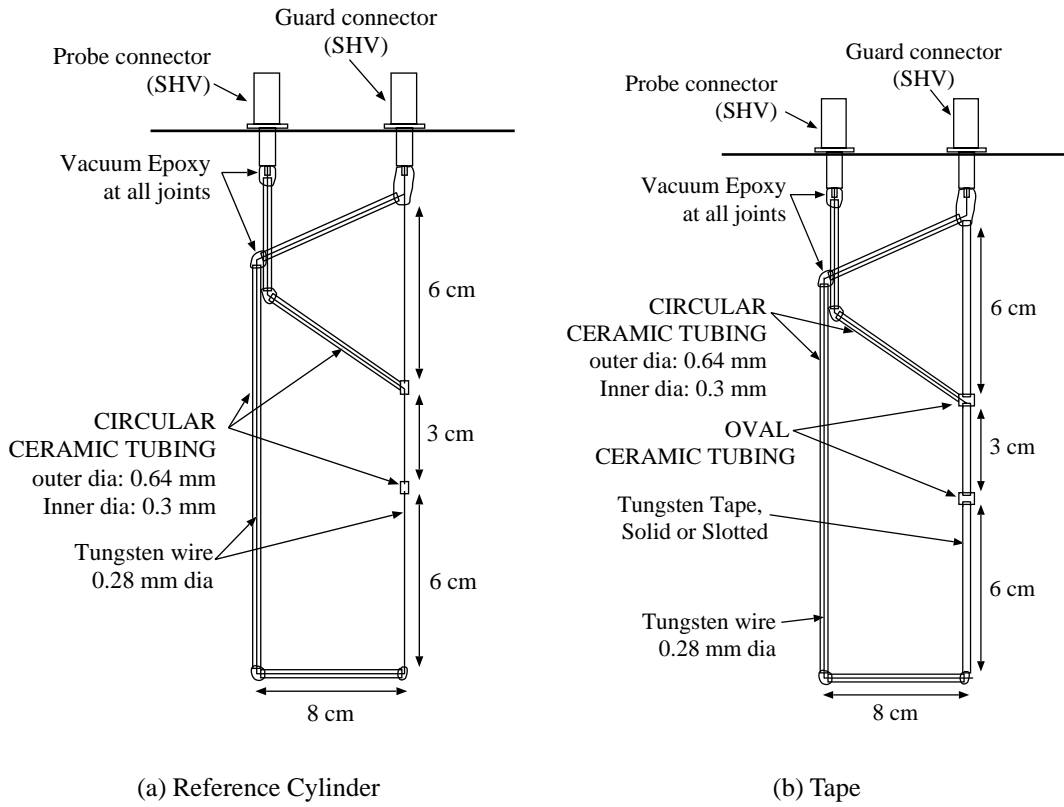


Figure 3.2: Assemblies of the reference cylinder (a) and tape (b) guarded tether samples.

is 3 cm long, are shown in Figures 3.1 and 3.2 together with the probes. The effect of the guards is to extend the cylindrical sheath to the full length of the sample, that is, five times the length of the center probe on which current is measured.

Schematics of the full assemblies of the guarded tether samples are shown in Figure 3.2. Due to the very small thickness of the tungsten samples under consideration here (0.1-mm thick), it was not physically possible to feed the center probe using a feeding wire that would have been inserted in one of the guards, as is typically done on some larger tri-axial Langmuir probes. Instead, the center feed wire runs through an oblique ceramic tube and connects to the center probe at one of its ends. On all samples, the feed wires to both the guards and the probe were both soldered to the center conductor of a bulk-head SHV (safe high voltage) connector; the connector-sample interfaces were then covered

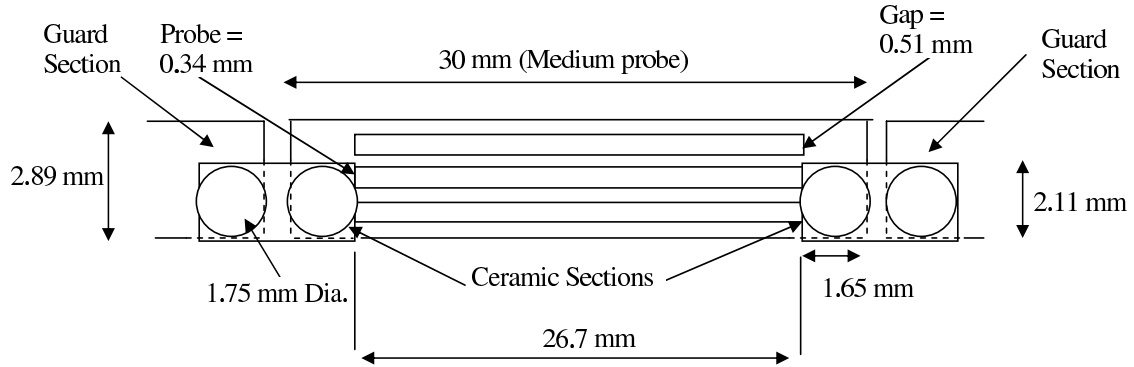
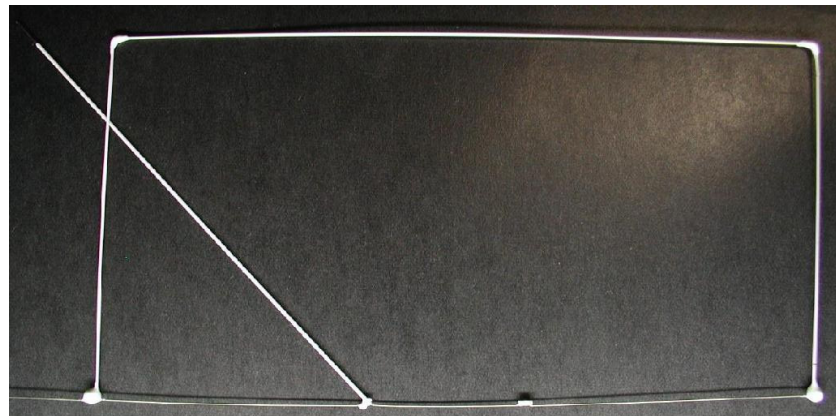


Figure 3.3: Example of the ceramic attachment used on all solid and slotted tape samples to attach the probe and guards while preserving electrical isolation.

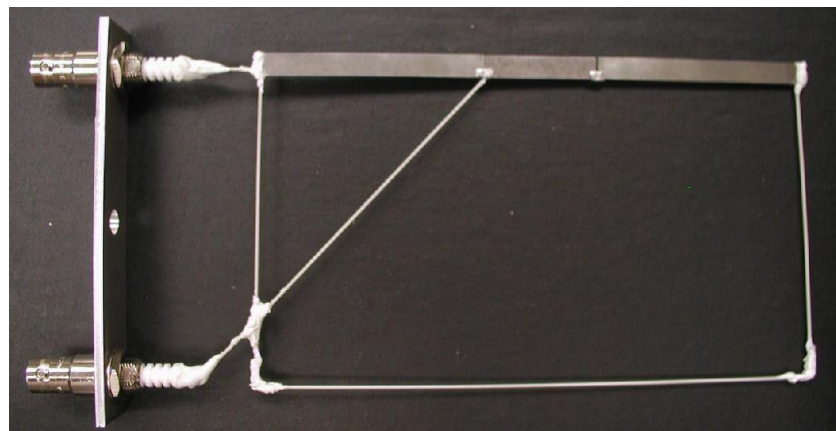
with vacuum epoxy. The aluminum support structure for the SHV connectors provided a localized ground.

The probe and guards also had to be physically attached but electrically insulated from each other. Ceramic joints were used to this effect, an example of which is shown in Figure 3.3, and were attached to the tungsten probes and guards using stainless-steel machine screws that were then carefully sanded down into a flat surface, in order to best emulate the surface of the sample. The portion of the surface area of the ceramic joint covering the tungsten probe and not covered by the screw head was accounted for in the calculation of the total area of each probe.

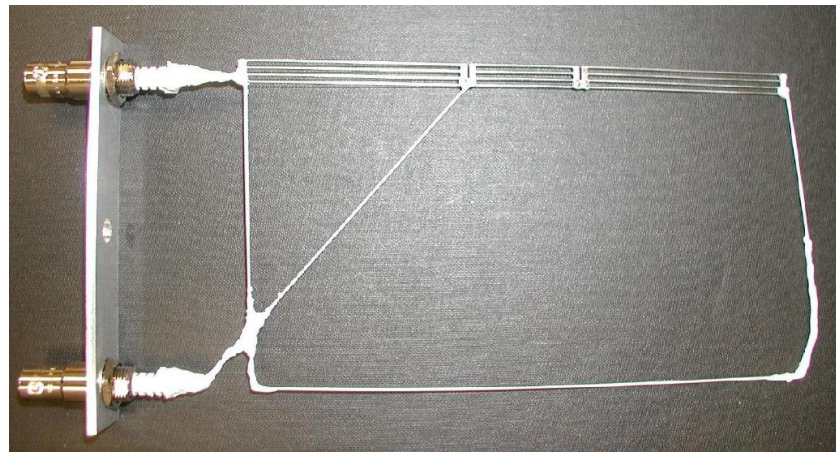
Figure 3.4 shows pictures of three of our tether sample assemblies: the reference cylinder, the wide solid tape, and the 75%-porous wide slotted tape. The solid and slotted samples are shown with both SHV connectors installed, while the reference cylinder sample is shown prior to the installation of the connectors.



(a)



(b)



(c)

Figure 3.4: Pictures of three typical tether samples: (a) the 0.28 mm-diameter reference cylinder, (b) the 5.95-mm wide solid tape, and (c) the 75%-porous wide slotted tape.

3.3 Vacuum Chamber Setup and Plasma Source Characteristics

The vacuum chamber tests were performed in the Large Vacuum Test Facility (LVTF), a 9-meter by 6-meter cylindrical stainless-steel-clad tank located within the Plasmadynamics and Electric Propulsion Laboratory at the University of Michigan. For this experiment, four of the seven available nude cryopumps were used to reach a high vacuum.

Figure 3.5 shows a diagram of the experimental setup within the LVTF. Two positioning tables were used to change the separation distance between the thruster and sample plane and to locate the sample under test directly along the thruster’s centerline. The thruster was mounted on an x - y table that could move axially over a 1.0-m range and over sufficient radial range to cover all samples. The samples were mounted on an aluminum frame that was connected to an axial table that could span a 1.5-m axial range. Combined table movement allowed thruster–sample separation distance to change from 0.75 m to 3 m; our tests were performed at 0.75 m, 1.60 m and 3.00 m from the thruster. Changing separation distance was the primary mechanism for changing the plasma density seen at the sample plane.

Figure 3.6 shows an overall picture of the aluminum structure supporting the tether samples and Langmuir probes, together with the Hall thruster used as a plasma source. The latter is a 5 kW-class Hall thruster named “P5”, which was developed by the Plasmadynamics and Electric Propulsion Laboratory and the Air Force Research Laboratory; more detail is given by Haas *et al.* [73]. For these tests, the thruster was set at off-nominal conditions in order to lower the plasma velocity and density seen along the thruster’s axial direction. Its operating conditions are given in Table 3.3. The primary changes in those settings from the ones used previously [72] are the discharge current, which was raised to 12.5 A, up from 5.3 A and 4 A and, consequently, the anode flow rate, which had to be raised to 112.1 sccm to support the increased discharge current.

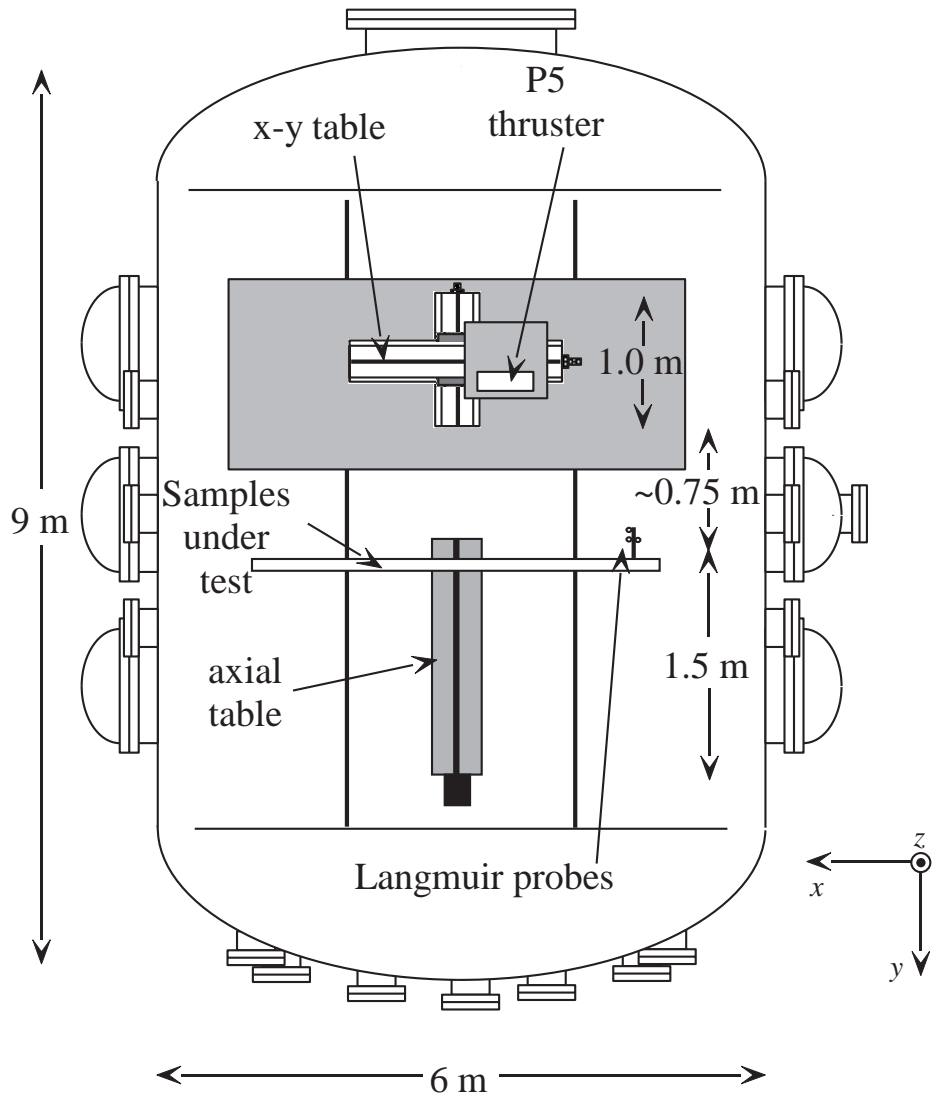


Figure 3.5: Experimental setup in the Large Vacuum Test Facility (LVTF) at the Plasma-dynamics and Electric Propulsion Laboratory (PEPL).

Assessment of the emitted beam energy was estimated using two different techniques. Laser-induced fluorescence (LIF) measurements have provided an estimate of 43 eV [74], whereas Langmuir probe (LP) measurements in the ion saturation regime (discussed in Appendix F) have yielded a value of 25.0 eV. More detail regarding the LIF measurements is given by *Gilchrist et al* [72] and *Williams et al* [75]. It should be noted that the LP value of 25.0 eV is close to, if not within, the bounds of the error on the LIF-determined beam energy value, which is about 40%, given that the reported typical error on the velocity



Figure 3.6: Picture of the guarded sample support structure and the P5 Hall thruster used as a high-speed plasma source.

determined using the multiplex technique is 20% [76].

The values given for both the LIF and LP measurements were measured 75 cm away from the thruster on its centerline axis. According to the LIF measurement, the ions have an offset Maxwellian distribution, with a directed energy as given above, and a temperature of about 0.4 eV at 75 cm. The electron temperature, as determined by the LP measurements, varied as a function of position between 1.4 eV and 1.8 eV (see Table 3.4).

Maximum Chamber Pressure	9.1 μ torr
Discharge Voltage, V_d	100 V
Discharge Current, I_d	12.5 A
Inner Magnet Current, I_{im}	3.0 A
Outer Magnet Current, I_{om}	2.0 A
Cathode Voltage, V_c	[−17, −18] V
Heather Voltage, V_{htr}	8.3 V
Anode Flow rate, \dot{m}_a	112.1 sccm
Cathode Flow rate, \dot{m}_c	6.0 sccm

Table 3.3: Operating parameters of the plasma source (P5 Hall thruster).

Position	n_e (m $^{-3}$)	T_e (eV)	λ_{De} (mm)	μ_b
75 cm	4.95×10^{15}	1.80	0.14	95%
160 cm	1.37×10^{15}	1.72	0.26	53%
300 cm	0.51×10^{15}	1.47	0.40	32%

Table 3.4: Variation of the measured plasma parameters as a function of distance from the Hall thruster. Measurements were performed using the ion saturation and electron retardation data from a transverse LP. The beam energy value determined using the LP is 25 eV. The “beam fraction”, μ_b , indicates the fraction of all ions that are believed to be beam (high-speed) ions. Density, temperature and Debye length estimates have about 6%, 1% and 3.5% accuracy, as discussed in F.1.

A schematic of the current–voltage measurement system is given in Figure 3.7. We connected a Universal Voltronics BRC 20 000 HV power supply to the tether samples through a high-voltage relay box inside the chamber. The HV power supply was controlled via RS–232 by the computer controller running a custom virtual instrument (VI) under LabVIEW™. The computer commanded the HV power supply to a specified voltage and then quickly back to zero (within 50 to 100 ms), followed by several seconds of cool-down to minimize sample heating. Current measurement on the sample probes was achieved using an American Aerospace Controls 835–2–10 current sensor; increased current sensitivity was obtained by looping the HV supply line ten times through the sensor. The current to the sample guards was measured separately using a F.W. Bell ma-2000 current sensor. An HP 34970 data acquisition unit was used to measure the voltage signals generated by both current sensors. The data were recorded as triplets containing the applied voltage, the probe current, and the guard current.

3.4 Plasma Parameter Measurements Using Negatively-Biased Langmuir Probes

Plasma density, temperature, flow speed, and the fraction of beam ions to background ions were determined using a 4-cm long, vertically oriented (i.e., perpendicular to the flow)

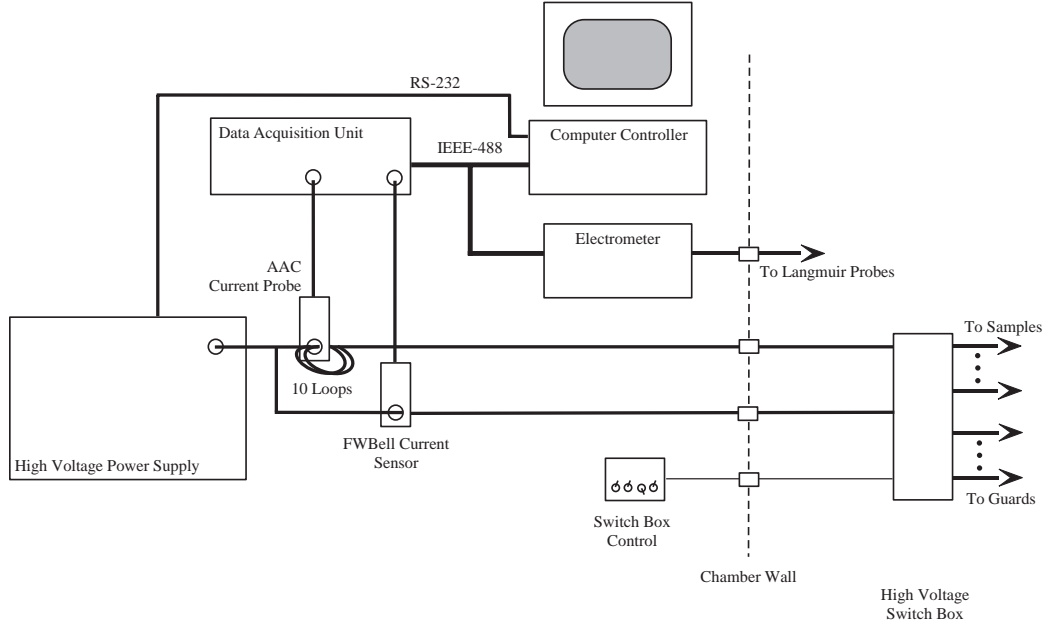


Figure 3.7: Schematic of the computer-controlled high-voltage test equipment setup.

Langmuir Probe (LP) with a diameter of 0.28 mm (same diameter as for the reference cylinder sample). All LP sweeps were performed using a Keithley 2410 source electrometer controlled via a custom LabVIEW™ script running on a personal computer.

The plasma parameters, shown in Table 3.4, were extracted from the ion saturation (OML regime) and electron retardation regions of the I-V characteristics using a LP oriented transverse to the direction of the flow. In the OML regime, there are several advantages to selecting the ion saturation as opposed to the electron saturation region for parameter extraction. A cylindrical probe oriented transverse to the flow in a high-speed plasma is known to be virtually free of end effects [39]. In addition, a simple but fairly accurate collection model is available that accounts for the velocity of the flow in that regime [29]. By contrast, there are currently no accurate models for the electron collection to an electron-attracting probe that can account for the plasma flow. In the mesosonic regime, where the plasma flow is much faster than the thermal ion velocity yet much smaller than the electron thermal velocity, important sheath asymmetries and elongations exist in

the electron-attracting mode that get stronger with the applied bias, which makes this a complex problem. One of the aims of the experimental work presented here is in fact to improve the understanding of the macroscopic effect of plasma flow on electron collection. Finally, using a negatively-biased LP provides an independent assessment of the plasma parameters, since all the test samples are biased positively.

The procedure that was used for the plasma parameter extraction from the Langmuir probe current characteristics is detailed in Appendix F. In addition to providing plasma density and temperature readings, this analysis quantifies the ion “beam fraction” and describes what appears to be effective workfunction variations.

The results of this analysis indicate the existence of a population of thermal ions far from the high-speed plasma source, which is born out of cumulative charge-exchange collisions between the incident high-speed ions and the neutral background xenon gas. The number-density ratio of high-speed ions to thermal ions is quantified in Table 3.4 and ranges from an assumed 95% at the closest distance (75 cm) to a calculated 32% at the farthest distance (300 cm). This fall-off of the fraction of beam ions can be best-fitted to an equivalent “beam ion survival characteristic distance” of 2.14 m, which is just short of the theoretical charge-exchange mean free path of 2.6 m corresponding to the measured background pressure, ion energy, and assuming a background neutral temperature of 350 K. The fall-off is likely due to a combination of effects, such as the beam loss through charge-exchange collisions and the geometrical divergence of the beam, which may explain the smaller value obtained.

3.5 Experimental Results & Analysis

Our results are presented here in four parts: the reference cylinder, the solid tapes, the slotted tapes, and, finally, a comparison of the solid and slotted tapes. All results are pre-

sented in normalized form. The collected current is normalized to the electron thermal current I_{the} collected at the plasma potential, as defined in (3.1). All probes should collect this amount of current when biased at the plasma potential. The normalization of potential consists of a translation corresponding to the plasma potential, followed by a scaling by the inverse of the electron temperature, T_e . An OML theoretical plot, scaled this way, would result in (3.3) and would be independent of temperature, as discussed in the introduction. This normalization provides a means of evaluating the performance of various probes by comparing them to OML theory as well as by comparing their respective “electron collection efficiencies.” Note, however, that the extent of the normalized voltage axis varies from one graph to another, due to changes in the electron temperature used in the normalization of this axis, and from variations in the collected data range.

3.5.1 Reference Cylinder

Figure 3.8 shows the normalized results for the reference cylinder at the three distances from the plasma source (Figure 3.9 shows identical information for the reference cylinder). The reference cylinder at 75 cm is seen to collect much more current than that predicted by OML theory, by as much as 40% at a bias of $100 T_e$. This enhancement is seen to decrease as we move away from the thruster to 160 cm and 300 cm. In fact, there is no enhancement at 300 cm. Since the fraction of beam ions was also determined to fall off with distance (95% at 75 cm, 53% at 160 cm, and 32% at 300 cm), this observed enhancement could be linked to the effects of the high-speed flow. This change in enhancement level is most likely not due to the change in the effective size of the reference cylinder (2.0, 1.1, and 0.7 Debye lengths) since decreasing the size would theoretically have the opposite effect, that is, to increase the collection efficiency rather than to decrease it as observed here. In addition, even if there were any residual end effects despite the use of our guard structures, we

believe that the enhancement could not be attributed to those end effects, since the stronger end effects should occur at the location where the cylinder is the shortest in terms of the local Debye length (at 300 cm), whereas the observed enhancement is strongest where the effective cylinder length is the longest (at 75 cm).

3.5.2 Solid Tapes

Figure 3.8 presents results for all solid tape samples and the reference cylinder at all three distances from the plasma source (75 cm, 160 cm, and 300 cm). The effective tape widths, shown in terms of the Debye lengths in the legend as well as in Table 3.1, span from 4.9 to 41.9 electron Debye lengths. Three major observations are noted from these results:

1. All samples collect electrons less efficiently than the reference cylinder, as is expected because of their larger sizes. Likewise, all samples are seen to collect less efficiently as the effective width of the tape is increased, regardless of their orientation. This is true whether we are looking at a mostly high-speed plasma (at 75 cm) or a mostly quiescent plasma (at 300 cm). When compared to the reference cylinder, the relative collection efficiency of all solid tapes decreases with increasing tape width, similar to the “current ratio” characteristic reported by *Estes et al* [12, Figure 4(b)] based on an effective circular cylinder radius equal to four times the tape width ($R_{eq} = 4w_{tape}$ [11]). The overall relative efficiency is seen to be somewhat lower than that predicted by Estes and Sanmartín [12] and is closer to, although still lower than, our steady-state kinetic simulation results (see Chapter 4). This reduced efficiency may be explained by the reduction in collection efficiency due to the presence of mounting screws that account for a small fraction of the total collecting area.
2. At both the 75-cm and 160-cm distances, all solid tape samples collected more cur-

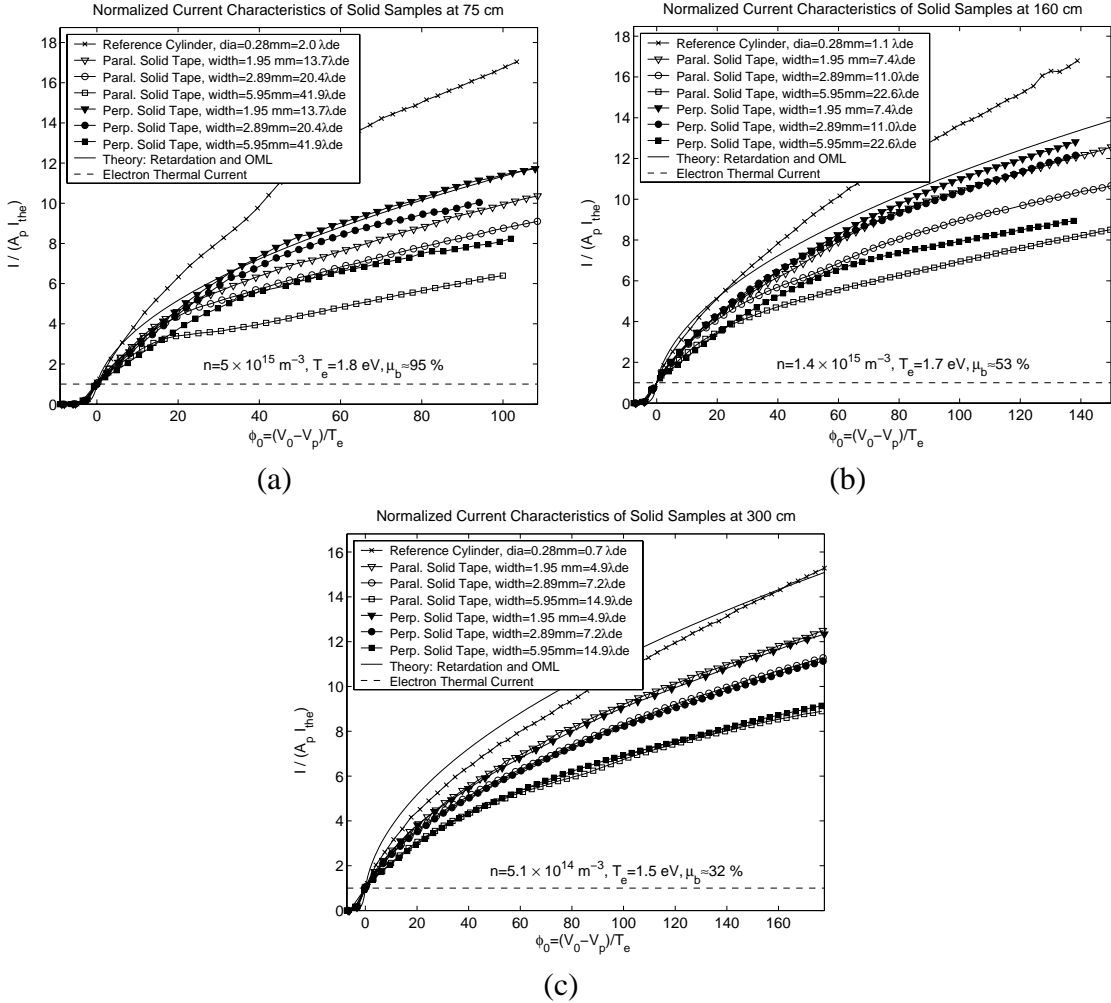


Figure 3.8: Normalized I-V characteristics of parallel and perpendicular solid tapes at (a) 75 cm, (b) 160 cm and (c) 300 cm.

rent when oriented perpendicular (transverse) rather than parallel to the flow. In addition, the contrast between perpendicular and parallel results is observed to get stronger as the effective width of the tape increases. However, such a clear distinction is not evident in the measurements taken at 300 cm, which is likely a consequence of the low fraction of beam ions that was measured at that location, combined with the lower effective widths of the tapes (the Debye length was highest at that location) as compared to the two other locations. The near-overlapping of the perpendicular and parallel results at 300 cm also serves as qualitative confirmation that the measured

fraction of beam ions has dropped down as compared to that measured at 75 cm.

3. The previous observation of the increase of collected current from parallel to perpendicular is seen to occur when the probes are biased above a certain threshold, which varies from about 25 to 40 volts. This level is on the order of the estimated ion beam energy (somewhere between 25 eV, according to the LP results, and 43 eV, according to the LIF results). At this threshold bias, the parallel results are seen to present a “knee”, which is most apparent in the widest effective tape at 75 cm. These observations are in agreement with previous results based on a similar experiment [72].

3.5.3 Slotted Tapes

Figure 3.9 presents results for all slotted tape samples and the reference cylinder at all three distances from the plasma source. The effective center-to-center line spacings, shown in terms of the Debye lengths in the legend as well as in Table 3.2, span from 1.4 to 13.2 Debye lengths. It should be emphasized that the overall widths of the slotted tapes, including the gap spacings, are the same as the solid tape widths (1.95 mm, 2.89 mm, and 5.95 mm). The following are some observations regarding these results:

- Similar to the tape results, the slotted samples collected electrons less efficiently, on a per-area basis, than the reference cylinder at all three distances, although they were more efficient than the solid tapes. This is an indication that the individual-line sheaths were strongly interacting.
- The contrast between the results in the parallel and perpendicular orientations has a similar character as that observed for the solid tapes: the perpendicular slotted tapes collect more current than their parallel counterparts. However, distinct from the solid tape results is the smaller variation between the responses of the three perpendicular

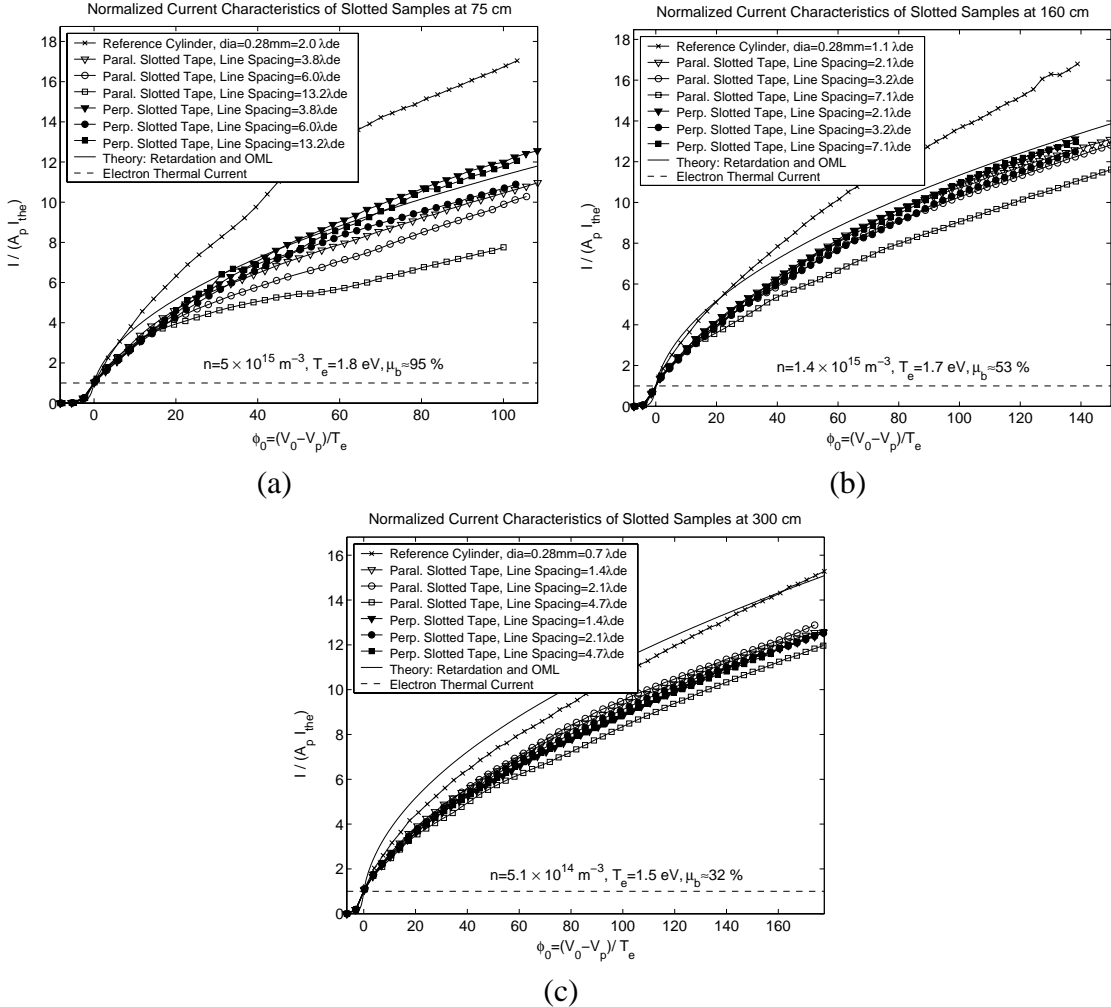


Figure 3.9: Normalized I–V characteristics of parallel and perpendicular slotted tapes at (a) 75 cm, (b) 160 cm and (c) 300 cm.

slotted tapes widths (especially at 75 cm and 160 cm) as compared to the parallel slotted ones. Specifically, the efficiency of the widest (and most porous) slotted tape, with a line spacing of 13.2 Debye lengths at 75 cm, is roughly on par with that of the medium slotted tape (6.0 Debye lengths at 75 cm), and even goes above it at the highest bias potentials. This may indicate that the widest line spacing was close to a critical value, corresponding to the minimum efficiency, and beyond which the collection efficiency would start increasing again, up to the very wide spacing limit where all four lines become independent and collect as efficiently as the reference

cylinder. We seem to have attained this limit only in the perpendicular orientation, which can be explained by the fact that the sheath elongations in the direction of the flow [77, 78] would cause the sheath interactions to grow stronger when aligned with (i.e., parallel to) the flow, thereby moving the critical spacing to a higher value for the parallel case. Clearly, testing of wider line spacings will be required to determine those critical values and relate them to the flow energy.

- A “knee” is most apparent in the results for the widest parallel slotted tapes at 75 cm and 160 cm, around 29 and 21 volts, respectively (note that the positions of the knees on the graphs need to be scaled with their respective electron temperatures), which is close to the estimated ion beam energy. The parallel and perpendicular results separate at the potential bias corresponding to the location of this knee.

3.5.4 Comparison of the Solid and Slotted Tapes

Figs. 3.10–3.12 show the same sets of results shown earlier, but with the solid and slotted tapes plotted on common graphs to facilitate their comparison. The absolute amount of current collected by the solid tape samples was higher than that collected by the slotted tape samples in all cases, as expected, and is not shown here. The slotted samples were somewhat more efficient on a per-area basis than their solid counterparts. This is true at all positions, and does not seem to be a function of the fraction of beam ions present. Hence, the slotted samples are always more efficient on a per-area basis, regardless of whether in a stationary or flowing plasma. For example, at 75 cm the parallel wide slotted tape collected about 37% of the current collected by the parallel wide solid tape at a normalized bias of $80T_e$, a somewhat higher fraction than the porosity of the sample, which was 28%.

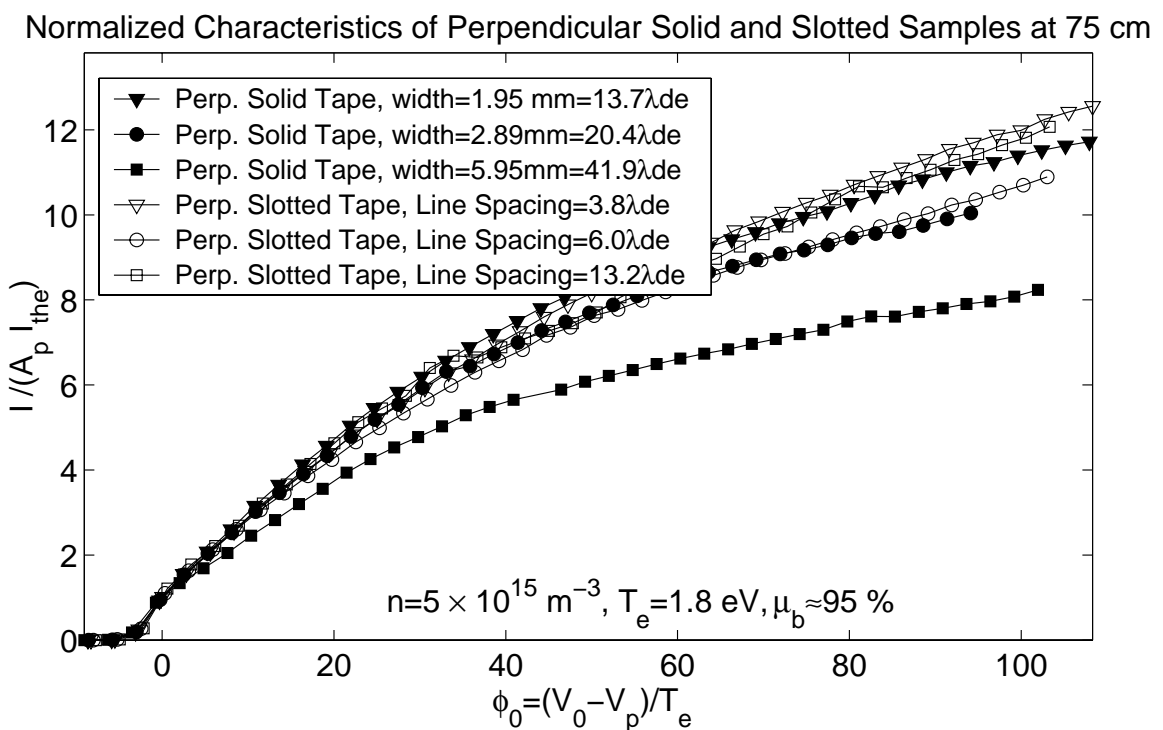
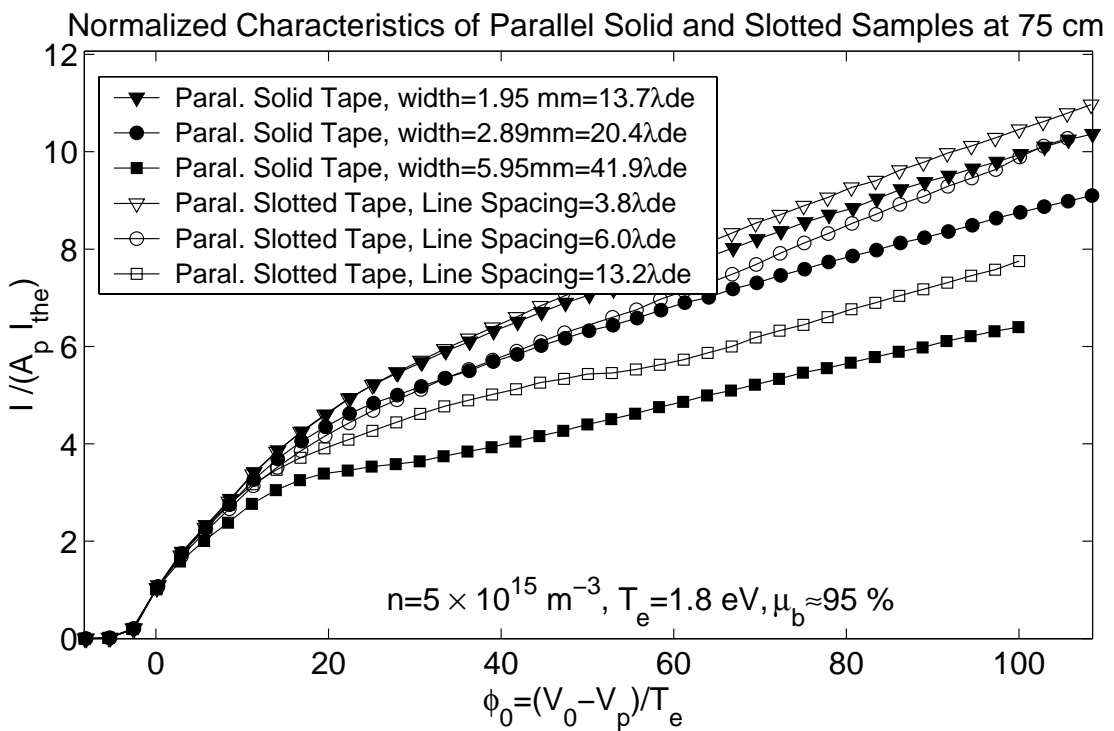


Figure 3.10: Comparison of the I–V characteristics of solid and slotted tapes at 75 cm.

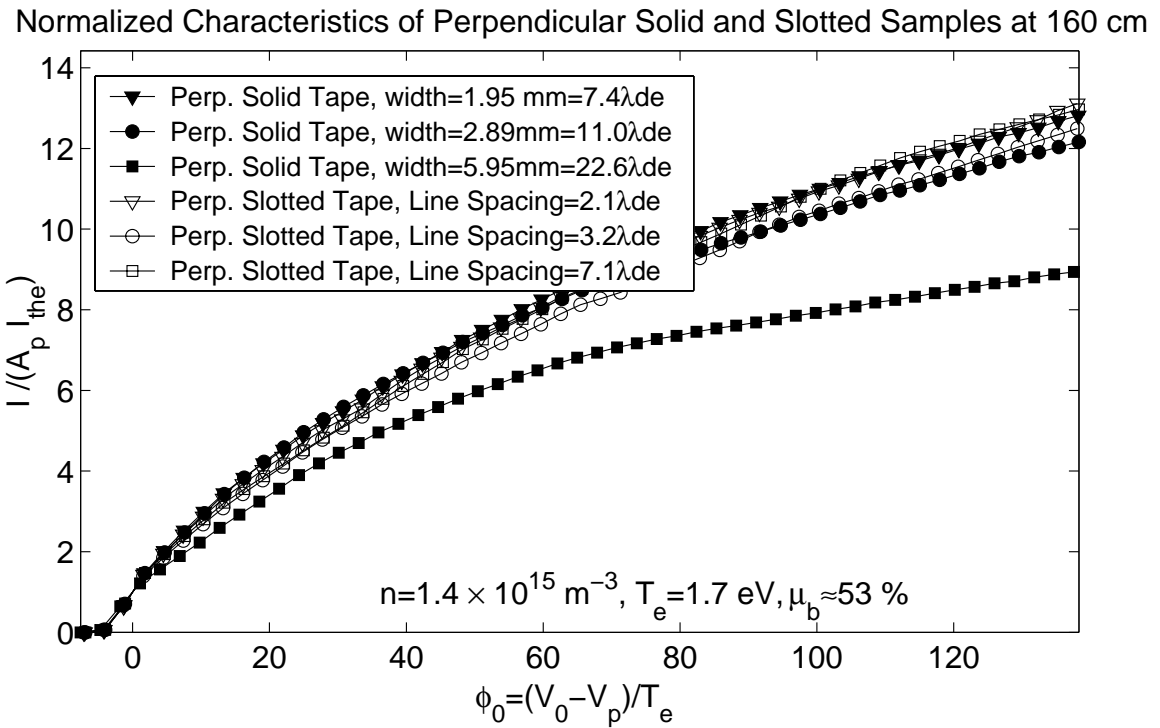
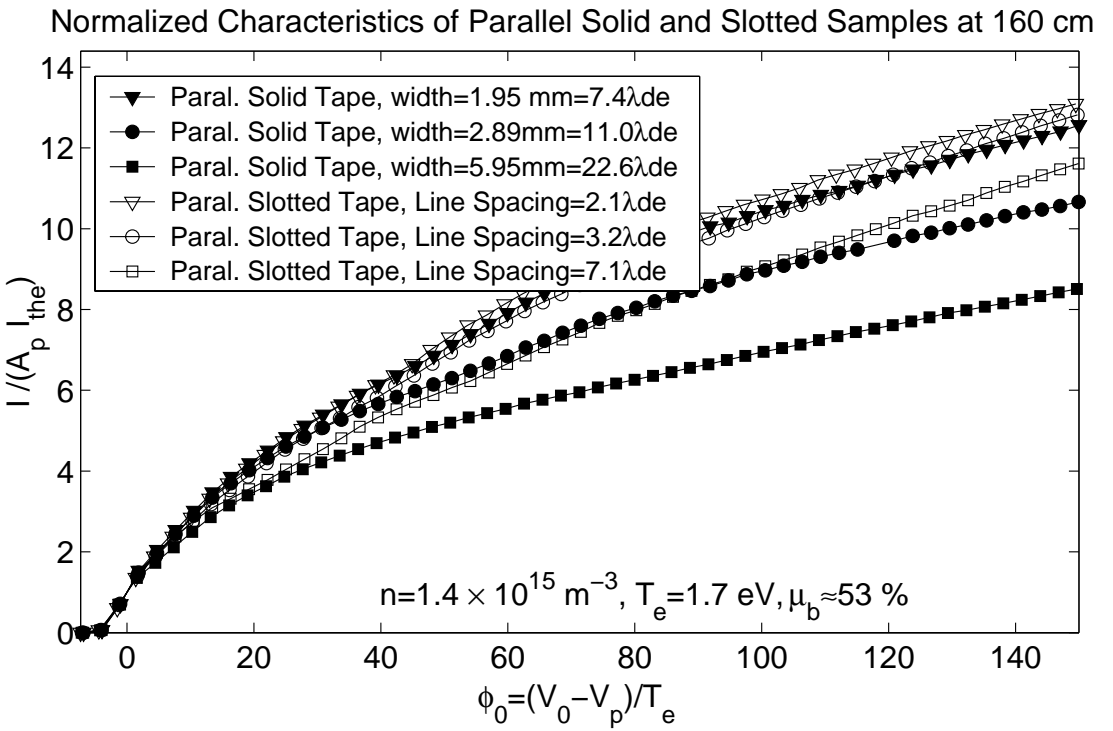


Figure 3.11: Comparison of the I–V characteristics of solid and slotted tapes at 160 cm.

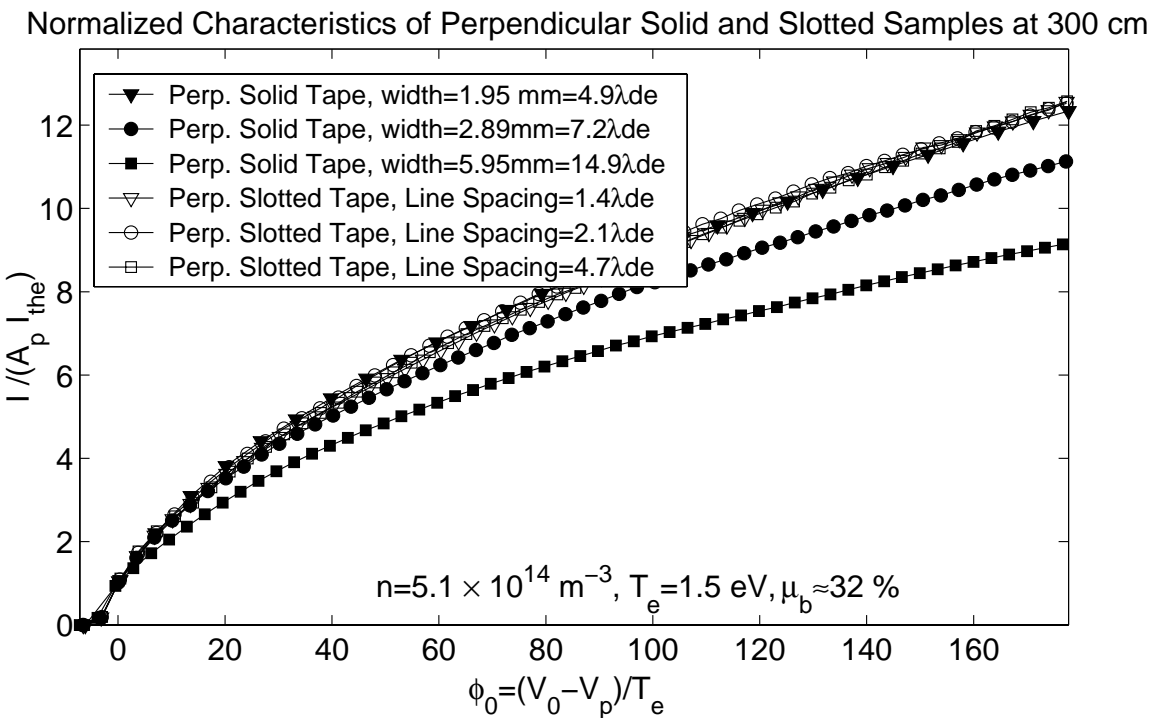
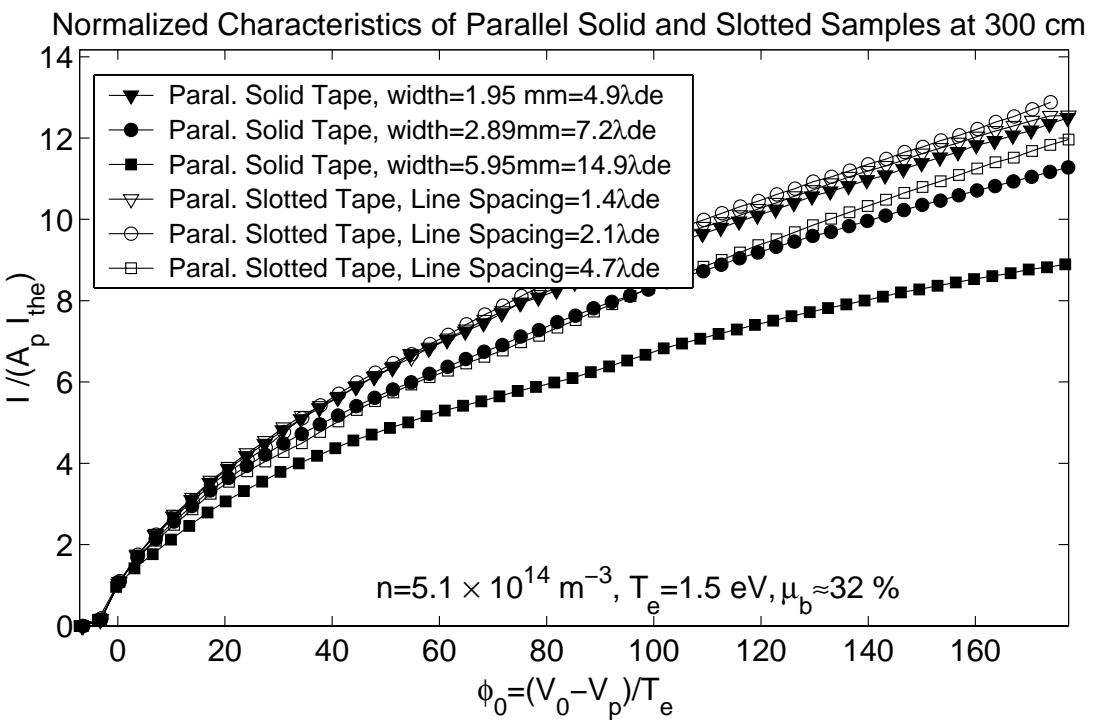


Figure 3.12: Comparison of the I-V characteristics of solid and slotted tapes at 300 cm.

3.6 Present Status and Conclusions

Several conclusions can be drawn from the analysis of these experimental results:

1. the plasma flow leads to significant current enhancements over that predicted by the orbital-motion-limited theory;
2. the electron collection efficiency of solid tapes (on a per area basis) decreases as the width of the tape is increased;
3. beyond a threshold bias close to the beam energy, solid and slotted tapes both collect more current when oriented transverse (perpendicular) to the flow;
4. equivalent-width slotted tapes are more efficient electron collectors than solid tapes on a per-area basis;
5. our data suggests the electron collection efficiency of slotted tapes decreases with increasing line spacing until a possible minimum efficiency is attained, beyond which it is expected to start increasing again. The minimum may have been attained in the case of the samples oriented transverse to the flow, but not in the case of the samples aligned with the flow, for which the critical spacing is likely higher due to an increased sheath interaction radius of each line caused by the elongation of the sheath associated with plasma flow.

Further experiments are needed to more completely quantify the observed effects. In addition, larger line spacings should be tested in both the parallel and perpendicular orientations to verify the existence of and quantify the critical spacing that corresponds to a minimum collection efficiency.

A lower background pressure might help improve the survival of the ion beam out to 3 meters, and could possibly be achieved with the use of additional cryopumps. For example,

using 7 cryopumps instead of 4, we could expect a drop of the background pressure by a factor $4/7$, and consequently an increase of the charge-exchange mean-free-path length by a factor $7/4$. Since the value shown for the high-speed beam fraction ($\mu_b = 32\%$) at 300 cm in Table 3.4 is consistent with a mean free path of about 2.6 meters, this additional pumping power could be expected to increase the mean free path to $2.6 \text{ m} \times 7/4 \approx 4.6 \text{ m}$. This would therefore improve the beam survival at 300 cm from 32% to 52% ($\exp(-\frac{3.0 \text{ m}}{4.6 \text{ m}}) = 0.52$).

Finally, in future experiments one should consider shifting the entire hardware setup further away from the downstream end of the vacuum chamber, which might reduce a possible accumulation of neutrals near that end of the chamber, since the cryopumps are located on the upstream end.

CHAPTER 4

Simulation Results and Validation

In this chapter we present and analyze our simulation results, and proceed to validations with other published results wherever possible. Section 4.1 describes the normalizations used throughout this chapter. Section 4.2 discusses the simulation results applicable to a round cylinder in a stationary plasma. Sections 4.3 and 4.4 discuss probe geometry effects using simulation results pertaining to the two-wire and thin tape cylinder, respectively. Finally, Sections 4.5 and 4.6 discuss the effects of plasma flow on sheath structure and current collection for ion- and electron-attracting round cylinders.

Note that for all of the simulations presented in this chapter, the electron and ion populations are at thermal equilibrium ($T_i = T_e$), because this setting is most representative of the ionospheric environments of interest. Although they were not tested as part of this analysis of results, the model does allow for settings of the temperature ratio T_i/T_e other than 1.¹³

4.1 Definition of Normalized Physical Quantities

All simulation parameters and results are presented in a normalized form in order to make them as general as possible. The normalizations used in this chapter are consistent

¹³Results shown in Ref. [8] indicate that, for temperature ratios T_i/T_e below unity, we should expect a reduction of the sheath dimensions as well as the collected ion current for ion-attracting bias potentials as compared to the case where $T_i = T_e$.

with those used to present our experimental results in normalized form in Chapter 3. The following is a description of the normalized parameters used throughout this chapter:

- The *number densities* are normalized with respect to the number density of the background plasma (the ambient density). The normalized density n_n is the ratio of the actual density n (in m^{-3}) to the background number density n_0 of the plasma: $n_n = \frac{n}{n_0}$.
- Similarly, the *net charge density* is normalized in terms of the ambient density and the electron charge e . At any location in space, the normalized net charge density ρ_n is given by

$$\rho_n = \frac{\rho}{en_0} = \frac{n_i - n_e}{n_0}, \quad (4.1)$$

where ρ is the actual net charge density.

- The *electric potentials* are normalized in terms of the electron plasma temperature T_e (units of eV) and the plasma potential V_p (in volts). At any location in space the normalized potential is thus given by

$$\phi = \frac{V - V_p}{T_e}, \quad (4.2)$$

where V is the local electric potential and V_p is the background plasma potential. The bias potential is similarly normalized according to $\phi_0 = \frac{V_0 - V_p}{T_e}$, where V_0 is the bias potential in volts.

- All *coordinates and dimensions* are normalized in terms of the electron Debye length in the ambient plasma. The normalized coordinates (x_n, y_n) are given by

$$x_n = \frac{x}{\lambda_{\text{De}}} \quad \text{and} \quad y_n = \frac{y}{\lambda_{\text{De}}}, \quad (4.3)$$

where (x, y) are the physical coordinates and λ_{De} is the electron Debye length, both given in units of meters.

- The *velocities* are normalized with respect to the electron thermal velocity $v_{the} = \sqrt{\frac{eT_e}{m_e}}$. The normalized velocity components $v_{x,n}$ and $v_{y,n}$ are given by

$$v_{x,n} = \frac{v_x}{v_{the}} \quad \text{and} \quad v_{y,n} = \frac{v_y}{v_{the}}. \quad (4.4)$$

- *collected current* is normalized with respect to the electron or ion thermal current, depending upon whether electrons or ions are being collected. In most situations that we will consider, the magnitude of the bias potential is large enough that only a single species is being collected at any given time. For positive bias potentials (collecting electrons), we use the normalized collected electron current I_{ne} , whereas for negative bias potentials (collecting ions), we use the normalized collected ion current I_{ni} . Both quantities relate to the physical currents I_e and I_i through the expressions

$$I_{ne,i} = \frac{I_{e,i}}{J_{the,i} A_p} \quad J_{the,i} = en_0 \sqrt{\frac{eT_{e,i}}{2\pi m_{e,i}}}, \quad (4.5)$$

where I_e/I_i is the physical electron/ion collected current in units of amperes and A_p is the total collecting area of the probe or tether. The thermal current densities $J_{the,i}$ are given in terms of the temperatures $T_{e,i}$ (in eV), the masses $m_{e,i}$ and the magnitude of the electron charge e .

- The *linear charge density* Q , given in Coulombs per meter (C/m) of cylinder length, is normalized consistent with the normalizations used for the net (volume) charge density $\rho_n = \frac{\rho}{en_0}$. The linear charge density Q contributed by a constant volume charge density ρ over a 2-D zone with area A is given by $Q = \rho A$. Correspondingly, when using a normalized charge density $\rho_n = \frac{\rho}{en_0}$ and normalized area $A_n = \frac{A}{\lambda_{De}^2}$, we obtain for the normalized linear surface charge

$$Q_n = \rho_n A_n = Q \frac{1}{en_0 \lambda_{De}^2} = \frac{Q}{\epsilon_0 T_e}. \quad (4.6)$$

- The *ion and electron temperatures* T_i and T_e are normalized to the electron temperature T_e , resulting in

$$T_{i,n} = \frac{T_i}{T_e} \quad \text{and} \quad T_{e,n} = \frac{T_e}{T_e} = 1, \quad (4.7)$$

which yields a trivial result of unity for the normalized electron temperature.

- The *particle masses* m_i and m_e are normalized to the electron mass m_e , i.e.

$$m_{i,n} = \frac{m_i}{m_e} \quad \text{and} \quad m_{e,n} = \frac{m_e}{m_e} = 1, \quad (4.8)$$

which yields a trivial result for the normalized electron mass.

- Similar to the masses, the *particle charges* q_i and q_e are normalized to the electron charge q_e , i.e.

$$q_{i,n} = \frac{q_i}{q_e} \quad \text{and} \quad q_{e,n} = \frac{q_e}{q_e} = 1. \quad (4.9)$$

The normalizations above are consistent with the following normalization of Poisson's equation (2.5):

$$\nabla^2 V \equiv \frac{d^2 V}{dx^2} + \frac{d^2 V}{dy^2} = -\frac{\rho}{\epsilon_0} \iff \underbrace{\nabla_n^2 \phi \equiv \frac{d^2 \phi}{dx_n^2} + \frac{d^2 \phi}{dy_n^2}}_{-\rho_n, \text{normalized form}} = -\rho_n, \quad (4.10)$$

where $\rho_n \equiv \frac{\rho}{\epsilon_0 T_e}$ and ∇_n is the Laplacian applied on the normalized space coordinates (x_n, y_n) . In addition, Vlasov's equation (2.9) can be recast in terms of the normalized quantities:

$$v_{x,n} \frac{\partial f_n}{\partial x_n} + v_{y,n} \frac{\partial f_n}{\partial y_n} - \frac{q_n}{m_n} \frac{\partial \phi}{\partial x_n} \frac{\partial f_n}{\partial v_{x,n}} - \frac{q_n}{m_n} \frac{\partial \phi}{\partial y_n} \frac{\partial f_n}{\partial v_{y,n}} = 0, \quad (4.11)$$

where f_n , q_n and m_n are normalized quantities that apply to either electrons or ions, i.e.,

$$f_n = \begin{Bmatrix} f_e/n_0 \\ f_i/n_0 \end{Bmatrix}, \quad q_n = \begin{Bmatrix} q_{e,n} \\ q_{i,n} \end{Bmatrix}, \quad \text{and} \quad m_n = \begin{Bmatrix} m_{e,n} \\ m_{i,n} \end{Bmatrix}. \quad (4.12)$$

Because both of the fundamental equations used in the computational model can be recast in normalized form as given by (4.10) and (4.11), any solutions that we obtain based

on the simulations can be applied to a vast number of practical cases based on the proper scaling of the normalized quantities using the physical values for the parameters n_0 , T_e , m_e , and q_e .

4.2 Single Round Cylinder in Stationary Plasma

The most simple configuration that can be analyzed using both the KiPS-1D and KiPS-2D models is that of the single round cylinder immersed in a stationary plasma. Although basic, this configuration allows for validations to be performed against previous publications, as well as validations of the more sophisticated KiPS-2D model against the simpler KiPS-1D model.

We should note that, because there is no plasma flow, all of the normalized results presented in this section can be applied to either ion or electron collection. That is, the normalized density profiles of the attracted and repelled species are independent of mass and therefore a change in the polarity of the bias potential simply has the effect of interchanging the density profiles of the electrons and ions, knowing that the ions are singly charged and that the electron and ion temperatures are equal, $T_i/T_e = 1$.

In addition to validations, the results from these simulation runs will allow us to answer an important question that was not addressed in previous works: how do the sheath dimensions scale at large bias potentials? To the author's knowledge, large bias potentials (up to $10,000T_e$) were not addressed using any self-consistent kinetic treatment before this work.

4.2.1 Validation of Potential & Density Profiles at Low Bias Voltages

We first present a validation of our simulation results against the widely accepted simulation results obtained by Laframboise [8] for low bias voltages. Figures 4.1–4.3 show a comparison of some of our KiPS simulation results against Laframboise's results for four

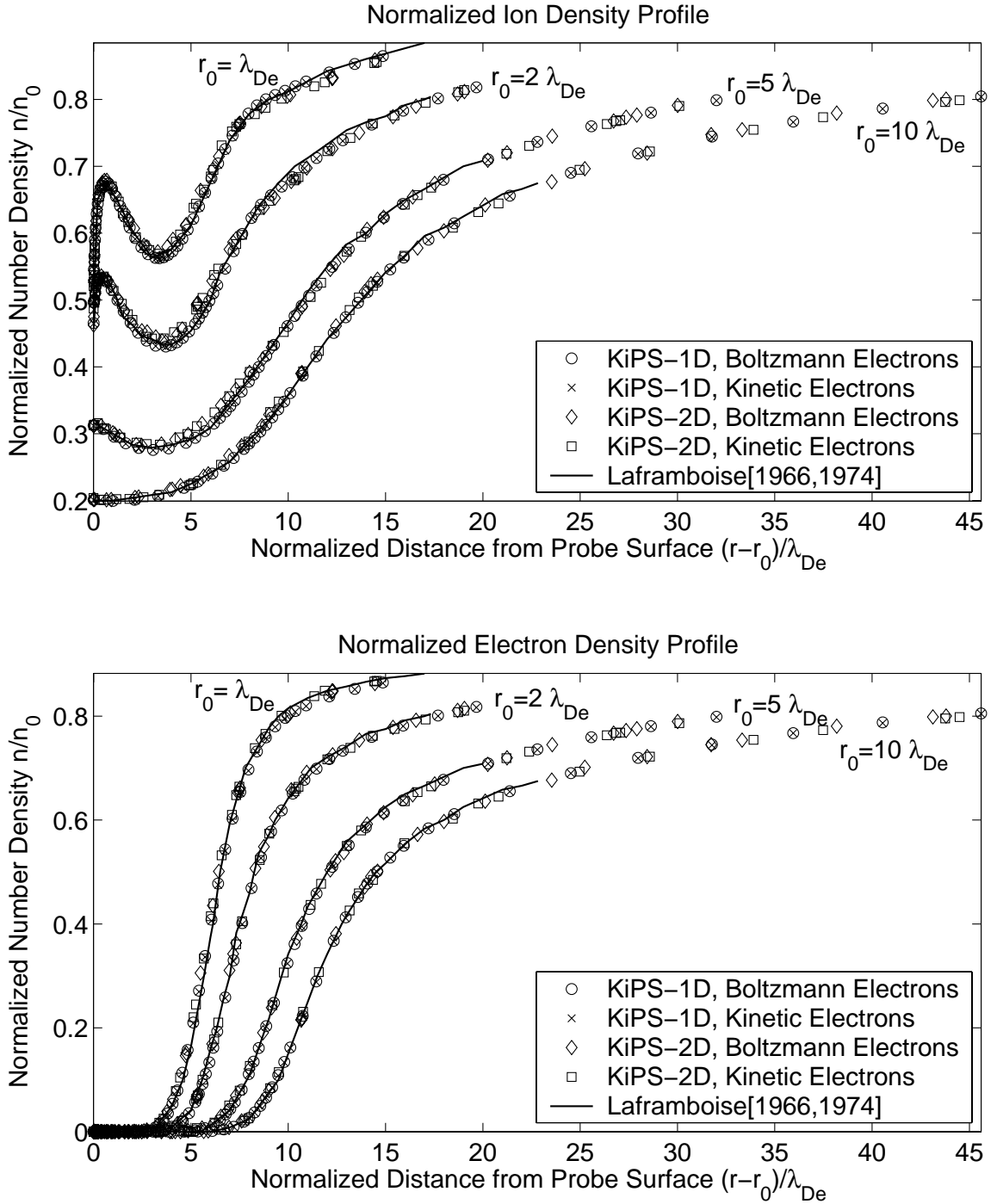


Figure 4.1: Normalized ion (top) and electron (bottom) charge densities as a function of normalized distance from the surface of a round cylindrical probe immersed in a stationary plasma, with $\phi_0 = \frac{V_0 - V_p}{T_e} = -25$ and $T_i = T_e$. Results obtained using the KiPS-1D and KiPS-2D solvers are shown for various probe sizes ($r_0/\lambda_{De} = 1, 2, 5$, and 10) and compared with results computed by Laframboise [8, 79]. All of the reference data were obtained from Laframboise's thesis [8], except for the $r_0 = \lambda_{De}$ data which include a minor, recent correction [79].

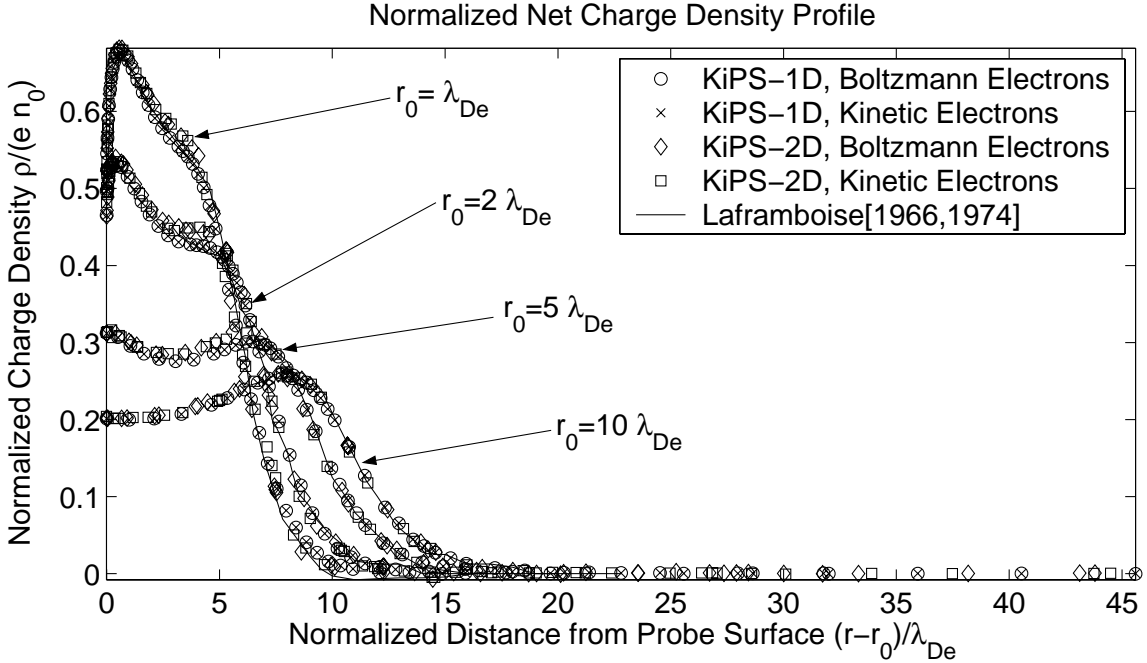


Figure 4.2: Normalized net charge density as a function of normalized distance from the surface of a round cylindrical probe immersed in a stationary plasma, with a bias potential $V_0 - V_p = -25T_e$ and $T_i = T_e$. Results obtained using the KiPS-1D and KiPS-2D solvers are shown for various probe sizes ($r_0/\lambda_{De} = 1, 2, 5$ and 10) and compared with the simulation results computed by Laframboise [8, 79].

different cylinder radii: 1, 2, 5 and 10 Debye lengths. Results are shown for both KiPS-1D and KiPS-2D, and for both kinetic and Boltzmann¹⁴ electrons. Excellent agreement is seen between the reference data and both our KiPS-1D and KiPS-2D simulation results. The Boltzmann approximation for the repelled electrons is also seen to be very accurate when compared to the results obtained using kinetic electrons. The attracted ion density at the probe surface is seen to be maximized for the smaller probe radius, with a maximum value of half the ambient density. This is expected, as is shown by (1.7): for small probe radii, the OML is attained and the surface density reaches its maximum value of half the ambient density. The net charge density shown in Figure 4.2 shows a large region of quasi-neutrality, indicating that a sufficiently large computational domain was selected.

¹⁴The Boltzmann approximation consists of approximating the repelled electron density using $n_e \approx n_0 \exp((V - V_p)/T_e)$, or simply $n_e \approx n_0 \exp(V/T_e)$ if we assume $V_p = 0$.

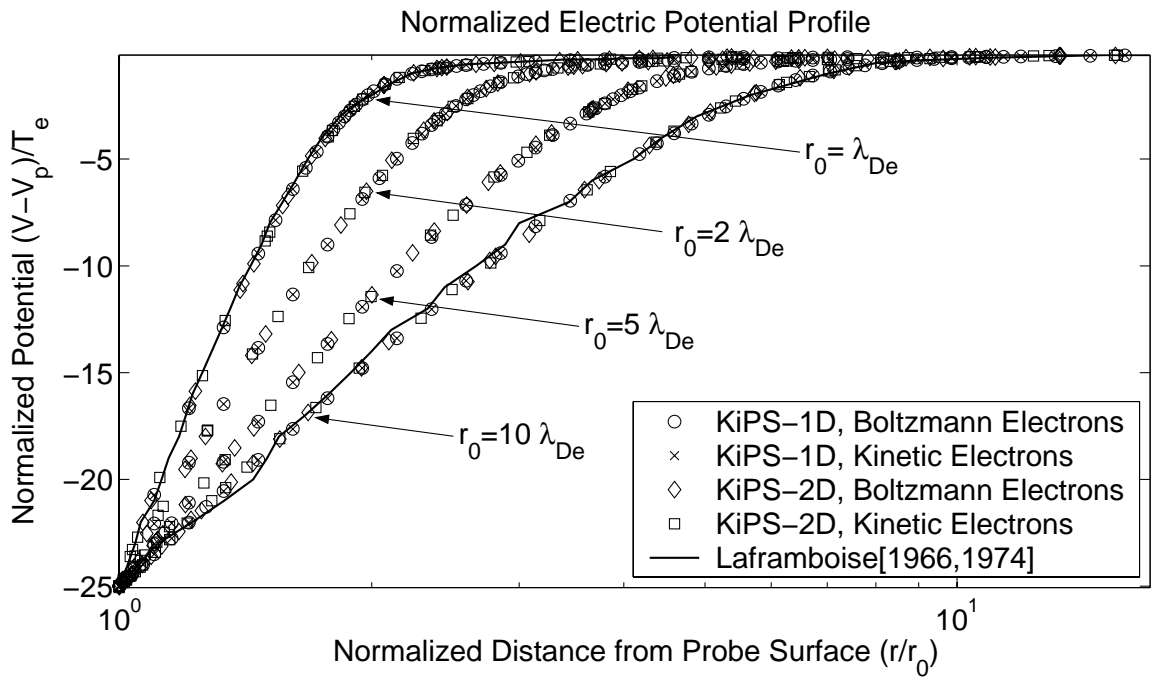
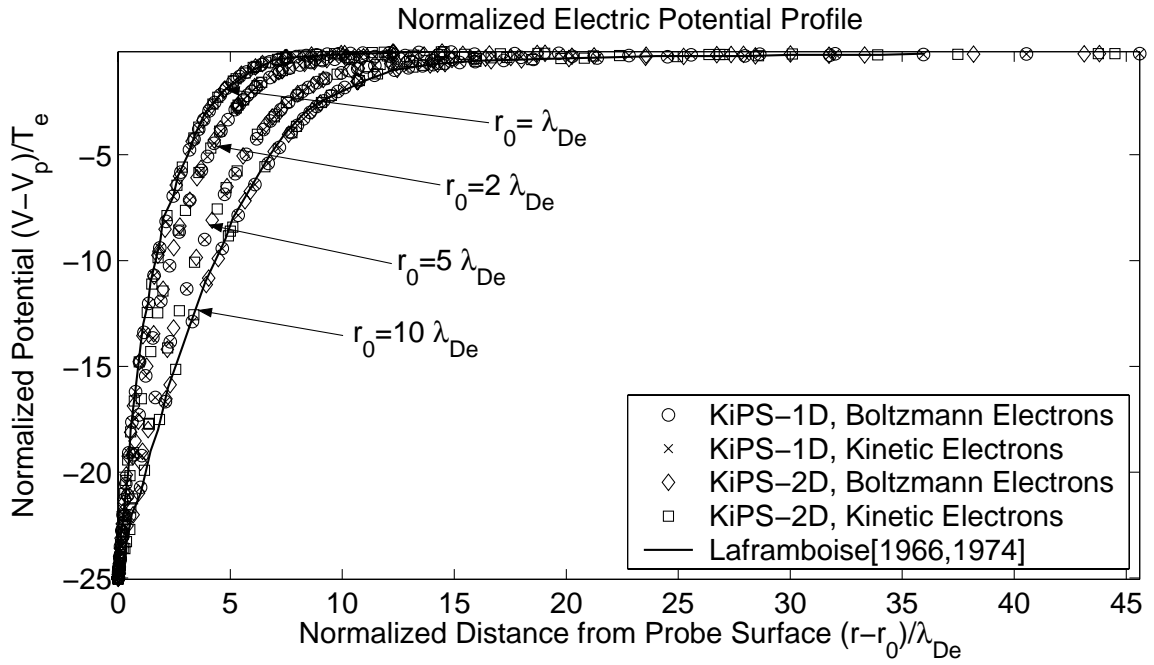


Figure 4.3: Normalized electric potential $(V - V_p)/T_e$ as a function of normalized distance from the surface of a round cylindrical probe immersed in a stationary plasma, with a bias potential $V_0 - V_p = -25T_e$ and $T_i = T_e$, shown in both linear and semi-logarithmic formats. Results obtained using the KiPS-1D and KiPS-2D solvers are shown for two probe sizes ($r_0/\lambda_{De} = 1, 2, 5, 10$), some of which ($r_0/\lambda_{De} = 1, 10$) compared with the simulation results computed by Laframboise [8].

Another interesting observation regards the potential distribution shown on the semilog plot on the bottom of Figure 4.3. The behavior of the graphs close to the probe is seen to follow a linear dependence on the semilog scale, which simply is a result of the fact that space charge only starts to significantly affect the potential profile at a sufficient distance from the probe for cumulative space charge to amount to a significant fraction of the surface charge held by the probe. The region of logarithmic dependence of the potential extends with increasing bias potential, as will become obvious when we consider large bias potentials.

Unfortunately, the author has not found in the literature any appropriate experimental data set that could be used for the validation of these potential and density profiles in stationary plasmas. Obtaining some sort of experimental validation of these profiles would be very valuable.

4.2.2 Validation of Collected Current at Low Bias Voltages

In addition to validating the potential and density profiles, we now proceed to validate the collected currents computed using KiPS-1D and KiPS-2D for a round cylinder in a stationary plasma. Figure 4.4 shows a comparison of the collected current characteristics for various probe radii. The agreement is excellent between the KiPS results and the results obtained by *Laframboise* [8], although our results appear to be somewhat higher by about 0.5%. This slight discrepancy could be explained by a combination of a number of factors such as:

- the quadrature tolerance used in the current calculation performed using our model, which was set to 1%; and
- the error involved in manually copying data points off of *Laframboise*'s graphs [8].

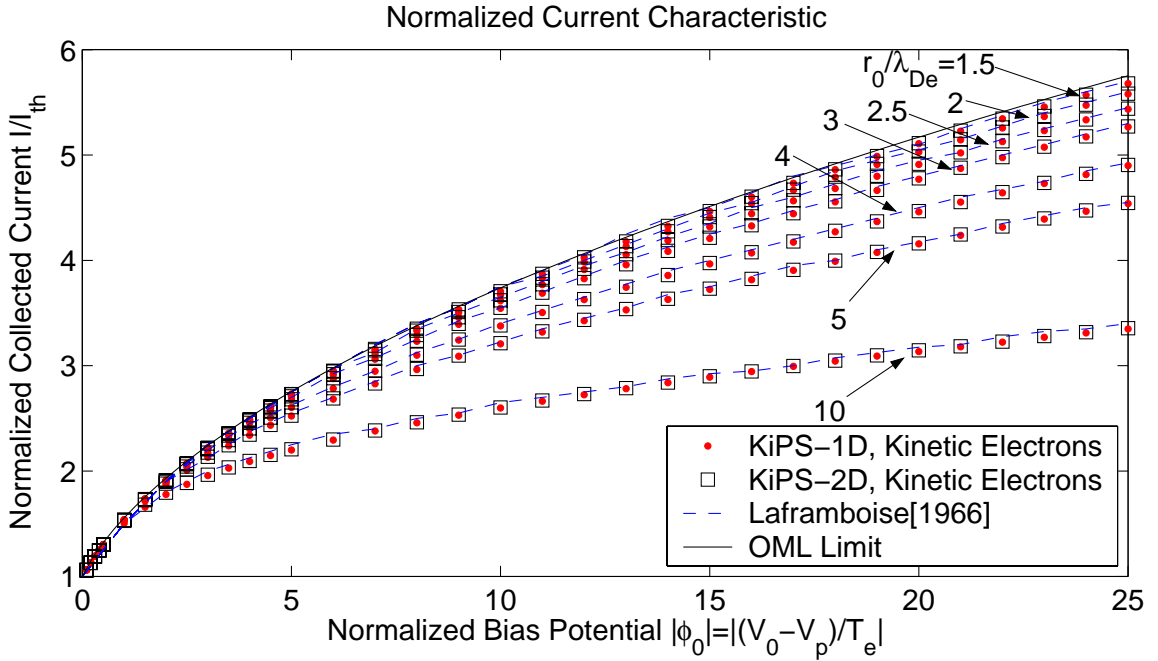


Figure 4.4: Normalized collected ion current I/I_{th} to a round conductive cylinder as a function of normalized bias potential $\phi_0 = (V_0 - V_p)/T_e$ with $T_i = T_e$. Results obtained using the KiPS-2D solver are shown for various normalized probe radii $r_0/\lambda_{De} = 1.5, 2, 2.5, 3, 4, 5$, and 10 and compared with the simulation results computed by Laframboise [8].

The excellent agreement between KiPS-1D and KiPS-2D collected current results provides further confirmation of the validity of both models.

It is observed, as a “sanity check”, that the collected current approaches the thermal current as the probe bias potential approaches the plasma potential, i.e., in Figure 4.4, the normalized current goes to 1 as the normalized bias potential approaches zero. In addition, we can see that as the probe radius becomes smaller, the collected current approaches the orbital motion limit current, i.e., the current collection efficiency is maximized on a “per area” basis.

4.2.3 Assessment of Collected Current at High Bias Voltages

Figure 4.5 shows the simulated current collection efficiency to 3 high-voltage cylinders, biased at $300T_e$, $1000T_e$ and $3000T_e$ as a function of the cylinder radius. We define the

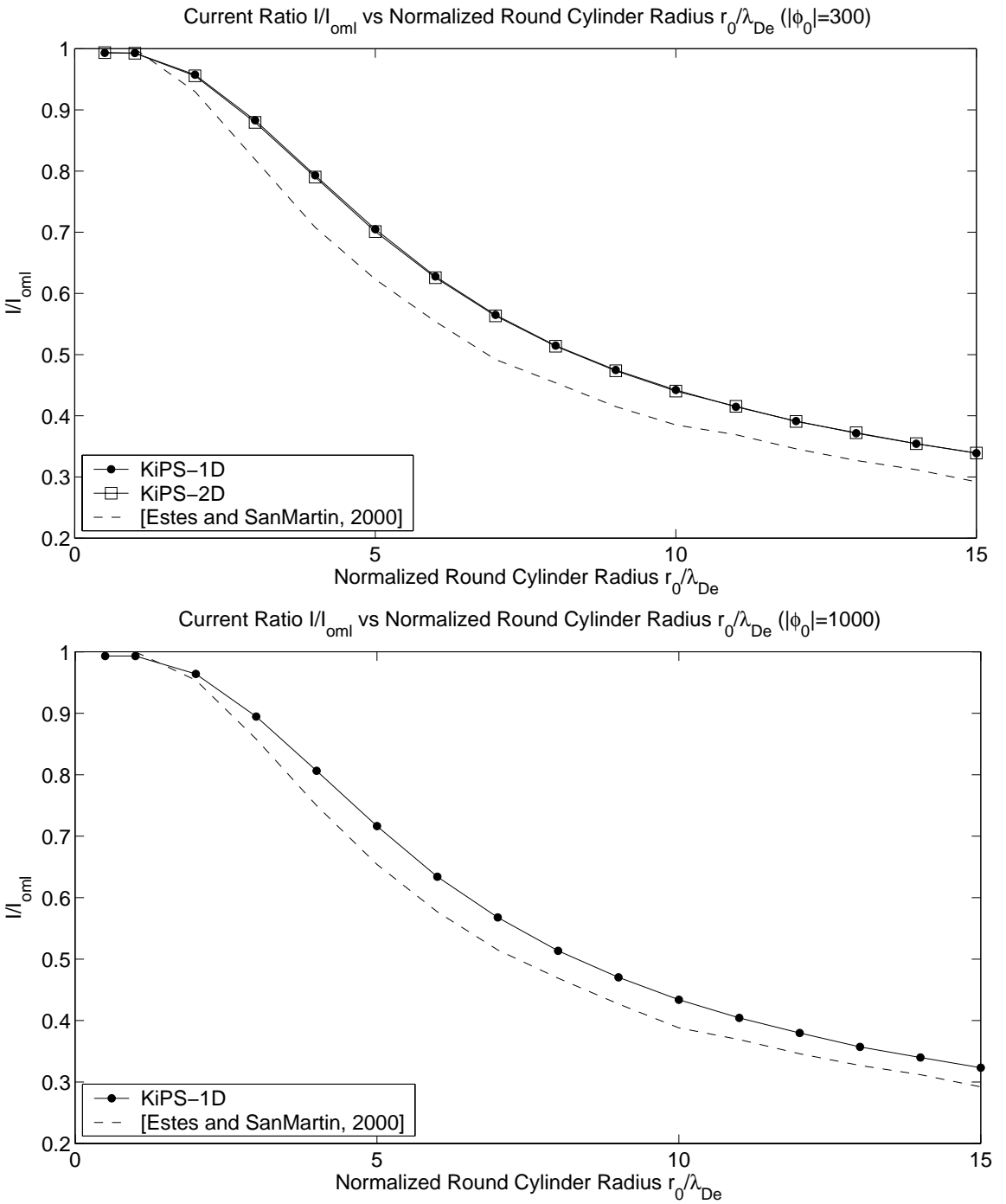


Figure 4.5: Current ratio I/I_{oml} (“current collection efficiency”) as a function of the radius of a round conductive cylinder immersed in a stationary plasma. Results obtained using the KiPS-1D and KiPS-2D solvers are shown for two bias potential values of $|\phi_0| = 300$ and $|\phi_0| = 1000$. A comparison is shown with calculations published by *Estes and Sanmartín* [12] for $T_i = T_e$.

“current collection efficiency” as the ratio of the collected current over the orbital motion limit current I_{oml} .

As expected, our results show a decrease in collection efficiency as the cylinder radius increases, because it results in a gradual breakdown of the orbital motion limit conditions. As the probe radius becomes larger, an increasing number of attracted-particle orbits connect two points on the probe surface. These unpopulated orbits create voids in the velocity distribution function of the inbound particles at the probe surface which grow as the probe radius increases.

Our results are compared against an approximate current calculation performed by *Estes and Sanmartín* [12]. The agreement with our simulation results is good, although not excellent. The source of the discrepancy is most likely the approximations used by *Estes and Sanmartín* [12], where an asymptotic approach is used that is only exact in the limit of thin cylinders. Our kinetic results allow us to confirm that, as observed by *Estes and Sanmartín* [12], the collection efficiency appears to be mostly dependent on the cylinder radius, and is only a weak function of the bias potential. This behavior provides a fairly simple rule that could be used by the designer of an electrodynamic tether system in the determination of an appropriate tether radius.

4.2.4 Plasma Profiles at High Voltages

Having validated our kinetic model in the low voltage regimes for which independent simulation data are available, we now turn to an important question that was not resolved by previous work in the field: how does sheath radius generally scale as a function of probe radius and bias potential?

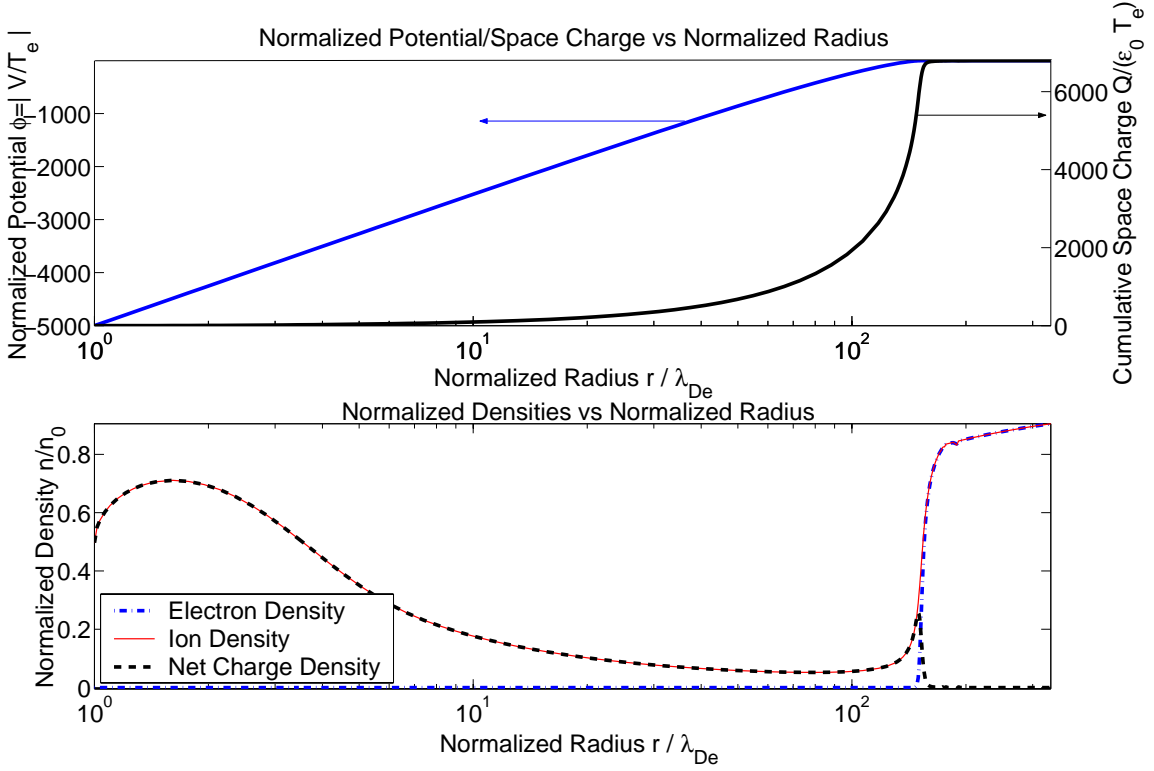


Figure 4.6: Typical high-voltage cylindrical sheath structure shown on a semilog scale. These profiles were obtained using KiPS-1D with a cylinder radius $r_0 = \lambda_{De}$ and a bias potential $\phi_0 = \frac{V_0 - V_p}{T_e} = -5000$.

4.2.4.1 Typical Plasma Profile from KiPS-1D

Figure 4.6 shows a typical self-consistent high-voltage plasma profile obtained using KiPS-1D for a one-Debye-length-radius probe negatively biased at $\phi_0 = -5000$ (5000 times the electron temperature). Note that the profiles are shown on a semilog scale to facilitate their interpretation.

The potential profile shown on the top half of Figure 4.6 is seen to follow a logarithmic trend out to a radius near 70 Debye lengths, which indicates that space charge effects are unimportant for smaller radii. To illustrate this, a plot of the “cumulative charge” is shown on the same figure which confirms that the amount of space charge due to the plasma is unimportant until we reach a sizable distance from the probe’s surface. The total amount of

negative linear surface charge on the cylinder $Q_n = -6800$ (unit-less, normalized value) is only neutralized by the plasma charge once we reach a radius of about 175 Debye lengths, at which point the cumulative space charge has reached a value very close to 6800, precisely balancing out the cylinder surface charge. Much of the charge neutralization thus seems to occur within an annular region of inner radius $r_{\text{inner}} = 70\lambda_{\text{De}}$ and outer radius $r_{\text{outer}} = 175\lambda_{\text{De}}$.

Because the potential profile has a logarithmic behavior for a sizable portion of the sheath, a useful approximation for the potential profile can be obtained using linear regression over its logarithmic portion. This best-fit approximation takes the form

$$\phi = \phi_0 \left(1 - \frac{\ln(r/r_0)}{\ln(r_s/r_0)} \right), \quad (4.13)$$

where r_0 is the cylinder radius, and r_s is defined as the *effective sheath radius*. The term “effective” refers to the fact that the potential profile is effectively the same as that which would exist if all of the space charge were lumped into a thin cylinder of charge located at a radius $r = r_s$. This can be thought of as an analogy to a coaxial capacitor, for which all of the outer charge is located on the outer conductor. Another reason for using the term “effective sheath radius” instead of simply “sheath radius” is to avoid any confusion with the classical notion of sheath edge, which is typically defined as the minimum radius at which the plasma is deemed quasi-neutral based on a somewhat arbitrary definition of quasi-neutrality [22]. For the present case shown in Figure 4.6, we find for the effective sheath radius a value of about 100 Debye length, which corresponds to the radius where the best-fit approximation intercepts a potential of zero. This definition of the sheath radius, which is based on the specific needs of the charge precipitation application, is believed to provide a better measure of the effective region of influence of the sheath than the classical definition and is most appropriate for high voltages, which cause the space charge to lump within an annular region of limited extent.

Now let us consider the density profiles shown on the bottom portion of Figure 4.6. First, the density of the repelled electrons is, not surprisingly, negligible over the vast majority of the sheath, having dropped sharply together with the ion density drop. Another observation of interest is that, as was observed at lower voltages, the ion density here reaches the orbital motion limit of half of the ambient density ($n_i/n_0 = 0.5$), because the cylinder radius is sufficiently small.

Now, one feature of crucial importance is the very low ion density that exists within the sheath. The minimum density seen on this particular profile is about 0.05, that is, 5% of the ambient density. This relatively low value of the minimum ion density is key to obtaining large sheath sizes because it represents a limitation in the shielding capability of the ambient plasma.

The very low minimum ion density observed within the sheath extends over a sizable range at high voltages (keep in mind that the scale used in Figure 4.6 is semi-logarithmic). This can be interpreted in one of two equivalent ways, which we state here:

Current conservation The quasi-conservation of the radial ion current forces the inward-directed component of the ion density to drop as the ions accelerate into the potential well of the sheath. The same reasoning applies equally well to the “outward-directed” component of the ion density, which must increase as the ions decelerate as they come out of the potential well. Although simplistic, this explanation can qualitatively explain the sudden drop of the ion density near a radius $r \approx 150 \lambda_{De}$. The validity of this reasoning is based on the fact that the vast portion of the incoming ions at the sheath edge will miss the small probe, so that we may assume that the inward and outward populations contribute equivalent amounts to the local density. In addition, most inward ions do not “turn back” before they get in relatively close range from the cylinder, which allows us to use the argument of conservation of current for the

inward and outward populations separately.

Angular Momentum limitations In the region just within the sheath but still far enough from the cylinder, the ion population is mostly radially-directed because of the acceleration it has experienced as it entered the sheath. In these locations, a large range of directions with relatively large angular momentum are therefore not populated because they are located on collisionless “trapped” orbits, i.e., orbits that are closed onto themselves and do not originate from the background plasma.

The reasons for these reduced ion densities will become more evident as we discuss the variation of the ion velocity distributions throughout the sheath in Section 4.2.4.4.

4.2.4.2 Typical Two-Dimensional Plasma Structure from KiPS-2D

Figures 4.7 and 4.8 illustrate the 2-D structure of the plasma surrounding the conductive cylinder, as computed using KiPS-2D, along with corresponding x -axis cross-sectional profiles. The dynamic meshing capability of KiPS-2D is shown by the high mesh density near the sheath edge, where a surge in the net charge density is observed. The obtained profiles are in agreement with results obtained using KiPS-1D.

4.2.4.3 Profile dependence on Bias Potential and Cylinder Radius

It turns out that the value of the minimum ion density goes down as the magnitude of the bias potential increases, which contributes to a further increase in sheath dimensions. This is seen in Figures 4.9 and 4.11, which show a set of various density and potential profiles corresponding to various bias settings for a cylinder of radius $r_0 = \lambda_{De}$. Similar families of curves are shown in Figures 4.10 and 4.12 for a much smaller cylinder radius $r_0 = 0.001\lambda_{De}$. Although both sets of curves behave somewhat similarly at large radii, the main difference with the smaller cylinder radius is that the ion density is allowed to ramp

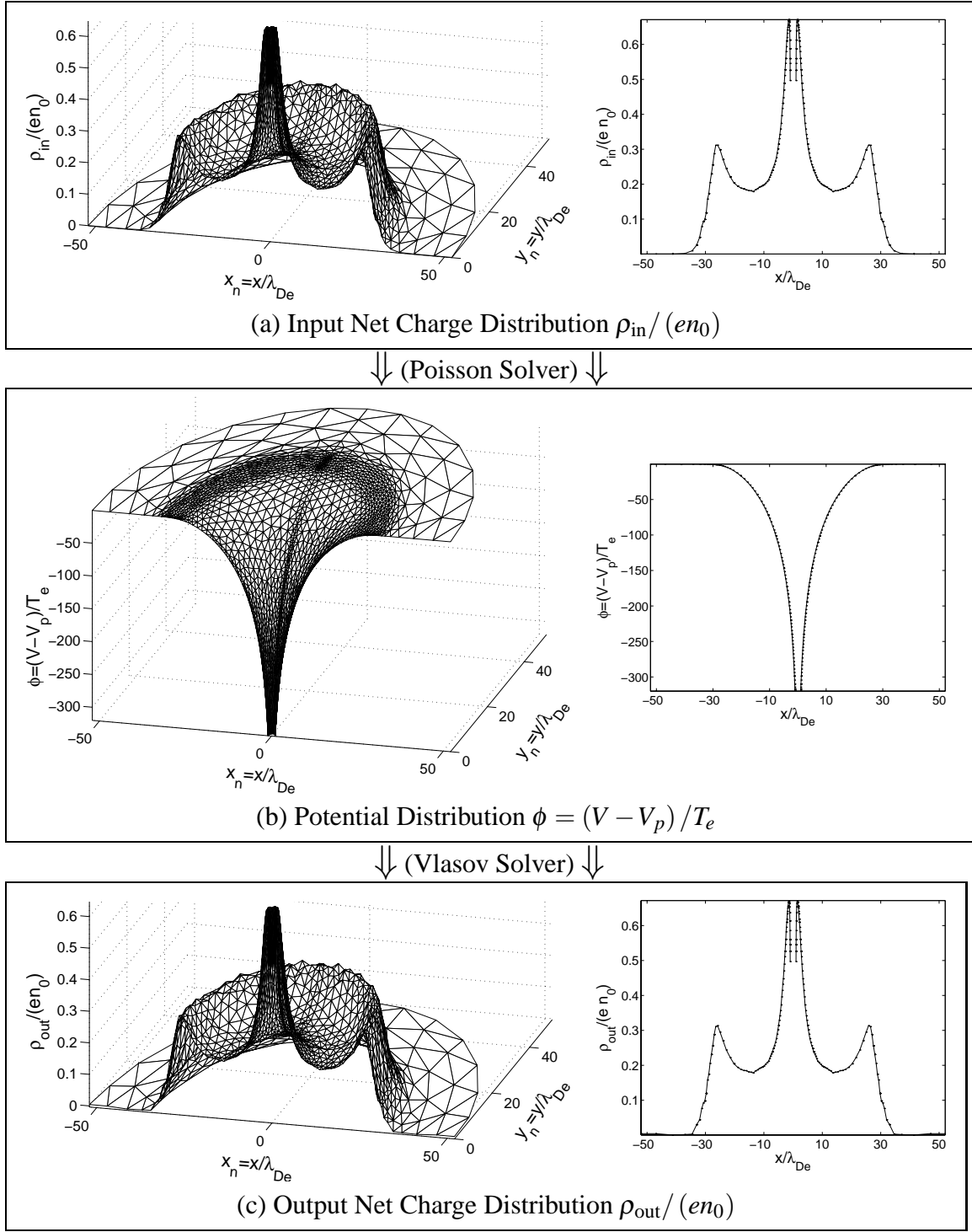


Figure 4.7: Poisson–Vlasov consistent solution for the single-cylinder configuration with a cylinder radius $r_0 = \lambda_{\text{De}}$ and normalized bias $\phi_0 = -320$. Self-consistency is shown by the similarity of ρ_{in} and ρ_{out} . 2-D solutions are shown on the left, and corresponding x -axis cross-section profiles are shown on the right. Ion and Electron density dist. are shown in Figure 4.8.

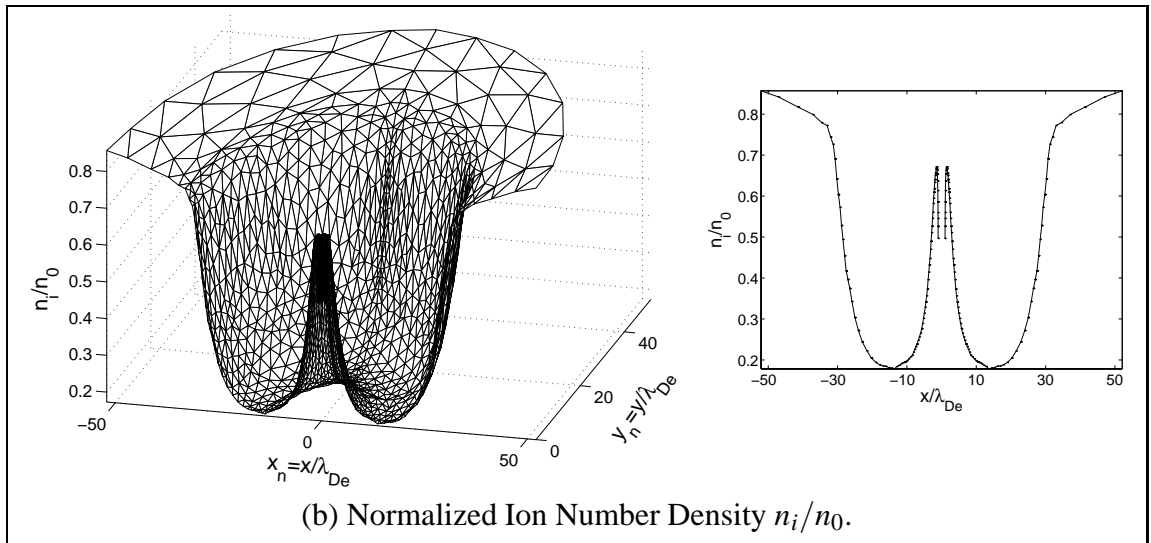
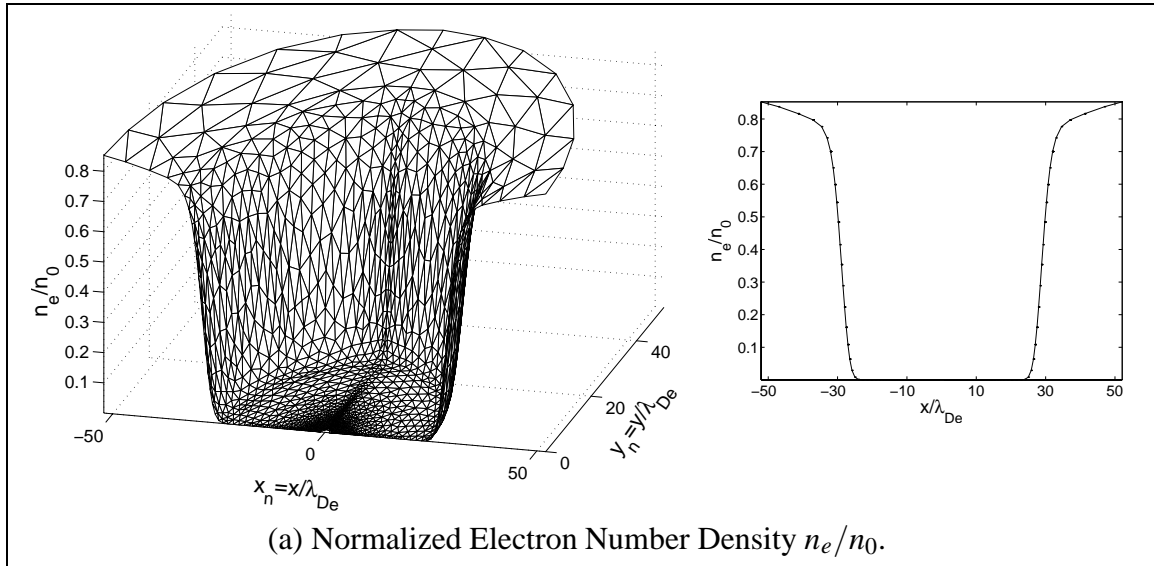


Figure 4.8: Poisson–Vlasov consistent electron and ion density distributions corresponding to the single-cylinder solution shown in Figure 4.7 ($r_0 = \lambda_{De}$, $\phi_0 = -320$). These density profiles constitute the output of the Vlasov solver and are subtracted to form the output net charge density profile $\vec{\rho}_{\text{out}} = e(n_i - n_e)$ shown in Figure 4.7(c).

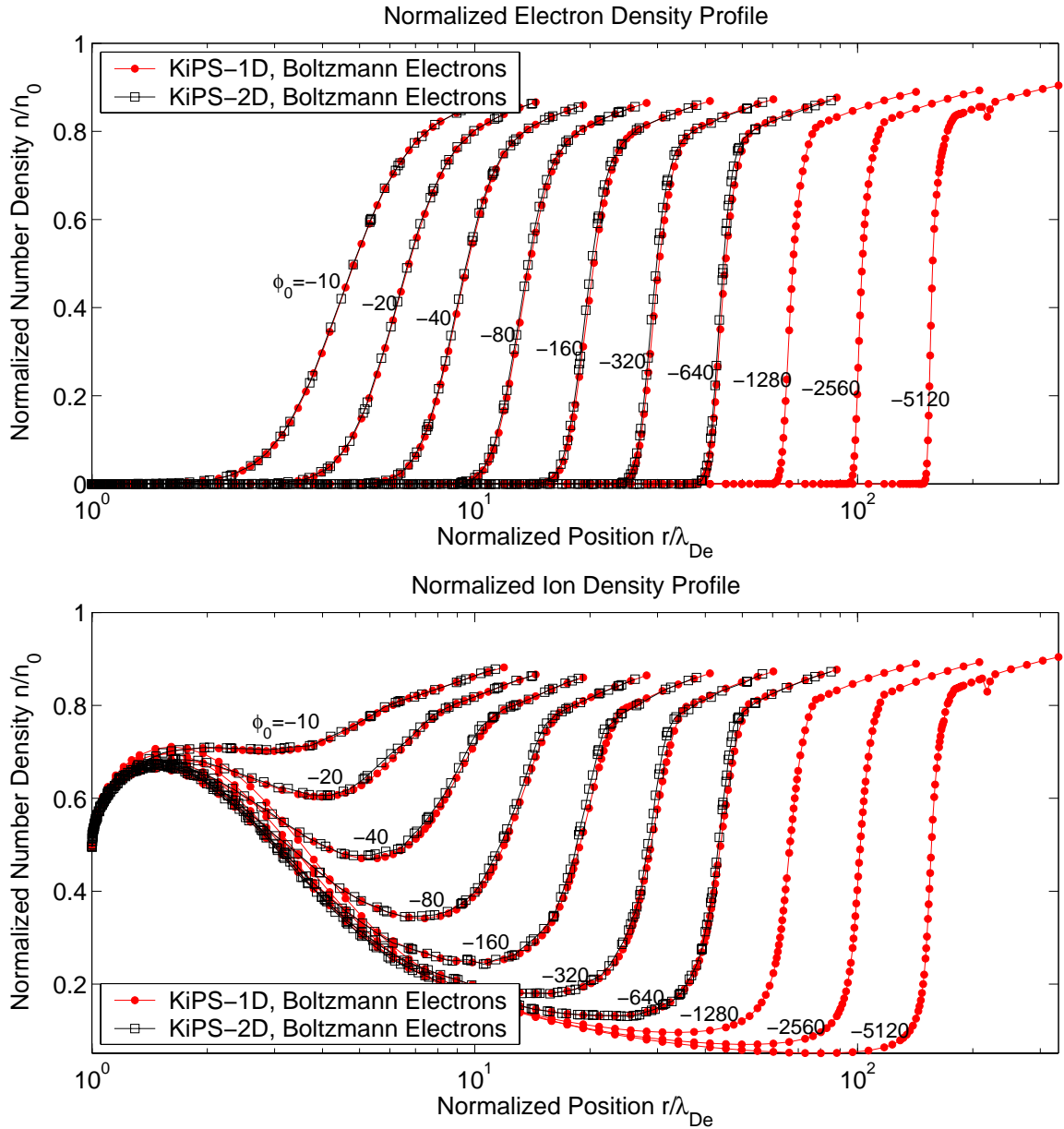


Figure 4.9: Family of electron and ion density profiles for a round conductive cylinder with radius $r_0 = \lambda_{De}$ in a stationary plasma. Several curves are shown corresponding to normalized biases $\phi_0 = V_0/T_e$ spanning from -10 to -5120 .

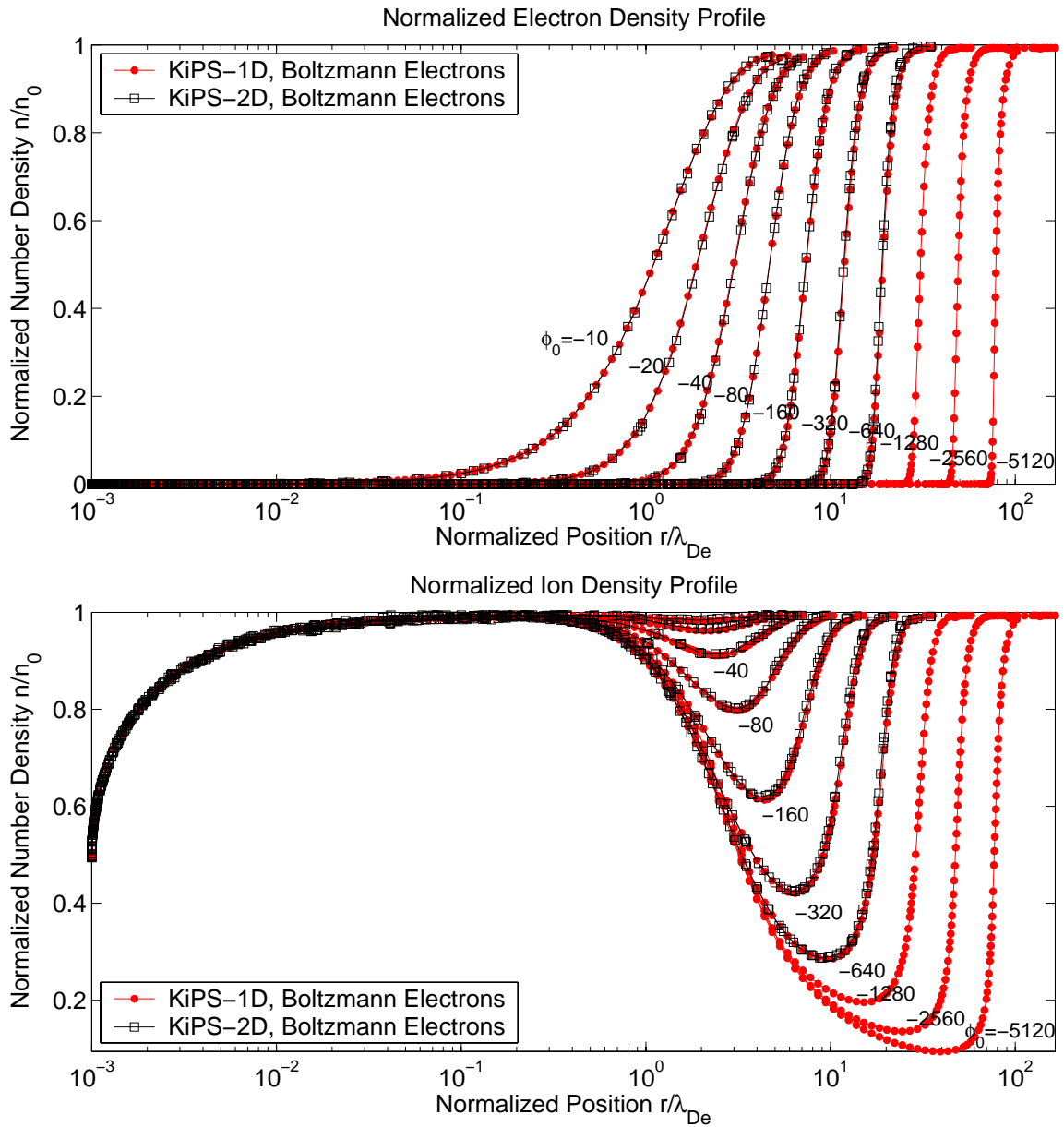


Figure 4.10: Family of electron and ion density profiles for a round conductive cylinder with radius $r_0 = 0.001\lambda_{De}$ in a stationary plasma. Several curves are shown corresponding to normalized biases $\phi_0 = V_0/T_e$ spanning from -10 to -5120 .

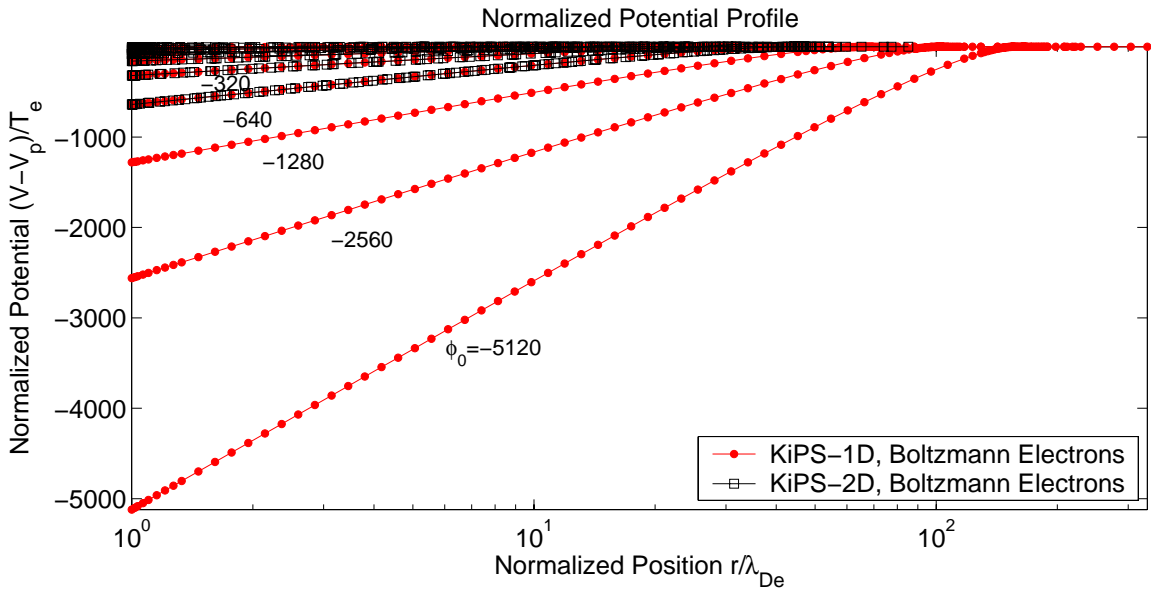


Figure 4.11: Family of potential profiles for a round conductive cylinder with radius $r_0 = \lambda_{De}$ in a stationary plasma. Several curves are shown corresponding to normalized biases $\phi_0 = V_0/T_e$ spanning from -10 to -5120 .

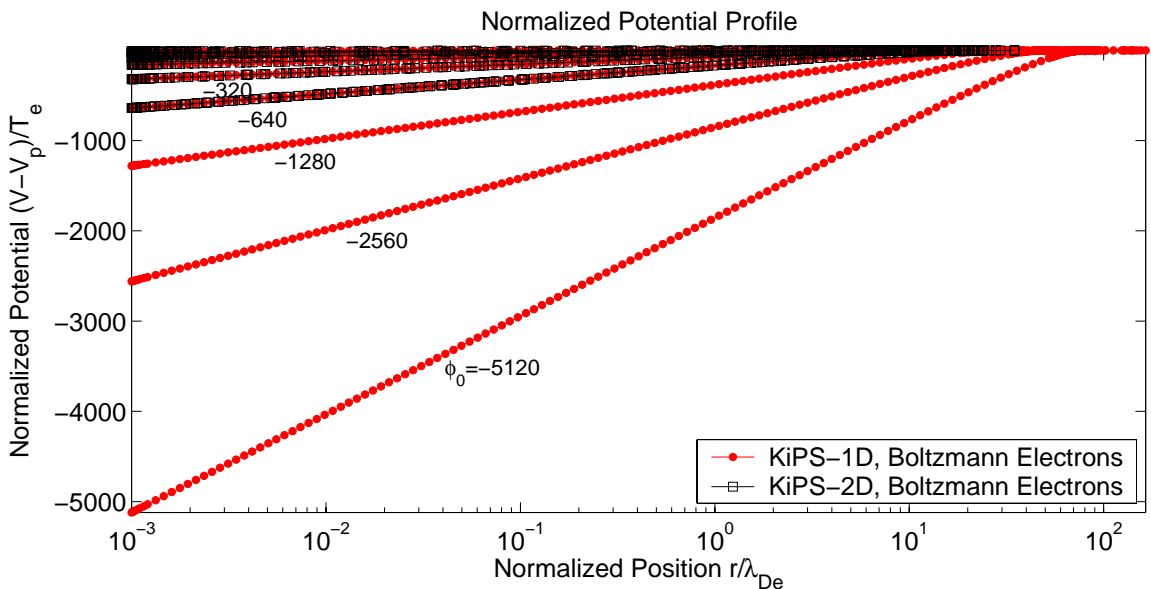


Figure 4.12: Family of potential profiles for a round conductive cylinder with radius $r_0 = 0.001\lambda_{De}$ in a stationary plasma. Several curves are shown corresponding to normalized biases $\phi_0 = V_0/T_e$ spanning from -10 to -5120 .

back up to the ambient density due to an improved geometric convergence at smaller radii, before dropping back to half of the ambient density at the probe surface, the orbital motion limit.

4.2.4.4 Variation of the Ion Velocity Distribution Throughout the Sheath

In order to better understand the nature of the pronounced ion density drop in the sheath, we now inspect the ion velocity distribution functions throughout the sheath. Since within the potential well, the velocity distributions are getting compressed onto a thin annulus, a perhaps better graphical representation of the velocity distribution function can be obtained using the concept of *directional-energy distribution*, which we now define. Let E be the total particle energy, including both potential and kinetic energy components. At a given location in the plasma, we may write E as

$$E = q_i V + \frac{m_i}{2} (v_r^2 + v_\theta^2) \quad (4.14)$$

where V is the local potential, $q_i = e$ is the ion charge, m_i is the ion mass, and the instantaneous velocity components in cylindrical coordinates are v_r and v_θ . In the ambient plasma (as $r \rightarrow \infty$), the *total energy* distribution of the ions is a Maxwellian:

$$f_E(E) = \frac{n_0}{eT} \exp\left(-\frac{E}{T}\right). \quad (4.15)$$

As we get closer to the sheath, the total energy distribution is no longer isotropic, so we introduce the concept of “directional-energy” $f(E_r, E_\theta)$, where E_r and E_θ are defined as

$$E_r = E \frac{v_r}{\sqrt{v_r^2 + v_\theta^2}}, \quad \text{and} \quad E_\theta = E \frac{v_\theta}{\sqrt{v_r^2 + v_\theta^2}}. \quad (4.16)$$

The directional distribution of particles can thus be given as a function of the two variables E_r and E_θ .

Figure 4.13 depicts the directional-energy distributions at various locations along the ion density profile.

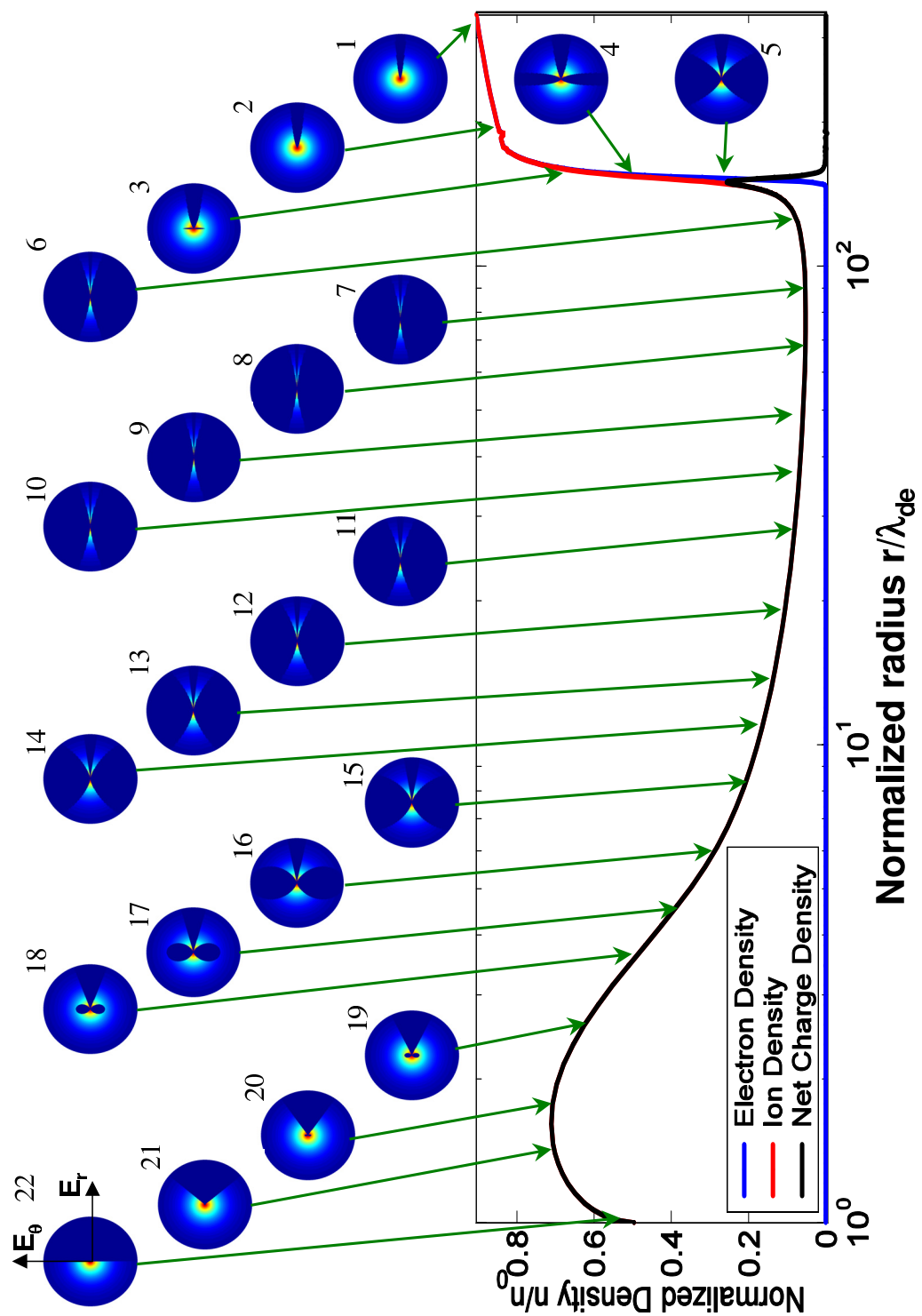


Figure 4.13: Ion “directional-energy” distributions in the high-voltage cylindrical sheath.

In the following we describe the nature of the velocity distributions as applicable to the various distributions labeled from 1 to 22 in Figure 4.13, going from the largest radius (point 1, farthest location) to the probe surface (point 22):

Locations No. 1–2 The inbound ions are Maxwellian. The outbound ions are only partially blocked out by the probe (probe shadow effect).

Location No. 3 The probe shadow grows as we get closer to the probe, just outside the sheath. Some very small unpopulated trapped orbits start to appear, due to some angular momentum limitations.

Location No. 4 The probe shadow is unchanged. The zone of unpopulated trapped orbits is rapidly expanding as we enter the sheath and ions are radially accelerated.

Location No. 5 The probe shadow now starts shrinking as we enter the sheath, since the “shadowed trajectories” are also being radially accelerated. The zone of unpopulated trapped orbits continues to expand significantly, and the directional-energy distribution appears to be increasingly radially-directed.

Locations No. 6–13 The probe shadow is fairly small within the sheath since shadowed trajectories are very radially directed. The ions are almost exclusively radially directed. The ion density has dropped significantly because of the radial acceleration as we enter the sheath, leaving the inaccessible large-angular-momentum orbits unpopulated. The ion density reaches its minimum at location No.7. Beyond this point, geometrical concentration of current will overcome the sheath acceleration effects and gradually populate the depleted zones, causing the density to increase.

Locations No. 14–20 The probe shadow is now growing as we near the probe. Geometrical concentration of current has overcome the sheath acceleration effects and the

depleted zones are gradually getting filled as we near the probe.

Location No. 21 There are virtually no unpopulated trapped zones anymore. This is because we have reached a small enough radius for geometrical concentration to have re-populated the depleted zones.

Location No. 22 We are now at the surface of this one-Debye-length-radius probe. Half of the directions are blocked by the probe, and consequently the density is half the ambient density. There are no unpopulated incoming directions at the surface of this small probe, which is why the surface ion density achieves its maximum possible value of half the ambient density; this is the orbital motion limit. A larger probe would result in a lower ion density because it would feature depleted zones which would correspond to a set of orbits linking two points on the probe's surface.

4.2.5 Sheath Radius at High Voltages

Having defined an effective sheath radius r_s consistent with an asymptotic best-fit of the potential profile given by (4.13), we now consider the effect of the bias potential ϕ_0 and probe radius r_0 on the effective sheath radius r_s . The top part of Figure 4.14 shows the variation of the normalized effective sheath radius r_s as a function of the normalized bias potential ϕ_0 , for several values of the cylinder radius r_0 . Not surprisingly, the effective sheath radius grows for increasing bias potential magnitudes and also grows monotonically as a function of the cylinder radius r_0 .

As we have discussed before, at large voltages the space charge in the immediate vicinity of the probe should have a negligible effect on the local potential which is overwhelmingly dominated by the effect of the cylinder surface charge. For sufficiently thin cylinders, which cause little shadowing effect on outbound trajectories over most of the sheath, the electrodynamic processes in the bulk of the sheath should become nearly independent of

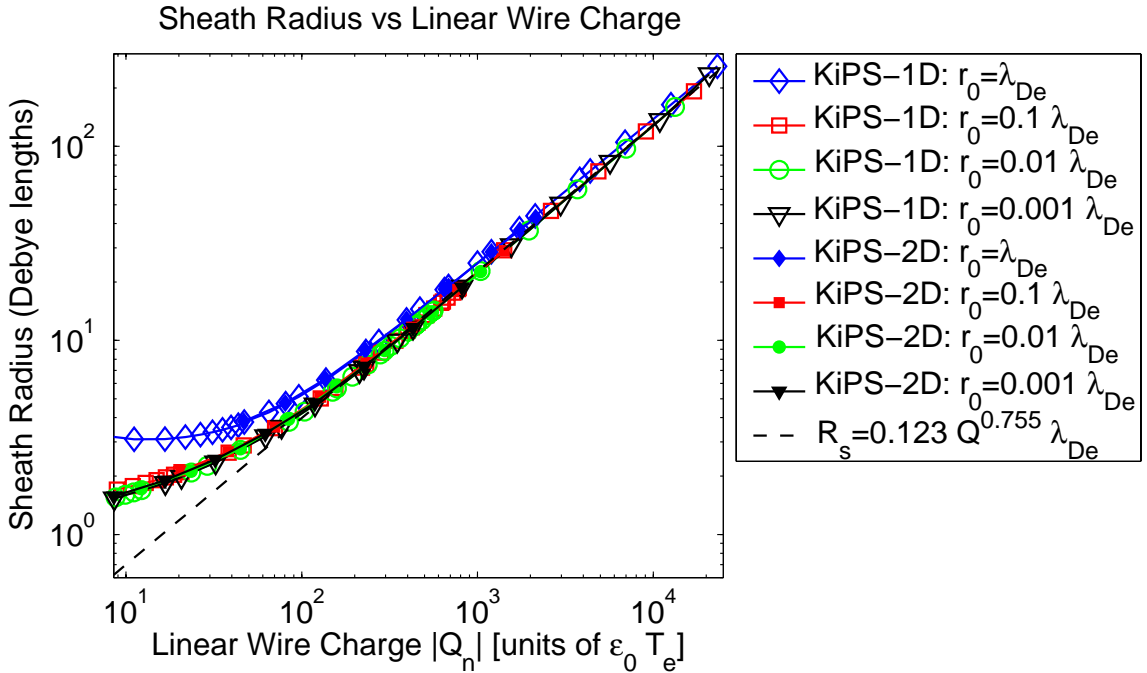
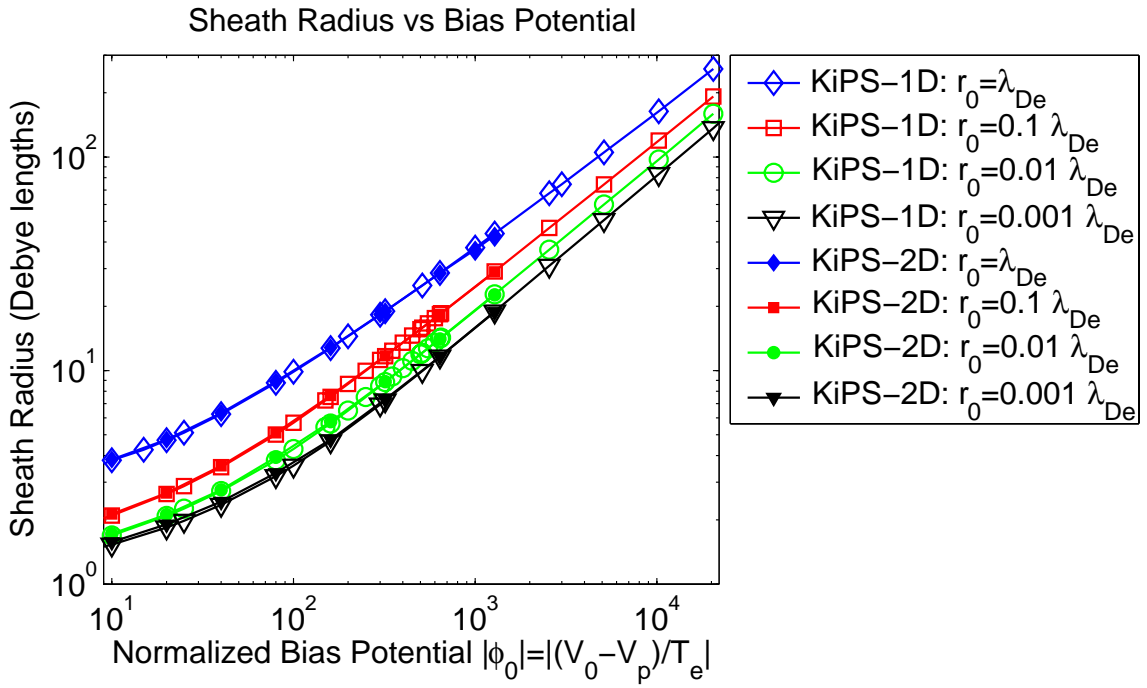


Figure 4.14: Equivalent sheath radius as a function of normalized bias potential $|(V - V_p)/T_e|$ and normalized line charge $Q/(\epsilon_0 T_e)$ for an ion-attracting round conductive cylinder immersed in a stationary plasma with $T_i = T_e$. Results obtained using the KiPS-1D and KiPS-2D solver are shown for various cylinder radii.

the cylinder radius for a given cylinder surface charge. Instead of plotting the sheath radius as a function of bias potential, on the bottom part of Figure 4.14 we now plot it against the magnitude of the negative linear charge present on the cylinder's surface, which can be obtained through one of two equivalent methods:

- by integrating the positive total plasma space charge surrounding the cylinder, which is equal and opposite to the total negative charge held by the cylinder;
- by inferring it from the knowledge of the cylinder radius r_0 , bias ϕ_0 and effective sheath radius r_s using the linear capacitance formula for a coaxial capacitor [43],

$$Q_n = \frac{2\pi\phi_0}{\ln \frac{r_s}{r_0}}. \quad (4.17)$$

All of the plots shown on the top part of Figure 4.14 now align over each other on the bottom part, except for the plot corresponding to the largest tested cylinder radius of $r_0 = \lambda_{De}$. This remaining discrepancy is due to the fact that this cylinder radius is sufficiently large to cause significant shadowing of some outbound ion trajectories which are left unpopulated, causing a reduction of the ion density throughout the sheath and a reduced shielding capability consistent with the observed larger sheath size as compared to cases with equal surface charge but smaller cylinder radius r_0 .

As is shown on the bottom part of Figure 4.14, an asymptotic best-fit of the r_s -vs- Q_n relationship was performed over the highest values of the linear wire charge Q_n , which applies accurately for $|Q_n| \geq 200$ and $r_0 \leq 0.1\lambda_{De}$. This best-fit asymptotic relationship is given by

$$\frac{r_s}{\lambda_{De}} = 0.123 |Q_n|^{0.755}. \quad (4.18)$$

Although this equation is not accurate for larger cylinder radii as is seen for $r_0 = \lambda_{De}$ on the bottom part of Figure 4.14, it may still be used for purposes of determining a lower

bound. This asymptotic equation can now be combined with (4.17) to determine an implicit asymptotic equation for the effective sheath radius r_s as a function of the bias potential ϕ_0 :

$$2.554 \left(\frac{r_s}{\lambda_{De}} \right)^{1.325} \ln \frac{r_s}{r_0} = -\phi_0. \quad (4.19)$$

Although this equation cannot be solved analytically for r_s , it can be inverted numerically or computed directly for a given set of negative values for the bias potential ϕ_0 . Consistent with the restrictions mentioned above, it can be used to accurately predict sheath radii for cylinder radii of a tenth of a Debye length or less ($r_0 \leq 0.1\lambda_{De}$) and for bias potentials ϕ_0 with a magnitude such that

$$|\phi_0| \geq \frac{200}{2\pi} \ln \frac{r_s}{r_0} \approx 31.8 \ln \frac{r_s}{r_0}. \quad (4.20)$$

For values of the bias potential ϕ_0 and cylinder radius r_0 beyond these limits, the sheath dimensions given by numerically solving (4.19) should be regarded as lower bounds.

4.3 Interference of Parallel Round Cylinders in a Stationary Plasma

In an effort to gain a basic understanding of the physics of plasma-immersed multi-wire conductive structures, we consider a structure consisting of two parallel, identical round cylinders with equal bias potential (see Figure 1.3(b)). The geometrical parameters are the cylinder radius r_0 and the center-to-center spacing Δx . All of the simulation results presented in this section were performed using a cylinder radius $r_0 = \lambda_{De}$ and a normalized bias potential $\phi_0 = \frac{V_0 - V_p}{T_e} = -320$.

We consider the effect of the center-to-center spacing on sheath structure and current collection, always comparing performances to those of a single round cylinder with radius $r_0 = \lambda_{De}$ and bias potential $\phi_0 = -320$. The value of the center-to-center spacing Δx will vary from $\Delta x = \lambda_{De}$ (cylinders touching) all the way to $\Delta x = 200\lambda_{De}$. This maximum

spacing corresponds to about 10.5 times the single-wire effective sheath radius of $19\lambda_{De}$ (see Figure 4.14).

In the negative bias potential situation under consideration, the ions are the attracted species. Since the plasma is not moving (no flow), the results we obtain are also directly applicable to the electron-attracting situation with equal and opposite bias potential, provided that we swap the ion and electron density profiles.

4.3.1 Treatment of Repelled Electrons

Our model allows for the full kinetic representation of both species. However, in a stationary situation we know that the electric potential will have the same sign as the bias potential, everywhere in space around the perturbation, and certainly everywhere within the computational zone. For a repelling bias potential of such a large magnitude as that considered here ($\phi_0 = -320$), we can affirm that, for all practical purposes, none of the electron trajectories which contribute to the electron density intersect the conductive cylinders. This means that all electron trajectories are connected to the background plasma, and allows us to use with excellent accuracy the Boltzmann equation for the electron density:

$$n_e = n_0 \exp \frac{V}{T_e}, \quad (4.21)$$

where we assume that $V < 0$ everywhere in space, and arbitrarily set the plasma potential to zero. This approach results in significant computational savings, due to the fact that only the ions need to be treated kinetically.

4.3.2 Orbits of the Attracted Ions

We now turn our attention to the orbits of the attracted ions. In the following we discuss the existence of complex ion orbits which do not exist in the single-cylinder case, and explain that the criteria used to determine whether an orbit is trapped (and unpopulated)

must be less restrictive than in the case of the single cylinder. We then show some examples of these complex orbits.

4.3.2.1 Criteria for Trapped Orbits

The symmetric potential structure which exists in the simple single-cylinder case does not allow any of the non-trapped trajectories to feature more than one change of “radial direction”, that is, one change of sign of the radial component of velocity, v_r . In other words, any orbit originating from the background plasma will either:

- approach the conductive cylinder ($v_r < 0$), miss it due to an excessive angular momentum and return to the background plasma ($v_r > 0$);
- approach the conductive cylinder and get collected onto it ($v_r < 0$ all along).

When two parallel cylinders immersed in a plasma are placed sufficiently close to one another (i.e., when the individual sheath radius is a non-negligible fraction of the center-to-center spacing Δx), the *shadow* effect created by one cylinder can affect the space charge surrounding the other sufficiently to create asymmetries in the potential structure. Those asymmetries, in turn, could allow for the existence of collisionless trajectories of an increased complexity, featuring for example several “radial oscillations” about a given cylinder, or even “figure eight” trajectories orbiting about both cylinders. At any given location, some of the directions in velocity space that were unpopulated when there was no neighboring cylinder may now be populated through relatively complex paths originating from the background plasma, while other directions that were previously populated may now be unpopulated due to the existence of new types of trapped orbits, such as the “figure eight”.

As a consequence, the simulation parameters used to determine whether a trajectory is trapped or not will be especially important for this asymmetric structure. We need to set a sufficiently large radial oscillation limit to allow for the existence of these more complex

orbits (described in Section 2.4.2.2), while at the same time keeping it down to a reasonable value to obtain reasonable simulation times. We have found that allowing for up to 20 radial oscillations ($M_{\text{rosc}} = 20$) provided such a compromise. The maximum angular displacement M_{orb} (see Section 2.4.2.2) was not used to impose further restrictions on the orbits, and M_{segcross} was set to 100.

4.3.2.2 Examples of Ion Orbits

In Figure 4.15 we show a few typical examples of ion orbits across the self-consistent potential structure of the two-cylinder configuration with a center-to-center spacing $\Delta x = 20\lambda_{\text{De}}$, a bias potential $\phi_0 = -320T_e$ and a cylinder radius $r_0 = \lambda_{\text{De}}$. The circle shown at one end of each trajectory indicates the location of the *interrogation* point where the velocity distribution function is being sampled. Following the trajectory from this point backward in time leads us to the “source” point of the trajectory, indicated by a square.

The source point can be either the background plasma, a cylinder’s surface (in which case the orbit is unpopulated since the cylinder is not a source), or it may be undetermined in the case of a trapped orbit.

Figures 4.15(a)–4.15(c) have a common interrogation point, located on a node on the right side of the mesh. Figure 4.15(a) shows an example of an unpopulated orbit originating from the surface of the rightmost cylinder; this orbit is not populated because the cylinder is not a plasma source. Figure 4.15(b) depicts a populated orbit that undergoes two loops around the rightmost cylinder before reaching the interrogation point, on the outer edge of the computational zone. Figure 4.15(c) depicts a very complex but populated ion orbit that originates from the background plasma, undergoes several loops around both cylinders, and finally reaches the interrogation point.

Figure 4.15(d) corresponds to a different interrogation point. It is shown here to illustrate one example of an unpopulated orbit that was deemed “trapped”, having exceeded the

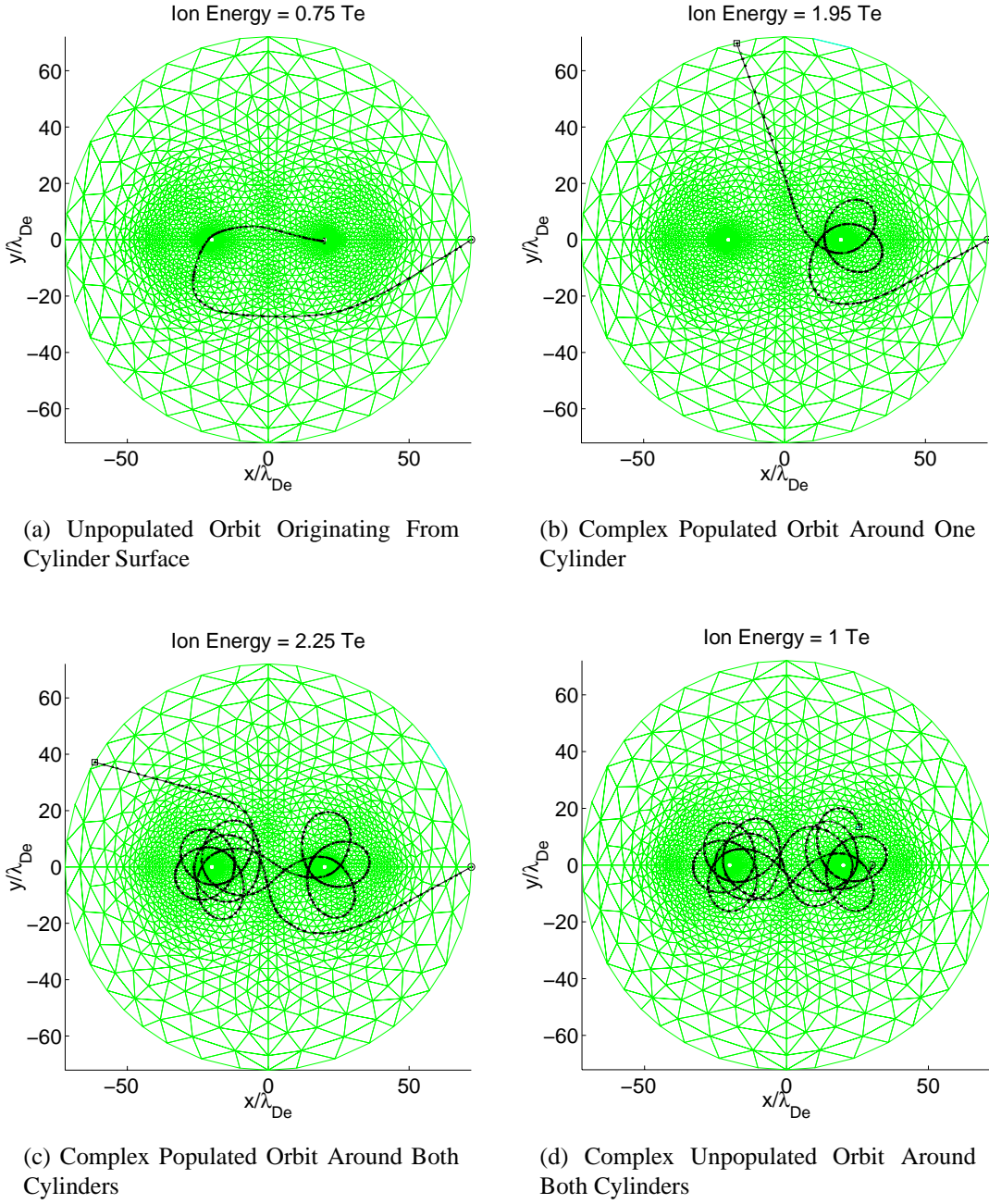


Figure 4.15: Examples of some typical ion orbits within the self-consistent potential structure of a two-cylinder system. The square and circle indicate the source and interrogation points of the orbits, respectively. The total ion energy (potential plus kinetic) is indicated above each plot in terms of the electron temperature (in units of eV). Intersections with the background mesh are marked with small dots.

maximum number of radial oscillations set for this simulation, which was $M_{\text{rosc}} = 20$.

4.3.3 Inspection of the 2-D Sheath Structure

We now consider the general aspect of the sheath structure surrounding both cylinders for a few values of the center-to-center spacing: $\Delta x = 2\lambda_{\text{De}}, 10\lambda_{\text{De}}, 20\lambda_{\text{De}}, 40\lambda_{\text{De}}, 80\lambda_{\text{De}}$, and $160\lambda_{\text{De}}$. First, we note that all of the two-cylinder simulations presented here were performed using two axes of symmetry, as described in Section 2.6.2.2. In other words, only a single quadrant had to be simulated, thanks to the symmetry of the two-cylinder geometry and the fact that the plasma is not flowing. The distributions are shown over two quadrants, in order to clearly illustrate the two-cylinder geometry under consideration. The simulation results, performed in the quadrant $\theta \in [0, \pi/2]$, were simply “mirrored” to the second quadrant in $\theta \in [\pi/2, \pi]$. We have opted to only show the results in the half-space $\theta \in [0, \pi]$, so that the features of interest near the cylinders can be clearly seen. All of the distributions shown in Figures 4.16 through 4.25 are given in the following two formats:

- 2-D distributions are shown on the left, over the half-space $\theta \in [0, \pi]$;
- profiles of cross-sections performed along the x axis are shown on the right.

The self-consistency of the solutions that we show here can be verified by comparing the distributions for $\vec{\rho}_{\text{in}}$ and $\vec{\rho}_{\text{out}}$, which correspond to the input and output of the Poisson–Vlasov operator as specified in Figure 2.3. The distributions for $\vec{\rho}_{\text{in}}$ and $\vec{\rho}_{\text{out}}$ shown in Figures 4.16, 4.18, 4.20, 4.22, 4.24, and 4.26, are very close to one another, which proves the self-consistent nature of the solutions.

Figures 4.16 and 4.17 show the distributions pertaining to the smallest center-to-center spacing, $\Delta x = 2\lambda_{\text{De}}$ (cylinders touching). Due to the proximity of the two cylinders, the profiles obtained are very close to what would be obtained with a single cylinder. The ion density, shown in Figure 4.17(b), is seen to drop to half the ambient density on the

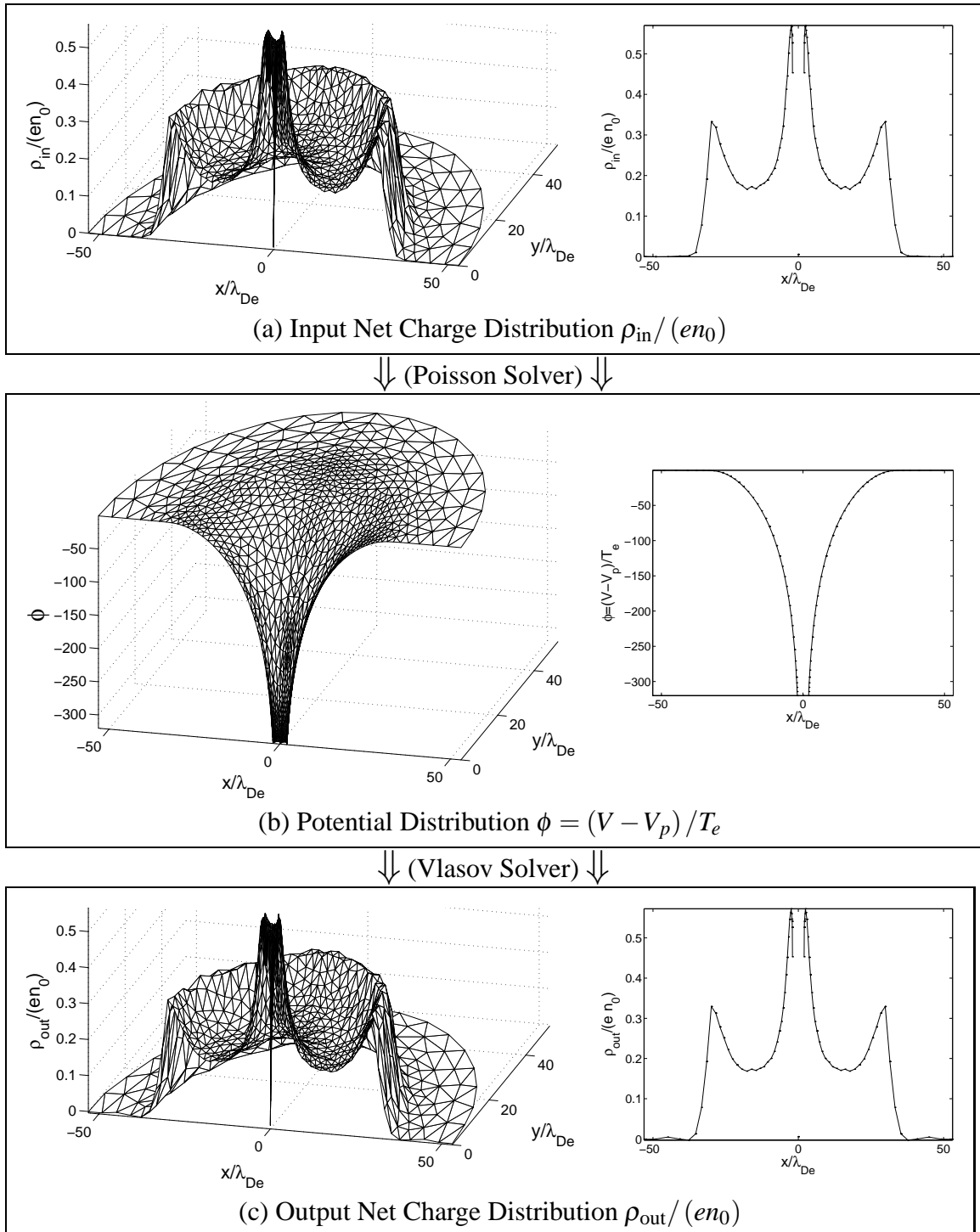


Figure 4.16: Poisson–Vlasov consistent solution for the two-cylinder configuration with a cylinder radius $r_0 = \lambda_{\text{De}}$, center-to-center spacing $\Delta x = 2\lambda_{\text{De}}$, and normalized bias $\phi_0 = -320$. 2-D solutions are shown on the left, and corresponding x -axis cross-section profiles are shown on the right. Ion and Electron density dist. are shown in Figure 4.17.

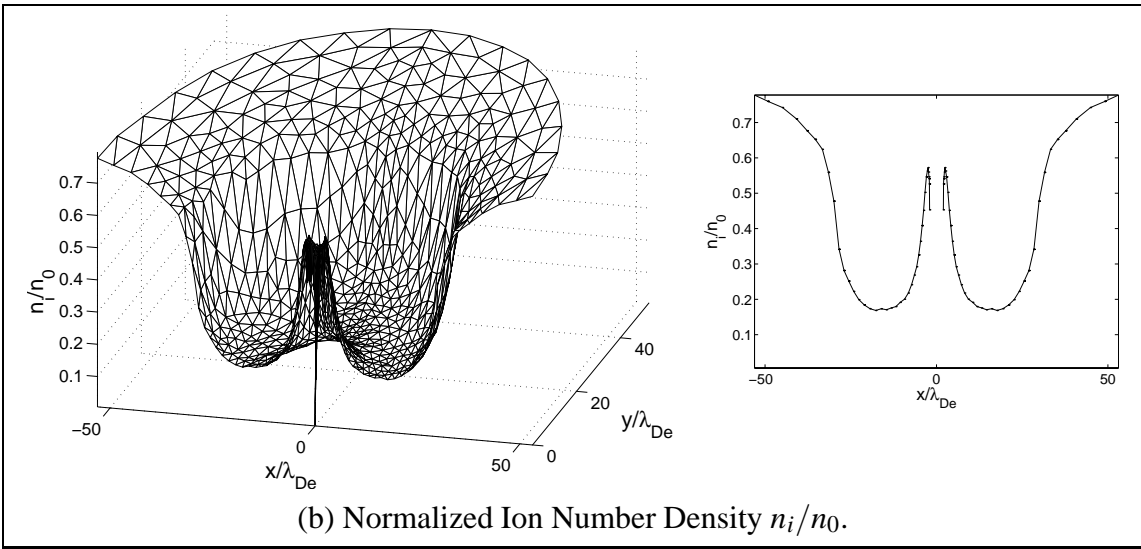
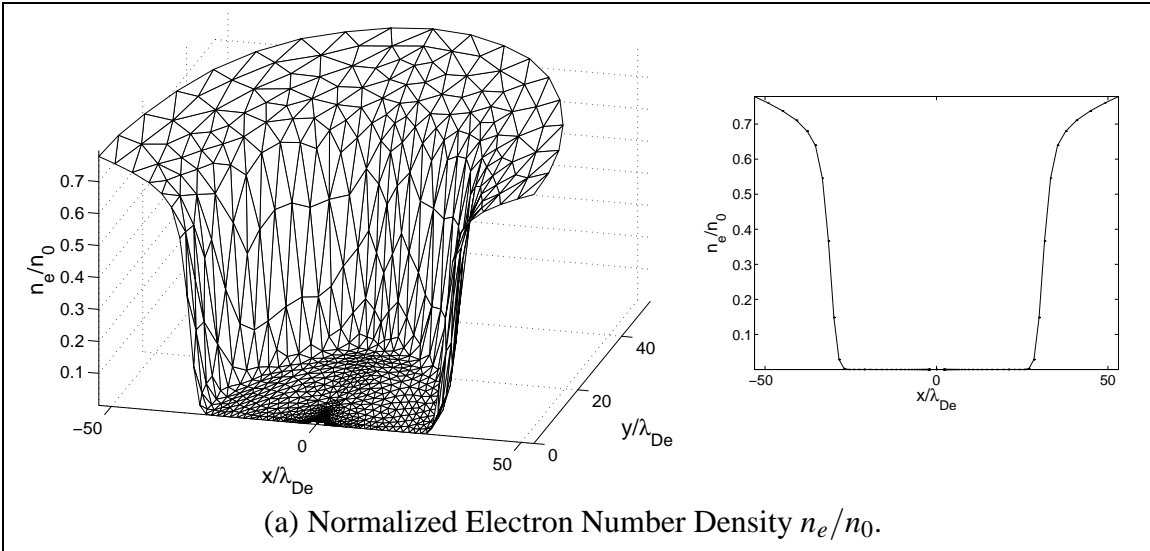


Figure 4.17: Poisson–Vlasov consistent electron and ion density distributions corresponding to the solution shown in Figure 4.16 ($r_0 = \lambda_{\text{De}}$, $\phi_0 = -320$, $\Delta x = 2\lambda_{\text{De}}$). These density profiles constitute the output of the Vlasov solver and are subtracted to form the output net charge density profile $\vec{\rho}_{\text{out}} = e(n_i - n_e)$ shown in Figure 4.16(c).

external surfaces of both cylinders, as is expected. Angular momentum limitations/ion radial acceleration are responsible for the significant drop in density as the ions enter the sheath, similar to what was seen in the single-cylinder case.

Figures 4.18 and 4.19 pertain to the spacing $\Delta x = 10\lambda_{De}$. The potential is seen to drop in magnitude in between the two cylinders, to a potential $\phi \approx -235$ from a bias potential of $\phi_0 = -320$. A similar drop of the ion density is seen in Figure 4.19(b) as the ions enter the sheath, with a minimum density of about $0.2n_0$. A relatively large ion density is seen to exist in between the two cylinders, which reaches a maximum of about $0.7n_0$ but only has limited extent. The ion density at the surfaces of the cylinders is seen to be much lower here than what was seen for the case where the cylinders are touching. The ion densities on the external and internal surfaces of the cylinders are about $0.27n_0$ and $0.19n_0$, respectively. This is an indication that the orbital-motion-limit was not achieved for current collection, due to the overall extent of this “two-cylinder” probe. The center-to-center spacing is not quite large enough for the two sheaths to have separated, so that the two cylinders are in effect emulating a larger structure, leading to reduced current collection, similar to what was seen for large cylinder radii in Figure 4.5.

Figures 4.20 and 4.21 pertain to the spacing $\Delta x = 20\lambda_{De}$. Here the potential is seen to drop down in magnitude to $\phi \approx -150$ in between the two cylinders; the electric fields from both cylinders are still strongly coupling. The ion density profile presents various “bumps” as we enter the sheath, which may be due to the partial filling of some of the velocity space’s directions that were left empty in the single-cylinder case due to angular momentum restrictions. Some of these directions are being populated by the complex trajectories described in Section 4.3.2. Those “bumps” may also be attributed, in part, to some momentum inaccuracies on some of the convoluted ion trajectories, due to the piecewise-linear approximation used for the potential structure. The ion acceleration through the sheath still results in a

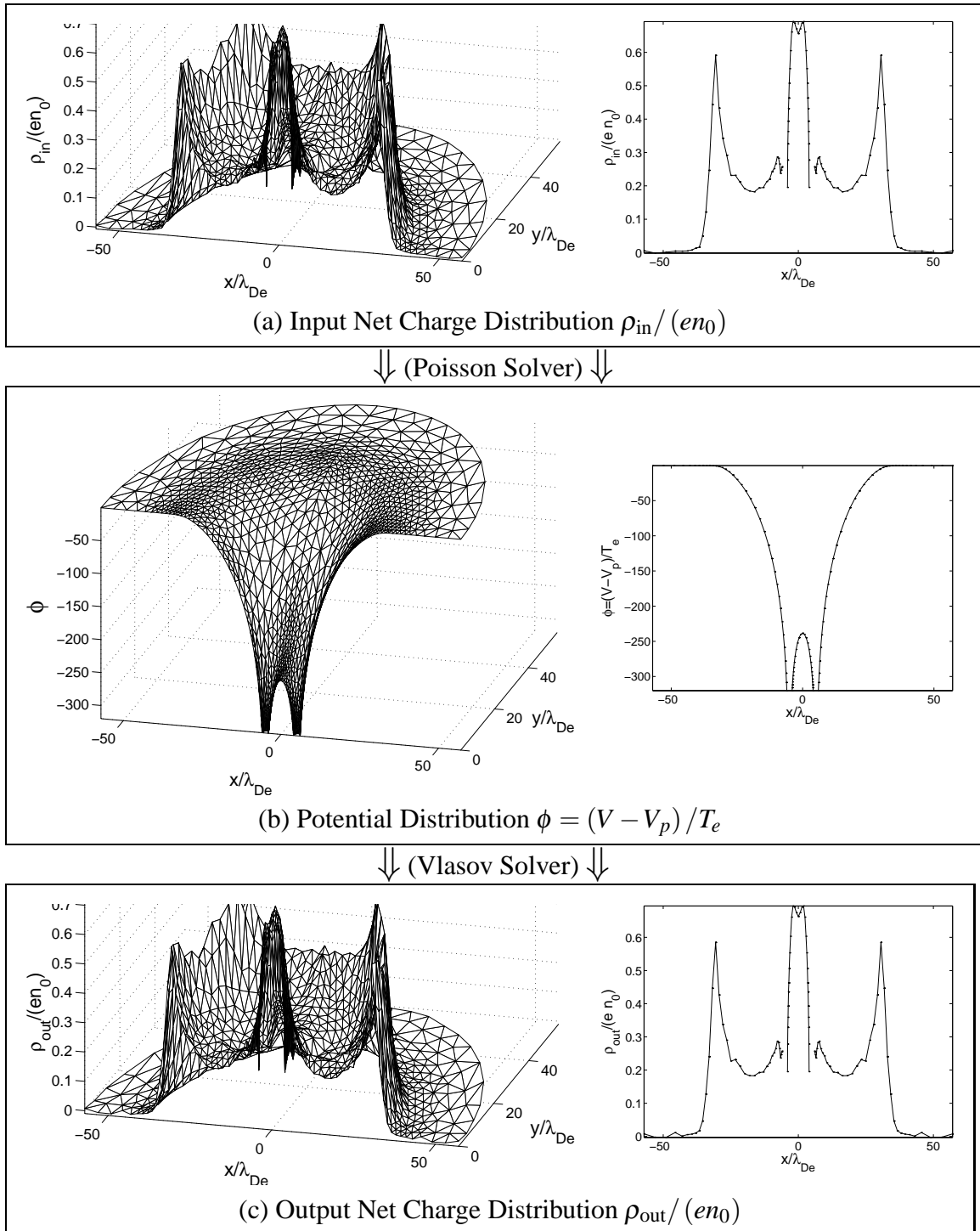


Figure 4.18: Poisson–Vlasov consistent solution for the two-cylinder configuration with a cylinder radius $r_0 = \lambda_{\text{De}}$, center-to-center spacing $\Delta x = 10\lambda_{\text{De}}$, and normalized bias $\phi_0 = -320$. 2-D solutions are shown on the left, and corresponding x -axis cross-section profiles are shown on the right. Ion and Electron density dist. are shown in Figure 4.19.

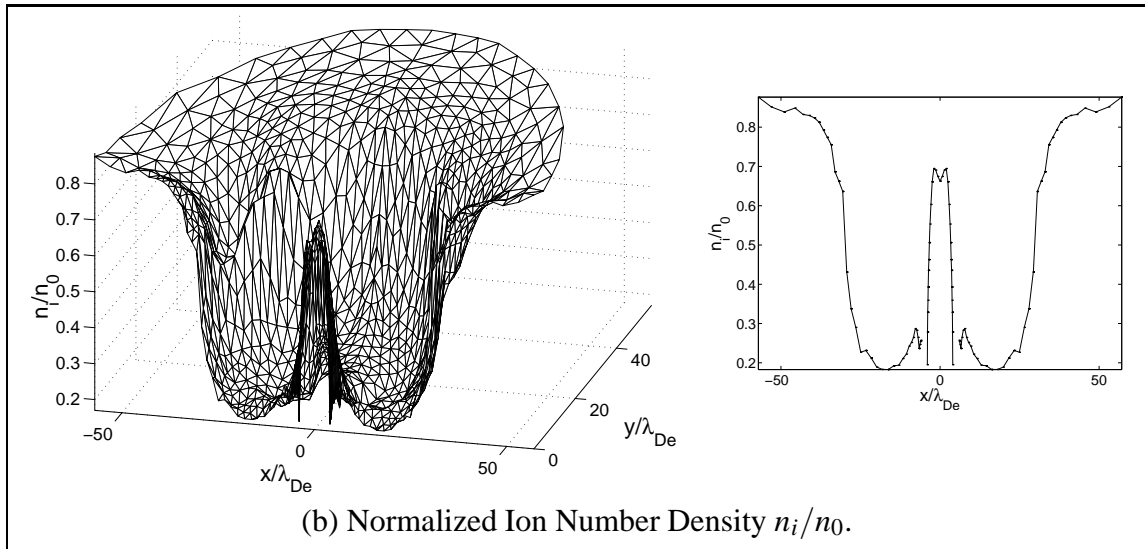
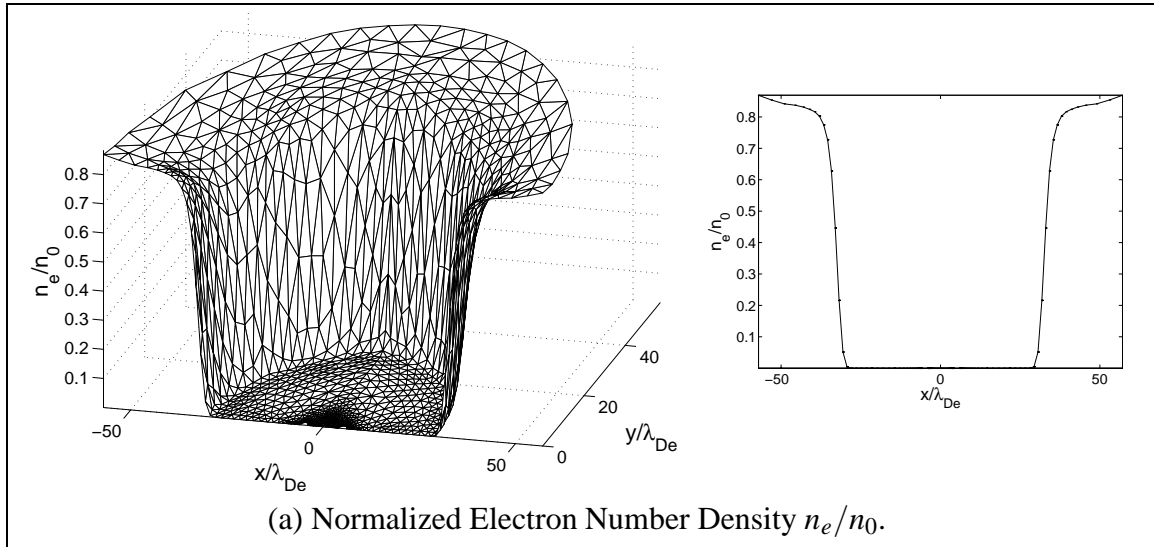


Figure 4.19: Poisson–Vlasov consistent electron and ion density distributions corresponding to the solution shown in Figure 4.18 ($r_0 = \lambda_{De}$, $\phi_0 = -320$, $\Delta x = 10\lambda_{De}$). These density profiles constitute the output of the Vlasov solver and are subtracted to form the output net charge density profile $\vec{\rho}_{\text{out}} = e(n_i - n_e)$ shown in Figure 4.18(c).

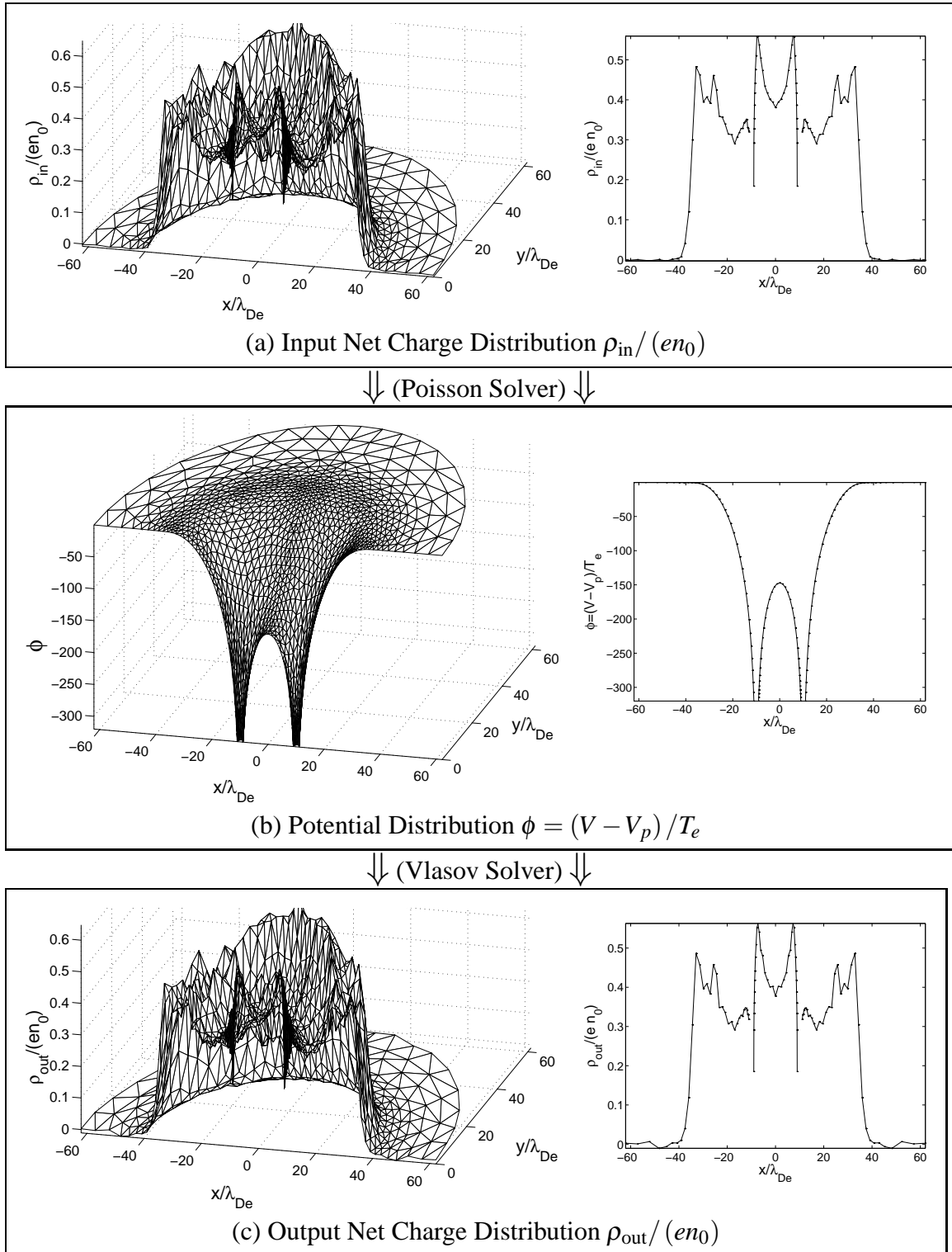


Figure 4.20: Poisson–Vlasov consistent solution for the two-cylinder configuration with a cylinder radius $r_0 = \lambda_{De}$, center-to-center spacing $\Delta x = 20\lambda_{De}$, and normalized bias $\phi_0 = -320$. 2-D solutions are shown on the left, and corresponding x -axis cross-section profiles are shown on the right. Ion and Electron density dist. are shown in Figure 4.21.

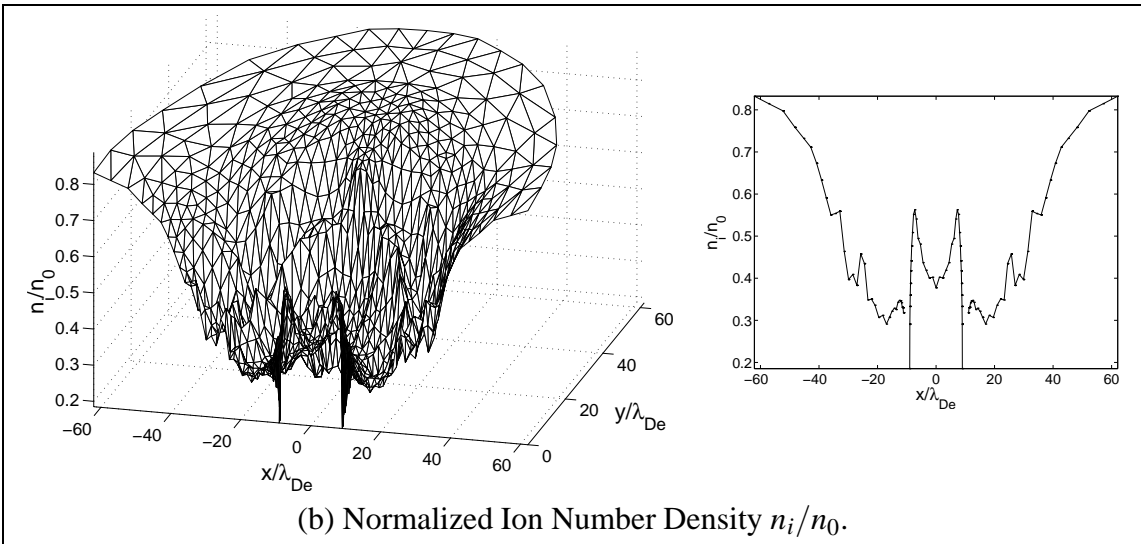
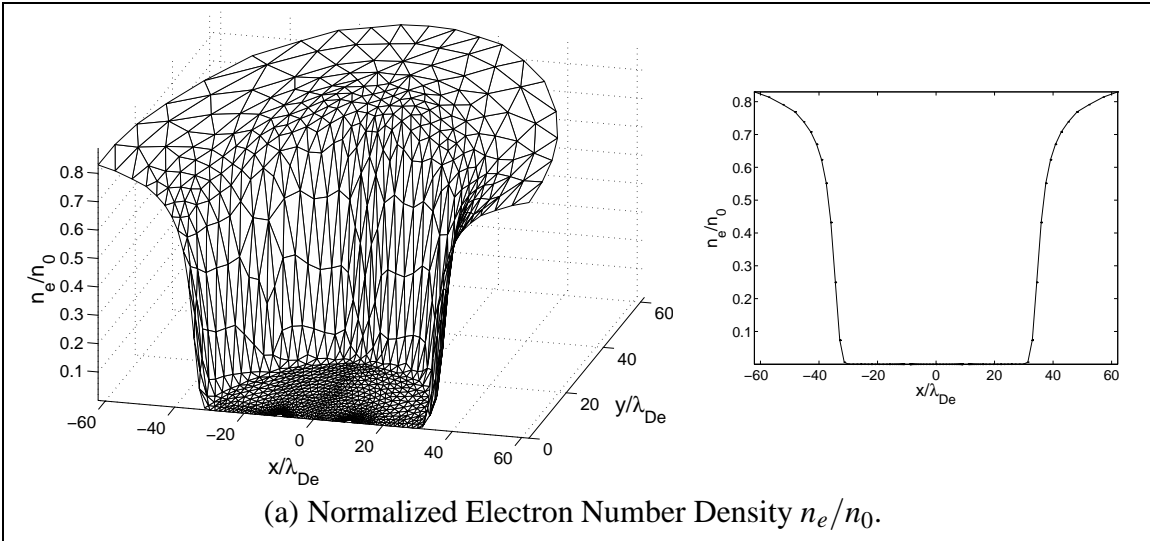


Figure 4.21: Poisson–Vlasov consistent electron and ion density distributions corresponding to the solution shown in Figure 4.20 ($r_0 = \lambda_{De}$, $\phi_0 = -320$, $\Delta x = 20\lambda_{De}$). These density profiles constitute the output of the Vlasov solver and are subtracted to form the output net charge density profile $\vec{\rho}_{out} = e(n_i - n_e)$ shown in Figure 4.20(c).

significant drop of the ion density, albeit for a somewhat smaller range of distances from the cylinder's surface. The ion density at the surface is still well below the orbital motion limit: we have $n_i \approx 0.2n_0$ on the inside surface and $n_i \approx 0.3n_0$ on the outside surface. We can therefore still expect a significant current reduction as compared to the OML limit. The peak in ion density previously seen for $\Delta x = 10\lambda_{De}$ has dropped to about $n_i \approx 0.58n_0$, as the sheath has begun to separate into two separate sheaths, which causes some restrictions of the angular momentum with respect to each cylinder's axis.

Figures 4.22 and 4.23 pertain to the spacing $\Delta x = 40\lambda_{De}$. The magnitude of the potential in between both cylinders has now dropped significantly, to $\phi \approx -24$, which is still sufficient to fully blow away the electrons from a large region formed by the accretion of two overlapping disk-shaped sheaths. The ion density has similar features as those observed for $\Delta x = 20\lambda_{De}$, i.e., the density has some “bumps” as we enter the sheath.

Figures 4.24 and 4.25 pertain to the spacing $\Delta x = 80\lambda_{De}$. At this large spacing, the two cylindrical sheaths have now separated, and the electron density now peaks at above half of the ambient density in between the two cylinders. We begin to distinguish a net charge distribution which features two structures resembling the net charge distribution around a single independent cylinder, except for some remaining strong asymmetry. This asymmetry remains in spite of the fact that the surface charges located on one cylinder practically no longer contribute to the electric fields within the sheath around the other cylinder. Rather than being due to a direct field coupling, the remaining asymmetry is due to the fact that some velocity space directions in the sheath around one cylinder are left unpopulated because their corresponding trajectories originate from the surface of the other cylinder. This effect can be significant because of the focusing effect between the two sheaths which concentrates trajectories toward the inside of the sheath even as they are moved apart significantly. The asymmetries are also amplified by the changes that

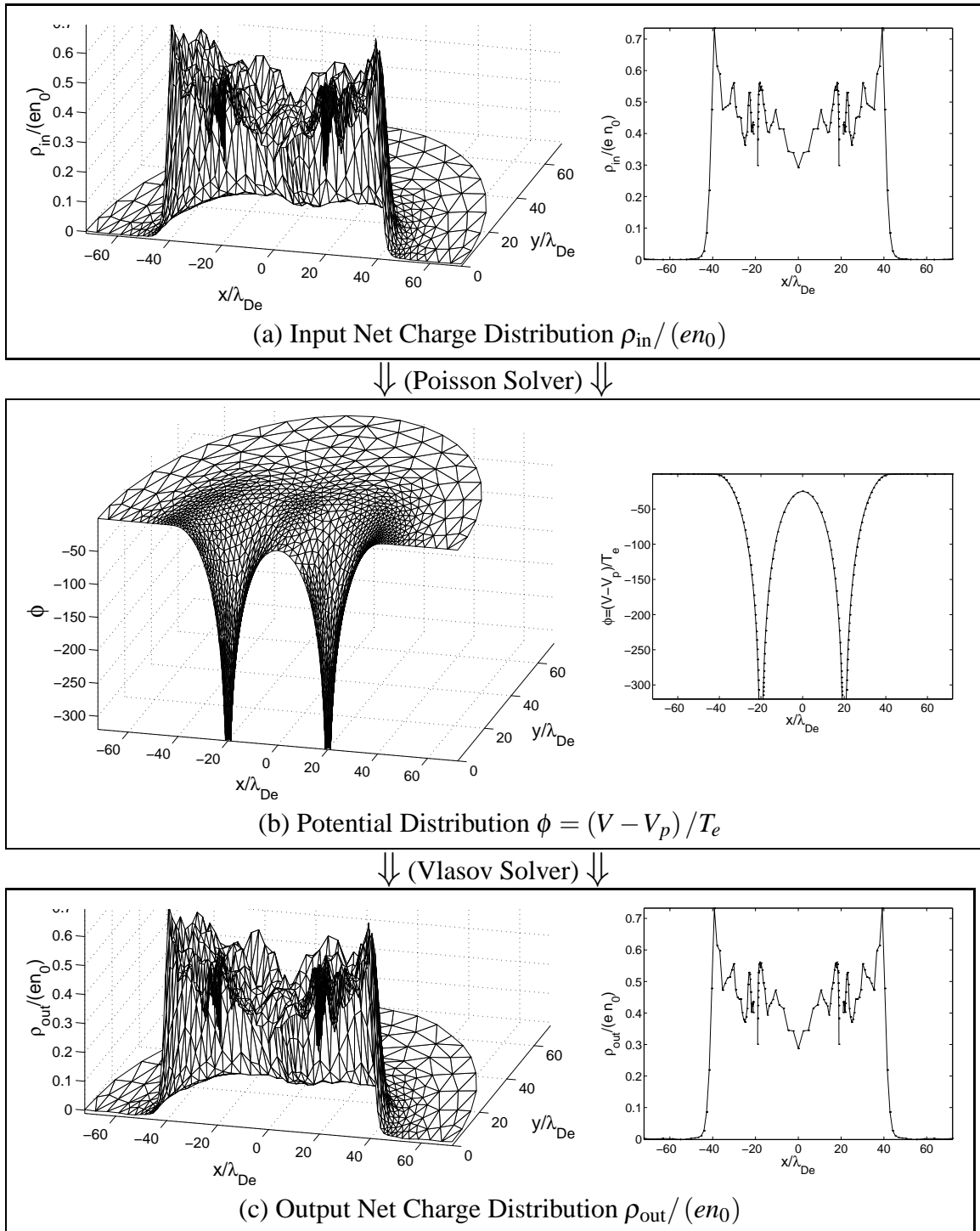


Figure 4.22: Poisson–Vlasov consistent solution for the two-cylinder configuration with a cylinder radius $r_0 = \lambda_{\text{De}}$, center-to-center spacing $\Delta x = 40\lambda_{\text{De}}$, and normalized bias $\phi_0 = -320$. 2-D solutions are shown on the left, and corresponding x -axis cross-section profiles are shown on the right. Ion and Electron density dist. are shown in Figure 4.23.

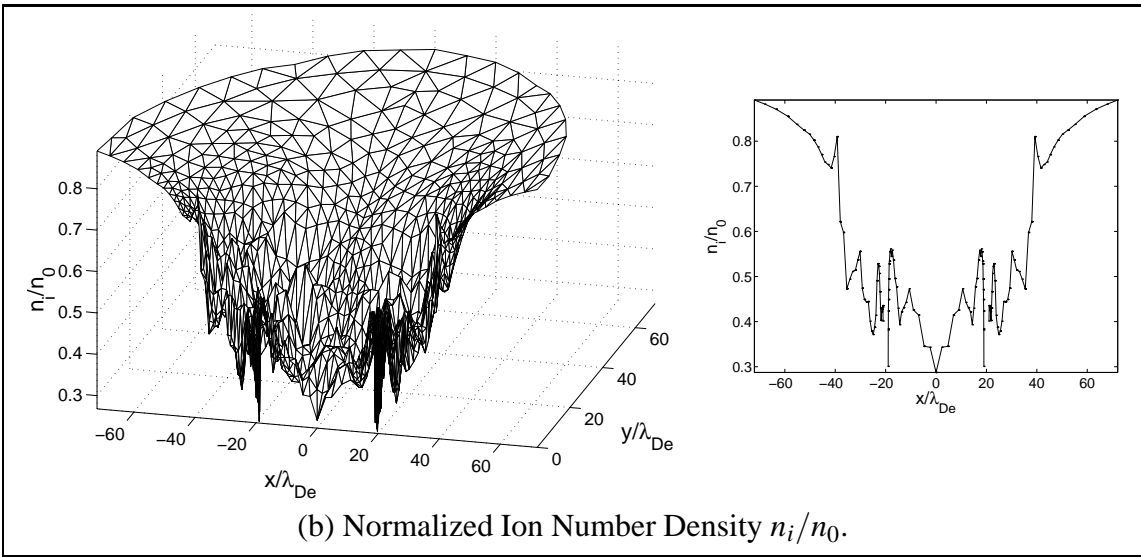
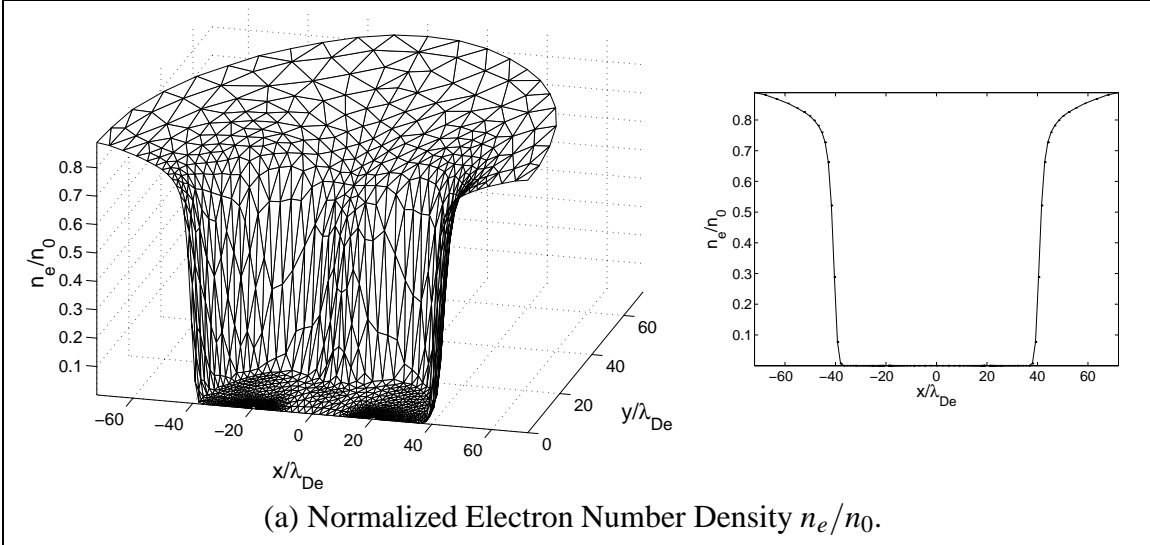


Figure 4.23: Poisson–Vlasov consistent electron and ion density distributions corresponding to the solution shown in Figure 4.22 ($r_0 = \lambda_{\text{De}}$, $\phi_0 = -320$, $\Delta x = 40\lambda_{\text{De}}$). These density profiles constitute the output of the Vlasov solver and are subtracted to form the output net charge density profile $\vec{\rho}_{\text{out}} = e(n_i - n_e)$ shown in Figure 4.22(c).

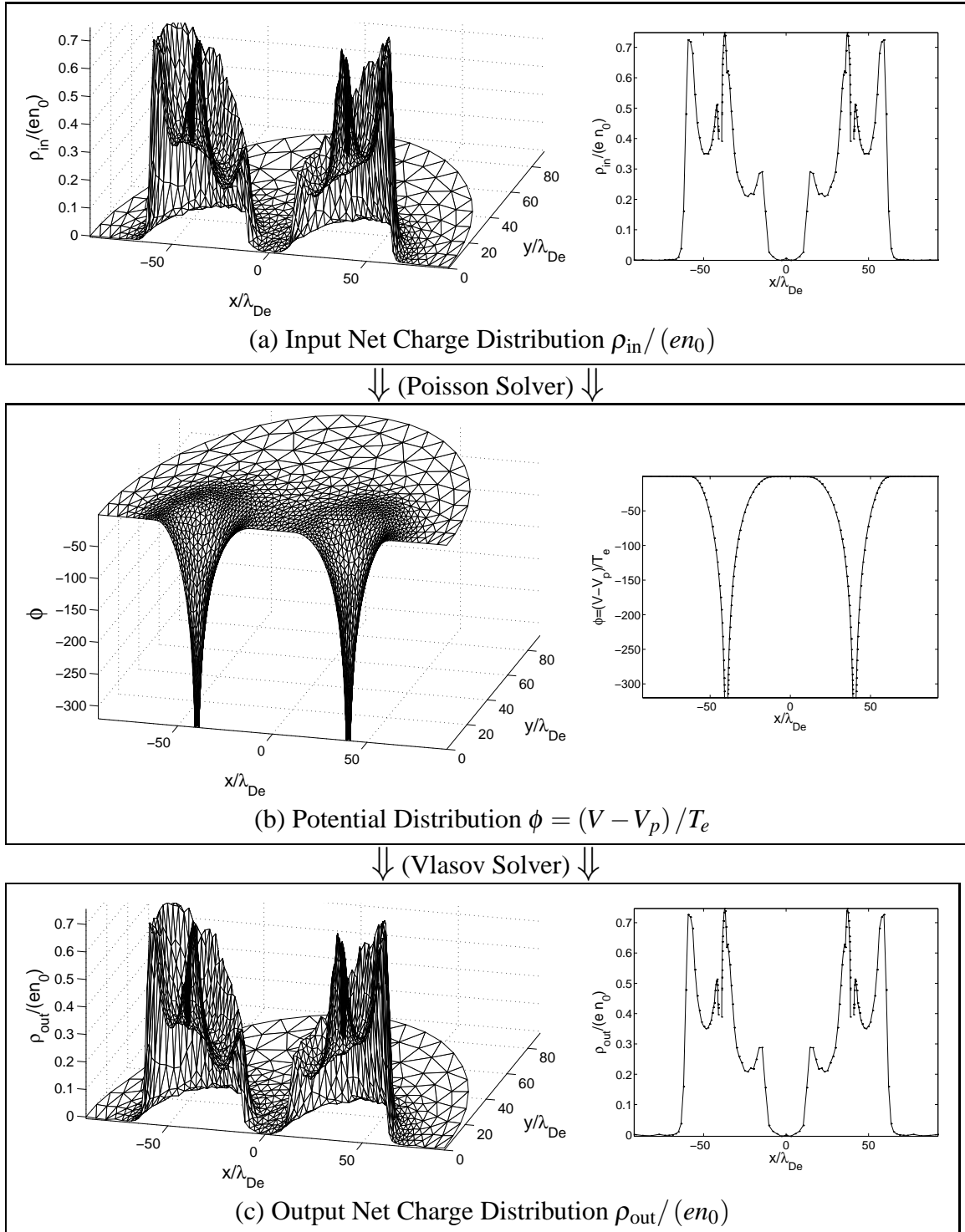


Figure 4.24: Poisson–Vlasov consistent solution for the two-cylinder configuration with a cylinder radius $r_0 = \lambda_{\text{De}}$, center-to-center spacing $\Delta x = 80\lambda_{\text{De}}$, and normalized bias $\phi_0 = -320$. 2-D solutions are shown on the left, and corresponding x -axis cross-section profiles are shown on the right. Ion and Electron density dist. are shown in Figure 4.25.

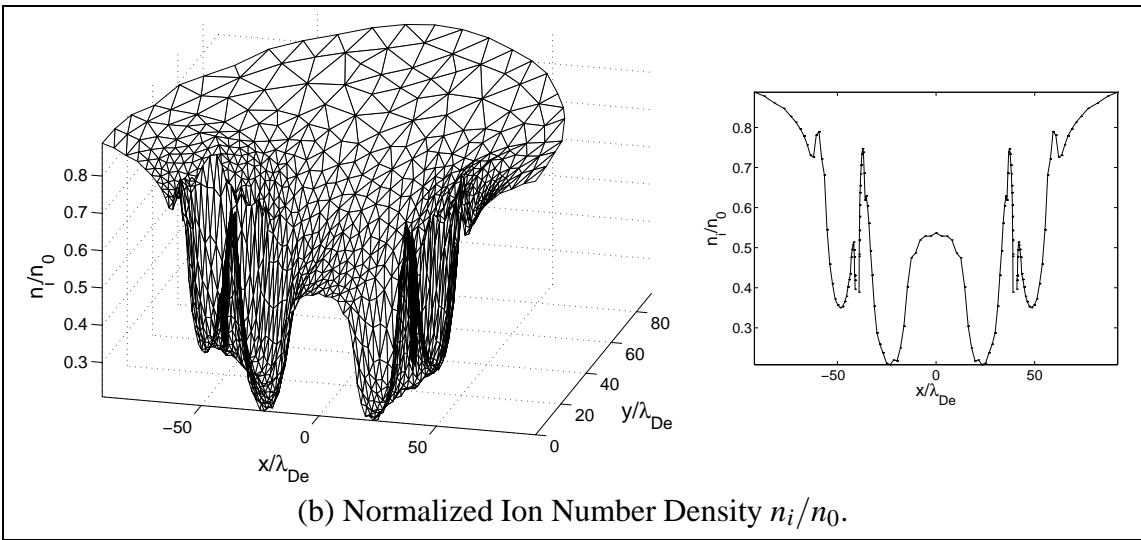
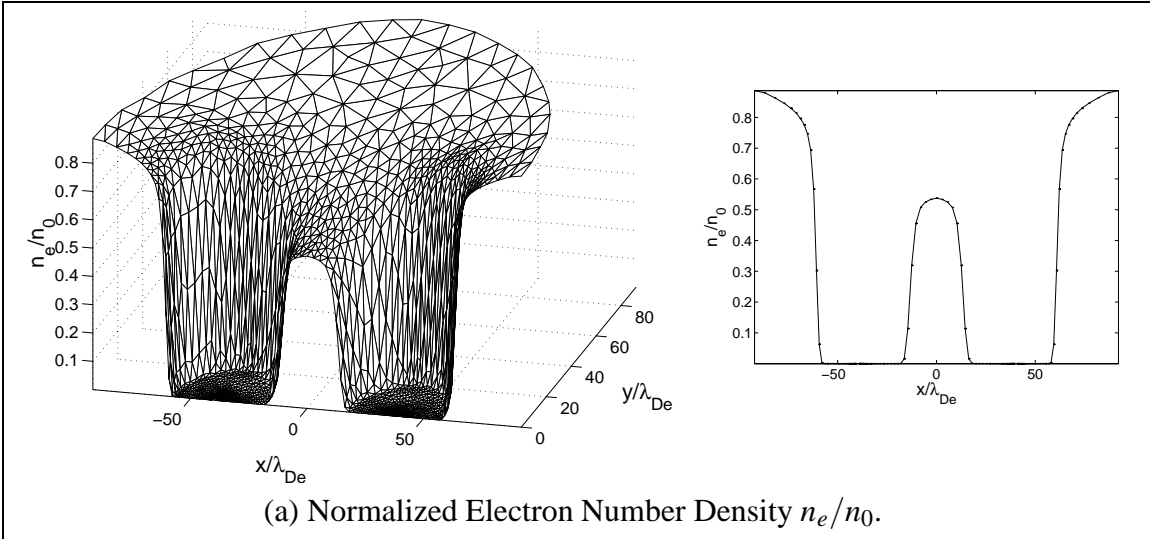


Figure 4.25: Poisson–Vlasov consistent electron and ion density distributions corresponding to the solution shown in Figure 4.24 ($r_0 = \lambda_{\text{De}}$, $\phi_0 = -320$, $\Delta x = 80\lambda_{\text{De}}$). These density profiles constitute the output of the Vlasov solver and are subtracted to form the output net charge density profile $\vec{\rho}_{\text{out}} = e(n_i - n_e)$ shown in Figure 4.24(c).

they induce in the population of the orbits that are normally “trapped and unpopulated” in the case of an independent cylinder. The ion density profile seen in Figure 4.25 shows two familiar patterns resembling the ion density profile that we have found for a single independent cylinder, albeit with some asymmetry. The ion density reaches a value of about $0.54n_0$ on the x axis in between the two cylinders. We observe that this is a significantly lower density than would be observed at such a large distance from an independent cylinder (about $0.75n_0$). The asymmetry however causes some increase of the “outside” density profile, where we observe a “bump”.

Figures 4.26 and 4.27 pertain to the spacing $\Delta x = 160\lambda_{De}$. Now the two sheaths are definitely not coupling through electric fields as can be seen from the potential profile which goes to virtually zero for a distance of almost 100 Debye lengths. The asymmetry however still remains. It is attributed, as discussed before, to the voids created in the ion densities in one sheath by the shadowing effect of the cylinder in the other sheath, amplified by its effect on unpopulated orbits.

The observations that we have made concerning the wider separations can be summarized as follows:

1. the ion densities on the outermost side of a given cylinder are somewhat increased by the potential asymmetries caused by the trajectory connections among both sheaths;
2. the ion densities on the innermost side of a given cylinder are somewhat decreased due to the unpopulated trajectories originating from the surface of the other cylinder.

While the first observation may lead to a decrease of the effective sheath radius as measured on the outermost side as compared to that of an independent cylinder, the second observation may cause an increase of the “inner” effective sheath radius. The overall outcome of these two competing effects is difficult to predict. We will assess it in the following two

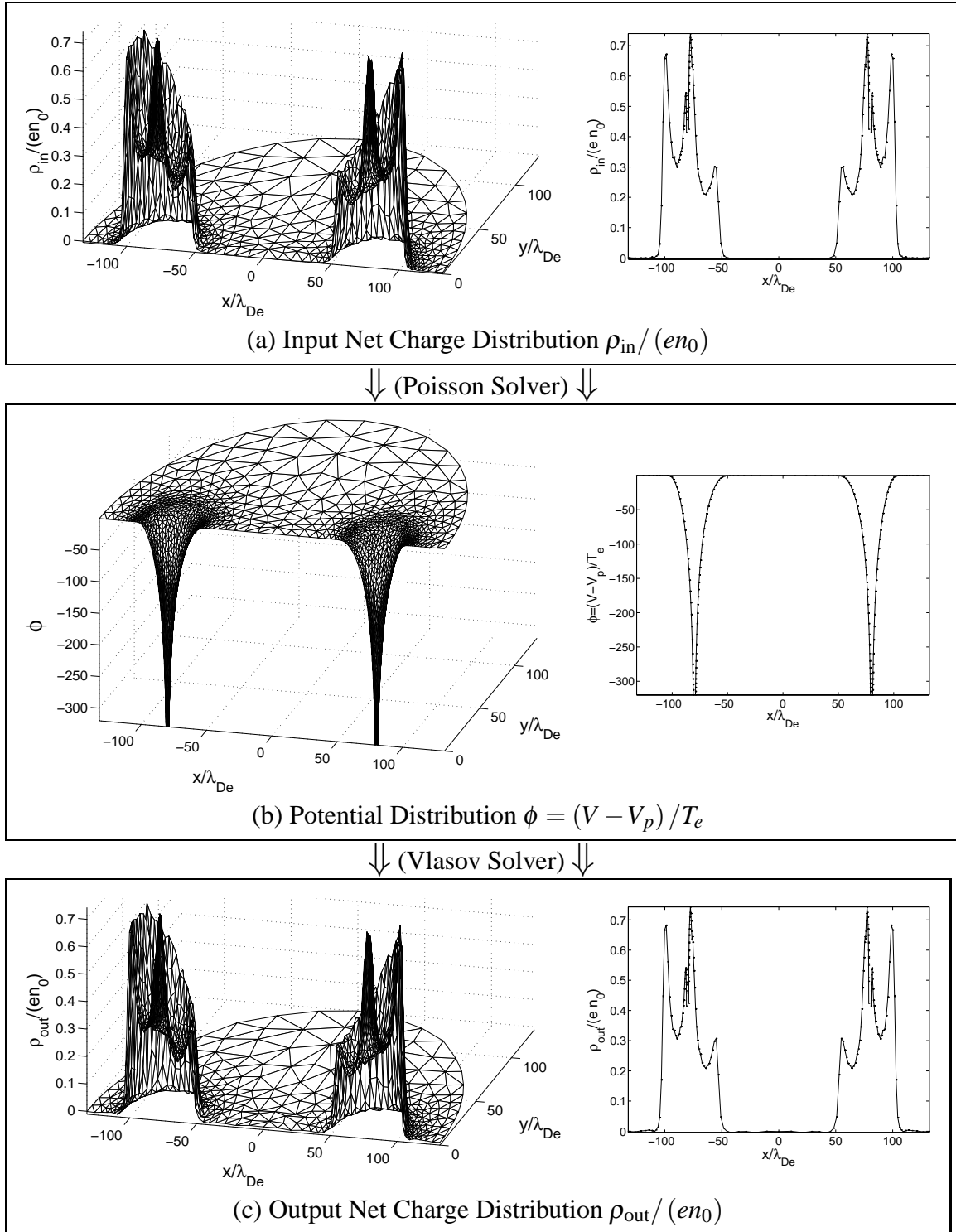


Figure 4.26: Poisson–Vlasov consistent solution for the two-cylinder configuration with a cylinder radius $r_0 = \lambda_{\text{De}}$, center-to-center spacing $\Delta x = 160\lambda_{\text{De}}$, and normalized bias $\phi_0 = -320$. 2-D solutions are shown on the left, and corresponding x -axis cross-section profiles are shown on the right. Ion and Electron density dist. are shown in Figure 4.27.

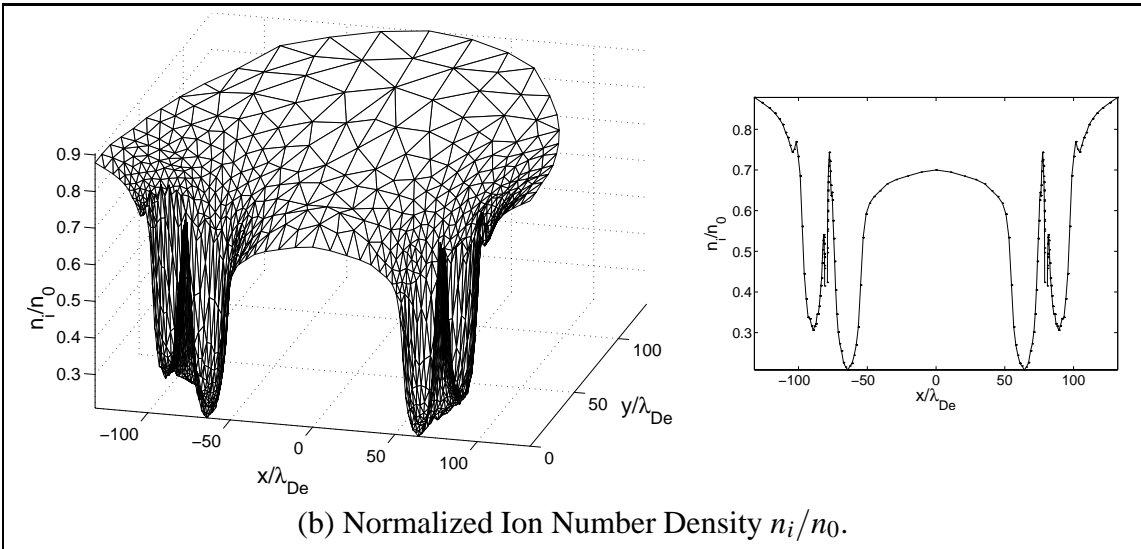
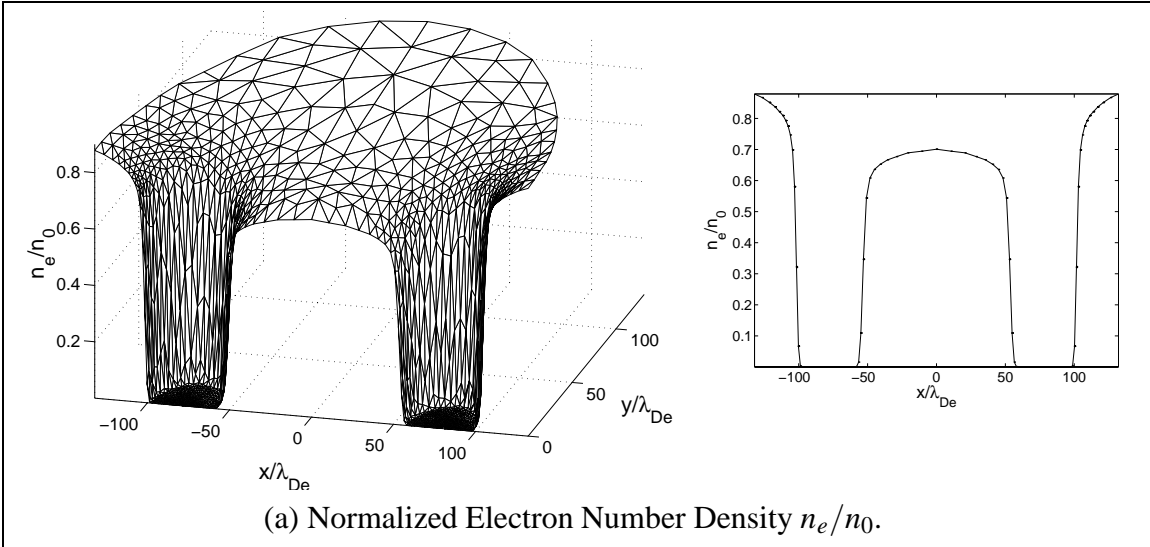


Figure 4.27: Poisson–Vlasov consistent electron and ion density distributions corresponding to the solution shown in Figure 4.26 ($r_0 = \lambda_{\text{De}}$, $\phi_0 = -320$, $\Delta x = 160\lambda_{\text{De}}$). These density profiles constitute the output of the Vlasov solver and are subtracted to form the output net charge density profile $\vec{\rho}_{\text{out}} = e(n_i - n_e)$ shown in Figure 4.26(c).

sections based on a more general measure of the sheath dimensions, the *effective sheath area*.

4.3.4 Definition of an *Effective Sheath Area* Concept

In Section 4.2.4.1 we have defined a metric for the effective sheath radius r_s consistent with the asymptotic form of the potential profile given by (4.13), which applies for the symmetric sheath structure in the vicinity of a round cylinder. We now seek to generalize the concept of effective sheath radius for use with non-symmetric sheaths, while providing a metric consistent with that used for round cylinders.

Let us first consider a sheath with circular symmetry, for which (4.13) applies. We may define an *effective sheath area* A_s consistent with our previous definition of the *effective sheath radius* r_s based on the relationship

$$A_s = \pi r_s^2, \quad (4.22)$$

where we include the area of the cylinder itself as part of the effective sheath area. Similarly, we define

$$A = \pi r^2 \quad \text{and} \quad A_0 = \pi r_0^2, \quad (4.23)$$

where A is the area enclosed by any equipotential circle of radius r , and A_0 is the cylinder's cross sectional area. Using (4.22) and (4.23), we re-write the potential profile given by (4.13) in terms of A_s , A and A_0 :

$$\phi = \phi_0 \left(1 - \frac{\ln(A/A_0)}{\ln(A_s/A_0)} \right). \quad (4.24)$$

This asymptotic relationship, relating the potential on any contour level to the area it encloses, holds from the surface of the cylinder out to a fairly large radius r (or area A). In the case shown in Figure 4.6, the asymptotic approximation is a good approximation until we reach a radius of about $r = 175\lambda_{De}$, or until the enclosed area reaches about $A = 175^2\pi^2\lambda_{De}^2$.

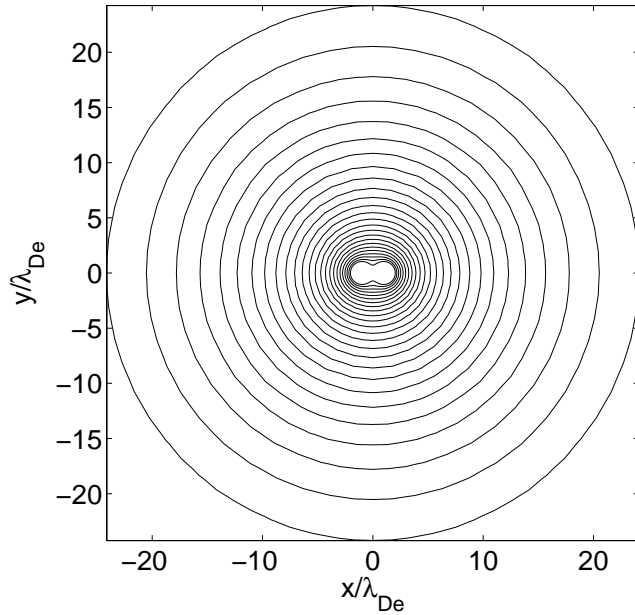
We may now generalize (4.24) to any type of sheath structure, by considering the variation of the potential ϕ as a function of the area A enclosed within the corresponding contour level, and finding an appropriate measure of the sheath area A_s based on some asymptotic behavior of the ϕ -vs- A plot. As was just demonstrated, in the case of the single round cylinder, this definition will provide us with a measure for the effective sheath area A_s consistent with the effective sheath radius r_s that was defined in Section 4.2.4.1, i.e., $A_s = \pi r_s^2$.

4.3.5 Determination of the Effective Sheath Area of the Two-Cylinder Configuration

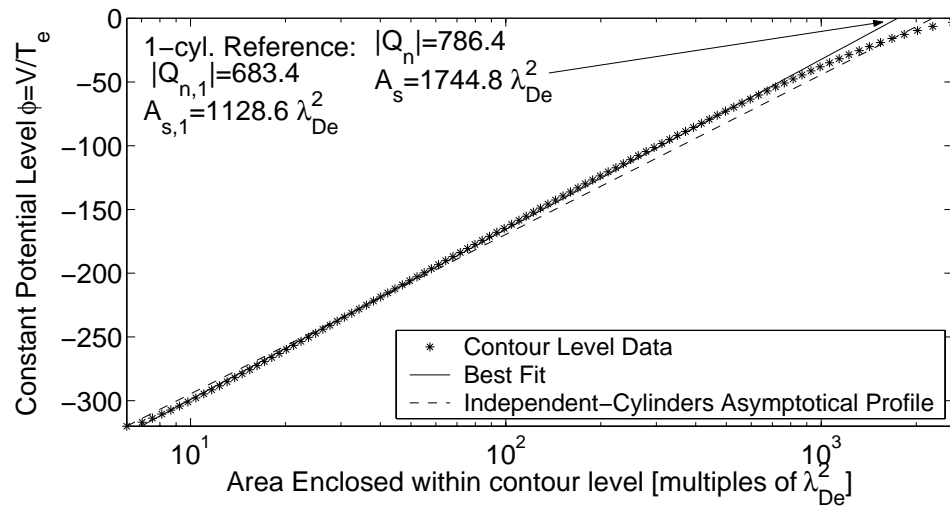
Figures 4.28–4.33 graphically illustrate, for a subset of 6 different center-to-center spacings ($\Delta x \in [2, 10, 20, 40, 80, 160]$), the process that was used to determine an effective sheath area A_s , consistent with the definition given in Section 4.3.4. On each of these figures, part (a) shows a set of equipotential contour levels and part (b) shows a plot of the potential ϕ as a function of the surface area A enclosed by the corresponding contour level. Consistent with the method used for the determination of the *effective sheath radius* performed in Section 4.2.4.1, the *effective sheath area* A_s is determined by the A -intercept¹⁵ of the extrapolated asymptotic behavior of the ϕ -vs- A data. Values for both the single-cylinder effective sheath area $A_{s,1} = \pi r_s^2$ and two-cylinder effective sheath area A_s are given in Figures 4.28–4.33.

The results for the smallest spacing, $\Delta x = 2$, are shown in Figure 4.28. The contours quickly become circular as the potential drops from the cylinders' surfaces. As a consequence, the ϕ -vs- A data shown in Figure 4.28(b) almost immediately follows a logarithmic pattern (which shows as a linear variation on this semi-logarithmic scale), just like would be expected of a single-cylinder structure. This logarithmic relationship is consistent with a negligible effect of the space charge in the vicinity of the two-cylinder structure, and is

¹⁵The A -intercept is defined as the value of A at which the linear graph intersects the A axis.

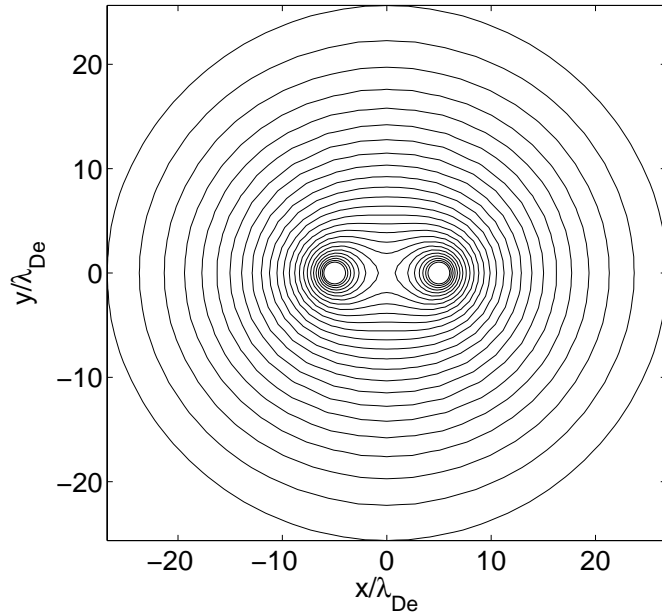


(a) Contour Levels

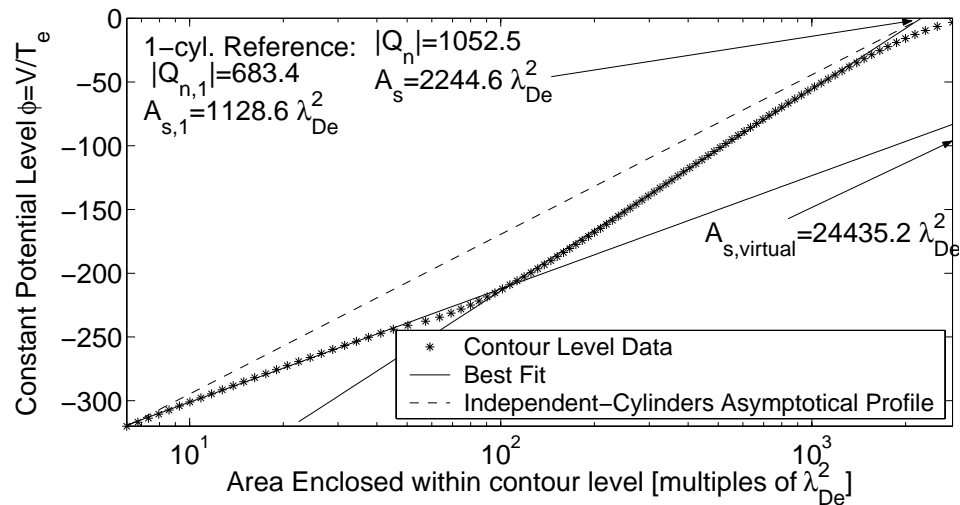


(b) Potential vs Enclosed Area

Figure 4.28: Potential contour levels (a) along with a plot of the contour level as a function of the area enclosed by a given contour (b), for two cylinders with a center-to-center spacing $\Delta x = 2\lambda_{De}$. The cylinder radius is $r_0 = \lambda_{De}$ and both cylinders are biased at a normalized potential $\phi_0 = -320$.

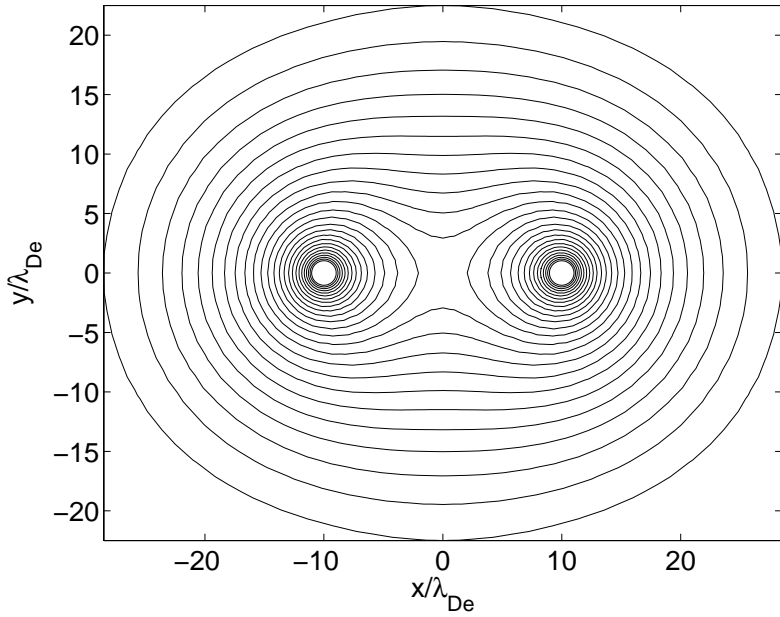


(a) Contour Levels

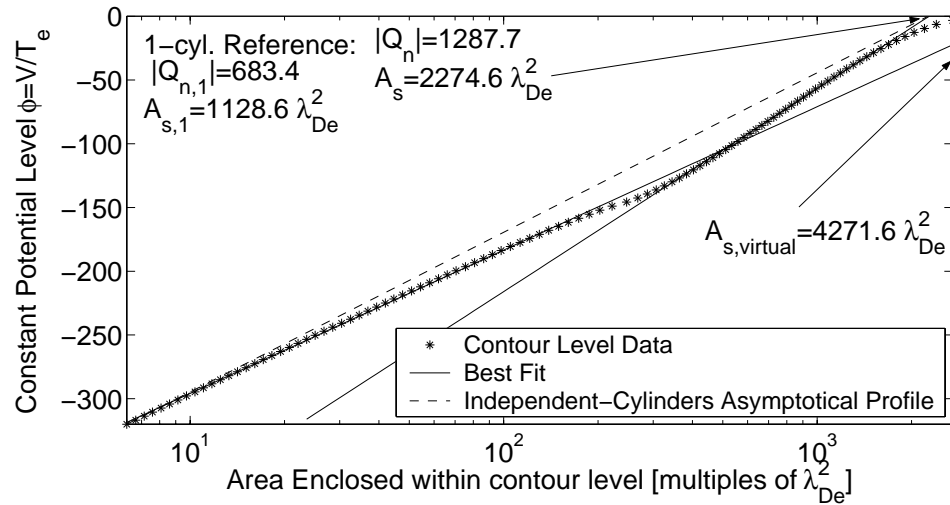


(b) Potential vs Enclosed Area

Figure 4.29: Potential contour levels (a) along with a plot of the contour level as a function of the area enclosed by a given contour (b), for two cylinders with a center-to-center spacing $\Delta x = 10\lambda_{De}$. The cylinder radius is $r_0 = \lambda_{De}$ and both cylinders are biased at a normalized potential $\phi_0 = -320$.

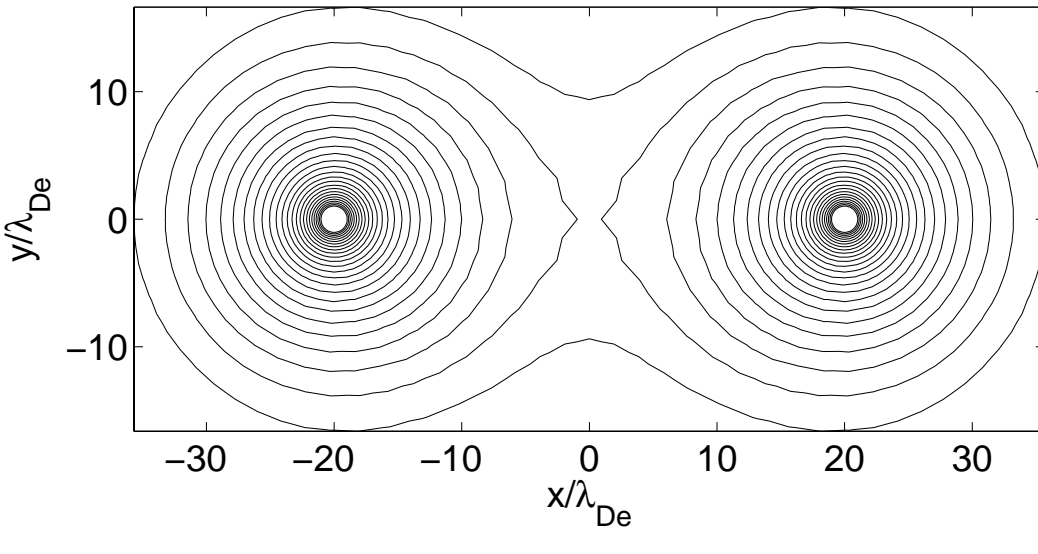


(a) Contour Levels

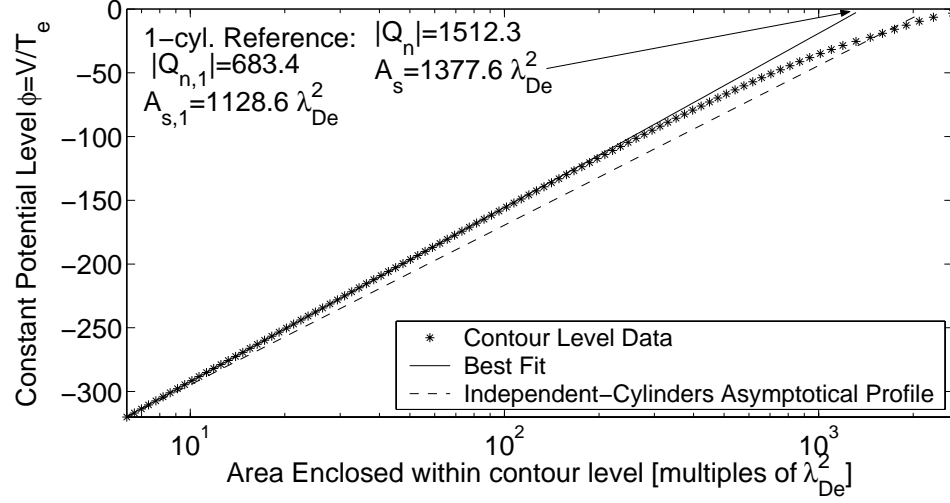


(b) Potential vs Enclosed Area

Figure 4.30: Potential contour levels (a) along with a plot of the contour level as a function of the area enclosed by a given contour (b), for two cylinders with a center-to-center spacing $\Delta x = 20\lambda_{De}$. The cylinder radius is $r_0 = \lambda_{De}$ and both cylinders are biased at a normalized potential $\phi_0 = -320$.

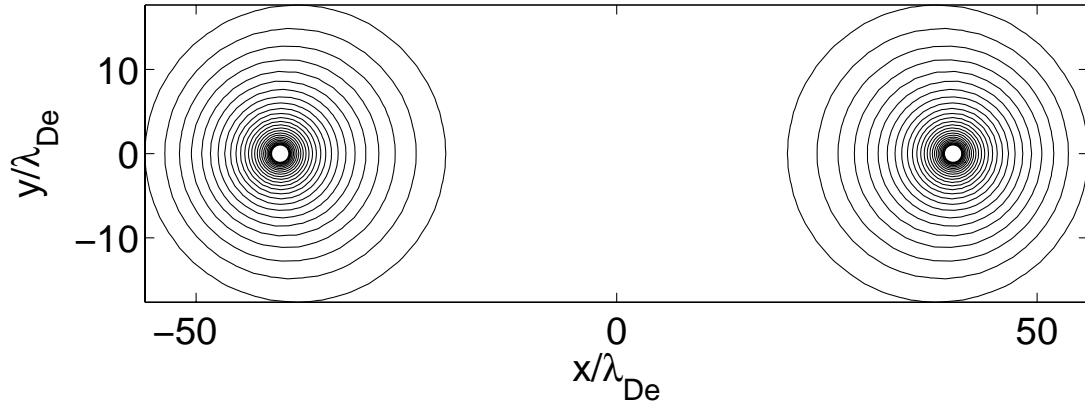


(a) Contour Levels

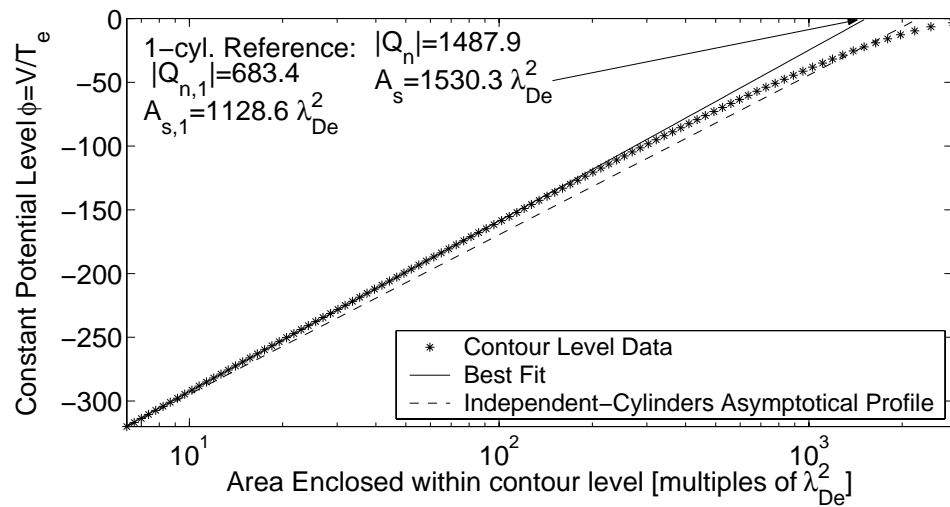


(b) Potential vs Enclosed Area

Figure 4.31: Potential contour levels (a) along with a plot of the contour level as a function of the area enclosed by a given contour (b), for two cylinders with a center-to-center spacing $\Delta x = 40\lambda_{De}$. The cylinder radius is $r_0 = \lambda_{De}$ and both cylinders are biased at a normalized potential $\phi_0 = -320$.

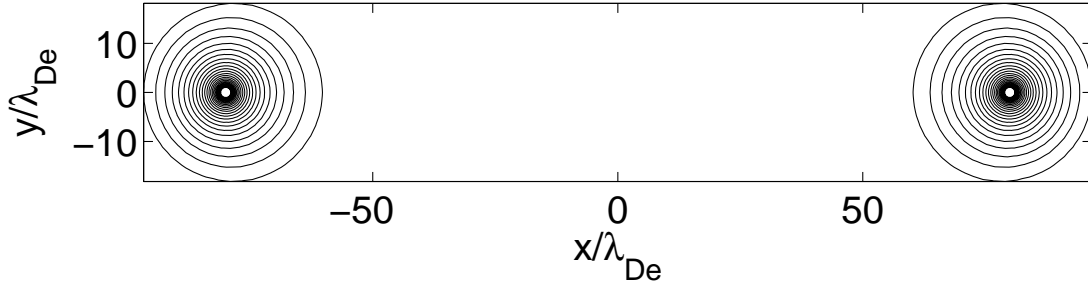


(a) Contour Levels

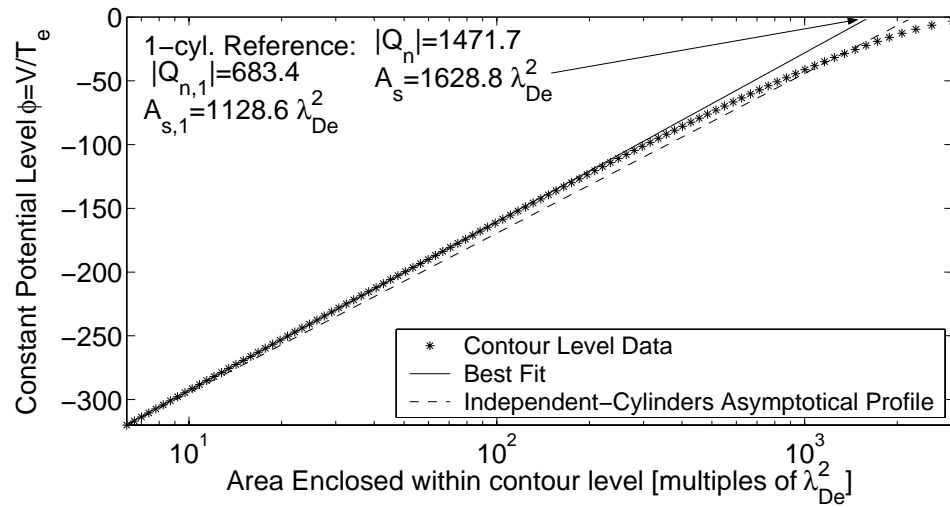


(b) Potential vs Enclosed Area

Figure 4.32: Potential contour levels (a) along with a plot of the contour level as a function of the area enclosed by a given contour (b), for two cylinders with a center-to-center spacing $\Delta x = 80\lambda_{De}$. The cylinder radius is $r_0 = \lambda_{De}$ and both cylinders are biased at a normalized potential $\phi_0 = -320$.



(a) Contour Levels



(b) Potential vs Enclosed Area

Figure 4.33: Potential contour levels (a) along with a plot of the contour level as a function of the area enclosed by a given contour (b), for two cylinders with a center-to-center spacing $\Delta x = 160\lambda_{De}$. The cylinder radius is $r_0 = \lambda_{De}$ and both cylinders are biased at a normalized potential $\phi_0 = -320$.

followed by a “tail” attributed to space charge effects, as was seen in the single-cylinder case. The effective sheath area corresponding to the graphed asymptote is larger than that of a single cylinder, for which the ϕ -vs- A would have fallen logarithmically *immediately* starting at the cylinder’s surface. In the present case, the physical extent of the touching cylinders is sufficiently large to allow them to hold a larger total surface charge than a single cylinder would at that same bias potential, resulting in a 55% increase of the effective sheath size over that of a single cylinder:

$$\frac{A_s}{A_{s,1}} = \frac{1744.8\lambda_{De}^2}{1128.6\lambda_{De}^2} \approx 1.55. \quad (4.25)$$

The effective sheath area is however smaller than the combined sheath area of two independent cylinders.

Upon increasing the center-to-center spacing to $\Delta x = 10$, as shown in Figure 4.29, the semilog graph of the ϕ -vs- A data now shows two distinct linear regions, indicated by separate linear “best fits”. The first linear region (on the left) corresponds to the set of circular contour levels enclosing each cylinder separately. The slope associated with this first region is not as steep as that which would be expected of an independent cylinder, and is consistent with the observed lower amount of normalized surface charge Q_n held separately by each of the cylinders as compared with the surface charge held by an independent cylinder.¹⁶ This lower charge can be attributed to a “virtual” effective sheath edge enclosing an area $A_{s,virtual}$ (shown on the figure to be further out on the right of the graph) that is much larger than the effective sheath area of an independent cylinder. The fact that each cylinder holds a lower amount of surface charge than an independent cylinder is consistent with the large area $A_{s,virtual}$, as is evidenced by the following equation applicable to coaxial capacitors:

$$Q_{n,1} = 4\pi \frac{\phi_0}{\ln(A_{s,1}/A_0)}, \quad (4.26)$$

¹⁶Note that even though the surface charge $Q_n = 1052.5$ shown in Figure 4.29 is larger than the surface charge held by an independent cylinder $Q_{n,1} = 683.4$, the amount of charge held individually by each cylinder, $\frac{1}{2}Q_n = 526.25$, is lower.

where $Q_{n,1}$ is the normalized surface charge held by a cylinder and $A_0 = \pi r_0^2$ is the single-cylinder area. The expression given by (4.26) clearly shows that the surface charge $Q_{n,1}$ goes down with increasing sheath area A_s .

The leftmost linear region extends until we approach a critical point where the equipotential contours of both cylinders connect together to form a single contiguous contour. The ϕ -vs- A data then rapidly switches to the rightmost linear region corresponding to the set of circular contour levels enclosing both cylinders. The effective sheath area of the system is defined as the A -intercept of the rightmost linear fit. In this particular case, it turns out that the sheath area A_s is almost exactly equal to the combined sheath areas of two independent cylinders, i.e., $A_s \approx 2A_{s,1}$.

Space charge effects can be seen at two different locations in Figure 4.29. The first one occurs near the inflection point between both linear regimes, where the ϕ -vs- A data is seen to momentarily drop below the leftmost linear best-fit before it starts growing faster toward the rightmost linear best-fit. This momentary slope reduction is attributed to the shielding effect of space charge, which is having a detectable effect because of the sufficient spacing between the cylinders, where some space charge exists. Beyond the turning point of this graph, the effect of space charge becomes negligible again for a large portion of this outer sheath, until we reach beyond an area $A \approx 1000\lambda_{De}^2$, where we notice the typical tail-like behavior of the potential associated with space charge shielding.

For a center-to-center spacing of $\Delta x = 20\lambda_{De}$, we still observe two linear regimes, as seen in Figure 4.30. The inflection point between both linear regions now occurs at a much larger area, in the vicinity of $A = 500\lambda_{De}^2$. The system capacitance has increased such that the total amount of charge held by both cylinders is now almost equal to that held by two completely independent cylinders, i.e., $\frac{Q_n}{2Q_{n,1}} \cong 0.94$. This explains why the slope of the first linear region has gotten closer to the dashed line which applies to 2 fully independent cylinders.

ders. One might observe that the effective area A_s is essentially unchanged from that seen in the case where $\Delta x = 10\lambda_{De}$, in spite of the significant increase of the surface charge held by the cylinders. This apparent contradiction is resolved when one considers the “virtual” effective sheath area $A_{s,virtual}$, which relates to the potential drop in close proximity of each cylinder, and is much lower for $\Delta x = 20\lambda_{De}$ as compared to the $\Delta x = 10\lambda_{De}$ case, consistent with the observed increase in capacitance and with (4.26) as applied to each cylinder taken separately.

The results for a center-to-center spacing of $\Delta x = 40\lambda_{De}$ are shown in Figure 4.31. Interestingly, the total sheath area is now a smaller fraction of the independent-cylinder sheath area: $\frac{A_s}{2A_{s,1}} \cong 0.61$. This is consistent with the fact that the system capacitance has gone above the combined capacitance of two single independent cylinders, i.e., $\frac{Q_n}{2Q_{n,1}} \cong 1.11$. This reduced sheath area is explained by the ion density increase on the outermost side of each cylinder, as explained earlier in Section 4.3.3.

The results shown in Figures 4.32 and 4.33, which apply to $\Delta x = 80\lambda_{De}$ and $\Delta x = 160\lambda_{De}$, correspond to a regime where both sheaths have become “Poisson-uncoupled” while still being “Vlasov-coupled”. What we mean by this is that the charges present in one sheath do not significantly contribute to the fields in the other sheath (“Poisson-uncoupled”), but shadow effects and asymmetry-induced effects on unpopulated orbits (discussed in Section 4.3.3) create connections between both sheaths (“Vlasov-coupled”). Results for both of these spacings show that in both cases the cylinders hold a total surface charge slightly above the surface charge that would be held by two independent cylinders, and that their total sheath area is correspondingly slightly smaller than the total sheath area created by two independent cylinders.

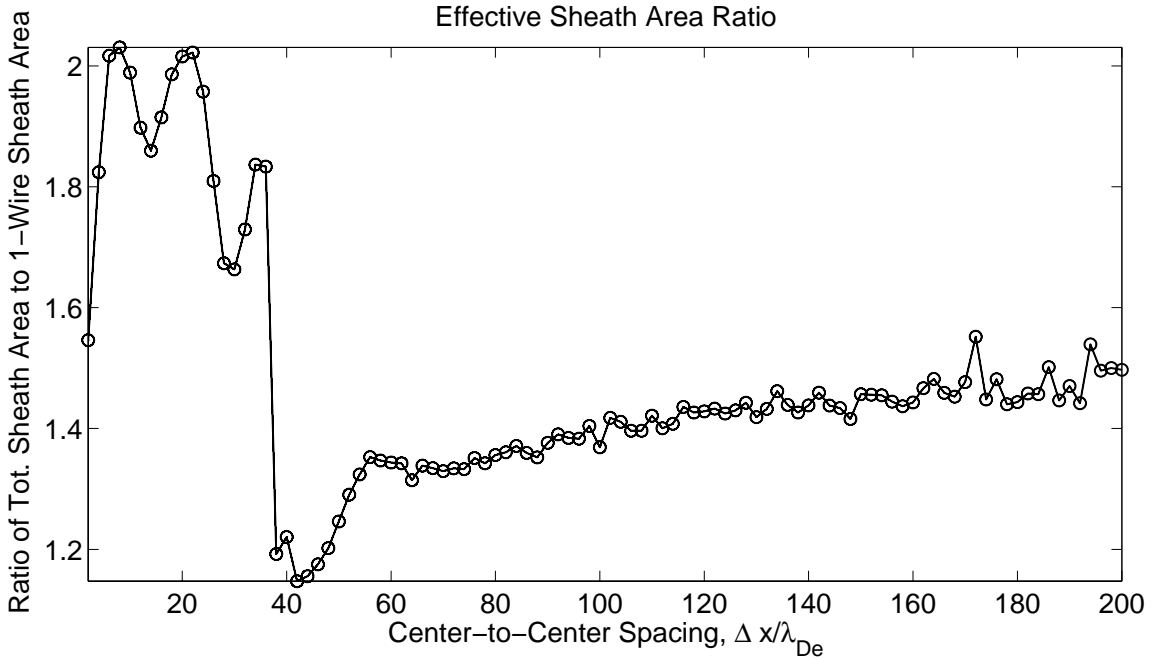


Figure 4.34: Effective sheath area ratio as a function of the center-to-center spacing of two parallel cylinders. The results shown here apply to the case of two cylinders of radius $r_0 = \lambda_{De}$ with normalized bias $\phi_0 = -320$. The effective sheath area ratio is the ratio of the two-cylinder sheath area to the single-cylinder sheath area.

4.3.6 Parametric Analysis of the Sheath Structure

Using the definitions given in the previous section, we can now consider an analysis of the effects of center-to-center spacing on the effective sheath area and total surface charge held by the cylinders.

First we define the *effective sheath area ratio* as the ratio of the total effective sheath area A_s of a two-cylinder system to the effective sheath area $A_{s,1}$ of a single independent cylinder, i.e.,

$$R_{A_s} \equiv \frac{A_s}{A_{s,1}}. \quad (4.27)$$

Figure 4.34 depicts the variation of the effective sheath area ratio R_{A_s} as a function of the center-to-center spacing Δx of the two parallel cylinders.

The leftmost data point in Figure 4.34 corresponds to a spacing of $\Delta x = 2\lambda_{De}$ and

applies to “touching” cylinders since they both have a radius $r_0 = \lambda_{\text{De}}$. R_{A_s} is seen to start at about 1.55 when the cylinders are touching, indicating a total sheath area 55% larger than that of a single cylinder. For a smaller cylinder radius, we would expect to obtain $R_{A_s} = 1$ when the cylinders are touching because the full extent of the two touching cylinders would be small enough for the shadowing effect to be negligible on the density of outward-moving ions throughout the sheath (see a discussion on this topic in Section 4.2.5).

The ratio R_{A_s} rises above 2.0 for spacings of $\Delta x = 5\lambda_{\text{De}}$ and $\Delta x = 20\lambda_{\text{De}}$, indicating that the effective sheath area is *on par* with the sheath area expected of two independent cylinders. This represents an optimal spacing for purposes of maximizing the total sheath area, as is desired for the high-energy particle precipitation application. The ratio R_{A_s} then drops sharply to a minimum value at a spacing of about $\Delta x = 40\lambda_{\text{De}}$, and goes back up relatively quickly until the spacing reaches $\Delta x = 60\lambda_{\text{De}}$, beyond which it follows a slow upward slope for the remainder of the graph. It is seen that the total effective sheath area has only reached about 1.5 times the sheath area of a single independent cylinder at a spacing of $\Delta x = 200\lambda_{\text{De}}$, whereas we expect it to reach a ratio $R_{A_s} = 2.0$ when the spacing is sufficient for the two sheaths to be fully independent of each other. An extrapolation of a linear fit performed on this slow increase indicates that “full independence” would only be reached at an approximate spacing $\Delta x \approx 660\lambda_{\text{De}}$, which corresponds to about 35 times the independent cylinder sheath radius of $R_s \approx 19\lambda_{\text{De}}$.

An alternative measure of the sheath dimensions can be obtained by considering the “outward” effective sheath radius, which is measured from the center of the rightmost cylinder toward increasing values of x on the x axis. This radius is determined based on the cross section of the potential, consistent with the *effective sheath* concept used for single cylinders. Figure 4.35 shows a plot of the ratio of the outward effective sheath radius to the effective sheath radius of a single independent cylinder as a function of the center-to-

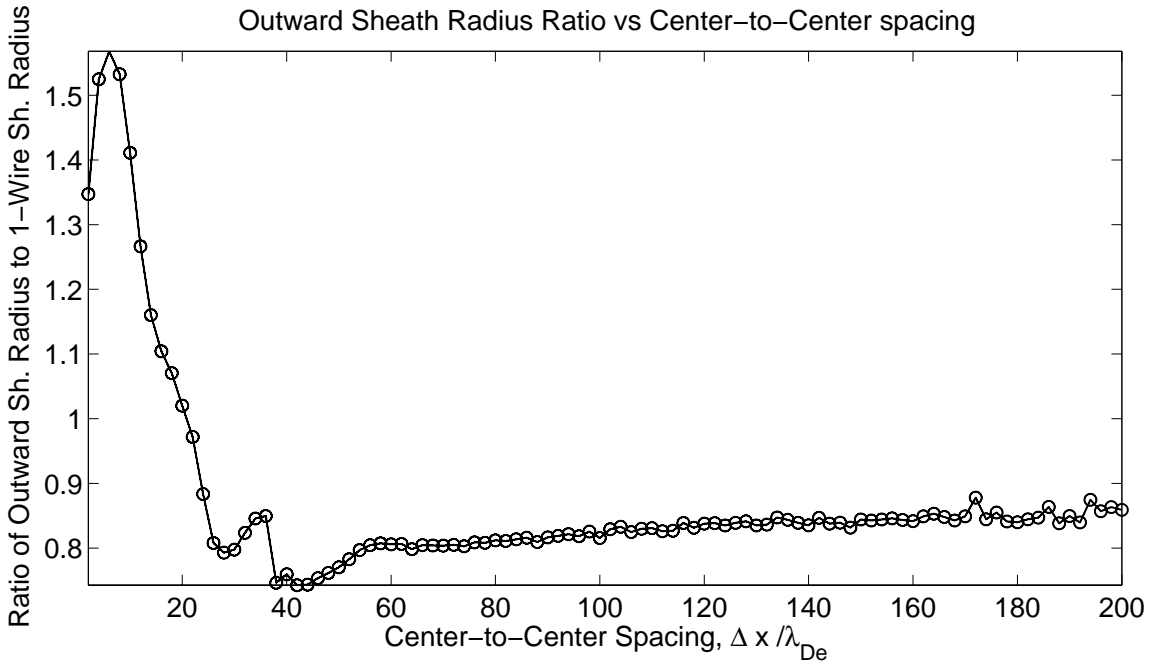


Figure 4.35: Ratio of the outward sheath radius to the single independent cylinder sheath radius $r_{s,1}$ as a function of the center-to-center spacing of two parallel cylinders. The results shown here apply to the case of two cylinders of radius $r_0 = \lambda_{De}$ with normalized bias $\phi_0 = -320$.

center spacing. It shows, as expected, an enhancement of the sheath radius for very small spacings, with an optimal spacing of $\Delta x = 5\lambda_{De}$. The minimum effective sheath radius is obtained for a spacing $\Delta x = 40\lambda_{De}$, a result which coincides with the spacing corresponding to the minimum effective sheath area, as seen in Figure 4.34. The outward effective sheath radius is then seen to slowly increase with increasing spacing, and is expected to reach the independent sheath radius at a sufficiently large spacing (ratio of 1 on the graph).

The surface charge ratio is shown in Figure 4.36. This ratio is defined as the ratio of the total surface charge held by both cylinders to the surface charge held by a single independent cylinder. As discussed before, thinner cylinders allowing reduced spacings would carry the same amount of charge as a single thin cylinder when approached sufficiently close to one another. Since here we are considering relatively large cylinders with a radius of one Debye length ($r_0 = \lambda_{De}$), they cannot be brought sufficiently close together to

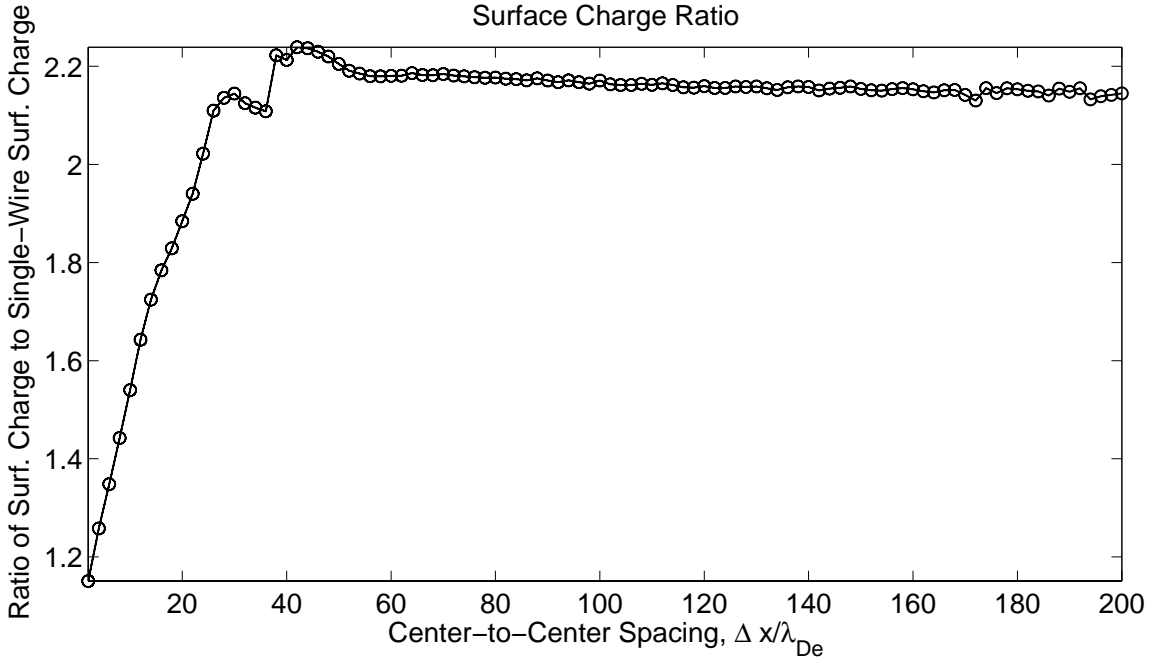


Figure 4.36: Ratio of the total surface charge on both cylinders to the surface charge held by a single independent cylinder. The results shown here apply to the case of two cylinders of radius $r_0 = \lambda_{De}$ with normalized bias $\phi_0 = -320$.

achieve as low a capacitance as a single wire. This is why the graph shown in Figure 4.36 starts above 1.0, at a ratio of about 1.15 for a spacing $\Delta x = 2\lambda_{De}$. As the cylinders are spaced apart, their combined capacitance increases so that the amount of charge they hold grows to a value of about 2.25 times the single-wire surface charge at $\Delta x = 40\lambda_{De}$. This is actually more than two independent cylinders could hold (2.0), and is consistent with the observed reduced effective sheath area seen in Figure 4.34 as compared to the total sheath area of two independent cylinders. The total charge then slowly ramps down as the spacing increases beyond $\Delta x = 40\lambda_{De}$, and the graphed ratio should eventually reach 2.0.

Figure 4.37 is an alternative representation of the information shown in Figure 4.34. It shows the “equivalent bias potential” for a single cylinder. This is the bias potential required on a single cylinder to generate an effective sheath area equal to that generated by our two-cylinder system biased at $\phi_0 = -320T_e$. It is seen that one could create a sheath as

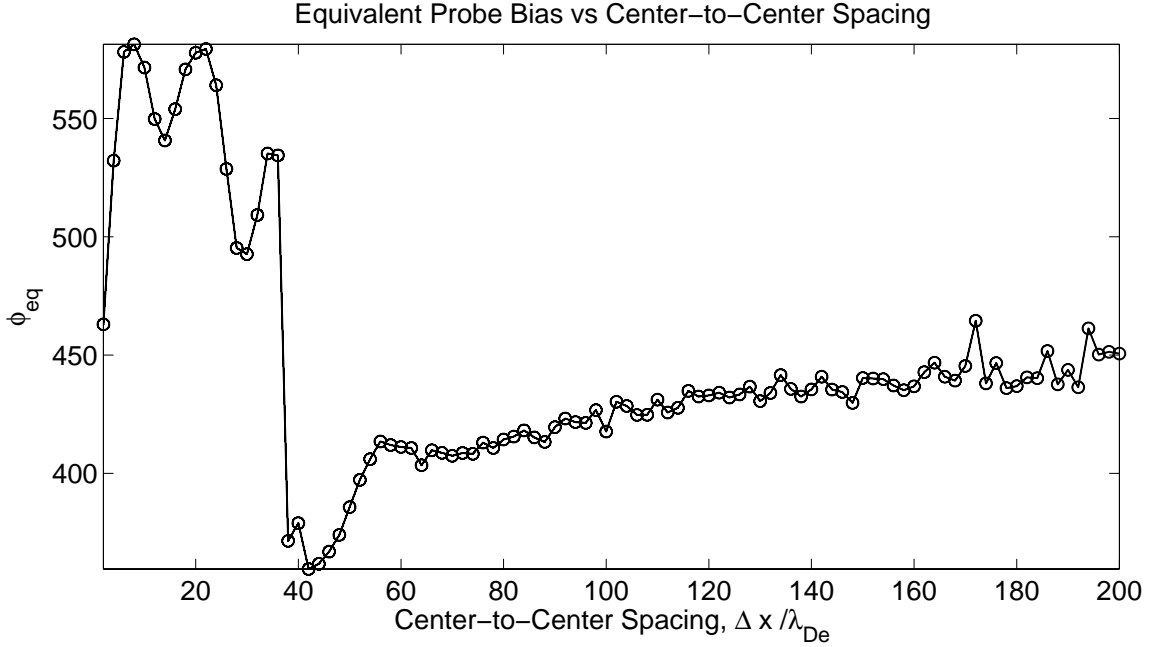


Figure 4.37: Equivalent bias potential of a single cylinder as a function of the center-to-center spacing of two parallel cylinders. The results shown here apply to the case of two cylinders of radius $r_0 = \lambda_{De}$ with normalized bias $\phi_0 = -320$. The equivalent bias potential is that which would be necessary for a single cylinder to yield the same sheath area as the combination of the two cylinders.

large as that which is created by a single cylinder of radius $r_0 = \lambda_{De}$ biased at $\phi_0 = -570T_e$ by using two cylinders of equal radius $r_0 = \lambda_{De}$ biased at $\phi_0 = -320T_e$ and spaced $5\lambda_{De}$ or $20\lambda_{De}$ apart.

Figure 4.38 is another alternative representation of the same information. It shows the “equivalent radius” of the two-cylinder system as a function of center-to-center spacing. This is the cylinder radius r_0 required of a single cylinder biased at the same bias potential $\phi_0 = -320T_e$ to generate the same equivalent sheath area as that generated by the two-cylinder system. At the optimal spacings $\Delta x = 5\lambda_{De}$ and $\Delta x = 20\lambda_{De}$, the equivalent radius is about $2.85\lambda_{De}$.

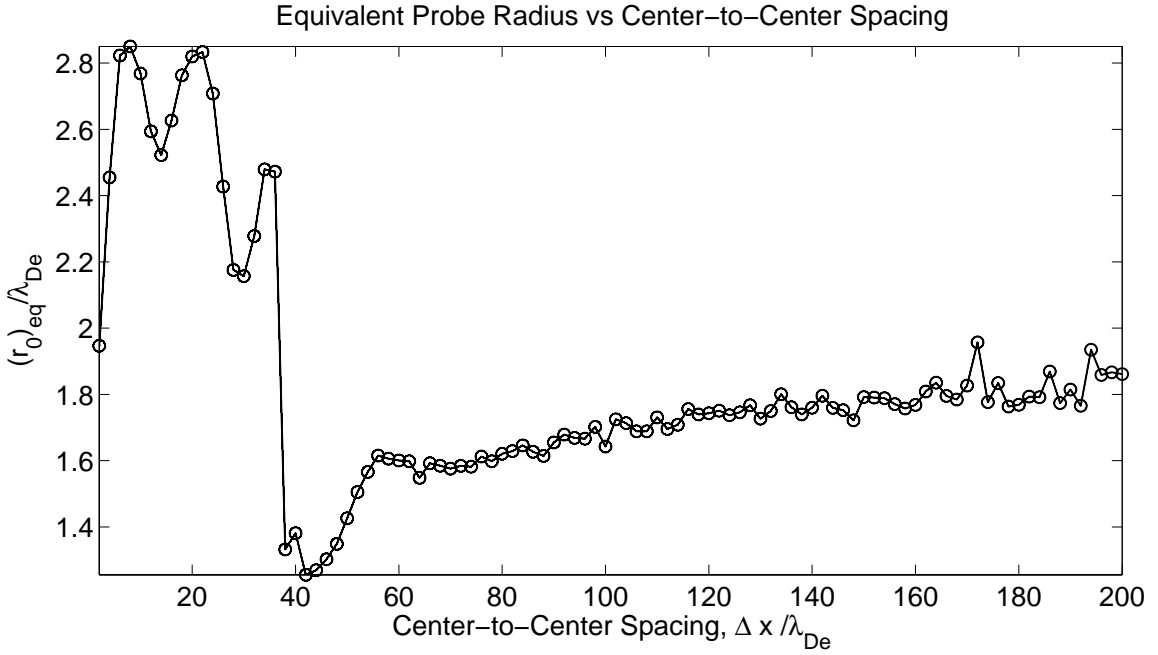


Figure 4.38: Equivalent radius of a single cylinder as a function of the center-to-center spacing of two parallel cylinders. The results shown here apply to the case of two cylinders of radius $r_0 = \lambda_{De}$ with normalized bias potential $\phi_0 = -320$. The equivalent bias potential is that which would be necessary for a single cylinder to yield the same sheath area as the combination of the two cylinders.

4.3.7 Interference Effect on Collected Current

Figure 4.39 depicts the variation of collected ion current as a function of center-to-center spacing. The graph is normalized to the current that would be collected by two independent cylinders, I_{indep} . In the present case, which involves cylinders with a relatively small radius $r_0 = \lambda_{De}$, I_{indep} is very close to the orbital motion limit, as can be seen in Figure 4.5.

When the cylinders are touching ($\Delta x = 2\lambda_{De}$), the current ratio I/I_{indep} is about 0.79. This reduced ratio is attributable primarily to the concave structure formed by the two cylinders, which prevents many incoming directions from reaching the facing internal surfaces of the two cylinders. In fact, one can approximate the current that should be collected based on the current entering a convex envelope enclosing both cylinders, as is shown in

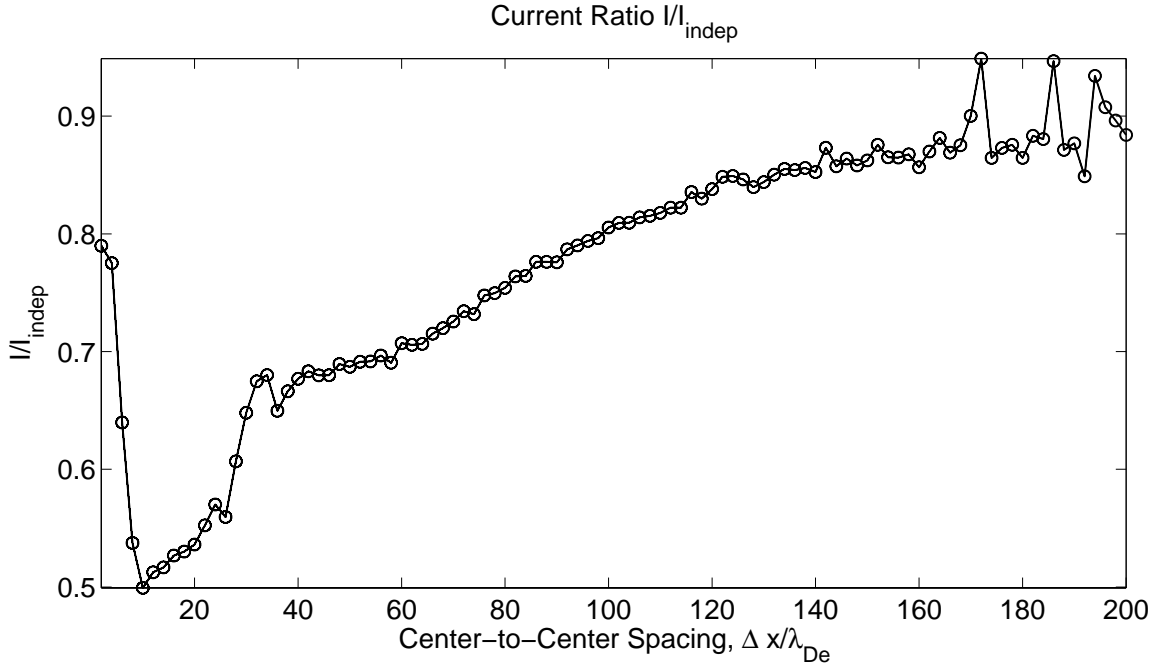


Figure 4.39: Current ratio as a function of center-to-center spacing for the two-cylinder configuration. The current ratio is defined as the ratio of the total collected current to the current that would be collected by two independent cylinders.

Figure 4.40. If we assume that the overall two-cylinder structure is still sufficiently small for orbital motion limit collection to apply, we can compute the expected collected current based on the ratio of the convex envelope's perimeter to the concave perimeter [18] as follows:

$$I_{\text{expected}} = I_{\text{oml}} \times \frac{\text{convex perimeter}}{\text{concave perimeter}} = \frac{4r_0 + 2\pi r_0}{4\pi r_0} \approx 0.82. \quad (4.28)$$

This value (0.82) is just above our result of 0.79. The remaining discrepancy can be attributed to a mild departure from the OML limit due to the overall size of the collecting structure. This is supported by the fact that the ion density at the external surface of the cylinders is slightly lower than half the ambient density, as seen on the x axis cross-section profile of Figure 4.17(b).

As the cylinder spacing is increased, the collected ion current is seen to drop to a minimum of half of the independent cylinder current near an optimal spacing of $\Delta x = 10\lambda_{\text{De}}$.

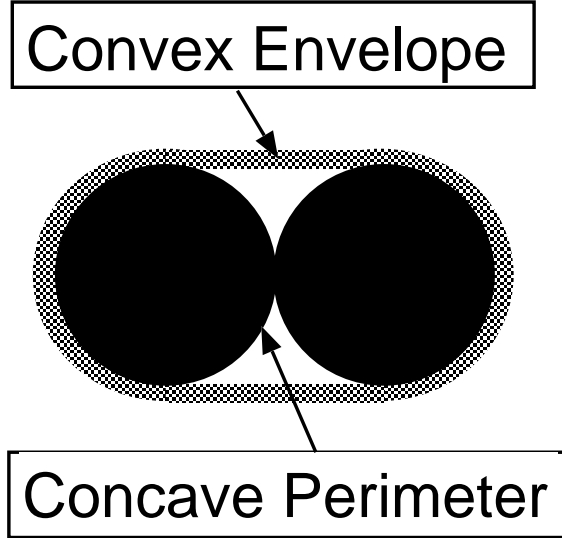


Figure 4.40: Illustration of the convex envelope surrounding both cylinders. The current collection to the concave portion of the perimeter is limited to some directions.

The current then rises sharply at a spacing $\Delta x = 30\lambda_{De}$, when two separate sheaths have begun to form. The remainder of the graph shows a rather steady increase of collected current with increasing spacing. This steady increase occurs once the sheaths have completely separated and are primarily coupled through the empty ion orbits connecting both cylinders' surfaces. The observed current increase is attributed to the gradual reduction of the number of connected ion orbits, which are not populated and therefore do not contribute current at the cylinders' surfaces. It is interesting to note that a similar observation was made in Section 3.6 concerning the experimentally measured current collected by slotted tape samples. The correlation between the experimentally observed decrease in the collection efficiency of the perpendicular slotted tapes with increasing gap widths and our simulation results indicate that the gap spacings sampled during our experiments were all located on the left of the expected minimum point on the current-vs-spacing graph.

4.4 Solid Tape Cylinder in Stationary Plasma: Current Collection

The solid tape geometry is of interest primarily for the spacecraft propulsion application of electrodynamic tethers. This geometry presents a few advantages over that of the circular cylinder wire:

- the orbital-motion-limited regime has been shown to hold for tape widths twice that of round cylinders, resulting in a maximum OML current collection 27% higher [11];
- a tape geometry is both lighter and more flexible [11];
- a wider tape structure would allow for improved collision survivability with orbiting debris.

In this section we consider the current collection capability of the solid tape geometry. The calculations were performed for electron-attracting bias potentials, but the normalized collected currents are equally applicable to ion-attracting bias potentials. In the following, we first make some comparisons with theoretical predictions given by *Sanmartín et al* [11] and *Estes and Sanmartín* [12], and then compare our simulation results with experimental data shown in Chapter 3.

4.4.1 Equivalent Cylinder Radius and Collected Current: Theoretical Comparisons

Using asymptotic analyses for both the circular cylinder and tape cylinder, *Sanmartín* and *Estes* [11] have identified a simple relationship between the tape width w and equivalent circular cylinder radius R_{eq} , given by $R_{eq} = \frac{w}{4}$ for sufficiently thin tapes where the thickness does not play a significant role. Their asymptotic analysis shows that, at a sufficiently large distance from the surface of a thin tape of width w but well within the *Laplace*-potential

region,¹⁷ the potential structure varies identically as in the vicinity of a circular cylinder of radius $R_{eq} = \frac{w}{4}$, that is,

$$\phi \approx \phi_0 \left[1 - \alpha_1 \ln \frac{r}{R_{eq}} \right], \quad (4.29)$$

where $\alpha_1 = \frac{C_n}{2\pi}$ is a function of the normalized linear capacitance $C_n = Q_n/\phi_0$, and Q_n is the normalized linear charge held at the surface of the cylinder. Recall that we had identified the same asymptotic form in (4.13) based on our numerical simulations and had chosen to write α_1 in terms of an *effective sheath radius* r_s , $\alpha_1 = \frac{1}{\ln(r_s/R_{eq})}$.

For a given bias potential ϕ_0 , α_1 simply relates to the normalized linear charge Q_n located on the cylinder's surface. Thus, the identification process that has led to the result $R_{eq} = \frac{w}{4}$ obtained by *Sanmartín et al* [11] is equivalent to finding the cylinder radius R_{eq} that would hold the same amount of linear charge Q_n as a solid tape of width w for a given bias potential ϕ_0 .

We may therefore independently determine an equivalent radius based on equal linear charge Q_n that is equivalent to the method used by *Sanmartín et al* [11], but is based on our consistent kinetic simulation results for tape and circular cylinder collectors. Figure 4.41 shows a comparison between the equal-charge probe radius as determined from our simulation results and the equivalent probe radius predicted by *Sanmartín et al* [11]. These simulations were performed with a bias $\phi_0 = 300$ and tape widths spanning from 1 to 50 Debye lengths. Our results show a somewhat larger equivalent radius than predicted by *Sanmartín et al* [11]. A best-fit linear relationship extracted from our simulation data and shown on the legend indicates an equivalent radius $R_{eq} \approx 0.29w$. The small discrepancy between these results is most likely due to the approximations used by Sanmartin and Estes [11] in calculating the electron space charge using an asymptotic approach that does not provide a fully

¹⁷For a cylinder (of any cross-section) biased at a large potential, we define the Laplace-potential region as the region in the immediate vicinity of the cylinder in which space charge effects do not have significant effects on the potential profile.

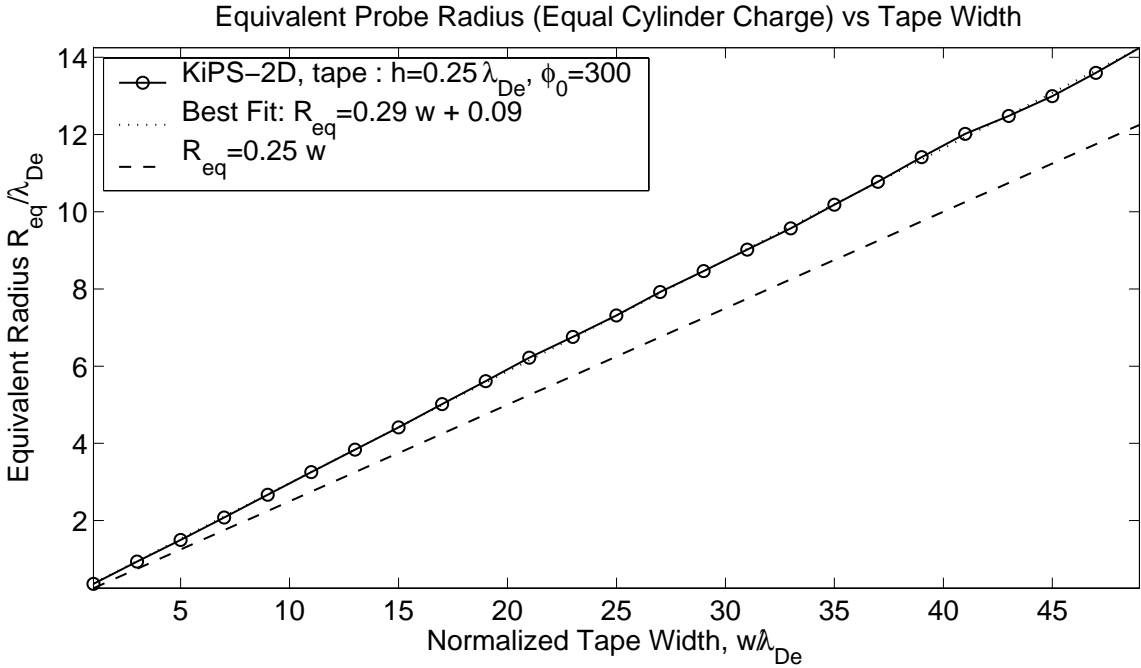


Figure 4.41: Equivalent circular probe radius as a function of width for a solid tape electron collector biased at $\phi_0 = \frac{V_0 - V_p}{T_e} = 300$. The equivalent probe radius R_{eq} is computed based on equal surface charge. Results are compared against the theoretical prediction $R_{eq} = w/4$ [11].

self-consistent Poisson–Vlasov solution. In fact, the relatively close agreement between our self-consistent 2-D simulation and their asymptotic calculation confirms the validity of Sanmartín and Estes’ asymptotic analysis as a first-order tool.

The main parameter of interest for propulsion applications is the efficiency of electron collection as a function of tape width. As we have seen in Figure 4.5, the efficiency of current collection, with respect to the orbital motion limit, decreases with the radius of a round cylinder. In Figure 4.42, we show the results of a similar evaluation of the current ratio I/I_{oml} as a function of solid tape width. As expected, the current ratio is seen to decrease with increasing tape width, a fact that is attributed to the existence of unpopulated orbits bounded on both ends by the tape’s surface (same as for circular cylinders). Our 2-D simulation results for the tape, performed for a bias potential $\phi_0 = 300$, are compared against the results of a 1-D simulation of a circular cylinder with equivalent radius $R_{eq} = 0.29w + 0.09$.

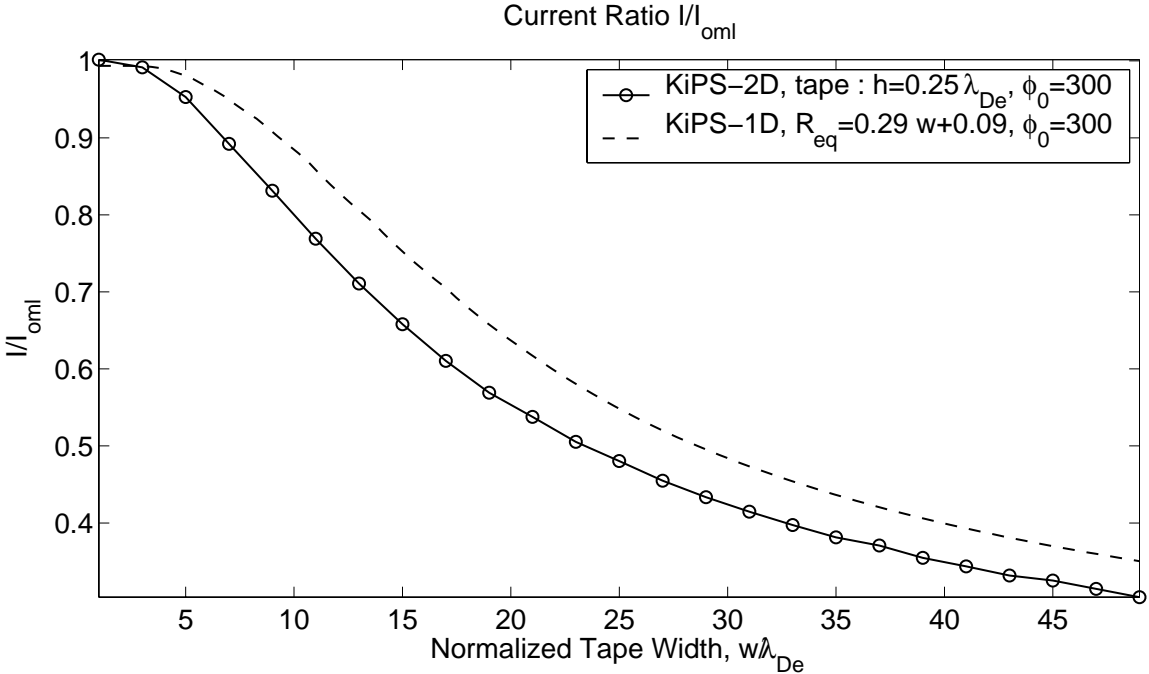


Figure 4.42: Current ratio I/I_{oml} as a function of tape width for a solid tape biased at $\phi_0 = \frac{V_0 - V_p}{T_e} = 300$. KiPS-2D simulation results for the tape are compared against KiPS-1D simulation results based on the equal-charge equivalent radius determined in Figure 4.41.

The comparison clearly shows that a tape current collector has a lesser current-collection efficiency than its equal-charge circular counterpart. From the same graph, one finds that the maximum width of a thin tape for the OML current expression to hold within about 1% is approximately $w_{max} \approx 2.5\lambda_{De}$, which is just shy of the maximum width predicted by Sanmartín and Estes [11] at this bias potential.¹⁸

4.4.2 Collected Current: Comparisons with Experimental Results

Here we consider comparisons of our simulation results with some of the experimental data pertaining to solid tapes that were shown in Chapter 3.

Figure 4.43 shows a plot of the current ratio I/I_{oml} , similar to that shown in Figure 4.42 but pertaining to a lower bias potential, $\phi_0 = 100$. Our simulation results are compared against three different sets of experimental data which were obtained at three distances

¹⁸According to Sanmartín and Estes. [11, Figure 6], $w_{max} = 4R_{max} \approx 4 \times 0.75\lambda_{De} = 3\lambda_{De}$.

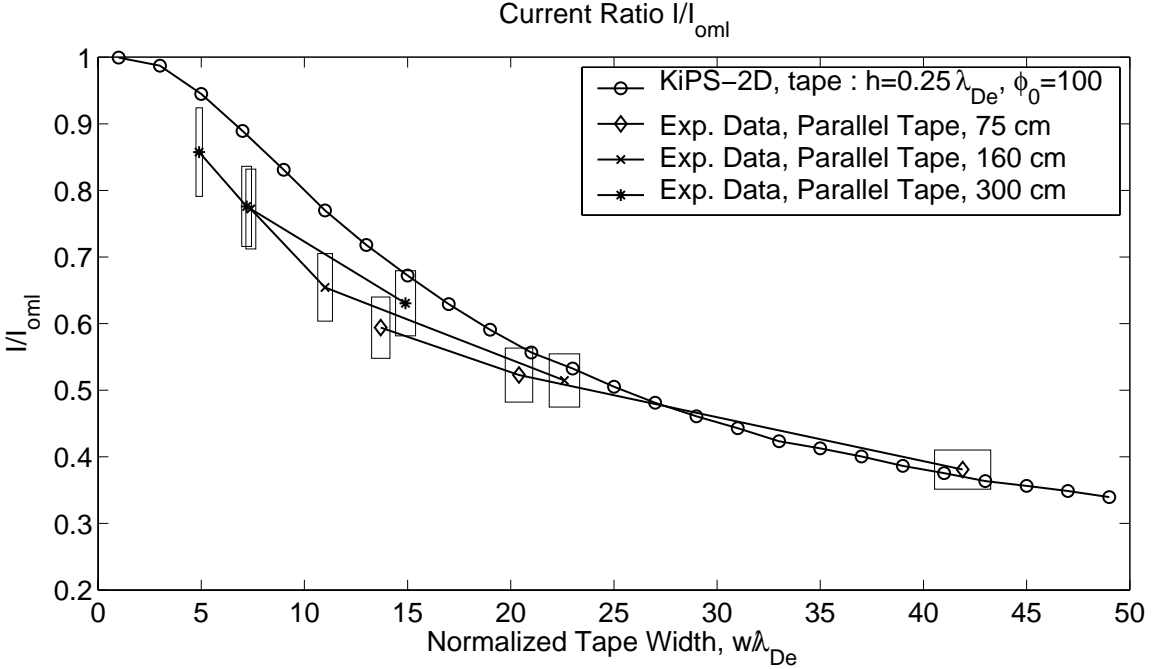


Figure 4.43: Simulated current ratio I/I_{oml} as a function of tape width for a solid tape biased at $\phi_0 = \frac{V_0 - V_p}{T_e} = 100$, along with experimental data. Simulations were done assuming a thin tape with finite thickness $h = 0.25\lambda_{De}$. Simulation results are compared against our experimental results (detailed in Chapter 3) obtained for a solid tape at three test locations from the plasma source: 75 cm (mostly flowing plasma), 160 cm and 300 cm (mostly stationary plasma). Note that the experimental data was calibrated using the round cylinder reference probe data instead of I_{oml} , in order to remove any flow enhancement effects for this comparison.

from a high-speed plasma source (see details in Chapter 3): 75 cm, 160 cm, and 300cm. Since these experiments were performed in a flowing plasma, we have attempted to “normalize out” any flow enhancement factors in order to compare with our stationary simulation results. Thus, instead of being normalized to the orbital-motion-limit current I_{oml} , the experimental data curves shown in Figure 4.43 are normalized to the reference cylinder data. In other words, we have plotted the following ratio in Figure 4.43 for the experimental data curves:

$$\text{Ratio} \equiv \frac{I_{\text{tape}}/I_{\text{tape,thermal}}}{I_{\text{refcyl}}/I_{\text{refcyl,thermal}}} \quad (4.30)$$

Note that the reference cylinder is sufficiently thin to collect current at the OML level in a

stationary plasma.

We observe a general qualitative agreement of the data with our simulation results at all 3 locations (75 cm, 160 cm, and 300 cm). We note that the experimental error in the determination of the ambient density and electron temperature could explain the existing discrepancies. Error boxes are shown in Figure 4.43 for the normalized experimental data. The sizes of these error boxes are determined based on three types of error sources:

1. current and voltage measurement errors on the tape samples themselves, which are estimated to amount to less than 1%;
2. systematic errors associated with the finite accuracy of the plasma parameters used as part of the normalization process. The plasma density n_0 and temperature T_e , obtained from our Langmuir Probe sweeps, were estimated to have 8% and 5% accuracy, respectively, as discussed in Appendix F;
3. a systematic error associated with the finite accuracy of the total tape sample electron-collecting area A_p , which is estimated to be on the order of 6%, similar to the error on the Langmuir probe area discussed in Appendix F.

So, using the 8% and 5% error estimates for density and temperature, we can infer a 6.5% error on the Debye length, since $\lambda_{De} \propto \sqrt{T_e/n_0}$. Now, since I_{oml} is proportional to $n_0 \times A_p \times \sqrt{V}$, where V is the applied tether voltage and A_p is the total area of the tape sample, the 1% error on voltage measurements and 6% error on tape area A_p combine with the 8% error on density to yield for I_{oml} an error of $8\% + 6\% + 0.5 * 1\% = 14.5\%$. Therefore, in Figure 4.43, the error boxes surrounding the normalized data points have a relative height of $1\% + 14.5\% = 15.5\%$, corresponding to the sum of the error on measured current I and the error on I_{oml} , and a relative width of 6.5% corresponding to the relative error on the normalized width w/λ_{De} , where we assume that the bulk of the error is contributed by

the error on λ_{De} while the actual widths w have a much better precision due to use of an electrical discharge machining process for tape sample fabrication.

Having first observed the dependence of collected current on tape width, we now consider the complete current characteristics (Current vs Voltage) of several tape configurations, which we compare against our experimental results. Figures 4.44 through 4.46 show the simulation/experiment comparisons pertaining to the three sample positions that were tested: 75 cm, 160 cm and 300 cm from the plasma source (see Chapter 3 for details).

Only the parallel tape data were used, since they featured less flow effects than the perpendicular tape data and were therefore more appropriate for comparison with our stationary plasma computer simulations. It should be emphasized that the experimental data were processed in such a way as to remove the remaining flow effects. This was done by multiplying all normalized tape current data by the ratio of the normalized reference cylinder data $I_{refcyl}/I_{refcyl,thermal}$ to the theoretical normalized OML current I_{oml} :

$$I_{\text{without flow}}(V) \approx I_{\text{with flow}}(V) \times \frac{I_{oml}(V)}{I_{refcyl}(V)/I_{refcyl,thermal}(V)}. \quad (4.31)$$

This is thought to remove much of the flow-induced current enhancement, since the reference cylinder experiences a similar enhancement. However, we must still keep in mind that some of the flow enhancement could still be present in the experimental data, especially at the closest range of 75 cm, since the correction above is only approximate. At the farthest range however (300 cm) we have determined that the plasma was mostly stationary, and therefore the normalization performed by (4.31) only had a minor effect.

The simulation and experimental results shown in Figures 4.44 through 4.46 are in good agreement for the widest tape configuration, whereas for the medium and narrow tapes the experimental data is less efficient than predicted by our simulations. The reduction of the current collection efficiency caused by the screw attachments is thought to be the most likely cause for this discrepancy, since the fraction of the collecting area contributed by the

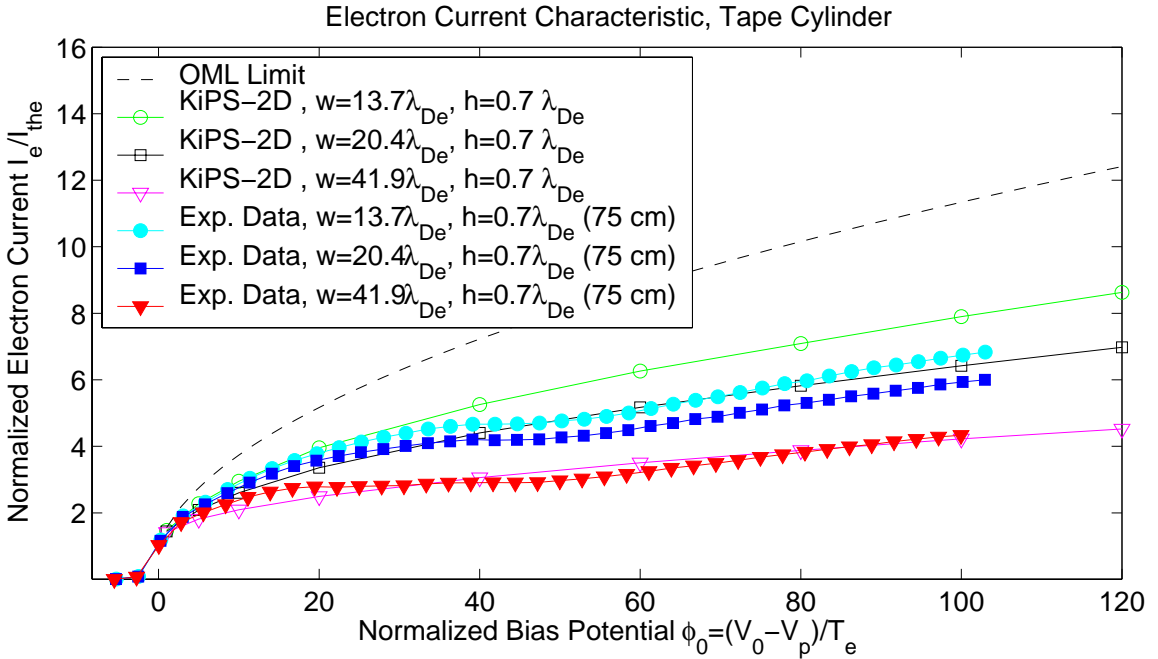


Figure 4.44: Normalized current characteristics of solid tapes: comparison of simulation results with experimental data obtained at 75 cm. Three different tape widths are compared. Tape widths w and thicknesses h are indicated in terms of the local Debye length.

screws is significantly more important in the case of a narrow tape than it is in the case of a wide tape. Note that the screw areas were accounted for in the calculation of the total sample area, as discussed in Chapter 3.

4.5 Flow Effects on Ion-Attracting Round Cylinder

We now consider the effects of plasma flow on the sheath structure and current collection of ion-attracting round cylinders. We will consider flow speeds U that are very small with respect to the electron thermal velocity v_{the} , i.e., $U \ll v_{the}$. Therefore, the electrons are essentially a stationary species that only respond to the asymmetries in the potential structure. Those asymmetries are introduced by the ions, whose thermal velocity is on the order or even slower than the flow speed U .

Throughout this section, we designate the flow speed using three alternate notations:

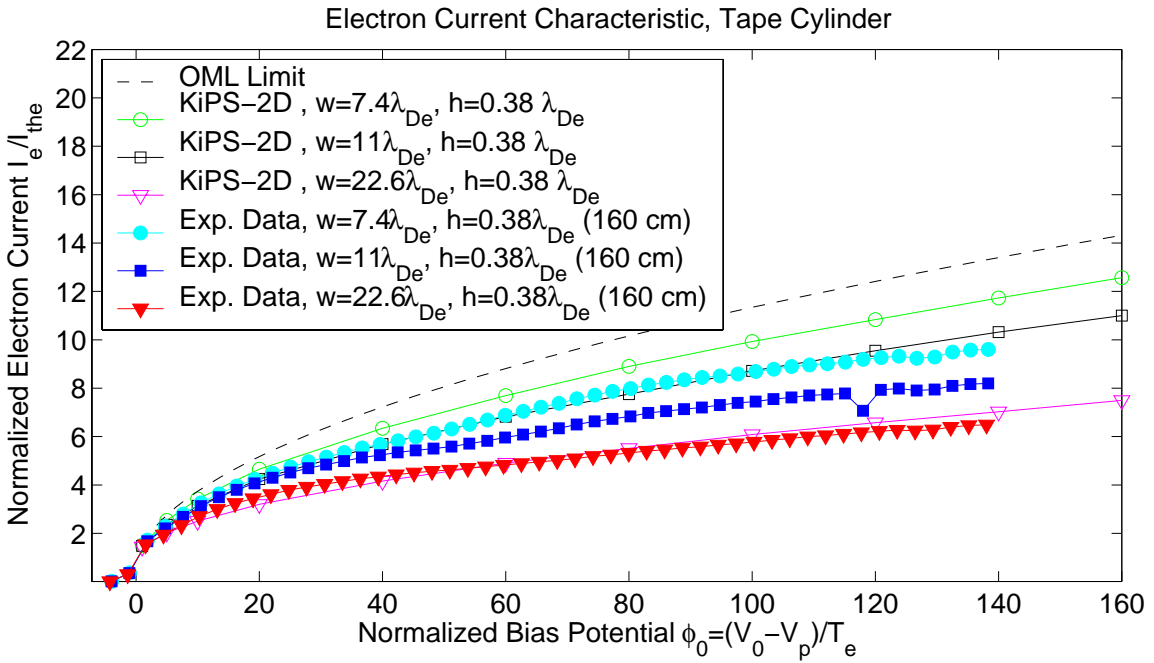


Figure 4.45: Normalized current characteristics of solid tapes: comparison of simulation results with experimental data obtained at 160 cm. Three different tape widths are compared. Tape widths w and thicknesses h are indicated in terms of the local Debye length.

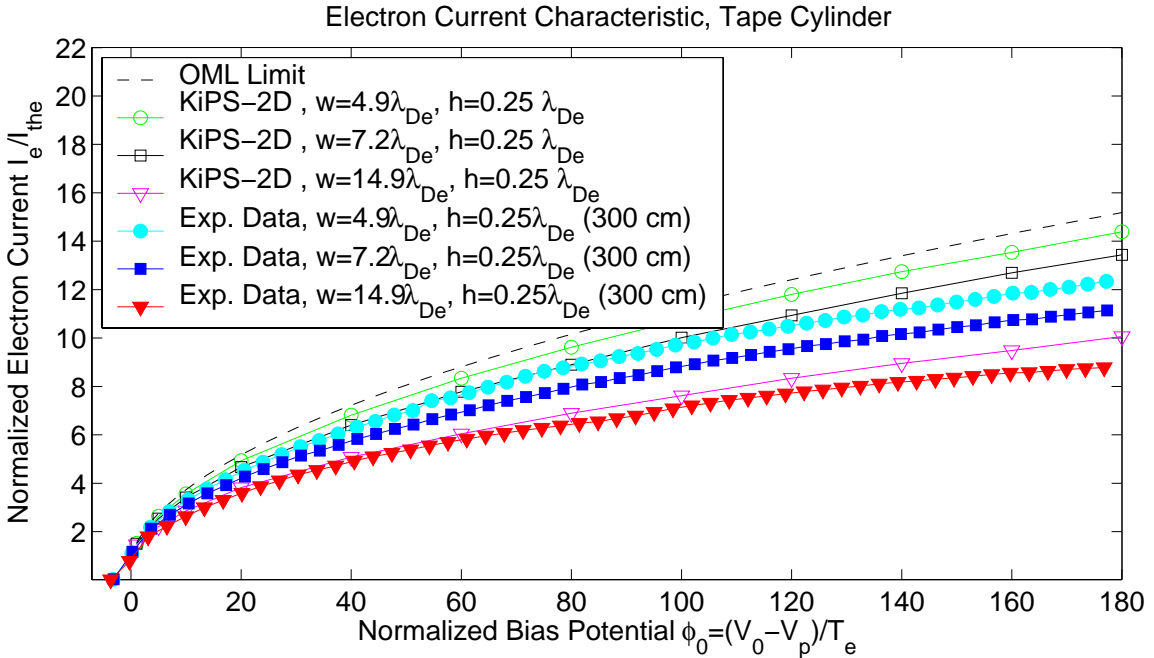


Figure 4.46: Normalized current characteristics of solid tapes: comparison of simulation results with experimental data obtained at 300 cm. Three different tape widths are compared. Tape widths w and thicknesses h are indicated in terms of the local Debye length.

- the flow velocity U , given in m/s;
- the flow energy U_{ev} , given in eV, which relates to the velocity U through the expression

$$U_{\text{ev}} = \frac{m_i U^2}{2e}, \quad (4.32)$$

where m_i is the ion atomic mass, and $e = 1.6 \times 10^{-19}$ C;

- the ion speed ratio S_d , which is the ratio of the flow velocity to the ion thermal velocity, given by

$$S_d = \frac{U}{v_{thi}} = \sqrt{\frac{U_{\text{ev}}}{T_i}}, \quad (4.33)$$

where T_i is the ion temperature in eV. The ratio S_d is used in section 4.5.3 when making comparisons with a publication using that notation.

In the following, we first describe the trapped orbit criteria, and the various treatments of electrons that were used here. In Section 4.5.3, we perform a few validations with the simulation results obtained by Xu [17]. Finally, in Section 4.5.4, we perform a detailed analysis of the impact of the ionospheric flow on the sheath structure and ion current collection at an altitude that is representative of the high-energy particle precipitation application.

4.5.1 Criteria for Trapped Orbits

The asymmetry introduced by the plasma flow allows for the existence of some orbits of increased complexity, although not quite as complex as in the two-cylinder case. To accommodate for these relatively complex trajectories, we have set the maximum number of orbits to $M_{\text{orb}} = 3$, which corresponds to a maximum angular displacement of 6π (see definition for M_{orb} in Section 2.4.2.2) beyond which a trajectory will be deemed trapped. A maximum number of radial oscillations was not necessary for these simulations, since it would be redundant.

4.5.2 Treatment of Electrons

For similar reasons as in the case of the two-cylinder electron-repelling configuration described in Section 4.3.1, the treatment of electrons can be greatly simplified in the present case, because the electron population is not effectively drifting. Since in the flowing case the potential can get slightly positive at some locations (on the ram side of the cylinder) even when applying a negative bias potential, an accurate collisionless treatment for electrons that provides excellent accuracy is based on the following “clipped” Boltzmann equation:

$$n_e = \begin{cases} n_0 \exp \frac{V}{T_e} & V \leq 0 \\ n_0 & V > 0. \end{cases} \quad (4.34)$$

This treatment is actually exact for a stationary species if all collisionless orbits are connected to the background plasma, which is the case here because the electrons are repelled, implying that no electron orbit intersects the probe for all practical purposes. Using a “full Boltzmann” approximation for electrons, i.e., setting $n_e = n_0 \exp \frac{V}{T_e}$ for both negative (repelling) and positive (attracting) potentials, is also appropriate as long as potentials do not significantly exceed zero. Doing so actually provides a feedback mechanism in the simulation which improves the convergence rate, and does not unduly impact the quality of the solution as long as the final potential profile does not significantly exceed zero.

Three different types of treatments were used to compute the electron density in the simulations presented in Section 4.5.3. They are:

Boltzmann Electrons This is the same approximation as was used by Xu [17], and is designated above as the “full Boltzmann” approximation.

“Clipped” Boltzmann Electrons This approximation is appropriate for low speeds only. It does not allow for any negative-energy electrons, and therefore could not be used for some combinations of high-voltage and/or high-speed settings due to numerical

stability issues.

Kinetic Electrons This is the same kinetic treatment as is used for the ions, and involves tracking thousands of trajectories in order to compute the density at a given interrogation point.

The last two methods, the “clipped” Boltzmann and kinetic electrons, have not reached convergence for all combinations of voltage and speed settings, due to the non-smoothness of the electrons’ Vlasov Jacobian matrix. For this reason and due also to time constraints, some of the graphs shown throughout Section 4.5.3 only contain simulation data for a subset of the three electron treatments just mentioned. All data points shown, however, are based on adequately converged, self-consistent simulations.

4.5.3 Validation with Existing Simulation Results

Before using our model for the analysis of our application of interest, we consider some comparisons with simulations performed by Xu [17]. Ion density profiles and collected ion current are compared below.

4.5.3.1 Ion Density Profile Validations

Figures 4.47 and 4.48 illustrate the cross-sectional ion density profiles obtained for various flow speeds along the axis of plasma flow (x axis) for a round conductive cylinder ($r_0 = \lambda_{De}$) biased at a normalized potential $\phi_0 = -25$. Four different flow speed settings are shown corresponding to speed ratios $S_d = 0.5, 1, 3$, and 6 or, alternatively, flow energies $U_{ev} = 0.25T_e, T_e, 9T_e$ and $36T_e$.

The agreement between our results and Xu’s results [17] is very good, except perhaps for some minor discrepancies on the ram side of the cylinders at low speed ($S_d = 0.5$ and 1).

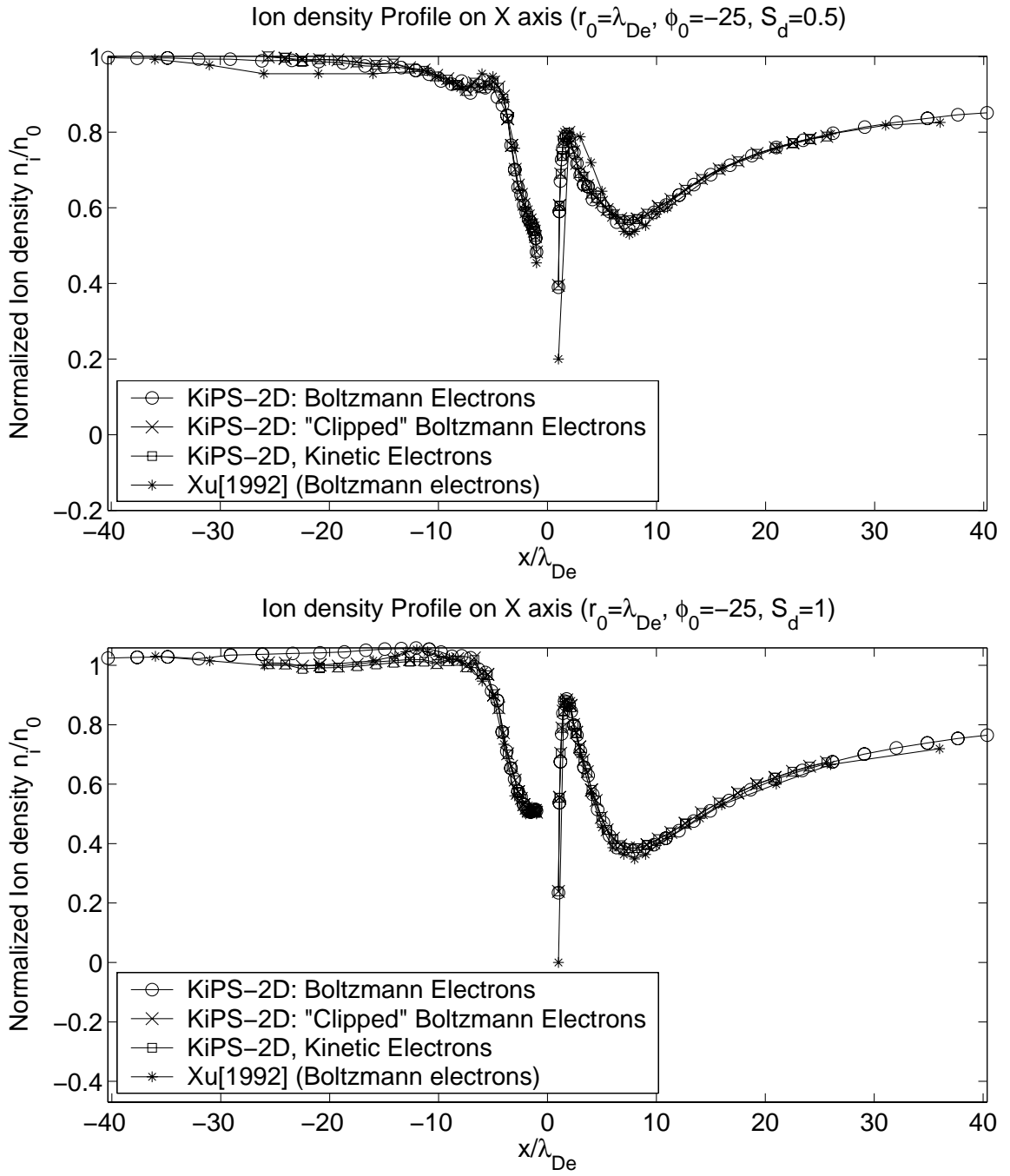


Figure 4.47: Ion normalized density profile along the central axis of a round conductive cylinder ($r_0 = \lambda_{De}$) biased at a potential of $-25T_e$ and immersed in a plasma flowing at speed ratios $S_d = 0.5$ and $S_d = 1$, with corresponding flow energies of $U_{ev} = 0.25T_e$ and $U_{ev} = T_e$. Results are compared against the simulation results published by Xu [17], which used the Boltzmann approximation for the electrons.

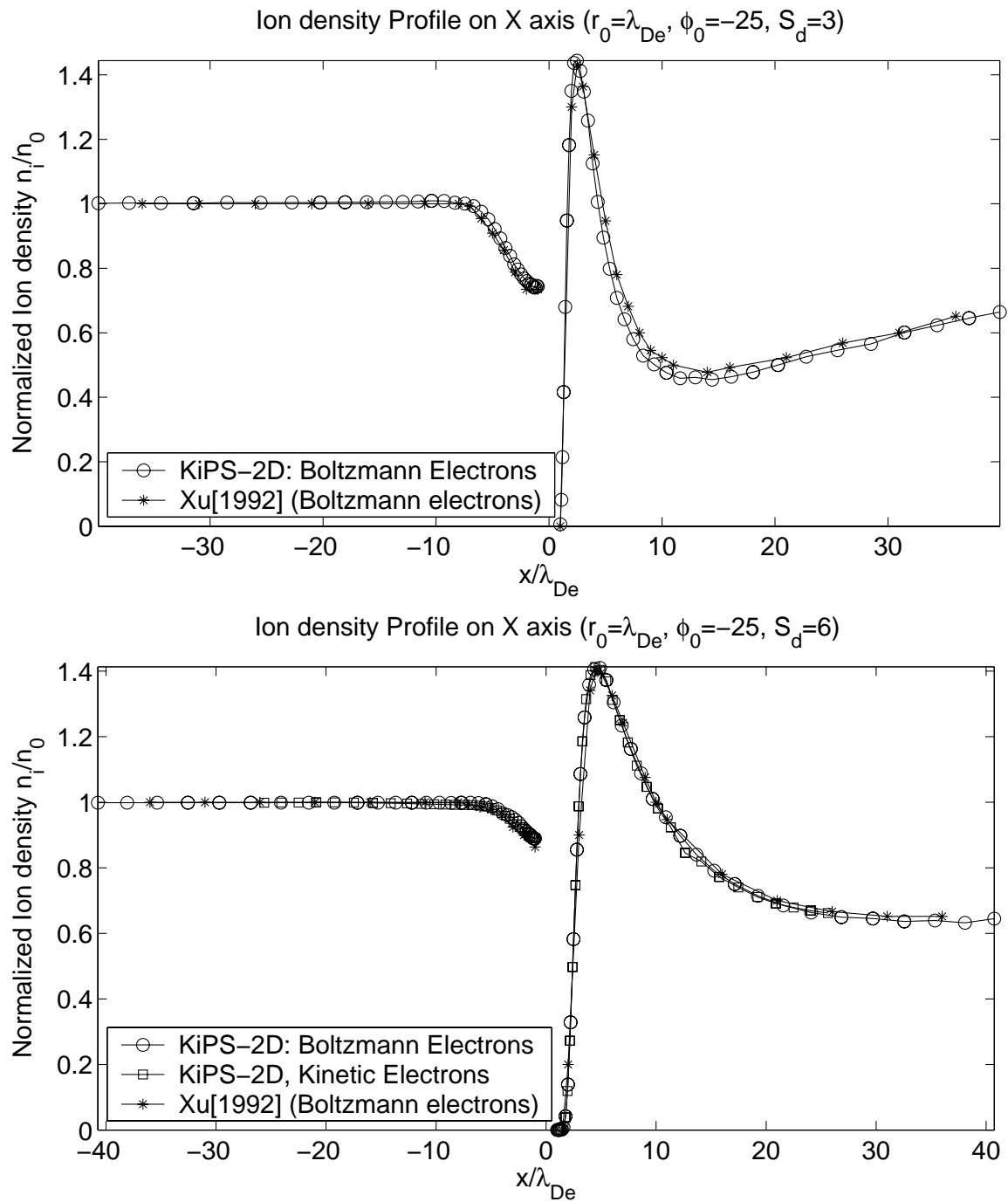


Figure 4.48: Ion normalized density profile along the central axis of a round conductive cylinder ($r_0 = \lambda_{De}$) biased at a potential of $-25T_e$ and immersed in a plasma flowing at speed ratios $S_d = 3$ and $S_d = 6$, with corresponding flow energies of $U_{ev} = 9T_e$ and $U_{ev} = 36T_e$. Results are compared against the simulation results published by Xu [17], which used the Boltzmann approximation for the electrons.

The ion density on the ram-side surface of the cylinder is seen to stay close to the ambient density up to a relatively close distance from the cylinder. The density then drops to a value which, for sufficiently large flow speeds ($S_d = 3$ and $S_d = 6$), is larger than the orbital-motion limit of half the ambient density. This is of course attributable to the average drift velocity of the ion population. In the limit of very high speeds, practically all of the ion population would be moving to the right at a uniform velocity and would “ram” the cylinder without having been deflected by its surrounding electric fields, translating into a density equal to the ambient density on the ram-side of the cylinder’s surface.

On the wake side of the cylinder, the depletion of ions due to plasma flow is seen to occur very quickly: the wake-side surface density has already dropped to around one-fifth of the ambient density for a speed ratio $S_d = 0.5$, and is zero for the three other speed settings.

4.5.3.2 Ion Current Collection Validations

Figures 4.49 and 4.50 show some comparisons of the ion current dependence on the flow speed ratio S_d for various probe radii: $r_0 = 0.2\lambda_{De}$, λ_{De} , $5\lambda_{De}$ and $10\lambda_{De}$. Agreement between our simulation data and Xu’s results [17] is very good. Our results show a similar departure from Godard and Laframboise’s symmetric-profile as was observed by Xu at intermediate values of the speed ratio. However, they indicate a less pronounced dip of the current at the critical speed corresponding to the minimum current collection. This observation is most obvious on the lower graph in Figure 4.49 at the highest bias potential setting, $\phi_0 = -25$: Xu’s data goes down to a minimum of 4.4, while our KiPS-2D simulation results do not go much lower than 5.0.

The non-monotonic nature of these current curves can be explained by the combination of two opposite phenomena: the decrease of the wake-side current and the increase of the ram-side current. As the flow speed is increased from zero, the wake-side density drops

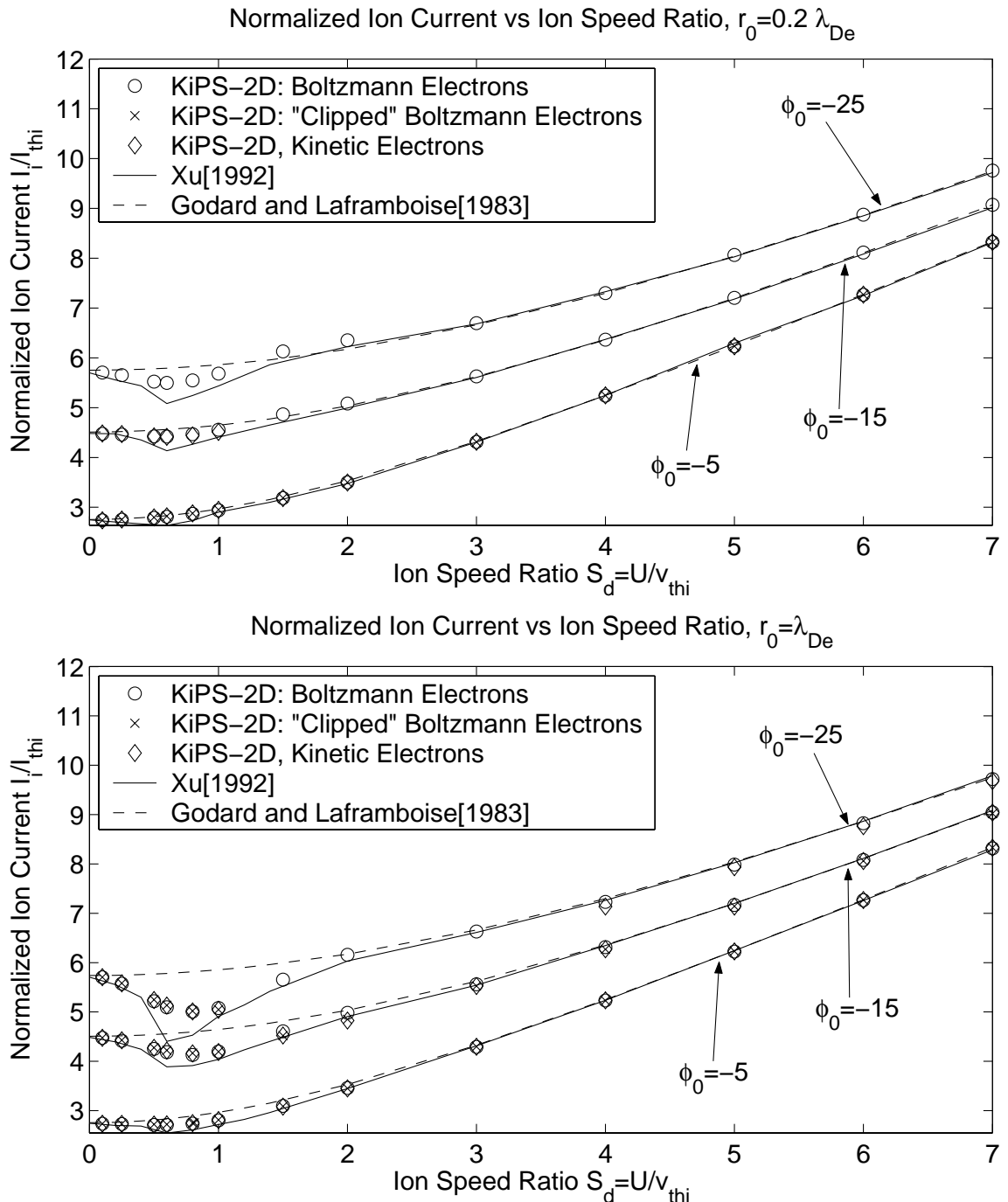


Figure 4.49: Collected ion current as a function of the ion speed ratio S_d , for a round conductive cylinder with probe radii $r_0 = 0.2\lambda_{De}$ and $r_0 = \lambda_{De}$, immersed in a flowing plasma with $T_i = T_e$. KiPS-2D results for three different bias potentials ($\phi_0 = -5, -15, -25$) are compared with simulation results published by Xu [17] (asymmetric profile, kinetic code) and Godard and Laframboise [30] (symmetric sheath approximation).

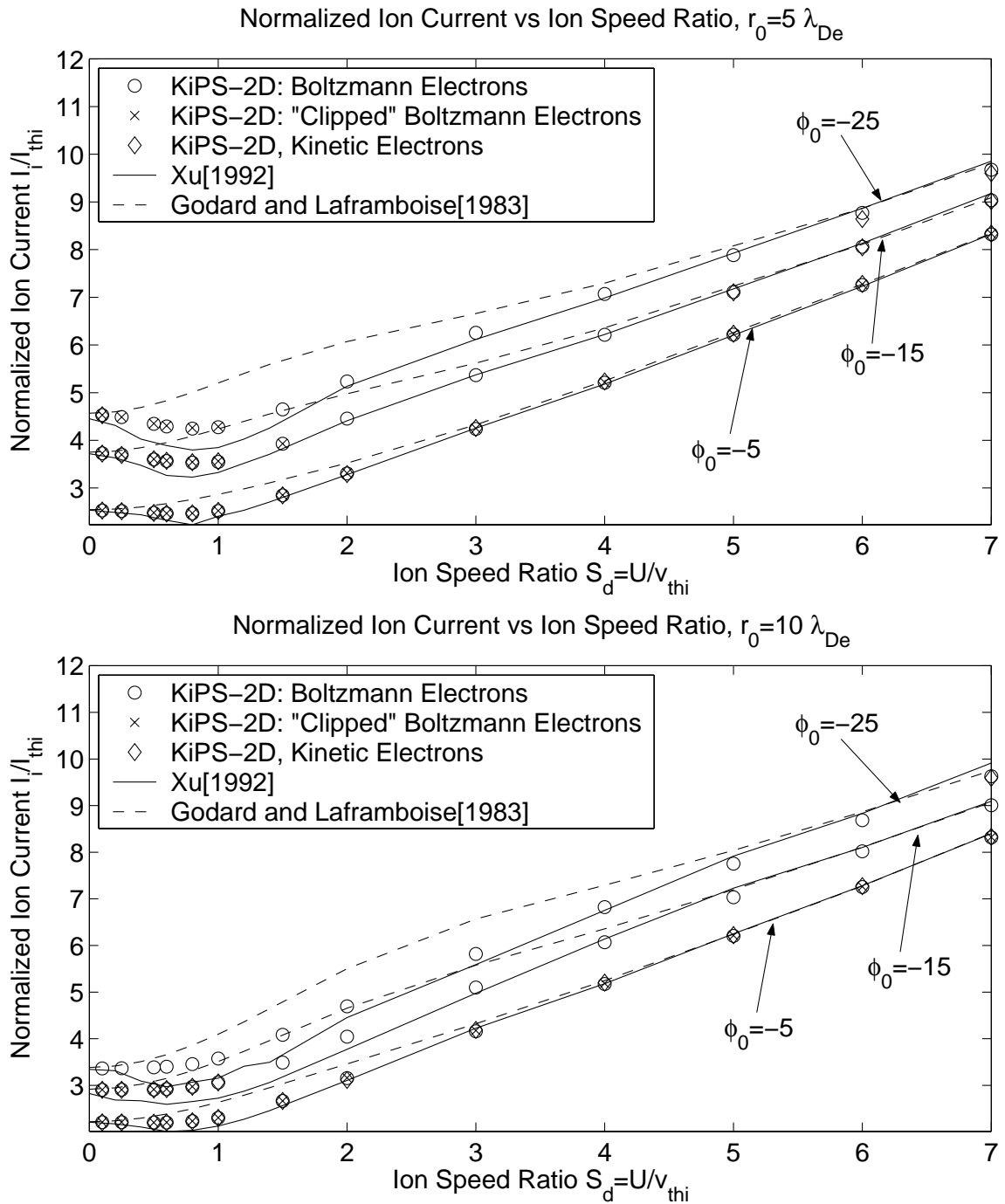


Figure 4.50: Collected ion current as a function of the ion speed ratio S_d , for a round conductive cylinder with probe radii $r_0 = 5\lambda_{De}$ and $r_0 = 10\lambda_{De}$, immersed in a flowing plasma with $T_i = T_e$. KiPS-2D results for three different bias potentials ($\phi_0 = -5, -15, -25$) are compared with simulation results published by Xu [17] (asymmetric profile, kinetic code) and Godard and Laframboise [30] (symmetric sheath approximation).

dramatically, as was seen on the ion density profiles shown in Figures 4.47 and 4.48. The relatively slow increase in ram-side current collection initially does not suffice to counter the decrease in wake-side current, which leads to a net decrease of the collected current. As the plasma speed increases further, the wake-side current eventually reaches zero. Beyond this point, the net current starts increasing again because its sole contribution is now the ram-side current, which increases with the incoming beam velocity.

4.5.4 Ionospheric Flow Effects at High Altitudes (H=1500 km)

For the energetic particle precipitation application (also known as the remediation of radiation belts), we are primarily interested in whether or not we should expect the orbital velocity of a tether, which can be interpreted as plasma flow as seen from the frame of reference of the tether, to affect the overall sheath dimensions and ion current collection properties as determined for a stationary plasma in Section 4.2. For the following study, we will consider a representative altitude of 1500 km for the operation of an electrodynamic tether as a scattering device. If the tether were located on an equatorial orbit, placing it at this particular altitude would allow for remediation of radiation belts in the vicinity of the $L = 1.24$ magnetic field shell¹⁹.

4.5.4.1 Flow Energy at Altitude of Interest

At an altitude of 1500 km, Hydrogen is the dominant ion species. If we assume a circular orbit, and further assume that the orbital velocity $U = 7113$ m/s [80] completely translates into plasma motion relative to the spacecraft,²⁰ we may compute the *flow energy*

¹⁹The L-shell level on the equatorial plane is computed as the ratio of the distance from the Earth's center to the Earth's radius. In this case, $L = \frac{1500\text{km}+6370\text{km}}{6370\text{km}} \approx 1.24$.

²⁰This is not rigorously accurate, since the ionosphere rotates around the Earth in the opposite direction, somewhat reducing the net relative velocity.

U_{ev} to be

$$U_{\text{ev}} = \frac{m_i v^2}{2e} = 0.265 \text{ eV}, \quad (4.35)$$

where we have used Hydrogen's atomic mass $m_i = 1.67 \times 10^{-27}$ kg, the orbital velocity $U = 7113$ m/s, and the constant $e = 1.6 \times 10^{-19}$ J/eV. Since we assume for the electron and ion temperature $T_i = T_e = 0.4$ eV (see Table 1.1), the normalized flow energy is $\frac{U_{\text{ev}}}{T_e} \approx 0.66$, and corresponds to a speed ratio $S_d = \sqrt{0.66} = 0.81$ with respect to the ion thermal velocity.

4.5.4.2 Inspection of the Sheath Structure

In order to address the question of the importance of flow effects, we set the flow speed at a fixed value $U_{\text{ev}} = 0.66T_e$ and observe the changes in the structure of the plasma as we gradually increase the bias potential on the cylinder. Figures 4.51 through 4.64 show some 2-D distributions along with corresponding x-axis cross sections of the net charge, potential, and density distributions corresponding to cylinder bias potentials of $\phi_0 = -5, -10, -20, -50, -100, -200$ and -300 . In addition, overlays of all of the potential and density cross-section profiles are provided in Figures 4.65 and 4.66. Note that the “clipped Boltzmann” treatment was used for electrons for all these simulations.

One immediately notices that the asymmetries present at low bias potentials do not fade away as the bias potential increases to values as large as $\phi_0 = -300$, a bias potential over 450 times the flow energy. This may be regarded as contrary to “common wisdom”, according to which an impinging flow energy as small as $\frac{U_{\text{ev}}}{T_e} = 0.66$ should have a negligible effect on the sheath structure with bias potentials a few orders of magnitude larger. As Figure 4.66 shows, the asymmetry in the ion and electron density profiles only gets stronger as the bias potential is increased. As far as the potential profile is concerned, it only shows visible signs of asymmetry as one gets closer to the pre-sheath, with the wake-side pre-sheath zone showing a slightly negative potential, offset from the ram-side pre-sheath potential by

an amount on the order of the beam energy. This “tail” in the potential profile is still clearly visible with a bias potential $\phi_0 = -300$.

A flow energy equal to 66% of the thermal energy ($U_{\text{ev}} = 0.66T_e$) introduces a significant asymmetry in the ion population’s Maxwellian velocity distribution in the background plasma. The resulting asymmetry in the ionic density distribution causes a corresponding asymmetry in the potential distribution, breaking the conservation of angular momentum associated with a central force. This has two effects:

- the unpopulated trapped orbits are compressed to the right, away from the cylinder on the wake side and closer to the cylinder on the ram side;
- the ion-depleting effect of the cylinder’s shadow becomes less important on the ram side and more important on the wake side.

Both of these effects cause the ion density to keep to the ambient value up to a much closer distance on the ram side of the cylinder, while stretching the depletion zone further out on the wake side. One observes that, even though the bias potential is large, the “ion source” feeding the high-voltage sheath is located in the background plasma, where the potential is zero. *Thus, when assessing whether asymmetries should be expected or not, the important parameter to compare against flow energy is not the bias potential, but the ion temperature at the source, in the background plasma.* An ion source which has a significant offset (\equiv flow speed) in its velocity distribution function will cause significant asymmetries in the ionic density profiles, especially as the bias potential increases.

Another aspect of interest that is noted from the ionic density profiles is the significant drop of the ion density on the wake side’s surface of the cylinder, down to a value near $0.15n_0$ for a bias potential of $\phi_0 = -300$. As we will see in what follows, this causes a reduction of the collected current as compared to the stationary case.

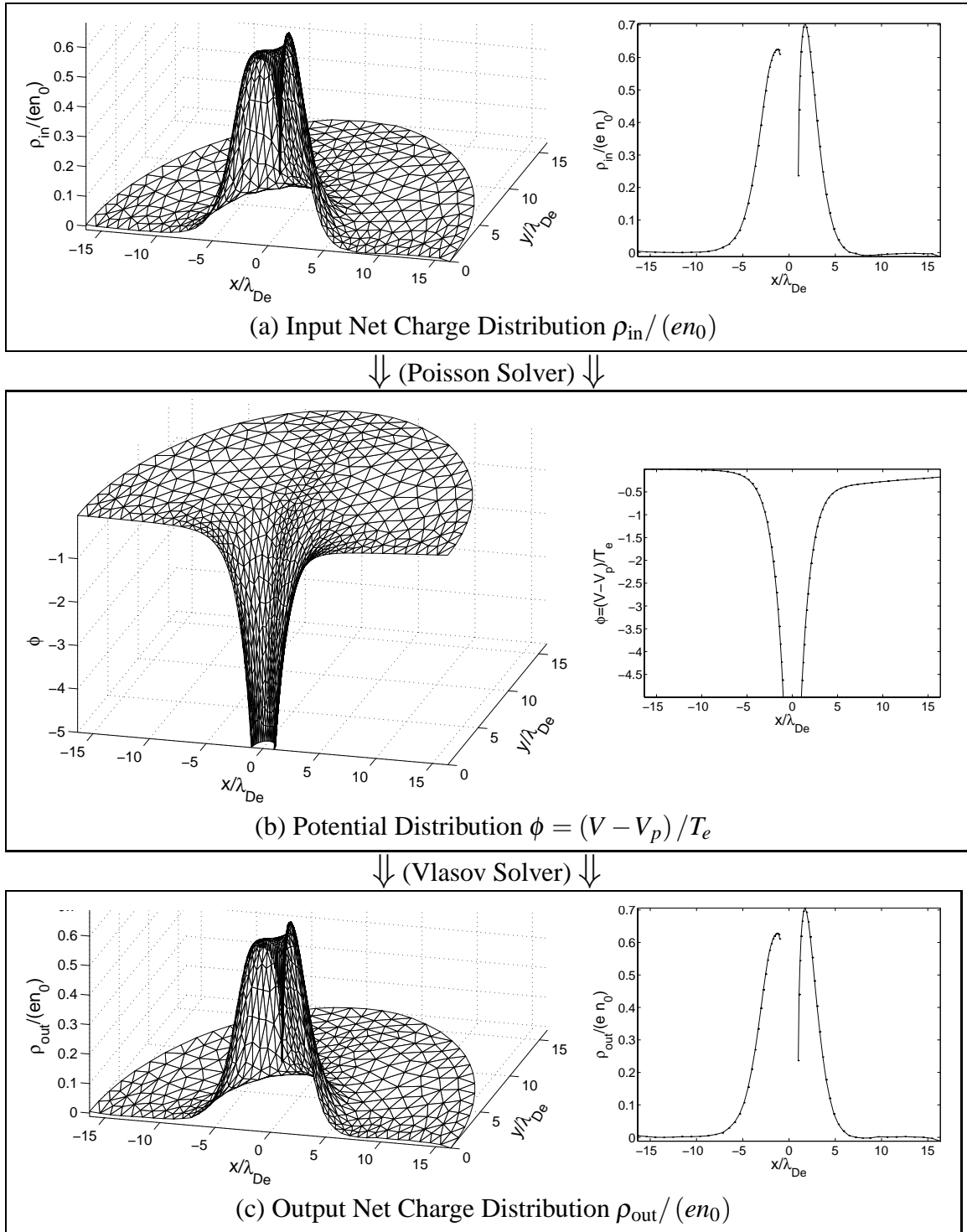


Figure 4.51: Poisson–Vlasov consistent solution for an ion-attracting cylinder ($r_0 = \lambda_{\text{De}}$) biased at $\phi_0 = -5$ and immersed in a flowing plasma with flow energy $U_{\text{ev}} = 0.66T_e$. Self-consistency is shown by the similarity of ρ_{in} and ρ_{out} . 2-D solutions are shown on the left, and corresponding x -axis cross-section profiles are shown on the right. Corresponding ion and electron density distributions are shown in Figure 4.52.

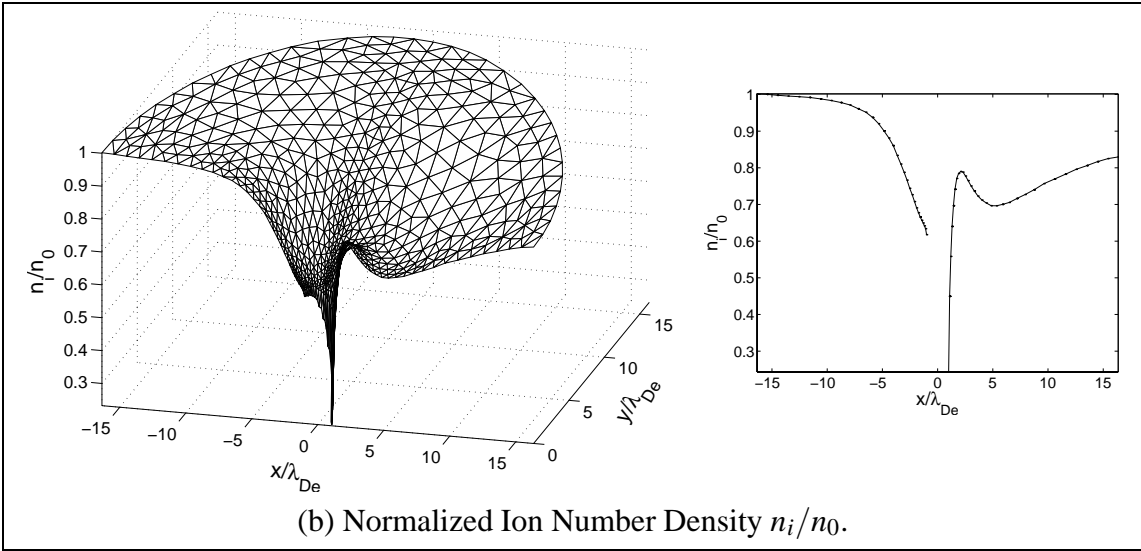
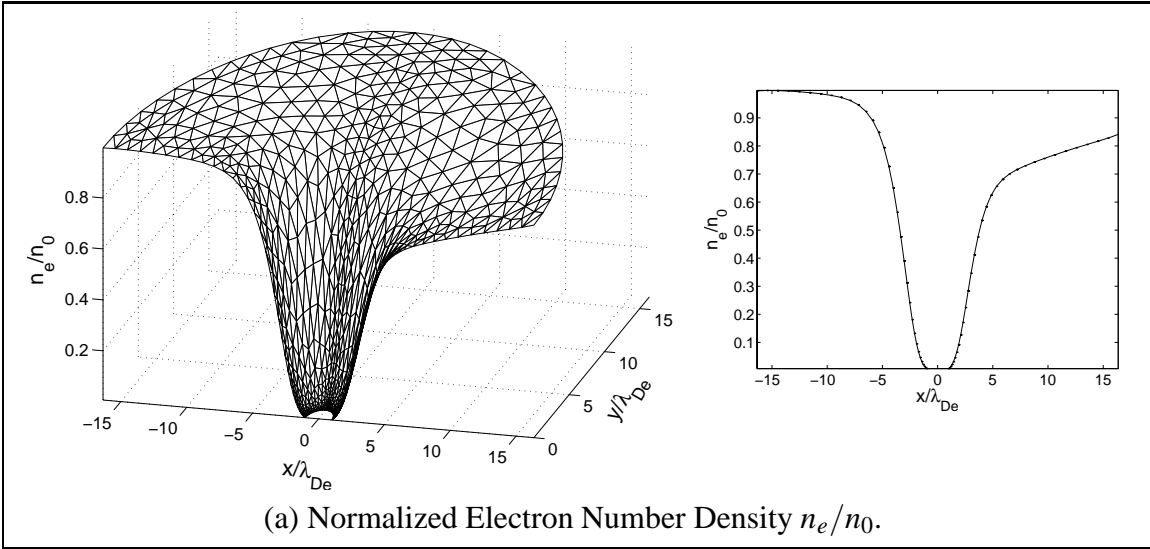


Figure 4.52: Poisson–Vlasov consistent electron and ion density distributions for an ion-attracting cylinder ($r_0 = \lambda_{De}$) biased at $\phi_0 = -5$ and immersed in a flowing plasma with flow energy $U_{ev} = 0.66T_e$. These density profiles constitute the output of the Vlasov solver and are subtracted to form the output net charge density profile $\vec{\rho}_{out} = e(\vec{n}_i - \vec{n}_e)$ shown in Figure 4.51(c).

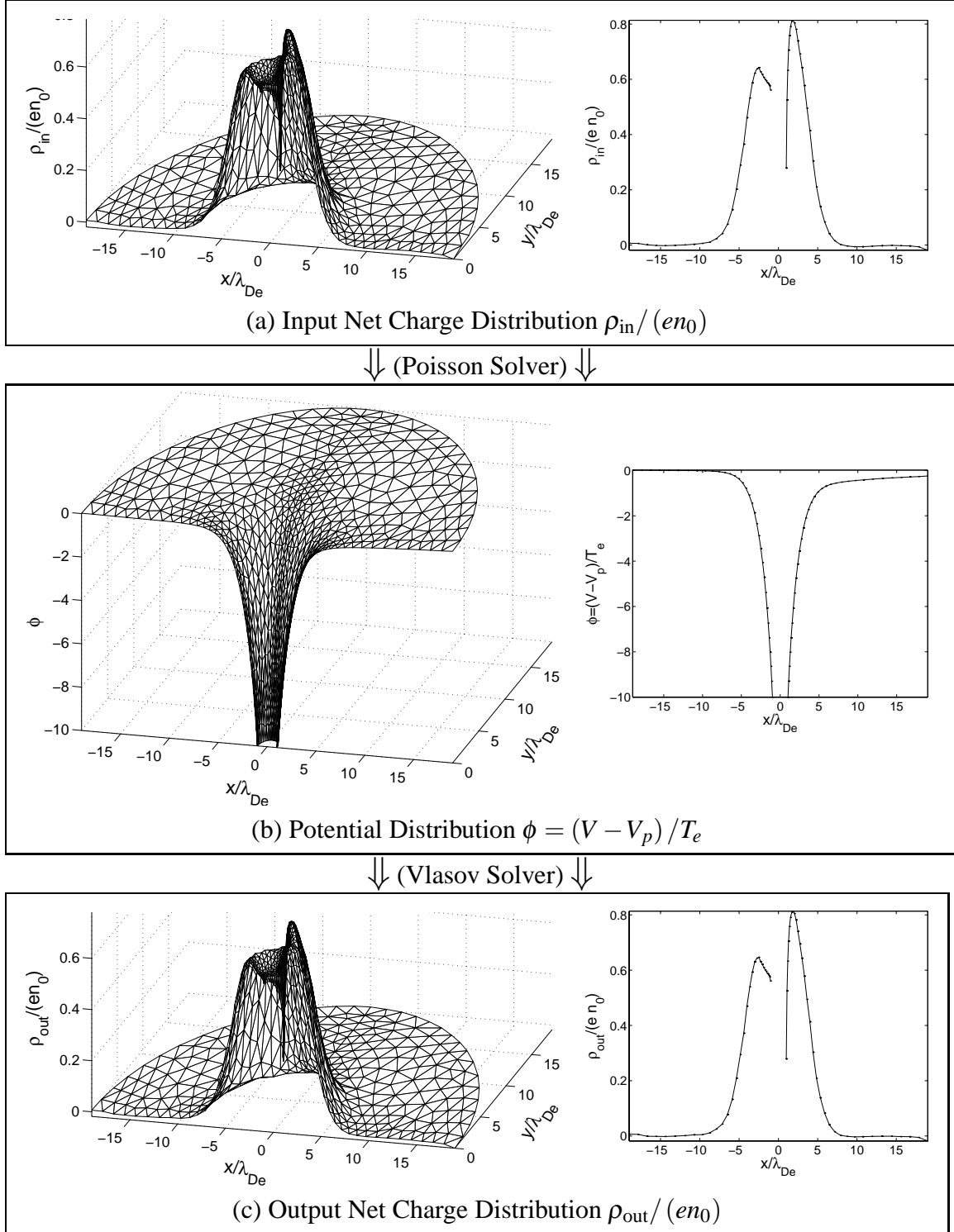


Figure 4.53: Poisson–Vlasov consistent solution for an ion-attracting cylinder ($r_0 = \lambda_{De}$) biased at $\phi_0 = -10$ and immersed in a flowing plasma with flow energy $U_{ev} = 0.66T_e$. Self-consistency is shown by the similarity of ρ_{in} and ρ_{out} . 2-D solutions are shown on the left, and corresponding x -axis cross-section profiles are shown on the right. Corresponding ion and electron density distributions are shown in Figure 4.54.

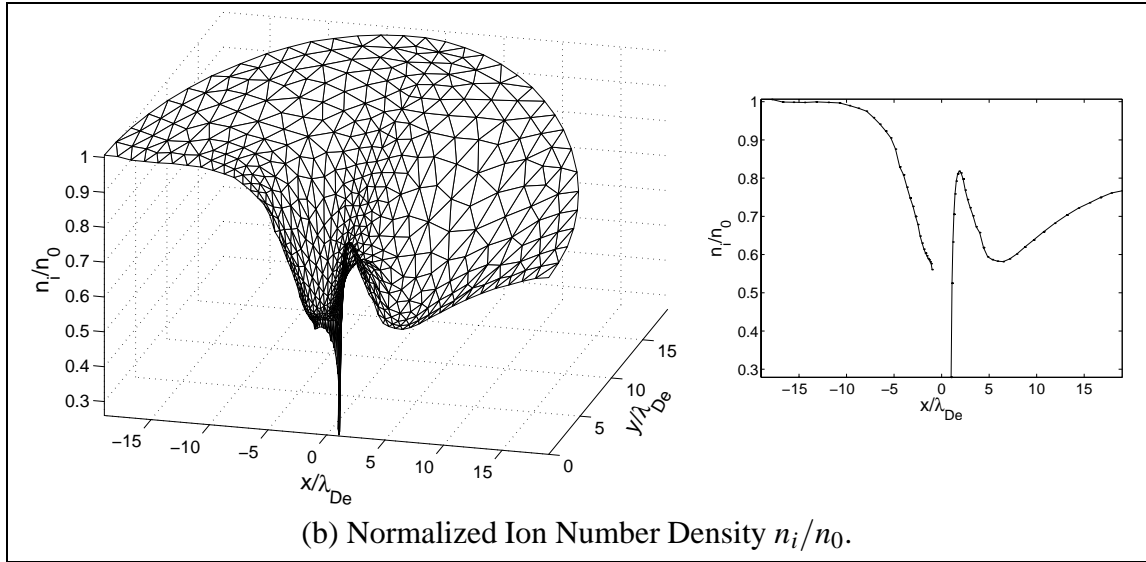
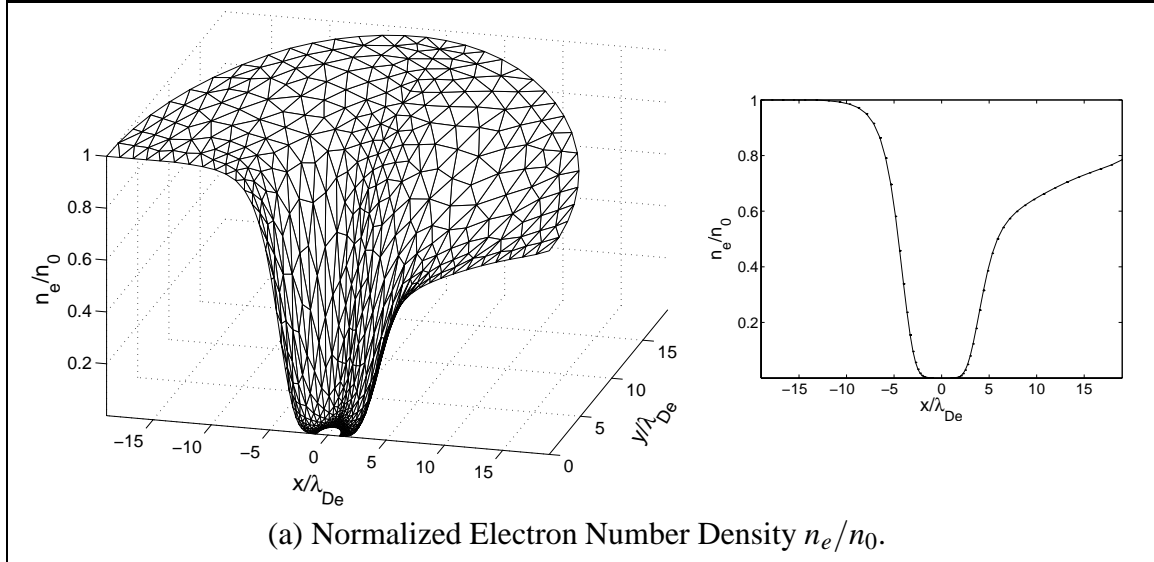


Figure 4.54: Poisson–Vlasov consistent electron and ion density distributions for an ion-attracting cylinder ($r_0 = \lambda_{De}$) biased at $\phi_0 = -10$ and immersed in a flowing plasma with flow energy $U_{ev} = 0.66T_e$. These density profiles constitute the output of the Vlasov solver and are subtracted to form the output net charge density profile $\vec{\rho}_{out} = e(\vec{n}_i - \vec{n}_e)$ shown in Figure 4.53(c).

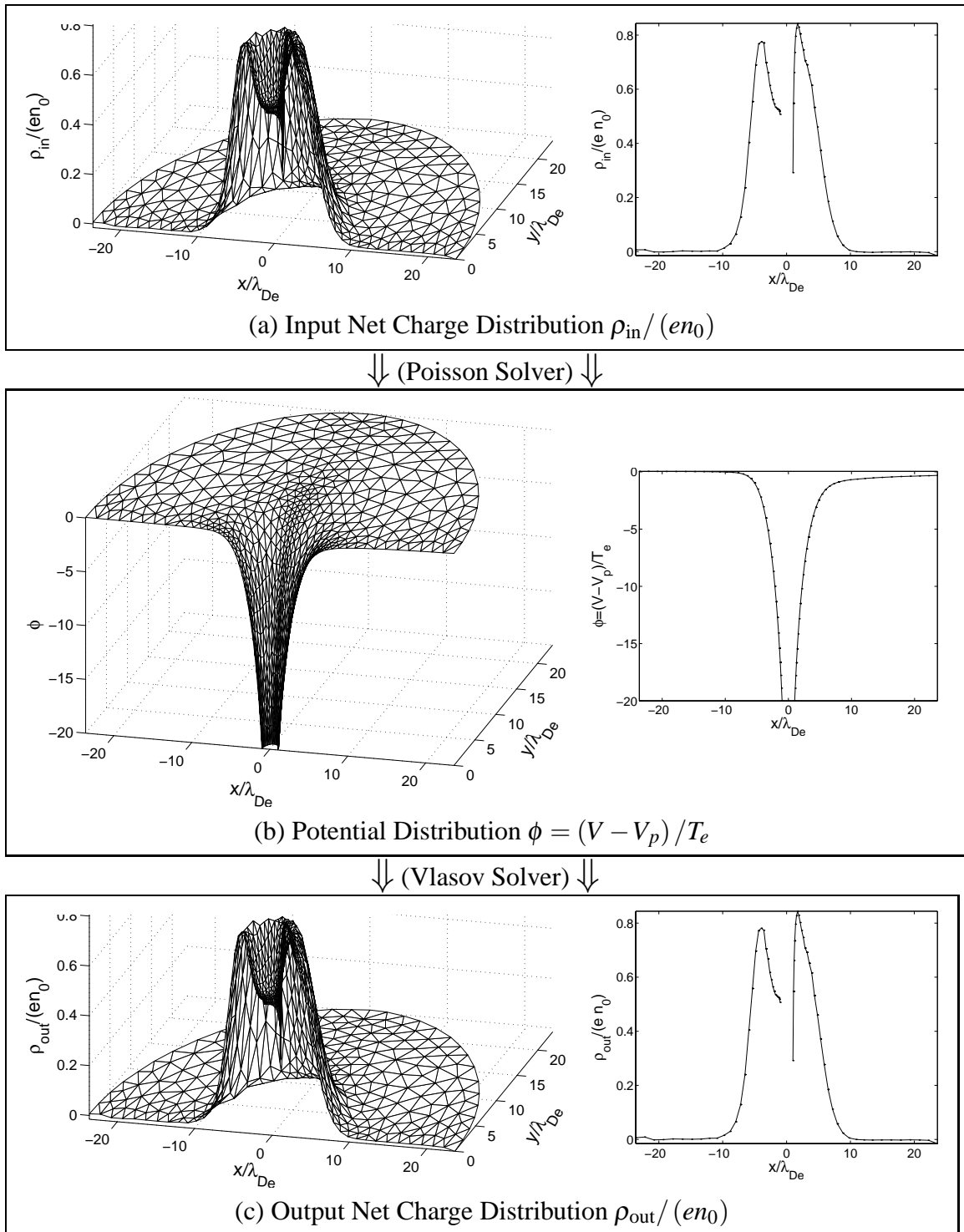


Figure 4.55: Poisson–Vlasov consistent solution for an ion-attracting cylinder ($r_0 = \lambda_{De}$) biased at $\phi_0 = -20$ and immersed in a flowing plasma with flow energy $U_{ev} = 0.66T_e$. Self-consistency is shown by the similarity of ρ_{in} and ρ_{out} . 2-D solutions are shown on the left, and corresponding x -axis cross-section profiles are shown on the right. Corresponding ion and electron density distributions are shown in Figure 4.56.

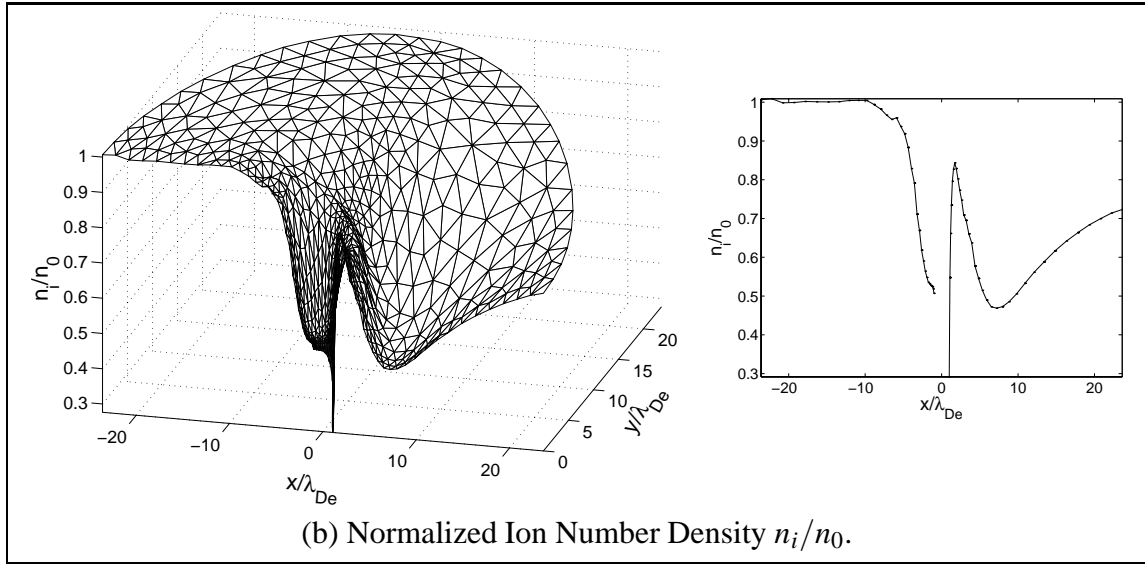
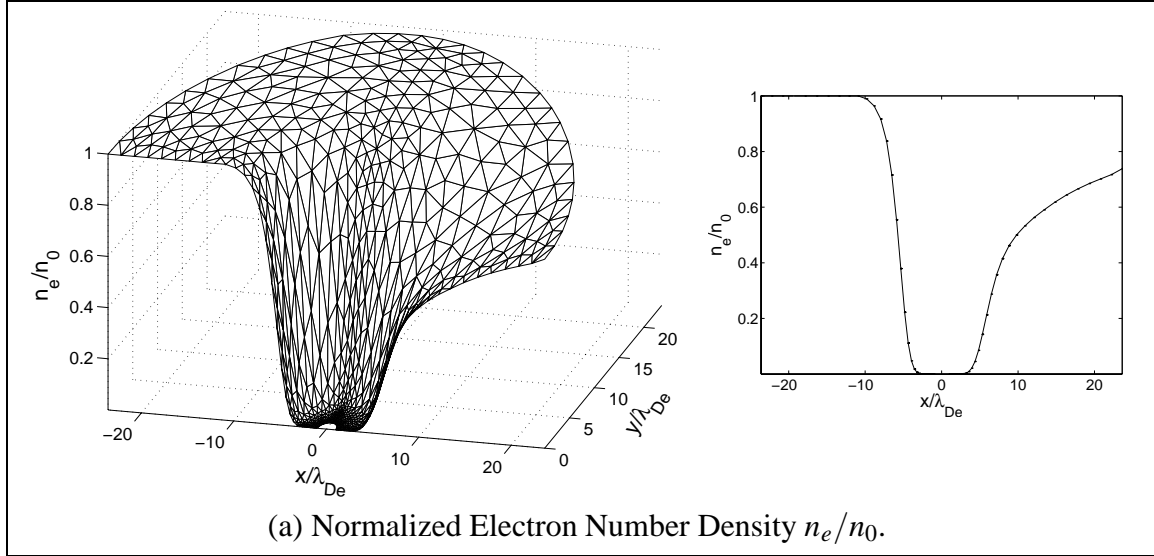
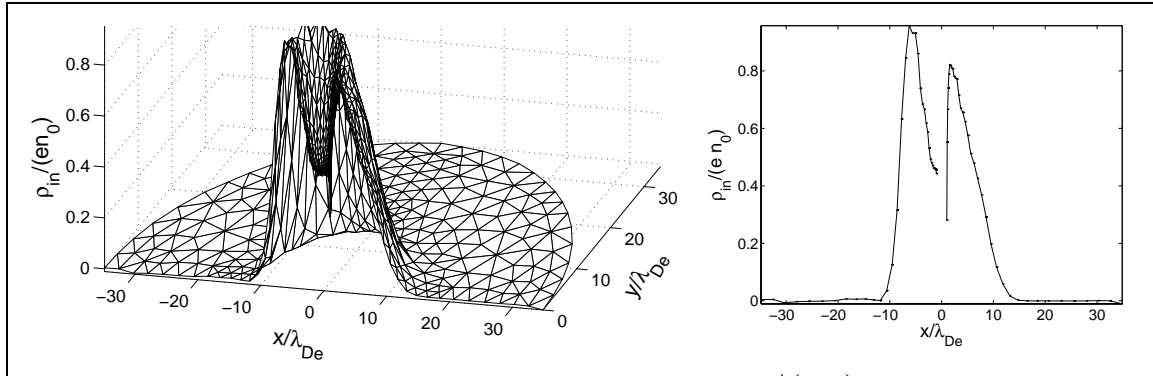
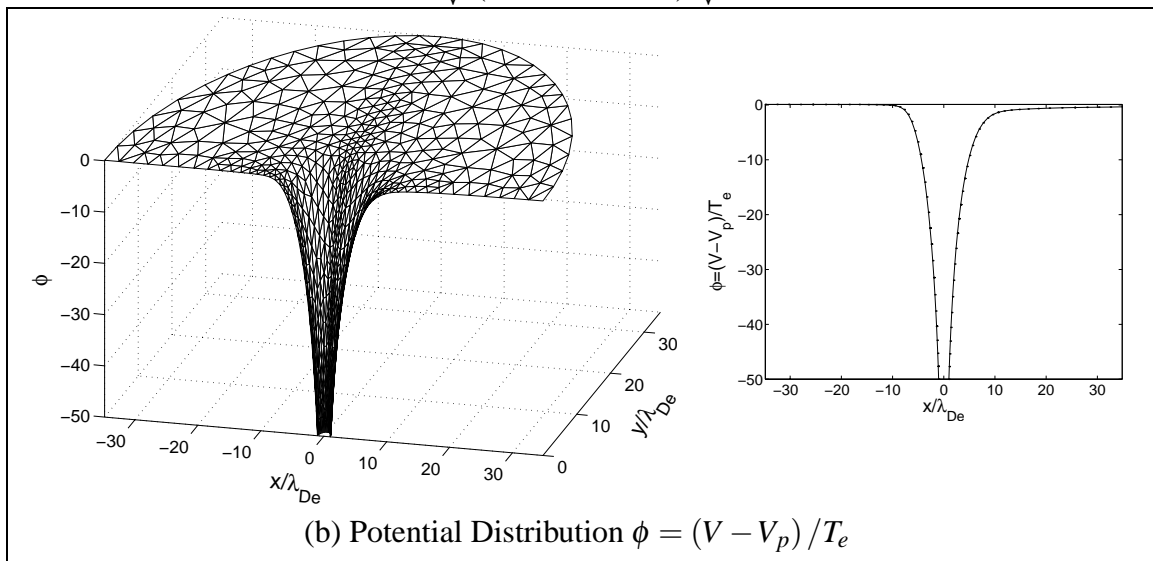


Figure 4.56: Poisson–Vlasov consistent electron and ion density distributions for an ion-attracting cylinder ($r_0 = \lambda_{De}$) biased at $\phi_0 = -20$ and immersed in a flowing plasma with flow energy $U_{ev} = 0.66T_e$. These density profiles constitute the output of the Vlasov solver and are subtracted to form the output net charge density profile $\vec{\rho}_{out} = e(\vec{n}_i - \vec{n}_e)$ shown in Figure 4.55(c).



\downarrow (Poisson Solver) \downarrow



\downarrow (Vlasov Solver) \downarrow

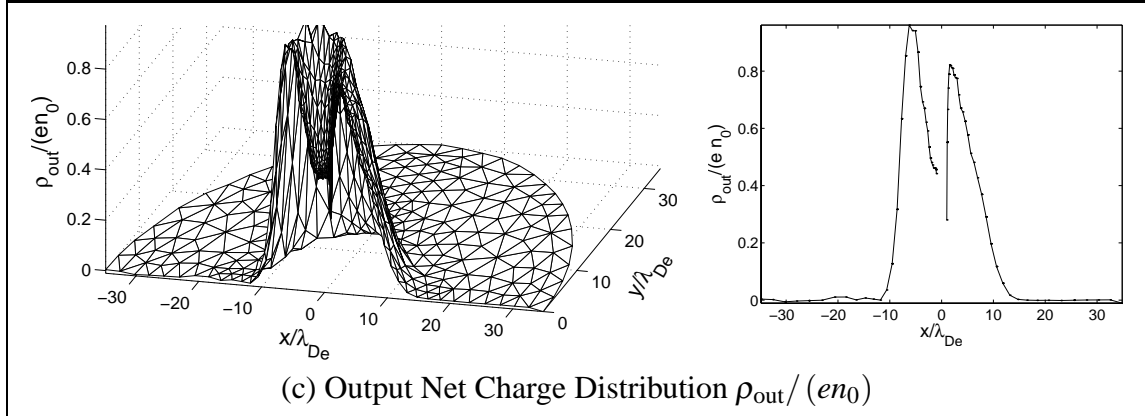


Figure 4.57: Poisson–Vlasov consistent solution for an ion-attracting cylinder ($r_0 = \lambda_{\text{De}}$) biased at $\phi_0 = -50$ and immersed in a flowing plasma with flow energy $U_{\text{ev}} = 0.66T_e$. Self-consistency is shown by the similarity of ρ_{in} and ρ_{out} . 2-D solutions are shown on the left, and corresponding x -axis cross-section profiles are shown on the right. Corresponding ion and electron density distributions are shown in Figure 4.58.

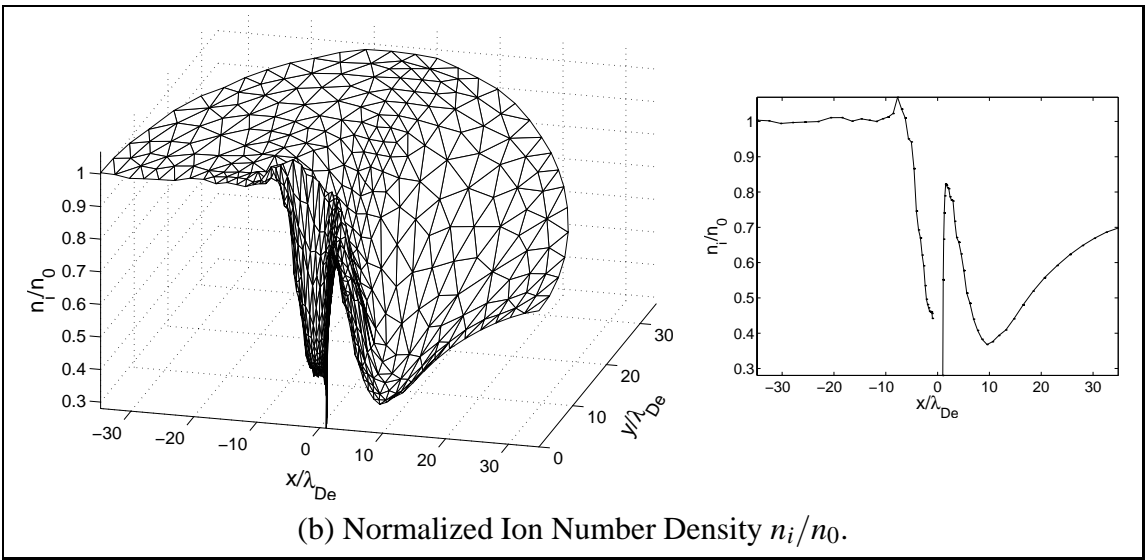
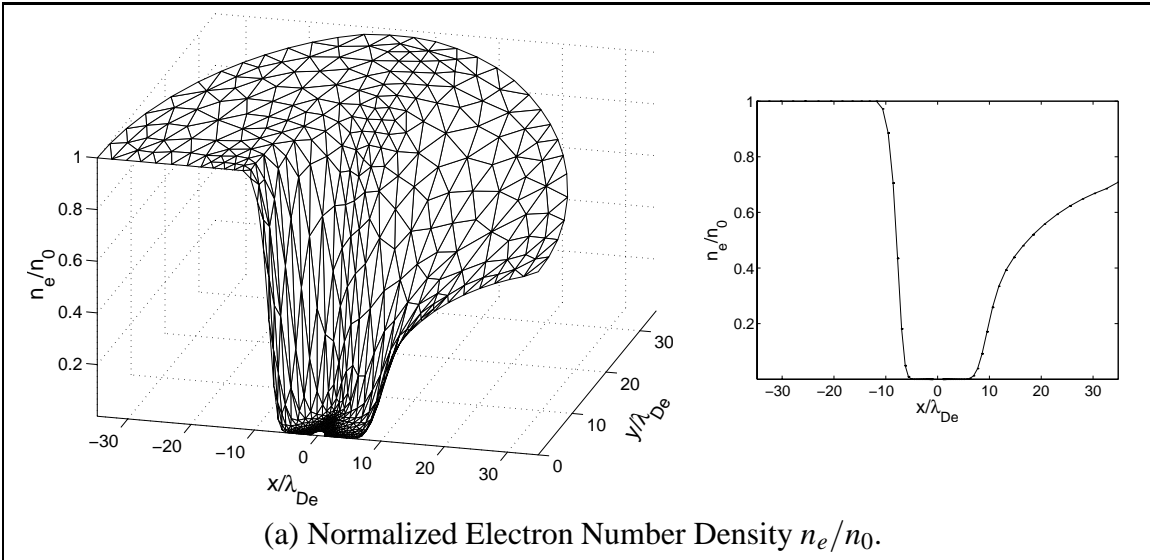


Figure 4.58: Poisson–Vlasov consistent electron and ion density distributions for an ion-attracting cylinder ($r_0 = \lambda_{De}$) biased at $\phi_0 = -50$ and immersed in a flowing plasma with flow energy $U_{ev} = 0.66T_e$. These density profiles constitute the output of the Vlasov solver and are subtracted to form the output net charge density profile $\vec{\rho}_{out} = e(\vec{n}_i - \vec{n}_e)$ shown in Figure 4.57(c).

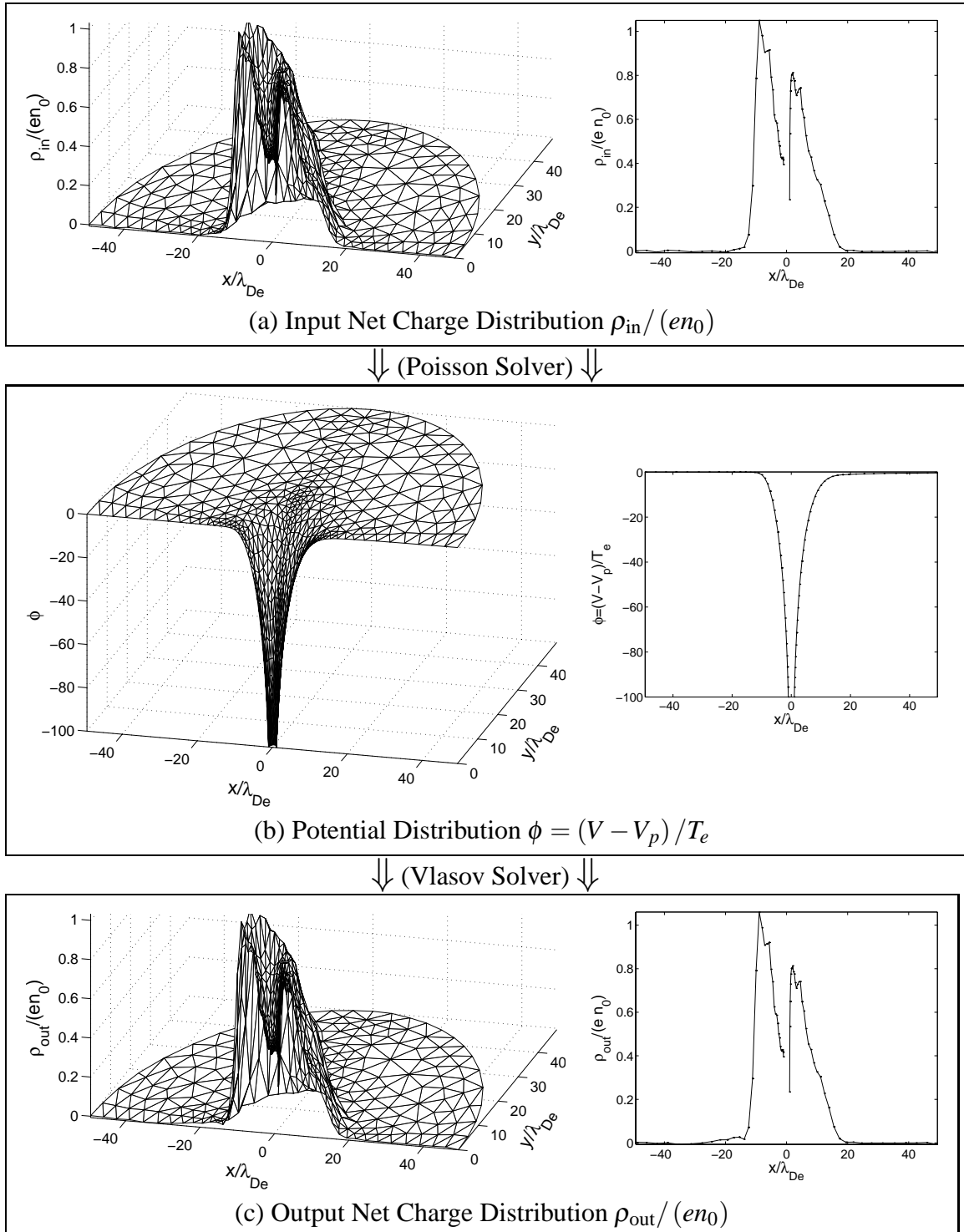


Figure 4.59: Poisson–Vlasov consistent solution for an ion-attracting cylinder ($r_0 = \lambda_{\text{De}}$) biased at $\phi_0 = -100$ and immersed in a flowing plasma with flow energy $U_{\text{ev}} = 0.66T_e$. Self-consistency is shown by the similarity of ρ_{in} and ρ_{out} . 2-D solutions are shown on the left, and corresponding x -axis cross-section profiles are shown on the right. Corresponding ion and electron density distributions are shown in Figure 4.60.

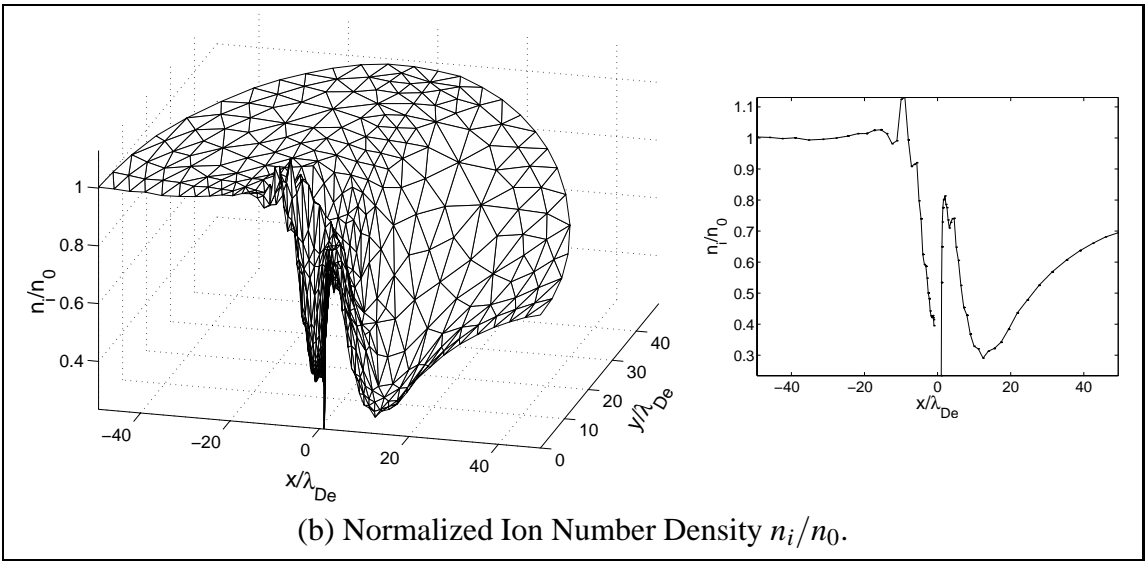
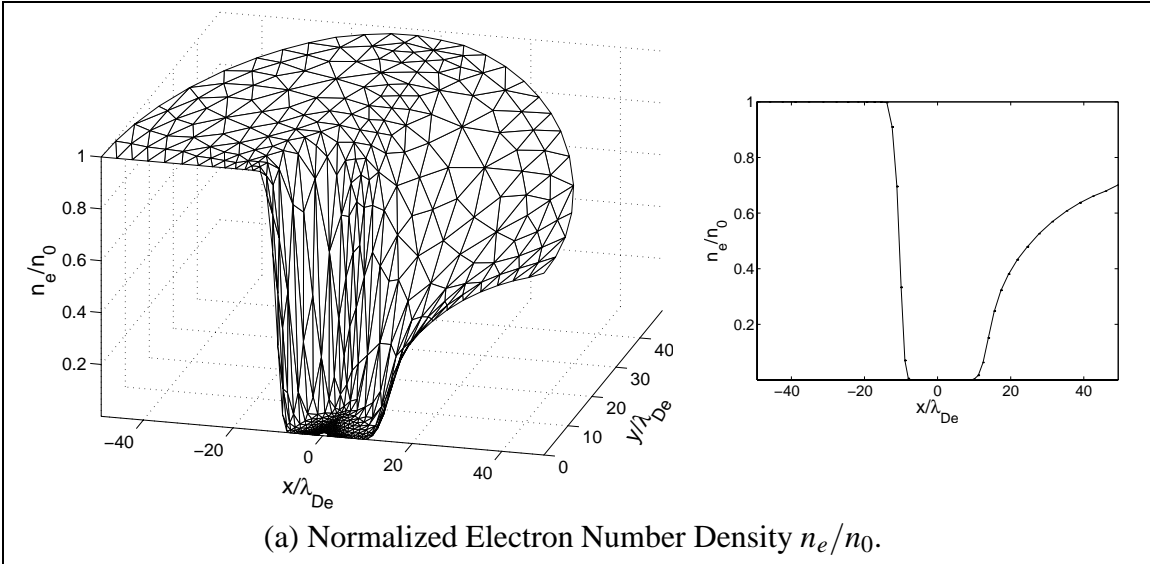


Figure 4.60: Poisson–Vlasov consistent electron and ion density distributions for an ion-attracting cylinder ($r_0 = \lambda_{De}$) biased at $\phi_0 = -100$ and immersed in a flowing plasma with flow energy $U_{ev} = 0.66T_e$. These density profiles constitute the output of the Vlasov solver and are subtracted to form the output net charge density profile $\vec{\rho}_{out} = e(\vec{n}_i - \vec{n}_e)$ shown in Figure 4.59(c).

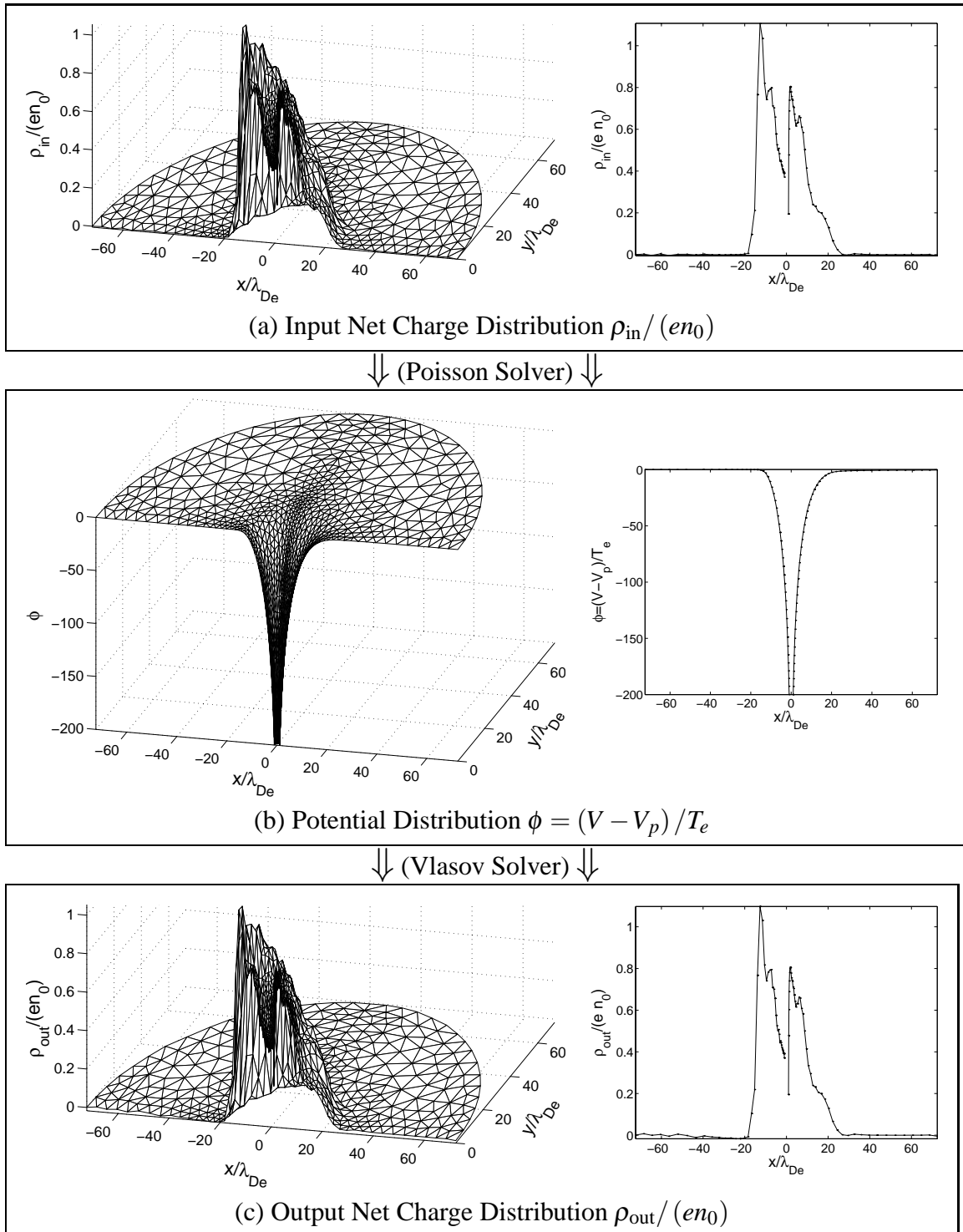


Figure 4.61: Poisson–Vlasov consistent solution for an ion-attracting cylinder ($r_0 = \lambda_{\text{De}}$) biased at $\phi_0 = -200$ and immersed in a flowing plasma with flow energy $U_{\text{ev}} = 0.66T_e$. Self-consistency is shown by the similarity of ρ_{in} and ρ_{out} . 2-D solutions are shown on the left, and corresponding x -axis cross-section profiles are shown on the right. Corresponding ion and electron density distributions are shown in Figure 4.62.

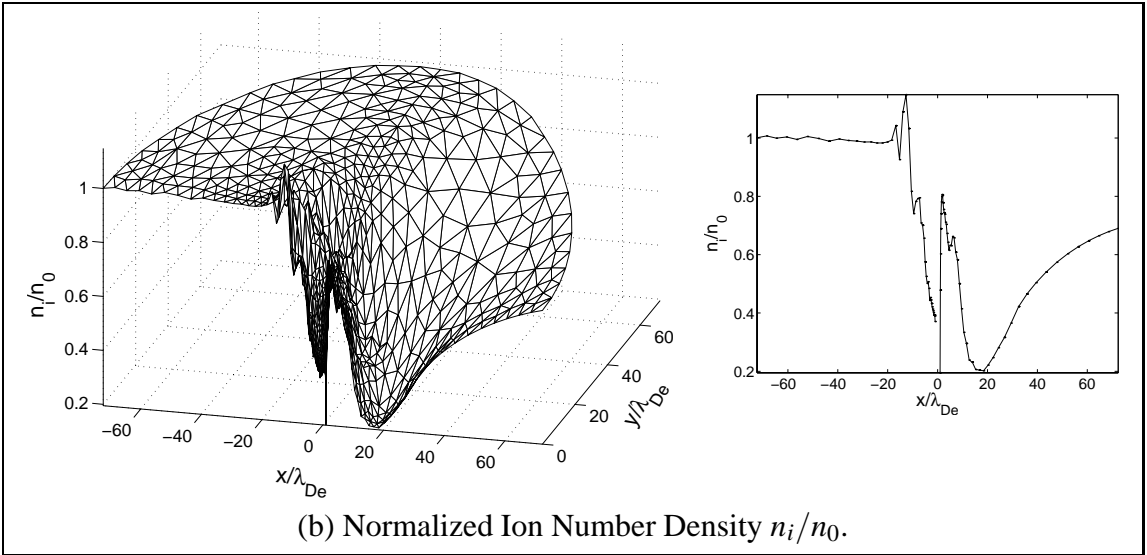
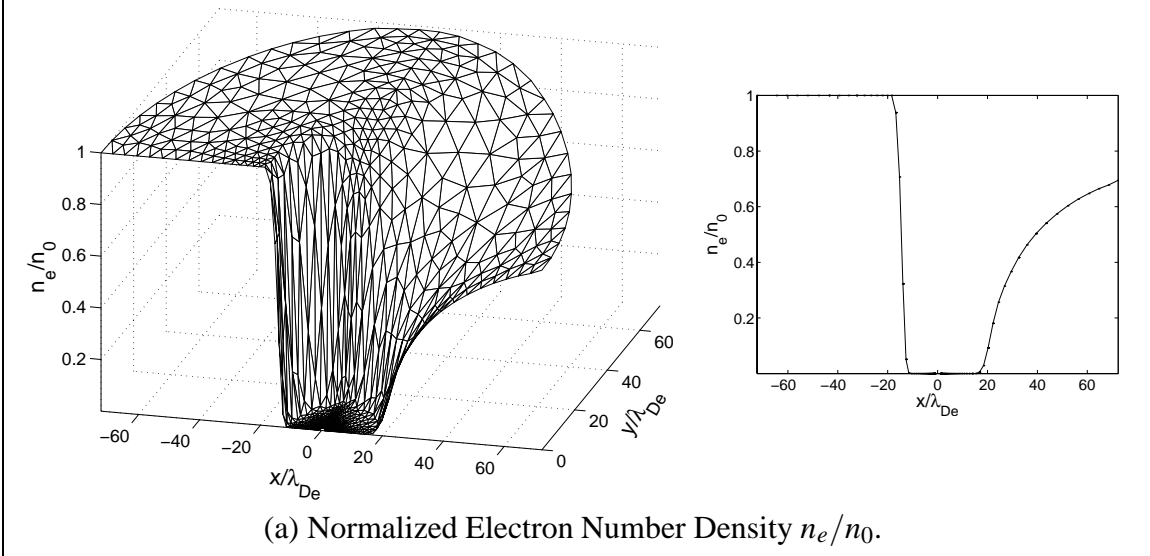


Figure 4.62: Poisson–Vlasov consistent electron and ion density distributions for an ion-attracting cylinder ($r_0 = \lambda_{De}$) biased at $\phi_0 = -200$ and immersed in a flowing plasma with flow energy $U_{ev} = 0.66T_e$. These density profiles constitute the output of the Vlasov solver and are subtracted to form the output net charge density profile $\vec{\rho}_{out} = e(\vec{n}_i - \vec{n}_e)$ shown in Figure 4.61(c).

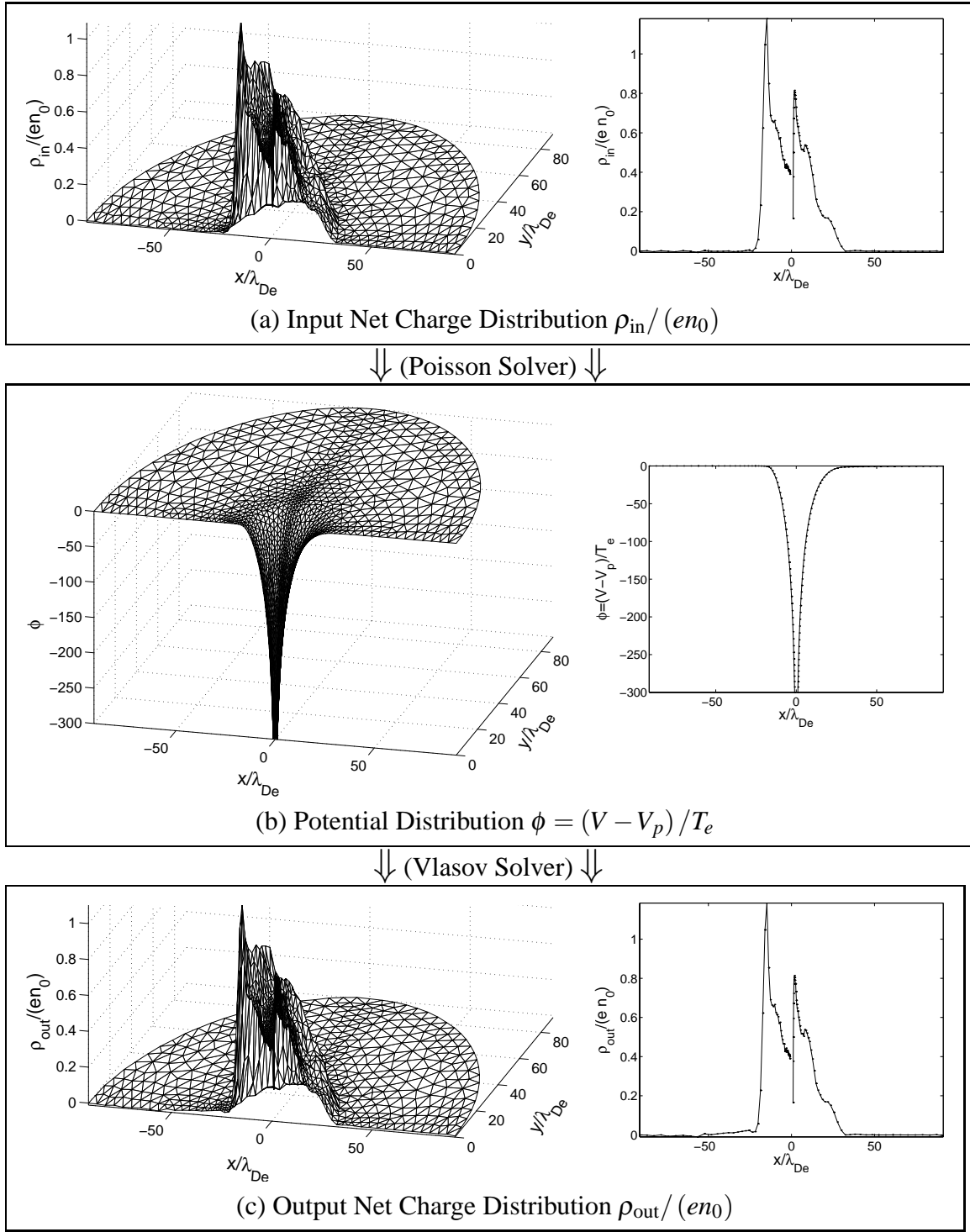


Figure 4.63: Poisson–Vlasov consistent solution for an ion-attracting cylinder ($r_0 = \lambda_{De}$) biased at $\phi_0 = -300$ and immersed in a flowing plasma with flow energy $U_{ev} = 0.66T_e$. Self-consistency is shown by the similarity of ρ_{in} and ρ_{out} . 2-D solutions are shown on the left, and corresponding x -axis cross-section profiles are shown on the right. Corresponding ion and electron density distributions are shown in Figure 4.64.

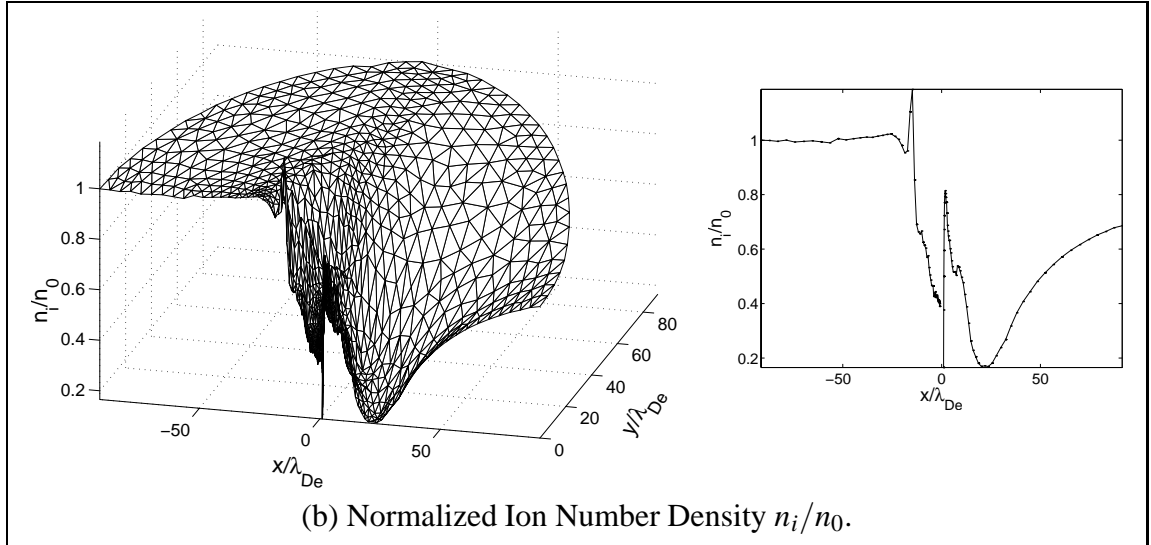
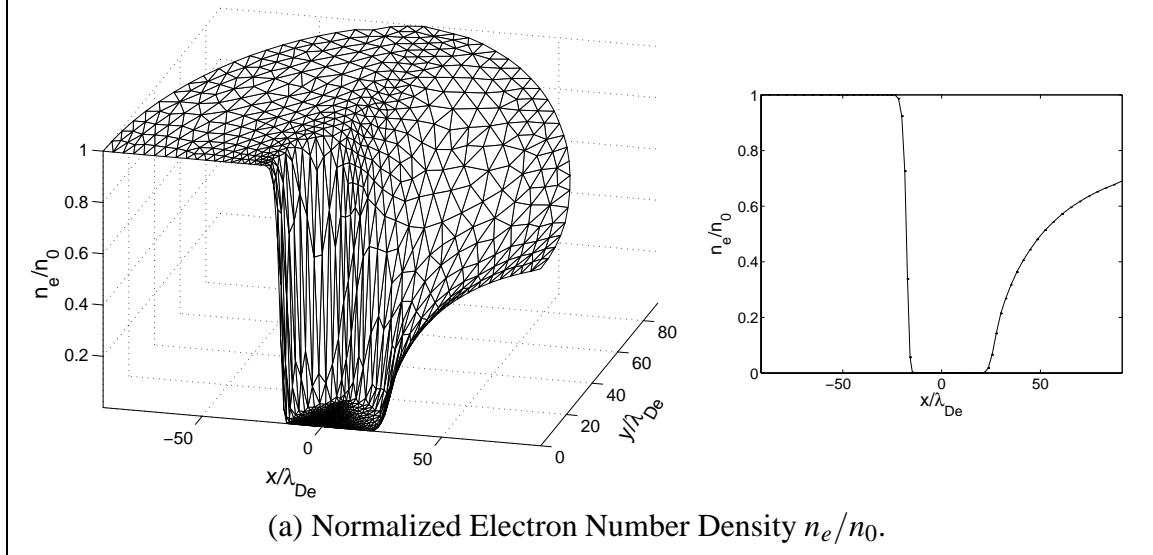


Figure 4.64: Poisson–Vlasov consistent electron and ion density distributions for an ion-attracting cylinder ($r_0 = \lambda_{De}$) biased at $\phi_0 = -300$ and immersed in a flowing plasma with flow energy $U_{ev} = 0.66T_e$. These density profiles constitute the output of the Vlasov solver and are subtracted to form the output net charge density profile $\vec{\rho}_{out} = e(\vec{n}_i - \vec{n}_e)$ shown in Figure 4.63(c).

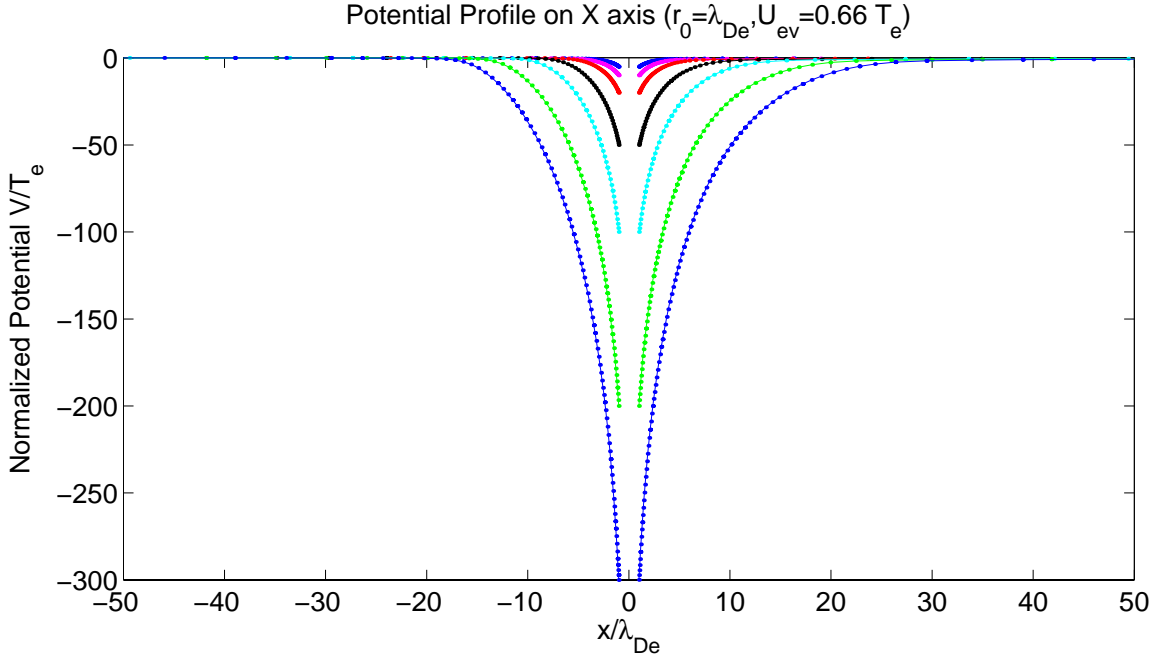


Figure 4.65: Set of curves of the axial potential profiles corresponding to various bias potentials for a one-Debye-length-radius round cylinder immersed in a flowing plasma with flow energy $U_{ev} = 0.66T_e$. The profiles are taken along the axis of the flow.

4.5.4.3 Plasma Flow Effects on Sheath Structure and Dimensions

One wonders what the overall effect of this asymmetric distribution will be on the sheath structure and size, since the main parameter of interest for charge precipitation applications is the overall sheath size. Using the concept of *effective sheath area* A_s which we defined in Section 4.3.5, we now proceed to a similar analysis as that which was performed in Section 4.3.6 for the two-cylinder configuration.

Figure 4.67 depicts the variation of the effective sheath area ratio, defined by (4.27), as a function of bias potential, for a round cylinder with a radius $r_0 = \lambda_{De}$ immersed in a flowing plasma with flow energy $U_{ev} = 0.66T_e$. The plot suggests that the effective sheath ratio stabilizes near half (50%) of the stationary effective sheath area, and there is no indication that this ratio would increase back to higher levels at larger bias potentials. However, simulations should be performed at higher bias potentials to confirm the observed trend. It

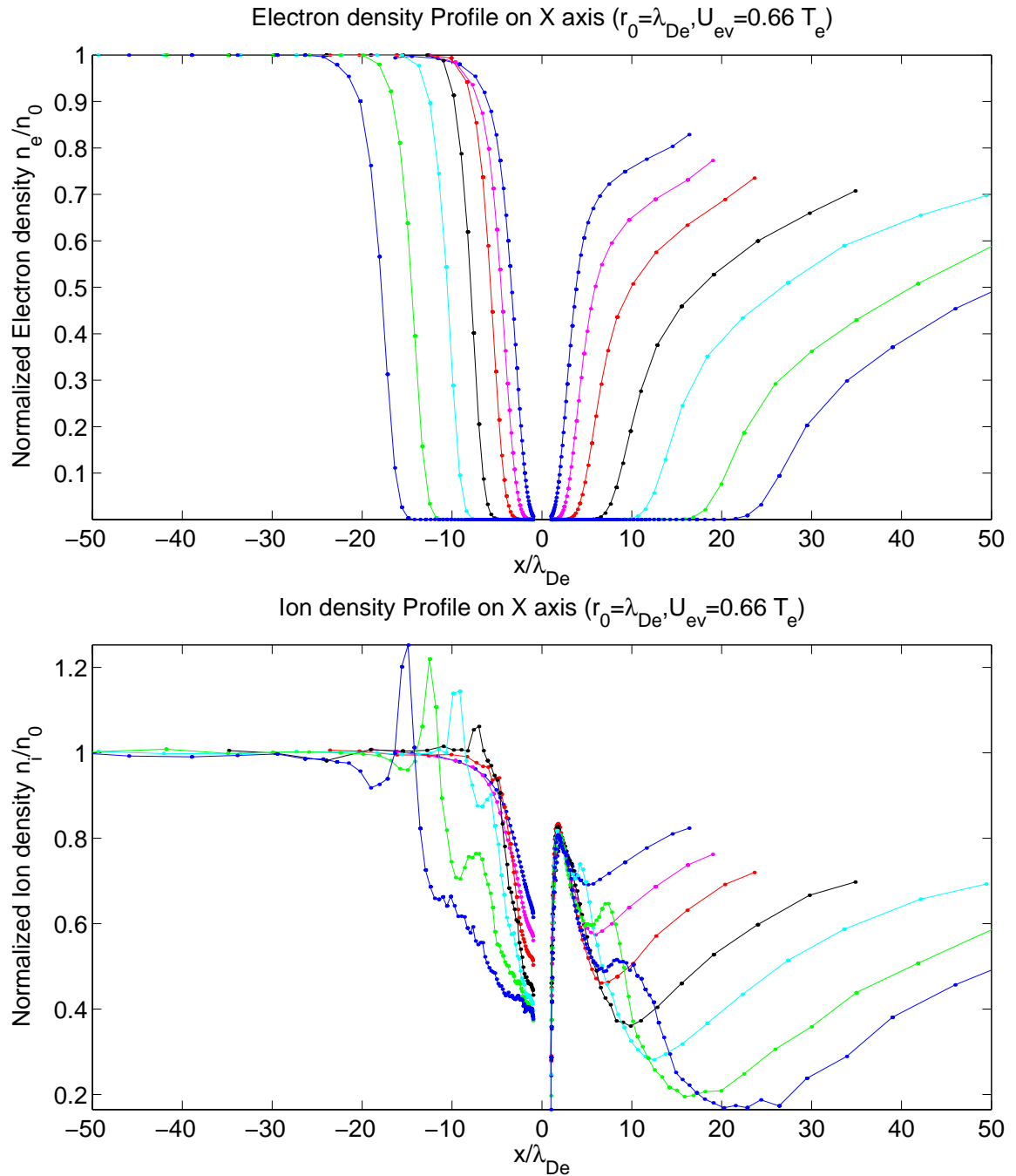


Figure 4.66: Set of curves of the electron and ion axial density profiles corresponding to various bias potentials for a one-Debye-length-radius round cylinder immersed in a flowing plasma with flow energy $U_{ev} = 0.66 T_e$. The profiles are taken along the axis of the flow.

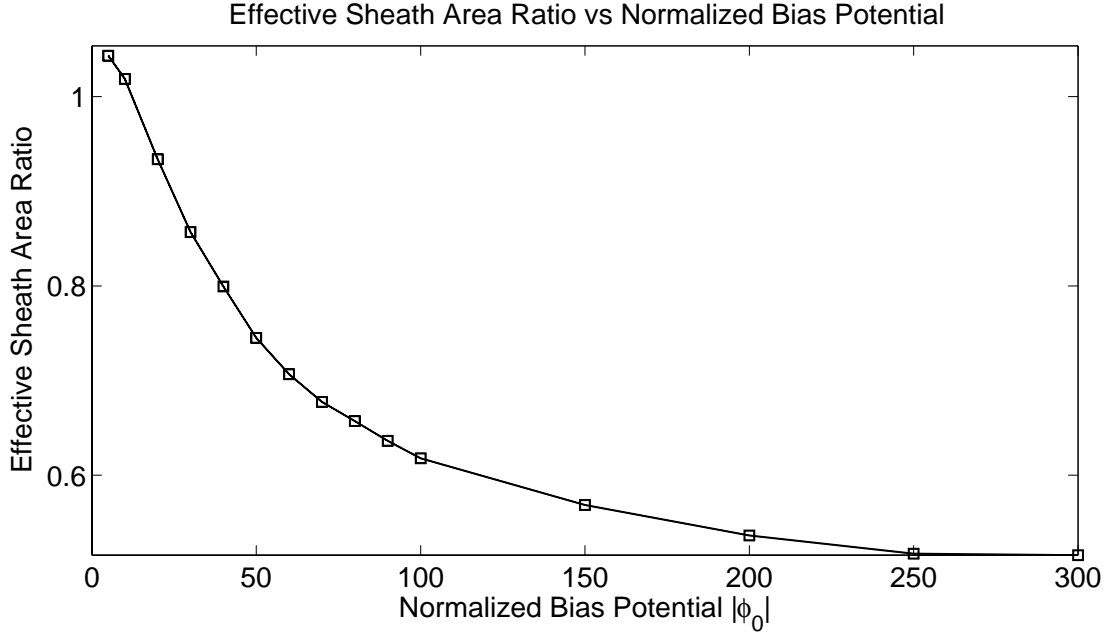


Figure 4.67: Effective sheath area ratio R_{A_s} as a function of normalized bias potential for an ion-attracting single round cylinder immersed in a flowing plasma with flow energy $U_{ev} = 0.66T_e$. The cylinder has a radius $r_0 = \lambda_{De}$. The effective sheath area ratio is the ratio of the sheath area obtained with a flowing plasma to that obtained at the same bias potential in a stationary plasma.

should be noted that this 50% reduction of the effective sheath *area* really corresponds to about a 30% reduction of the effective sheath radius, as compared to the non-flowing case ($1 - \sqrt{0.5} \approx 0.3$).

Figure 4.68 depicts the variation of the cylinder's surface charge as a function of bias potential. The displayed graph is normalized with respect to the surface charge held by an identical cylinder immersed in a stationary plasma. The excess surface charge is consistent with the reduced effective sheath areas shown in Figure 4.67, since they are directly related through (4.26), our definition of the effective sheath area. The surface charge peaks to a value of about 13.2% above the stationary surface charge at $\phi_0 = -250$, and then starts decreasing slowly.

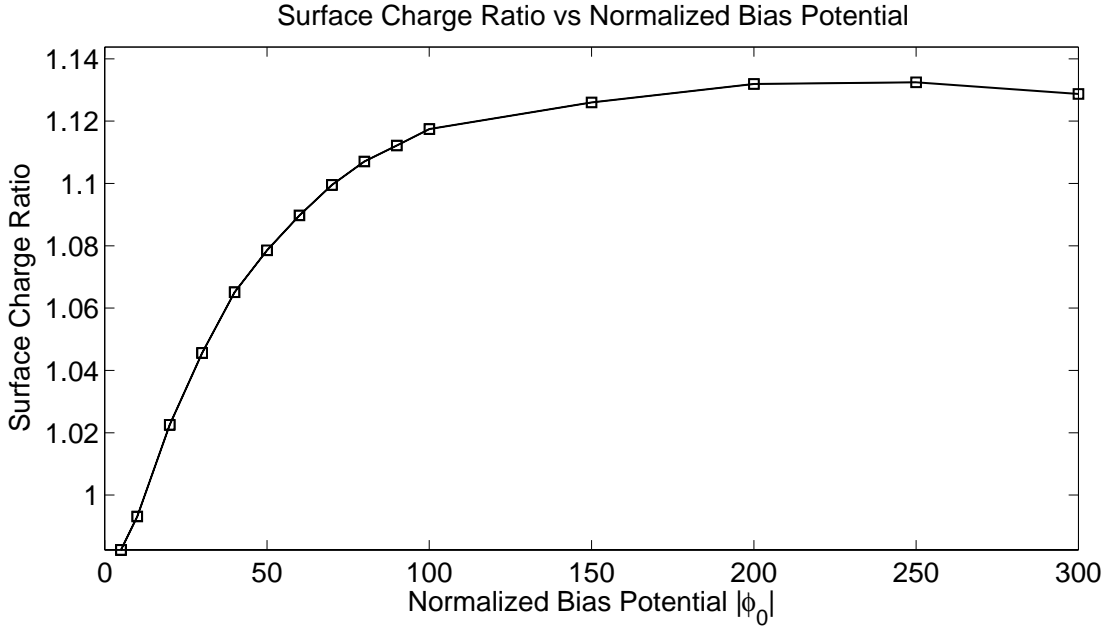


Figure 4.68: Ratio of surface charge to the “stationary” surface charge as a function of normalized bias potential, for an ion-attracting single round cylinder immersed in a flowing plasma with flow energy $U_{\text{ev}} = 0.66T_e$. The cylinder has a radius $r_0 = \lambda_{\text{De}}$.

4.5.4.4 Plasma Flow Effect on Ion Current Collection

Figure 4.69 depicts the variation of the ion current ratio as a function of normalized bias potential ϕ_0 . This “current ratio” is simply the ratio of the current collected with flow, I_{flow} , to the current collected without flow, I_{noflow} , for a given bias potential. The ratio is seen to drop below 0.7 and possibly follows an asymptotic behavior with an asymptote of about 0.65. This is consistent with the very low ionic density observed in Section 4.5.4.2 on the wake side of the cylinder’s surface. This current reduction is actually a unique feature of low flow energies, since as the lower graph in Figure 4.49 shows, a current reduction only occurs for a limited range of flow speeds, beyond which current enhancement becomes the norm.

For the particle precipitation application, the reduction of the sheath area observed in Section 4.5.4.3 will therefore be somewhat compensated by a reduction of the collected ion current. This implies that, for a given power budget, the bias potential could be set higher

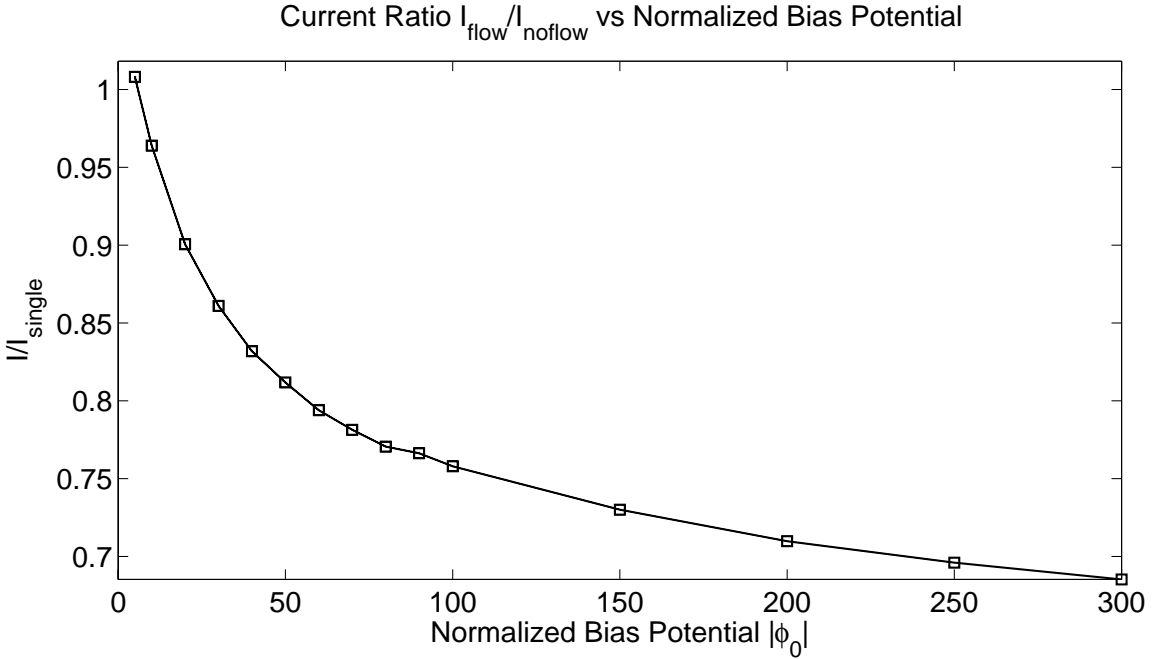


Figure 4.69: Current ratio as a function of normalized bias potential for an ion-attracting single round cylinder immersed in a flowing plasma with flow energy $U_{\text{ev}} = 0.66T_e$. The current ratio is defined as the ratio of the collected current to the current that would be collected by an identical cylinder immersed in a stationary plasma. The cylinder has a radius $r_0 = \lambda_{\text{De}}$.

in a flowing plasma than in a stationary plasma for equal current collection. The higher bias potential setting in the flowing plasma might help gaining back some or all of the “lost” sheath area.

4.6 Flow Effects on Electron-Attracting Round Cylinder

In this section, we discuss the effect of plasma flow on sheath structure and current collection to electron-attracting round cylinders. We concentrate on the same speed regime as in Section 4.5, that is, velocities U much smaller than the electron thermal velocity. Thus, any flow effect on the electron current collection is indirect, since the electron population is not drifting for all practical purposes. The electron density distribution and electron current collection can only be affected indirectly by the potential asymmetries induced by the ion

flow.

In the following analysis, we will only consider a single value of the normalized bias potential, $\phi_0 = 20$, and study the effect of flow speed on the sheath structure and current collection. We will then compare the simulated electron current collection to that observed experimentally in Chapter 3.

4.6.1 Potential and Density Profiles

In Figures 4.70 through 4.77, we show some examples of plasma profiles pertaining to an electron-attracting round cylinder biased at $\phi_0 = 20$ for various flow energies spanning from $U_{ev} = 0.2T_e$ to $U_{ev} = 1.5T_e$. The self-consistency of the results is illustrated by the fact that the input and output net charge density distributions $\vec{\rho}_{in}$ and $\vec{\rho}_{out}$ are very close to one another.

Although the potential profile corresponding to the lowest flow setting of $U_{ev} = 0.2T_e$ (shown in Figure 4.70) only shows what appears to be a minor asymmetry, a significant effect is seen on both density profiles, but especially on the electron density profile (the attracted species). The latter shows, on the ram side of the cylinder, a quasi-absence of the usual density drop associated with the shadowing effect and angular momentum limitations, and a deepening of the density drop on the wake side. The asymmetry allows more electrons to penetrate closer to the cylinder on the ram side, while increasing the shadowing effect of the cylinder on the wake side due to an increased focusing of the shadowed trajectories. At $U_{ev} = 0.2T_e$, the plasma flow is not sufficiently energetic to prevent electrons from reaching the wake-side surface of the cylinder, which is why a near-OML electron density (just short of half the ambient density) is seen in Figure 4.71 for both the ram and wake sides of the cylinder.

As the flow speed increases to higher values, several observations can be made:

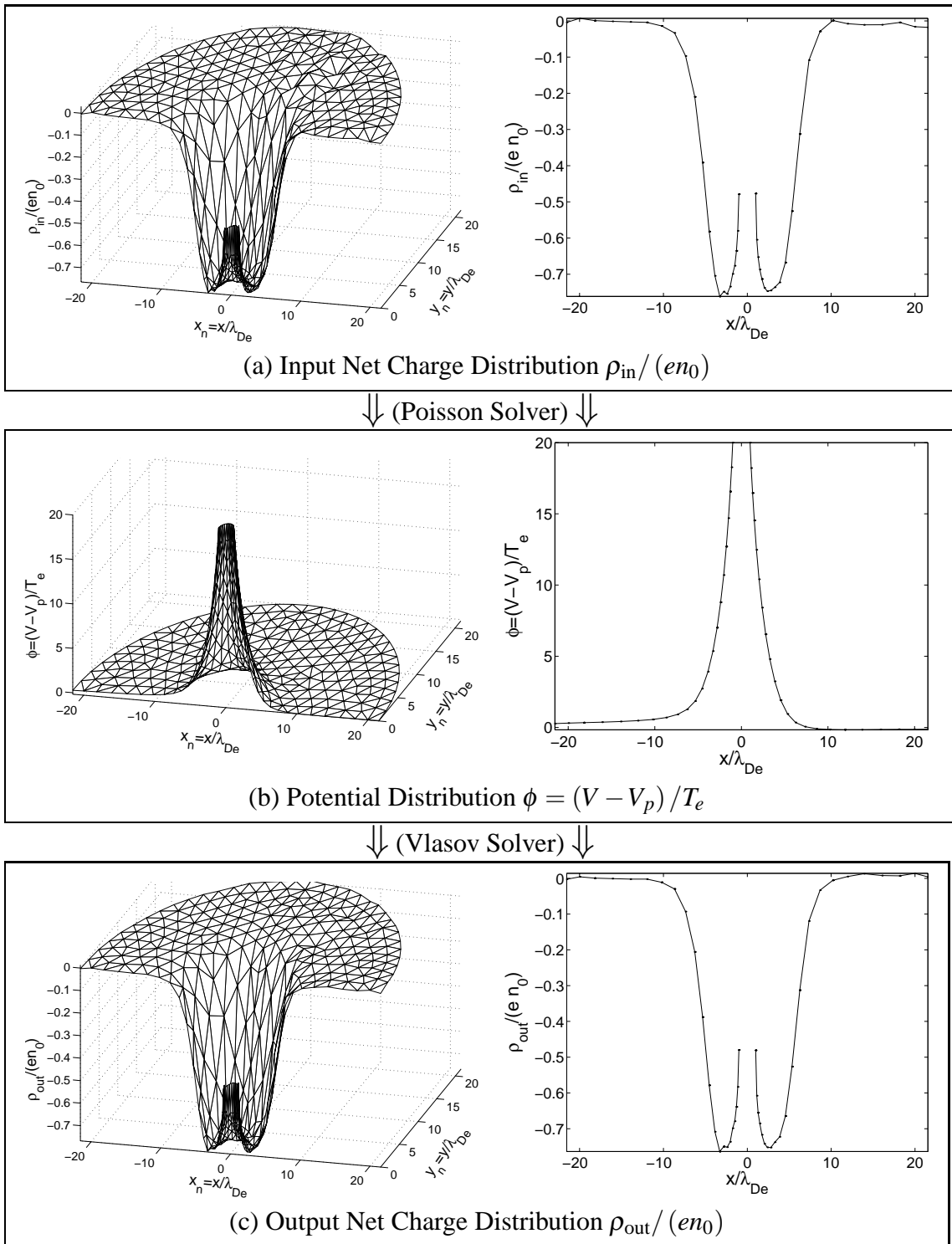


Figure 4.70: Poisson–Vlasov consistent solution for an electron-attracting cylinder ($r_0 = \lambda_{De}$) biased at $\phi_0 = 20$ and immersed in a flowing plasma with flow energy $U_{ev} = 0.2 T_e$. Self-consistency is shown by the similarity of ρ_{in} and ρ_{out} . 2-D solutions are shown on the left, and corresponding x -axis cross-section profiles are shown on the right. Ion and Electron density dist. are shown in Figure 4.71.

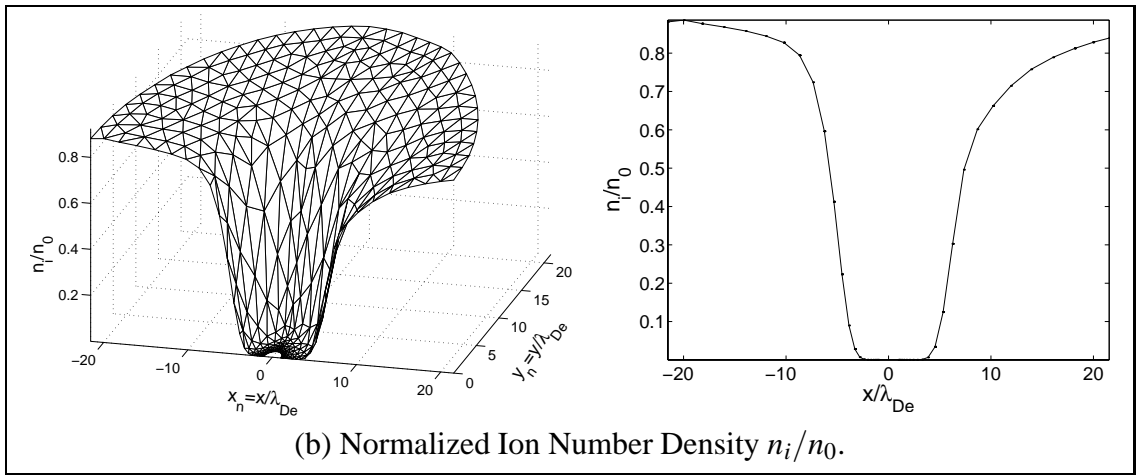
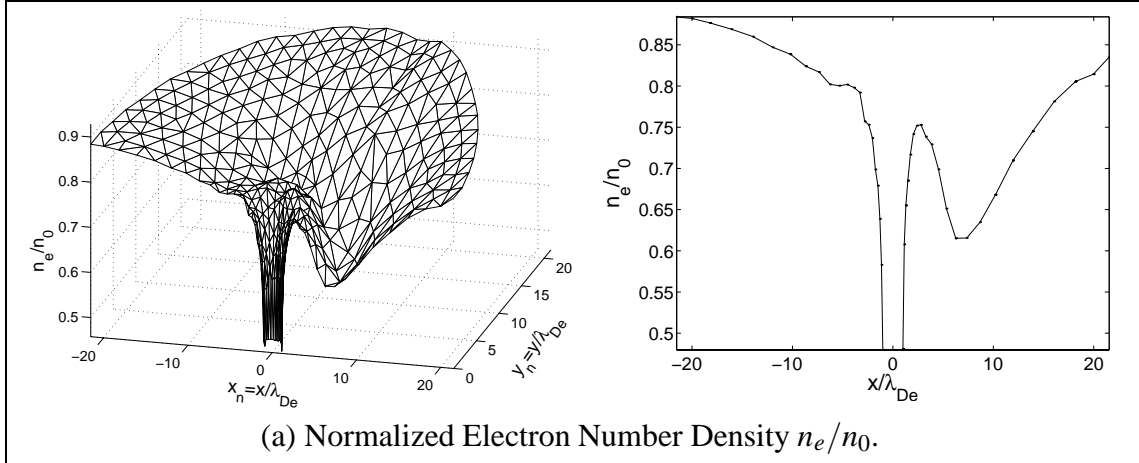


Figure 4.71: Poisson–Vlasov consistent electron and ion density distributions for an electron-attracting cylinder ($r_0 = \lambda_{De}$) biased at $\phi_0 = 20$ and immersed in a flowing plasma with flow energy $U_{ev} = 0.2 T_e$. These density profiles constitute the output of the Vlasov solver and are combined to form the output net charge density profile $\vec{\rho}_{out} = e(\vec{n}_i - \vec{n}_e)$ shown in Figure 4.70(c).

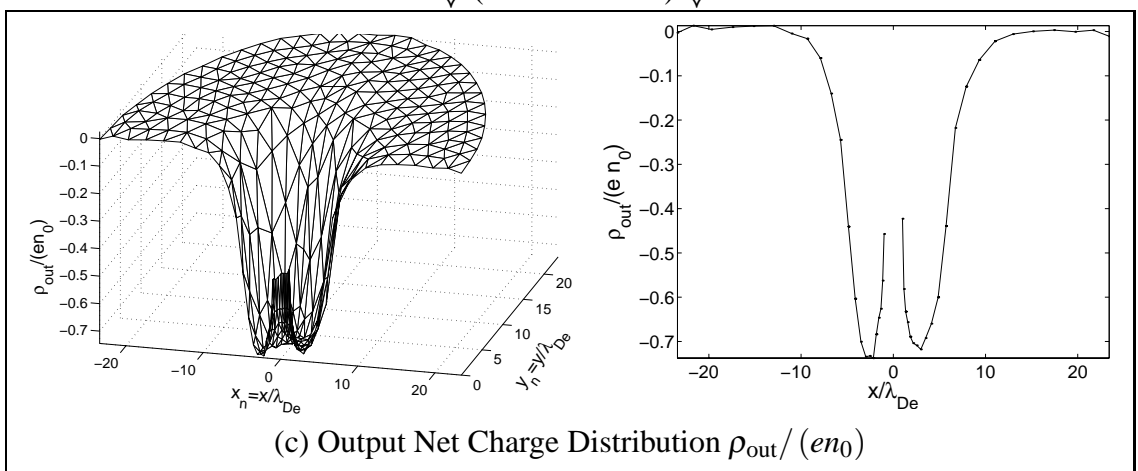
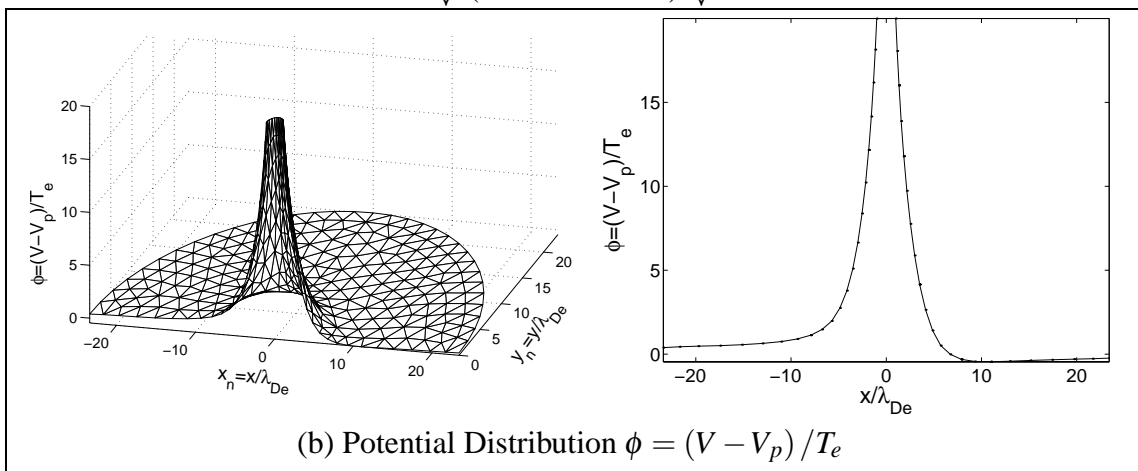
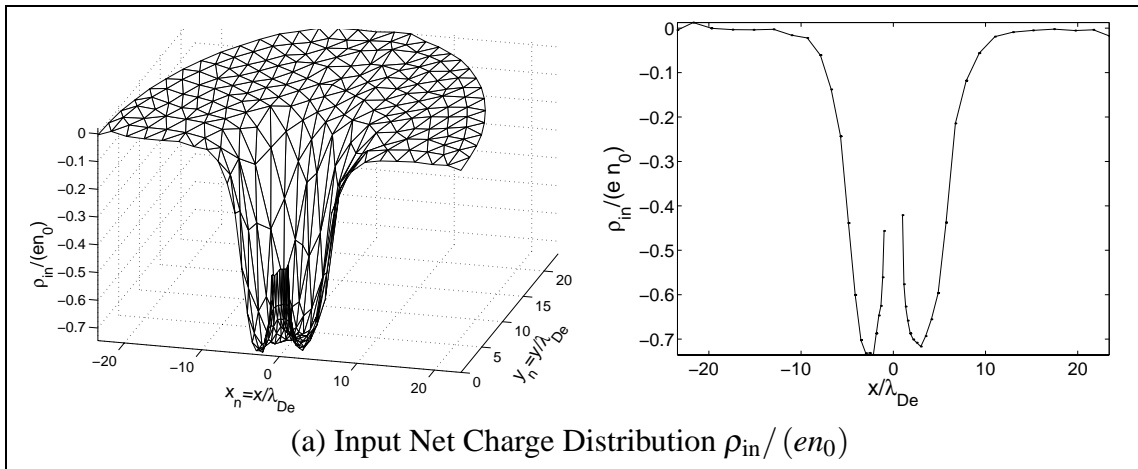


Figure 4.72: Poisson–Vlasov consistent solution for an electron-attracting cylinder ($r_0 = \lambda_{\text{De}}$) biased at $\phi_0 = 20$ and immersed in a flowing plasma with flow energy $U_{\text{ev}} = 0.5 T_e$. Self-consistency is shown by the similarity of ρ_{in} and ρ_{out} . 2-D solutions are shown on the left, and corresponding x -axis cross-section profiles are shown on the right. Ion and Electron density dist. are shown in Figure 4.73.

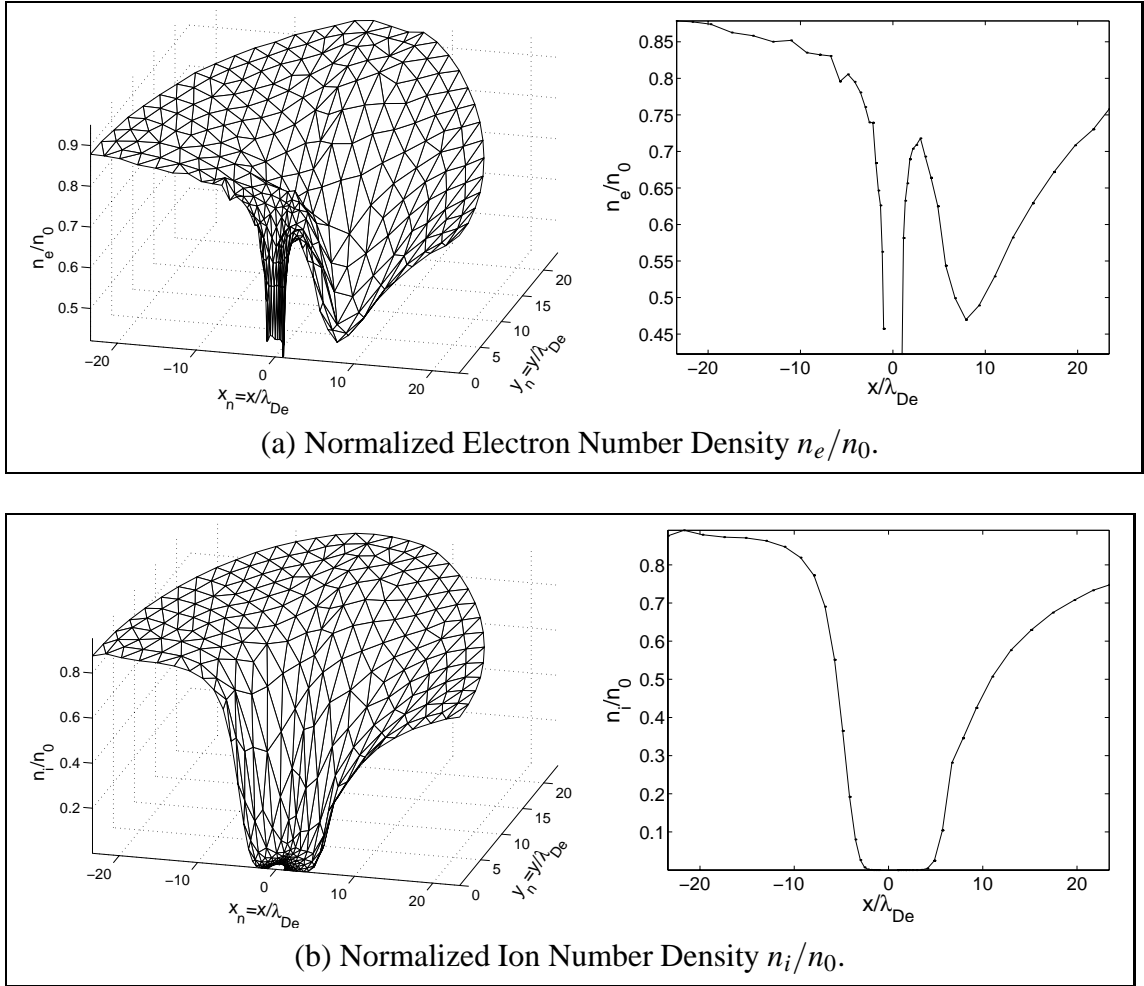


Figure 4.73: Poisson–Vlasov consistent electron and ion density distributions for an electron-attracting cylinder ($r_0 = \lambda_{De}$) biased at $\phi_0 = 20$ and immersed in a flowing plasma with flow energy $U_{ev} = 0.5 T_e$. These density profiles constitute the output of the Vlasov solver and are combined to form the output net charge density profile $\vec{\rho}_{out} = e(\vec{n}_i - \vec{n}_e)$ shown in Figure 4.72(c).

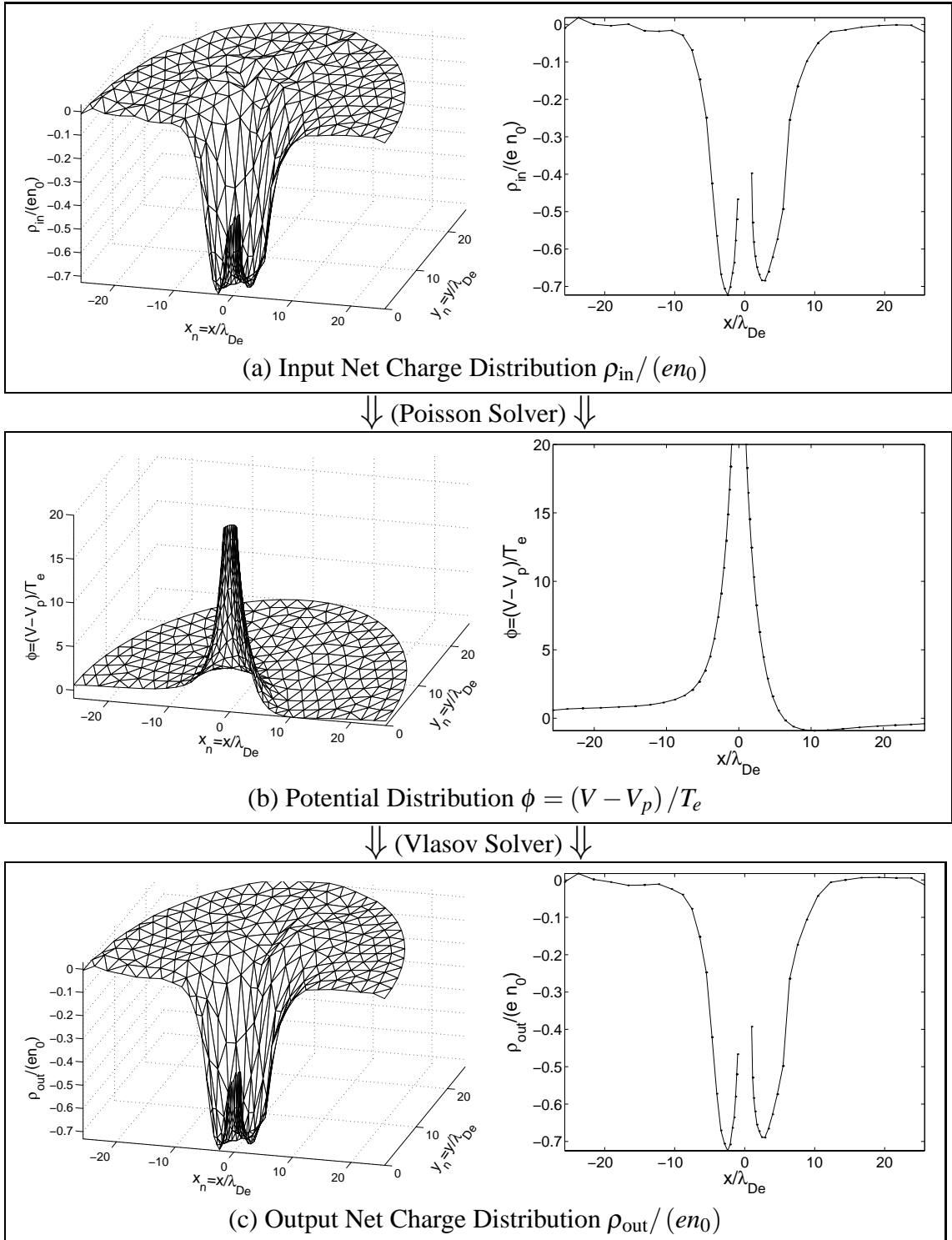


Figure 4.74: Poisson–Vlasov consistent solution for an electron-attracting cylinder ($r_0 = \lambda_{\text{De}}$) biased at $\phi_0 = 20$ and immersed in a flowing plasma with flow energy $U_{\text{ev}} = T_e$. Self-consistency is shown by the similarity of ρ_{in} and ρ_{out} . 2-D solutions are shown on the left, and corresponding x -axis cross-section profiles are shown on the right. Ion and Electron density dist. are shown in Figure 4.75.

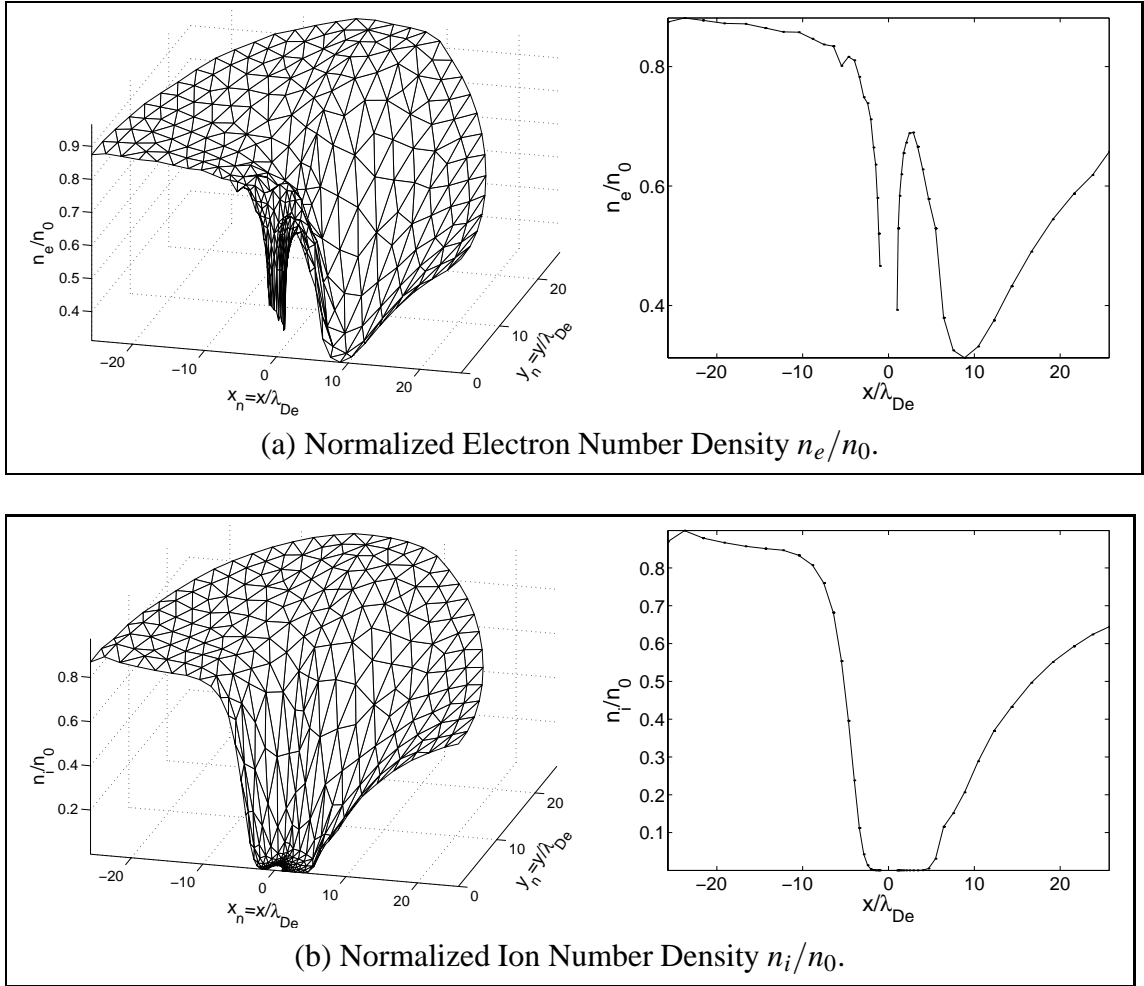


Figure 4.75: Poisson–Vlasov consistent electron and ion density distributions for an electron-attracting cylinder ($r_0 = \lambda_{De}$) biased at $\phi_0 = 20$ and immersed in a flowing plasma with flow energy $U_{ev} = T_e$. These density profiles constitute the output of the Vlasov solver and are combined to form the output net charge density profile $\vec{\rho}_{out} = e(\vec{n}_i - \vec{n}_e)$ shown in Figure 4.74(c).

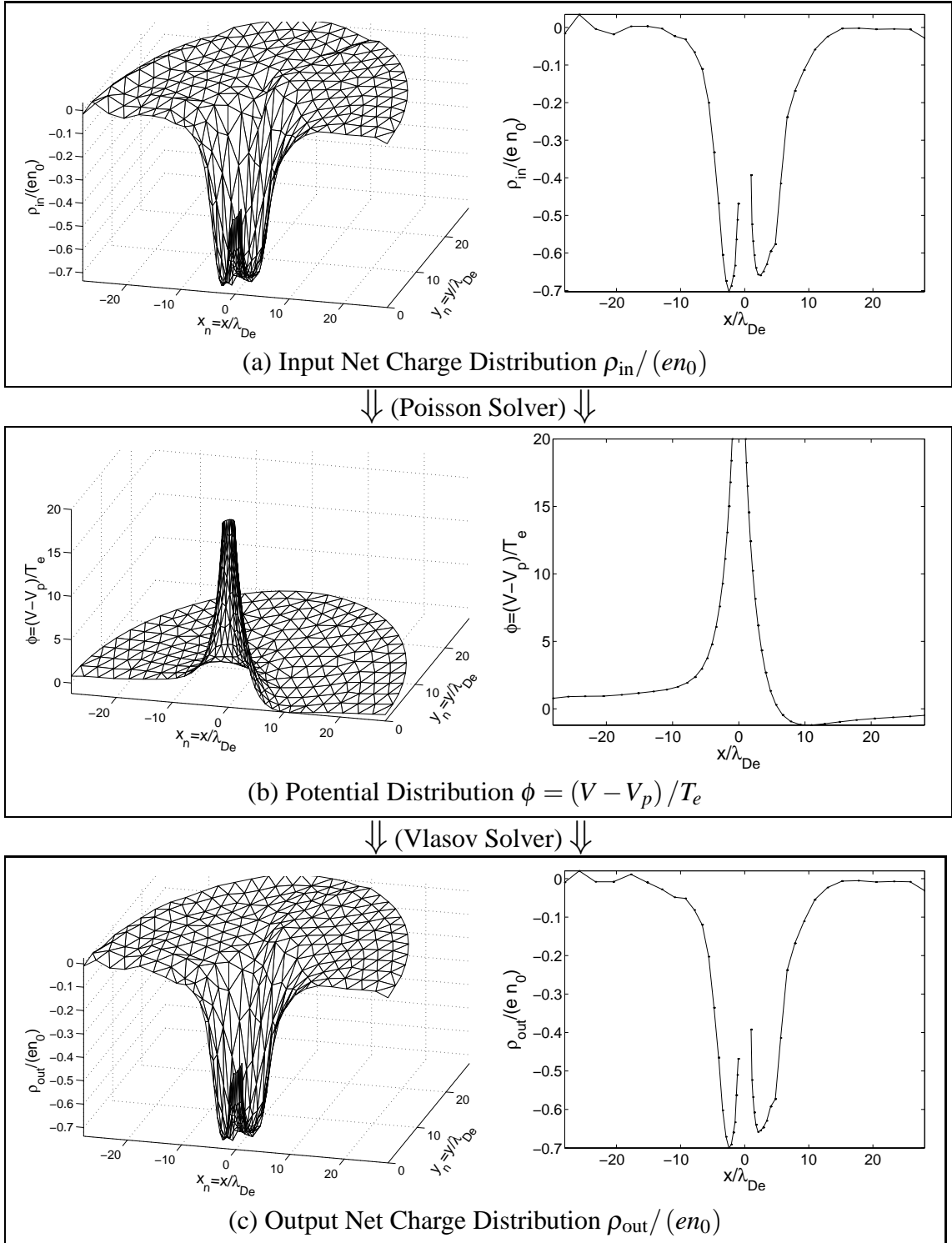


Figure 4.76: Poisson–Vlasov consistent solution for an electron-attracting cylinder ($r_0 = \lambda_{De}$) biased at $\phi_0 = 20$ and immersed in a flowing plasma with flow energy $U_{ev} = 1.5 T_e$. Self-consistency is shown by the similarity of ρ_{in} and ρ_{out} . 2-D solutions are shown on the left, and corresponding x -axis cross-section profiles are shown on the right. Ion and Electron density dist. are shown in Figure 4.77.

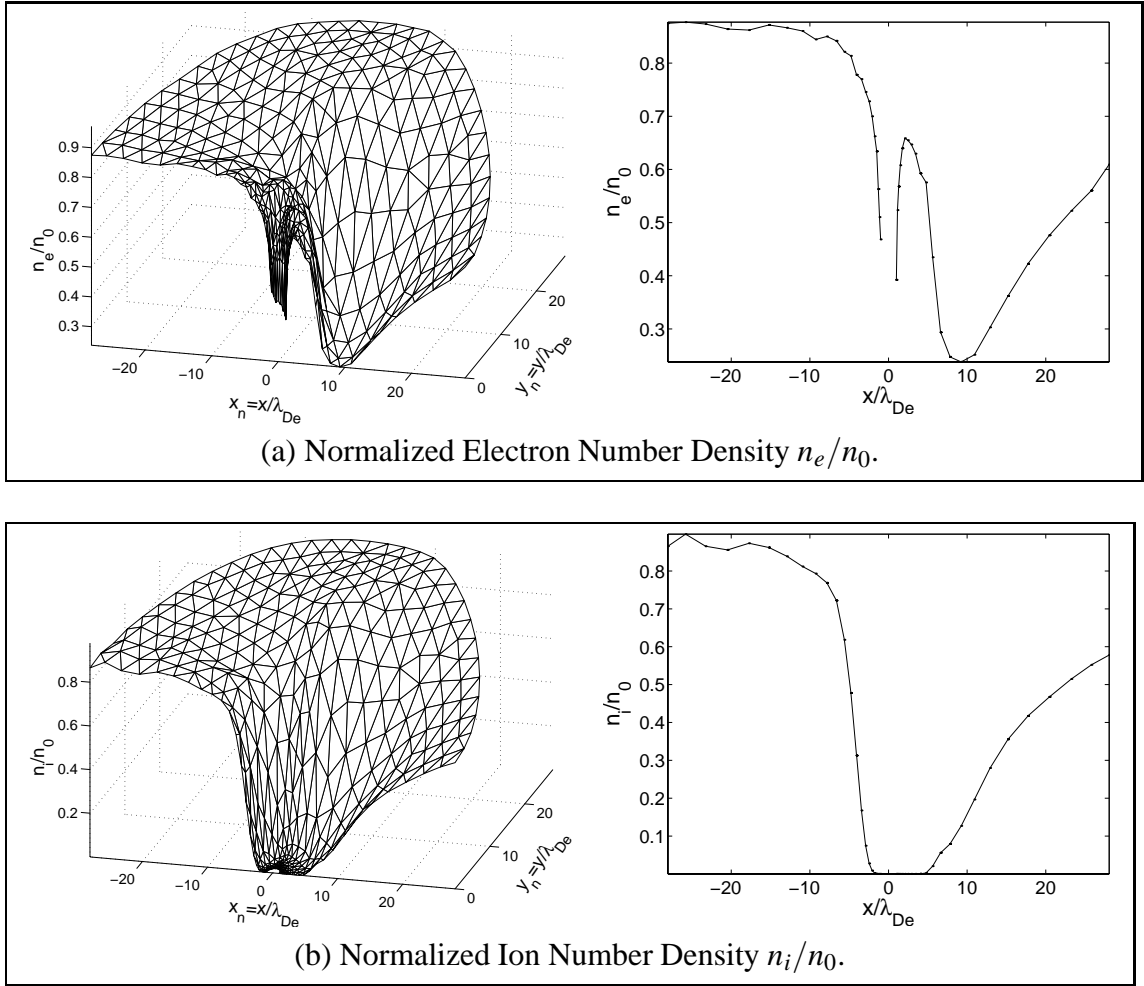


Figure 4.77: Poisson–Vlasov consistent electron and ion density distributions for an electron-attracting cylinder ($r_0 = \lambda_{De}$) biased at $\phi_0 = 20$ and immersed in a flowing plasma with flow energy $U_{ev} = 1.5 T_e$. These density profiles constitute the output of the Vlasov solver and are combined to form the output net charge density profile $\vec{\rho}_{out} = e(\vec{n}_i - \vec{n}_e)$ shown in Figure 4.76(c).

- A potential depression (below 0 V) appears on the wake side of the cylinder, which gets deeper with increasing flow energy. This acts as a potential barrier which prevents some electrons coming from the right from reaching close to the cylinder.
- The ion number density plateaus longer on the ram side, due to its increased inertia associated with the increasing flow energy.
- Since quasi-neutrality must be satisfied at sufficiently large distances from the cylinder's surface, the electron number density also plateaus longer on the ram side, before dropping to half the ambient density on the ram-side of the cylinder's surface. The mechanism that allows this is the focusing of leftward-directed electrons onto the ram-side potential “bump”.
- The bottom level of the wake-side dip in the electron number density goes deeper as the flow energy increases, which is due to the repelling effect of the wake-side potential depression, preventing some electrons from approaching the cylinder from the wake side.
- The wake-side surface electron density drops below the OML value to values below half the ambient density. This effect does not occur as quickly as the decrease of the previously described “wake-side dip level density” because it is countered by the geometrical concentration of electron current.

4.6.2 Electron Current Collection

We now turn to the analysis of electron current collection in a flowing plasma. Figure 4.78 shows the dependence of electron current on flow energy. It can be seen that the amount of collected electron current goes down with increasing flow energy. This can be explained by the action of the previously described wake-side potential barrier which

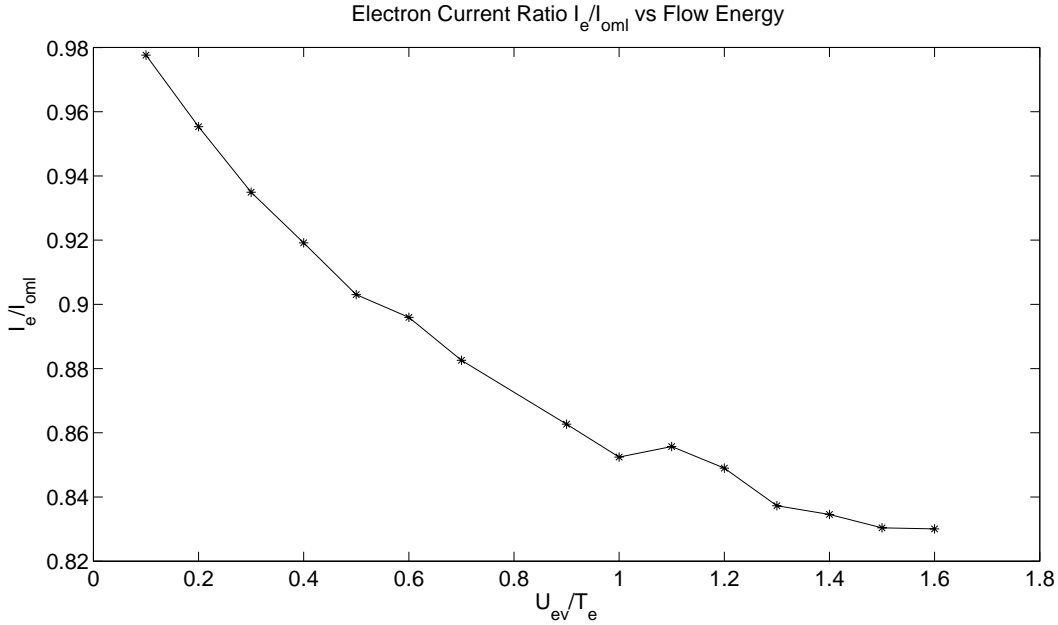


Figure 4.78: Collected Electron Current Ratio I_e/I_{oml} as a function of the normalized flow energy U_{ev}/T_e ($\phi_0 = 20$, $r_0 = \lambda_{De}$).

blocks electrons with insufficient energy from accessing the vicinity of the cylinder from the wake side. Since the potential barrier grows with increasing flow energy, the collected current drops accordingly. On the ram side, the electron current is just below the OML level (as can be inferred from the electron density profiles), so that the decrease in electron current is wholly attributed to the growth of the wake-side potential barrier.

Now, as the reader may recall from Chapter 3, our experimental measurements have led us to conclude that there is a significant enhancement of the electron current with respect to the orbital motion limit, contrary to what our simulation results indicate here. Figure 3.8 (a) indeed indicates strong enhancements of about 25% at $\phi_0 = 20$ and 40% at $\phi_0 = 100$ for the reference cylinder's collected electron current with respect to OML, when placed at the closest position with respect to the plasma source, where a large fraction of the ion population was determined to be high speed ions with an energy of about 25 eV, or $13.9T_e$. The reduced enhancement seen at 160 cm, along with the absence of any enhancement at 300 cm, re-enforce our confidence that the strong enhancement observed at 75 cm is

indeed a consequence of the plasma flow, as opposed to an artifact of the measurement errors involved in the determination of the plasma density for example.

If we assume that the observed enhancement was real, then there must be some additional important physics not included in our kinetic model that could potentially explain it. Let us first ask the question of how much electron collection is possible given the assumptions used in our kinetic model. Following are two key facts for this discussion:

1. the plasma is assumed collisionless, and therefore only collisionless trajectories connect the electron velocity distribution at a given point (r, θ) in space with a normalized potential $\phi = \frac{V - V_p}{T_e}$ to the background plasma ($r \rightarrow \infty$ and $\phi = 0$);
2. the electron population has no drift component in the background plasma, for all practical purposes, because the electron thermal velocity v_{the} is much larger than the drift velocity U . The background electron population (the source) can therefore be accurately represented by a pure Maxwellian distribution, as given by (2.4) with $U = 0$.

Given the collisionless assumption and the fact that the electrons are a stationary species, we conclude that, in our kinetic simulations, the electron density at any position within the potential structure cannot exceed the ambient density n_0 , nor can the collected electron current to a probe exceed the orbital motion limit, as we show in Chapter 1 in accordance with a proof given by *Laframboise* [6].

We hereby propose a possible mechanism for the experimentally observed current enhancement. As was seen in the collisionless self-consistent potential structures shown in Figures 4.70 through 4.76, the electric potential stabilizes to a relatively large value on the ram-side edge of the computational domain, which is on the order of the beam energy U_{ev} . The potential must therefore slowly drop from this relatively large potential down to zero

(the plasma potential) over a very large distance, since the electric field appears to already be very low at the outer boundary of the computational domain, as expected within the pre-sheath zone. Out at some distance on the x axis in the ram direction, the electric field will have dropped to such a low level that some collisional forces would start dominating electron behavior, even though the local potential would still be at a non-negligible fraction of the electron temperature. This is unlike the symmetric stationary problem, in which the electric potential drops sufficiently fast that it reaches a very small fraction of T_e before the electric field has dropped to a sufficiently low level to allow some collisional forces to dominate electron trajectories.

Mathematically speaking, we may compare the stationary and flowing cases by considering the asymptotic forms that the potential profile may take along the x axis, on the ram side. In the stationary case, we have the asymptotic result $\phi = \phi(R_{\text{ref}}) \frac{R_{\text{ref}}}{r}$, for sufficiently large values of r (see Section 2.3.2.1), where R_{ref} is some reference radius. Our flowing results seem to indicate a slower asymptotic drop of the potential on the ram side, i.e., $\phi = \phi(R_{\text{ref}}) \left(\frac{R_{\text{ref}}}{r}\right)^k$, with $k < 1$. The normalized radial component of the electric field is thus given by

$$E_{nr} = -\frac{\partial \phi}{\partial r} = \phi(R_{\text{ref}}) k \frac{R_{\text{ref}}^k}{r^{k+1}}, \quad (4.36)$$

which should be compared against the stationary electric field $E_{nr,nf} = \phi(R_{\text{ref}}) \frac{R_{\text{ref}}}{r^2}$. The ratio of the “flowing” to “stationary” electric field expressions is given by

$$\frac{E_{nr}(r)}{E_{nr,nf}(r)} = k \left(\frac{R_{\text{ref}}}{r}\right)^{k-1} < 1 \text{ for } r > R_{\text{ref}} \text{ and } k < 1, \quad (4.37)$$

which is clearly less than one as indicated, meaning that the radial component of the electric field is weaker in the case of a flowing plasma.

In the *collisional zone* of the pre-sheath, where collision forces dominate electric field forces, collisions gradually re-thermalize the electron population as it is accelerated down

the shallow potential well leading to the “collision-free” zone. In the process, the electron temperature may rise by a small amount (i.e., collisional heating), but, more importantly, there is an increased concentration of electrons on the ram-side of the collisional zone, where the potential is positive (and electron-attracting). In other words, the incoming electron density at the outer boundary of the collision-free zone is larger than the ambient density by an amount that depends primarily on the potential level on that boundary.²¹ A fair approximation for this potential dependence is given by the Boltzmann approximation $n_e \approx n_0 \exp(\phi(r))$, where n_0 is the ambient plasma density, ϕ is the local normalized potential V/T_e , and T_e is the electron temperature, which we assume here has not changed, i.e., no significant heating has occurred. This collisional concentration process would thus lead to an increased influx of electrons on the ram side of the sheath, and therefore an increased collected current primarily on the ram side of the cylinder. If we estimate that the electron flux to the ram side of the cylinder’s surface will increase by a factor corresponding to the increased electron density at the outer edge of the collision-free zone, and further assume that no electron collection takes place on the wake side at sufficiently large flow energies due to the repelling effect of the wake-side potential depression, we may approximate the enhanced electron current collection to a small cylinder by

$$\frac{I_{e,\text{flowing}}}{I_{e,\text{stationary}}} \approx \frac{1}{2} \exp(\phi_{\text{collision boundary}}). \quad (4.38)$$

According to this crude model, a 40% enhancement such as we have observed experimentally for a bias potential $\phi_0 = 100$ and flow energy $U_{ev} = 25T_e$ would correspond to a normalized potential at the frontier between the collisional and collision-free zones of $\phi_{\text{collision boundary}} \approx 1$, that is, a potential on the order of electron temperature. Given the ram-side pre-sheath potentials that were obtained in the simulation results shown in Fig-

²¹Note that we should more generally refer to a transitional zone between the collisional and collision-free zones rather than a well-defined boundary.

ures 4.70 through 4.77 which were applicable to low-speed flows from $U_{ev} = 0.1T_e$ to $U_{ev} = 1.5T_e$, a value of 1 for the ram-side pre-sheath potential does seem quite reasonable for such a large flow energy as $U_{ev} = 13.9T_e$.

The implementation of a dual model which includes both collision-free and collisional zones has previously been presented [77] and will require further refinement to accurately predict the observed enhancements.

4.7 Outline of Simulation Resource Requirements

In this section we give a coarse overview of the costs, in terms of computer resources and computing time, of the kinetic simulations that were performed as part of this work. A detailed “operation count” has yet to be performed for both the 1-D cylindrical implementation (KiPS-1D solver) and full 2-D implementation (KiPS-2D solver), but we can nonetheless provide an overall description of the resource costs involved.

4.7.1 1-D Cylindrical Implementation (KiPS-1D)

The KiPS-1D solver was implemented using *Matlab*TM and Fortran 90, as described in Section 2.7. It runs on a single computer using a single processor, and uses a relatively small amount of random-access memory (RAM), on the order of a few tens of megabytes, well below the amount of available RAM on our Linux workstation, which has 4 GB of RAM.

In order to illustrate the computing time requirements for KiPS-1D, we have run KiPS-1D with $r_0 = \lambda_{De}$ for several bias potential values from $\phi_0 = -10$ to $\phi_0 = -12800$. The number of unknowns (samples) required to properly sample the problem increases with the value of the bias potential. Figure 4.79 shows a plot of the number of iterations required for convergence as a function of the number of unknowns, along with a plot of the CPU pro-

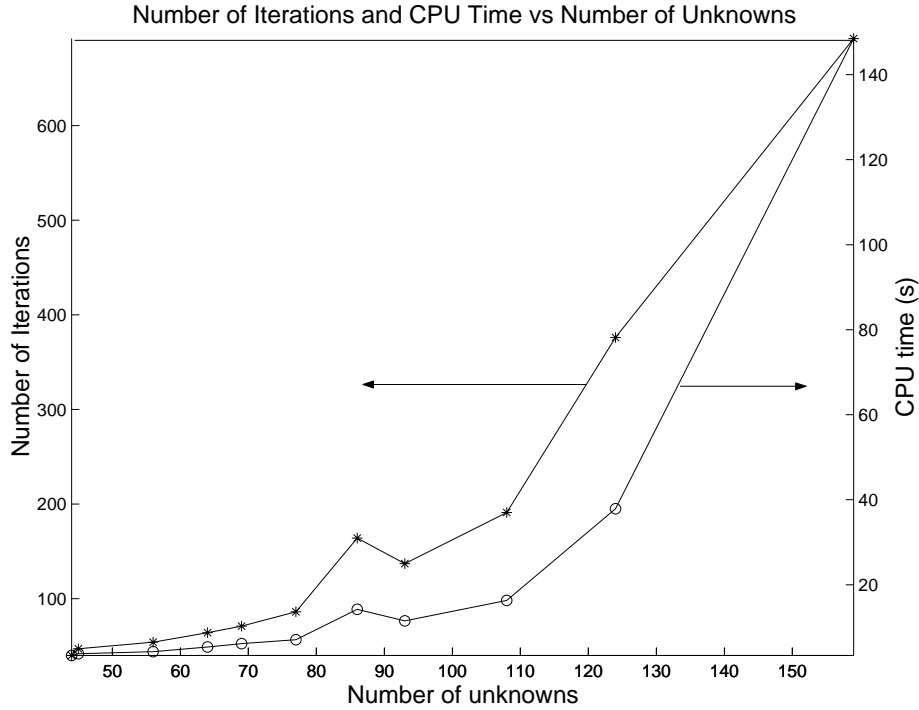


Figure 4.79: Number of iterations required for convergence and CPU time as a function of the number of unknowns in KiPS-1D simulations involving a cylinder radius of $r_0 = \lambda_{De}$. The number of unknowns was modulated by changing the bias potential, since higher potentials demand a larger number of grid samples.

cessing time required on our Linux workstation as a function of the number of unknowns. One can see that the type of 1-D simulations that we have run as part of this project only has modest computing time requirements, since the longest simulation on this graph took less than 150 seconds.

Figure 4.80 shows that, when the number of unknowns is sufficiently low, the computing time scales roughly linearly with the number of iterations required for a given problem. It appears that this behavior breaks down when the number of unknowns becomes larger, which is likely a consequence of the increased time required to invert the linearized system at each iteration.

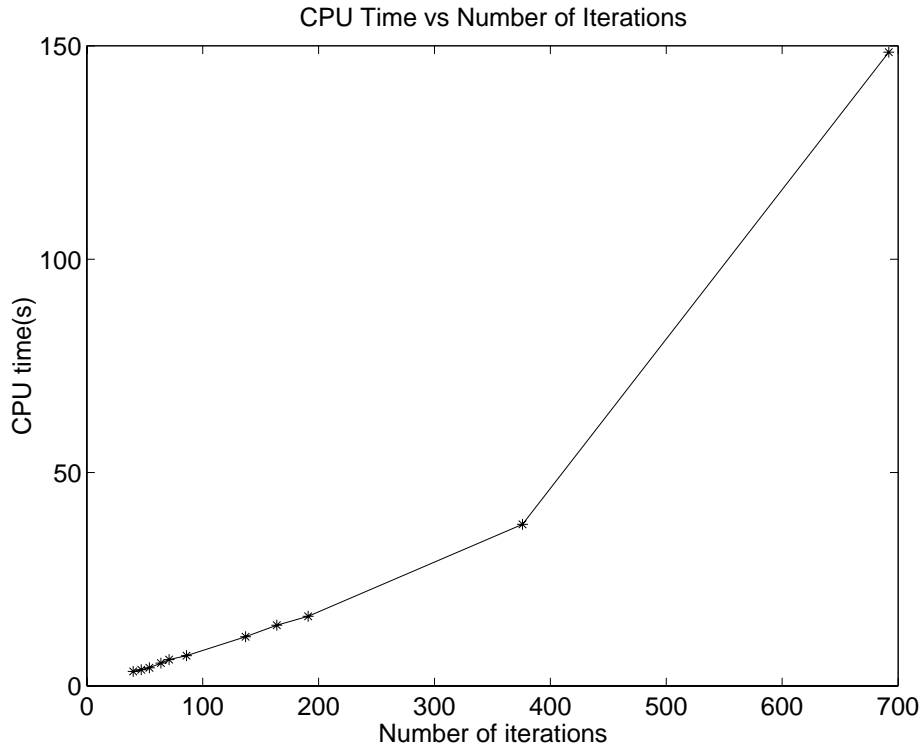


Figure 4.80: CPU time as a function of the number of iterations required for convergence in KiPS-1D simulations involving a cylinder of radius $r_0 = \lambda_{De}$. The number of unknowns was modulated by changing the bias potential, since higher potentials demand a larger number of grid samples.

4.7.2 2-D Cylindrical Implementation (KiPS-2D)

As was discussed in Section 2.7, the KiPS-2D solver is much more computationally demanding. As the reader may recall from Section 2.7, the Poisson solver and Tikhonov-regularized Newton iterative processes run on a single Linux workstation (2.4 GHz dual-Xeon), while the Vlasov solver uses a collection of about 150 slave nodes running on a dynamically-configured pool of Sun Blade™ 1000/1500 workstations in order to compute the plasma density samples.

4.7.2.1 Processing Time

Although a detailed, careful analysis of the computing time requirements has not been performed for KiPS-2D, we present in Figure 4.81 some timing data pertaining to the simu-

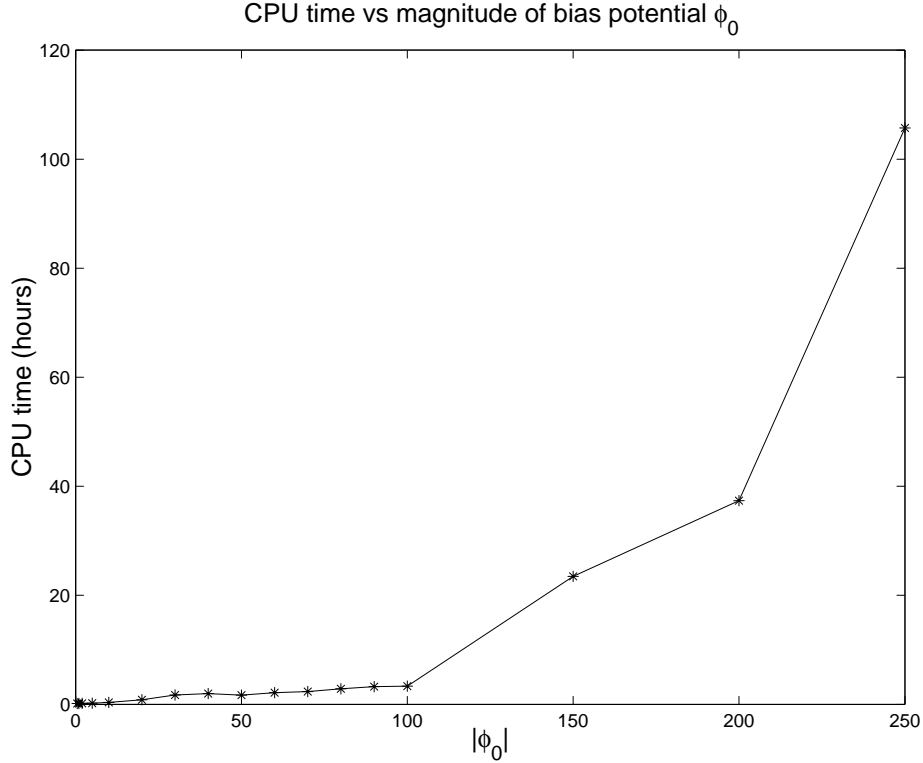


Figure 4.81: Simulation time required as a function of the magnitude of the normalized bias ϕ_0 , for the KiPS-2D simulations shown in Section 4.5.4, with $r_0 = \lambda_{De}$, $U_{ev} = 0.66T_e$, and one mesh refinement.

lation results shown in Section 4.5.4. Bare in mind that at least two other KiPS-2D simulations were running simultaneously, competing for resources. Thus, the actual time spent for these simulations would correspond to about one third of the values shown in Figure 4.81 or even less.

Generally speaking, the primary parts of the algorithm that contribute to the computing time in KiPS-2D are the following (not necessarily in that order):

1. the Vlasov solver, which uses all 150 slave workstations to compute the density samples based on several thousand particle trajectories;
2. building the Poisson-Vlasov Jacobian matrix, as described by equation (2.115);
3. performing the Tikhonov regularization, which includes the selection of the regular-

ization parameter λ in (2.133).

A future thorough assessment of the computing requirements should include separate timings for each of those three major computational hurdles.

For the time being, we have been able to determine that the computational bottleneck for KiPS-2D is different depending on the regime of operation. When the number of mesh nodes is relatively small (i.e. 500 or less), the bulk of the time is spent in the Vlasov solver (step 1), while steps 2 and 3 amount to a small fraction of the computing time; this is the most efficient mode of operation. On the other hand, when the number of mesh nodes becomes somewhat larger (1000 and above), the matrix manipulations involved in steps 2 and 3 now require the most computing time. The shift between these two regimes is apparent in Figure 4.81, and seems to occur around a bias potential $|\phi_0| = 100$. The larger bias potential values require more mesh refinement near the cylinder and therefore cause a dramatic surge in the number of mesh nodes. For example, at $|\phi_0| = 250$ about 1800 mesh nodes are required, which implies the manipulation of matrices with dimensions of 1800×1800 .

Thus, in its current state the 2-D solver is optimal for use at moderate bias voltages. Future modifications should seek to minimize the bottleneck associated with high mesh density in the vicinity of biased conductors. This could be done by using alternate representations for the Poisson solver, over small areas near high-voltage conductors, which are not based on a full discretization, but instead only discretize the perimeters surrounding those high-field areas. Such an approach would assume a negligible effect of the local space charge in high-field areas near high-voltage conductors.

Another, rather simple improvement could be done to reduce the computing time involved in step 2 above. The present implementation uses full matrices for \mathbf{J}_V when computing the Poisson-Vlasov Jacobian matrix \mathbf{J}_{PV} , which results in a pure matrix-matrix product

involving full matrices. However, as is explained in Appendix E, the approximation used for the Vlasov Jacobian \mathbf{J}_V is merely a diagonal matrix. One could take advantage of this fact in order to significantly speed up the matrix-matrix product involved in computing the Poisson-Vlasov Jacobian matrix.

4.7.2.2 Random-Access Memory Requirements

The RAM requirement on slave nodes is very reasonable, typically on the order of ten to a few tens of megabytes, and therefore does not constitute a bottleneck. On the master workstation, RAM requirements can sometimes reach as high as 2 gigabytes, when building very large matrices in problems involving high voltages probes, as described above. This requirement should be relaxed significantly when the optimizations discussed above are implemented. However, should the simulation of problems involving tens of thousands of mesh nodes be required, one would have to consider moving to a 64-bit computing platform, in order to reach beyond the memory addressing limit of 4 gigabytes ²² imposed by 32-bit platforms such as the one that was used for this thesis.

²²The practical limit is 3 gigabytes on a properly configured Linux kernel due to the operating system overhead.

CHAPTER 5

Conclusions and Recommendations for Future Research

Designing bare electrodynamic tethers for propellantless space propulsion or radiation belt remediation will demand a detailed understanding of the impact of tether geometry and ionospheric flow on plasma sheath structure and current collection. Geometries are being sought that improve structural merits and survivability from collisions with micrometeoroids, while optimizing sheath structure and current collection. Previous research on sheath structure and current collection has only addressed low-voltage regimes and simple round cylinders as collectors, whether it be in stationary or flowing plasmas.

5.1 Summary and Conclusions of Research

This research has sought to fill the gaps in the existing literature by investigating, through both simulation and experimentation, the sheath structure physics and current collection properties of cylindrical collectors with various cross-sectional geometries in stationary and flowing plasmas.

5.1.1 Self-Consistent Steady-State Kinetic Model

Because no suitable existing model could adequately support the structures and regimes of interest, a novel computational model was devised to address the problems under consideration. Using kinetic theory, a steady-state kinetic computational model was developed

which allows for the self-consistent modeling of collisionless, unmagnetized two-species plasmas in a vast region surrounding an arbitrarily-shaped 2-D conductive object. This model allows for both stationary and flowing plasmas. Following are some of its main features:

- it can provide kinetic treatment for both species based on the dynamic sampling of the velocity distribution function at a finite set of nodes;
- it provides a dynamic, adaptive, unstructured meshing strategy, allowing for the support of arbitrary 2-D geometries and the adequate resolution of plasma sheath features, such as the narrow surge of the net charge density which exists near the sheath edge in the case of high-voltage biases;
- it allows for the simulation of very large computational domains, based on tailoring the variable grid size to efficiently accommodate potential and density variations;
- it uses a new approach, called the *Progressive Tikhonov-Regularized Newton Method*, to efficiently minimize the Poisson–Vlasov residual in order to approximate the fixed point of the Poisson–Vlasov operator. This approach is robust to numerical instabilities and quadrature noise and has successfully been used to solve a wide class of 2-D problems without the need for empirical adjustments;
- it includes a coarse-grained parallel implementation for its Vlasov solver, allowing it to run on MPMD (Multiple Processors, Multiple Data) parallel architectures.

Based on this model, two solvers were developed: a 1-D cylindrical model, implemented in a solver called KiPS-1D, and a full 2-D model, implemented in KiPS-2D. The relative computational simplicity of the 1-D cylindrical model has allowed it to be used extensively to develop a basic set of sheath profiles for high-voltage circular cylinders, after an

initial validation was performed based on the available literature that covers low bias potential regimes. This also provided a reference for the validation of the more complex 2-D solver, in addition to the available literature. Several asymmetric problems were simulated in KiPS-2D, allowing for the characterization of the two-cylinder and solid tape configurations, as well as an assessment of flow effects on ion- and electron-attracting round cylinders.

5.1.2 Experimental Investigation of Electron-Collecting Tether Samples

An experimental investigation was performed which consisted of measuring electron current collection to cylindrical, solid tape, and slotted tape electrodynamic-tether samples in a mesosonic flowing xenon plasma. A Hall thruster was used to simulate a flowing unmagnetized space plasma in a large 6-m \times 9-m vacuum chamber. Solid tape samples with effective widths spanning from 4.9 to 41.9 Debye lengths, and slotted tapes with center-to-center line spacings spanning from 1.4 to 13.2 Debye lengths were tested. Several conclusions were drawn from the analysis of the results:

- plasma flow leads to significant current enhancements over that predicted by the orbital-motion-limited theory;
- the electron collection efficiency of solid tapes (on a per area basis) decreases as the width of the tape is increased, consistent with our computer simulations;
- beyond a threshold bias potential close to the beam energy, solid and slotted tapes both collect more current when oriented transverse to the flow;
- equivalent-width slotted tapes are more efficient electron collectors than solid tapes on a per area basis;

- the data suggests that the electron collection efficiency of slotted tapes decreases with increasing line spacing until a minimum efficiency is attained, beyond which it is expected to increase monotonically up to the orbital-motion limit expected of independent lines.

5.1.3 Important Simulation and Experimental Results

Kinetic simulations and experimental investigations have allowed several new results to be obtained. We describe the major results in the following.

5.1.3.1 Ion-Attracting High-Voltage Single Cylinder in Stationary Plasma

Acceleration of attracted ions into the high-voltage sheath results in a significant depletion of ions within a large portion of the sheath, primarily as a result of flux conservation. This is the primary mechanism allowing for the creation of relatively large sheath radii, as compared to what may have been expected from a uniform ion density assumption, for example. An asymptotic equation relating the normalized bias potential ϕ_0 and cylinder radius r_0 to the effective sheath radius r_s was obtained in (4.19) and is repeated here:

$$2.554 \left(\frac{r_s}{\lambda_{De}} \right)^{1.325} \ln \frac{r_s}{r_0} = -\phi_0. \quad (5.1)$$

5.1.3.2 Interference Effects of Parallel Cylinders

Interference effects between two parallel cylinders were shown to exist for spacings upward of 20 times the single-cylinder sheath radius, and an optimal spacing equal to the single-cylinder sheath radius was seen to maximize the overall sheath area to a value equal to twice the independent single-cylinder effective sheath area (for one value of the bias potential, $\phi_0 = -320$). In addition, for a spacing of half the single-cylinder sheath radius, current collection is reduced to a minimum of half of the current collected by two independent cylinders. This is attributed to the existing set of unpopulated collisionless

paths connecting both cylinders which create voids in the incoming velocity distribution at the cylinders' surfaces, thereby reducing the collected current. This particular spacing is thought to maximize the number of such unpopulated orbits bounded by the cylinders, hence the minimal current collection.

5.1.3.3 Geometry Effects of the Solid Tape Cylinder

The capacitance-based equivalent circular radius of a solid tape biased at a normalized bias potential $\phi_0 = -320$ was shown to be approximately equal to $0.29w$, where w is the tape width. This result was verified over a large range of tape widths spanning from 1 to 50 Debye lengths, and is slightly higher than a previous asymptotic result of $0.25w$ [11]. On a per-area basis, solid tapes have a reduced current collection capability as compared to that of an equal-capacitance circular cylinder. The general character of the departure of collected current from the orbital motion limit value has been shown to agree, within experimental uncertainties, with experimental current measurements on solid tapes after normalizing out flow enhancement effects using data from a reference cylinder.

5.1.3.4 Plasma Flow Effects on Ion-Attracting Cylinder

Flow effects on ion-attracting cylinders were investigated through kinetic simulations using KiPS-2D. Results indicate that flow energies representing any significant fraction of the plasma temperature are sufficient to cause significant sheath asymmetries, regardless of the bias potential applied on the cylinder. In fact, asymmetries were seen to grow with increasing applied bias potential. For a flow energy of 66% of the thermal energy of the plasma, results indicate a reduction of the effective sheath radius by about 30% (the sheath area was reduced by about 50%) at large bias potentials with respect to the stationary case. The collected current was also reduced by about 30%, which translates into a 30% savings in terms of power expenditure for a given bias voltage.

5.1.3.5 Plasma Flow Effects on Electron-Attracting Cylinder

Flow effects on electron-attracting cylinders were investigated through both kinetic simulations and experimental investigations. Kinetic simulations have shown strong sheath asymmetries with flow energies on the order of the plasma temperature, along with a reduction of the collected electron current attributed to the buildup of a potential barrier for electrons downstream of the cylinder. Our experimental results, however, have shown a clear enhancement of electron current collection over the orbital-motion limit for a cylinder immersed in a flowing plasma.

Even though this measured current enhancement could not be predicted by our collisionless simulations, the obtained simulated plasma profiles can help interpreting the cause for the enhancement. The strong elongation of the pre-sheath potential structure, upstream of the cylinder, points to the possible existence of a collisional zone for electrons with non vanishing potentials, far upstream from the cylinder, where even weak collisional forces would dominate electric field forces. The thermalizing effect of these weak collisions over an extended range where the electric potential is still above zero would cause a concentration of electrons with densities exceeding the ambient density upstream of the cylinder, providing an increased influx of electrons on the ram side and thereby enhancing the collected electron current. A somewhat analogous explanation of electron current enhancement, which applies in the case of magnetized plasmas, is given by Cooke and Katz [81].

5.2 Recommendations for Future Research

Suggestions for future research can be categorized into 1) computational modeling and 2) experimental testing efforts.

5.2.1 Computational Modeling

Several problems of interest that have not yet been addressed should be simulated using KiPS-2D:

1. The two-cylinder configuration should be generalized to allow for the simulation of an arrangement of N cylinders, and to allow for the comparison of the merits of various arrangements with the goals of minimizing current collection and maximizing sheath cross-section, two objectives pertaining to the particle precipitation application.
2. Similarly, the slotted tape samples that were investigated experimentally as part of this thesis should be simulated. This structure consists of a “fence” of four parallel narrow tapes.
3. The study of ionospheric flow effects on ion-attracting cylinders should be extended to include larger bias potentials, to verify the apparent asymptotic character of the sheath area ratio.

Following are some key fundamental improvements to the kinetic model that should be considered.

1. A more thorough study of the several “trapped” state criteria used for determining whether a given trajectory is populated should be performed. A more general criteria should be sought, if possible, that would be independent of the geometry under consideration.
2. At large negative bias voltages it is possible that the ion bombardment to a tether might cause secondary emission of electrons, causing an increase in the net collected current. In order to study the possible impact of this effect, support should be added

in KiPS-1D and KiPS-2D for particle emission from conductive surfaces. A separate, first-order initial analysis [82] has shown that, even though secondary electron emission can contribute a significant amount of electron density near the cylinder's surface, its overall effect on the sheath structure should be negligible. The outward acceleration of the repelled electrons is so important that, due to current conservation, the secondary-electron density drops very quickly as we move away from the cylinder's surface, to a degree such that the area over which significant electron density can exist is very small and therefore cannot contribute significantly to space charge.

3. In an effort to better understand and characterize the flow-induced electron current enhancement that was observed experimentally, support for weak thermalizing collisions based on a Krook model should be implemented or, alternatively, a dynamically-defined collisional zone should be included based upon the local magnitude of the electric field. Some work toward these tasks has already been initiated.
4. Support for periodic time variations could be added to the 1-D cylindrical implementation, in order to perform a self-consistent study of the effect of periodic excitations of tether bias potentials. Such excitations may be used to affect the sheath structure and current collection properties, using the ponderomotive force for example, as suggested by some analyses of the Oedipus C tethered payload experiment [83].
5. The computationally tractable range of the bias potential in the 2-D model could be expanded by either one of the following two additions.
 - Since the sheath solution is virtually independent of the density samples located sufficiently close to a high-voltage conductive surface, one could significantly reduce the computational cost of each iteration by excluding such nodes from the Vlasov density calculations for all iterations but the last one (that is, if

knowledge of those densities is required at all). This procedure would alleviate the steep increase in computational cost that results from the stringent requirements on mesh density near high-voltage surfaces, which are necessary for the accurate tracking of trajectories transiting through those zones.

- The implementation of a second-order, piecewise quadratic approximation for the potential and charge density distribution should be considered. It would entail a re-formulation of the finite-element Poisson solver and a re-formulation of the semi-analytical trajectory tracking process. This higher-order implementation would relax the meshing requirements for accurate trajectory tracking, and thereby enable the solution of more complex problems.
6. Support for magnetic fields should be implemented. Depending on the field's orientation, this may however imply the need for the representation of three-dimensional velocity space, which would come at a significant computational cost, but is nevertheless foreseeable for the near future, assuming that the exponential growth of computing power predicted by Moore's law [84] continues to hold...

5.2.2 Experimental Testing

Continued experimental testing is necessary for the validation and refinement of the analytical and computational models that will be used by designers. Following are suggestions of future experimental tests that should be considered.

1. Although our experimental tests of slotted tape samples have allowed us to sample a few effective gap spacings, they were not sufficient to adequately sample the current ratio curve shown on Figure 4.39, for example. An ideal test setup to validate this simulated data would consist of two thin cylinders (wires) which could be mechanically moved to dynamically adjust the spacing between them, therefore providing a

means to adequately sample the relationship of current ratio as a function of spacing using a dynamic selection of the spacing.

2. The sheath structure forming around one or several thin cylinders biased at a high voltage is of primary interest for this research, and has only been investigated through simulations as part of this thesis. The experimental validation of the sheath profiles obtained in this thesis is instrumental for the future use of our kinetic model for design purposes. A low-voltage bias probe could be used to sample the electron density structure around such a high-voltage system in order to determine a measure of the sheath structure and dimensions. This could then be used to validate the model. One of the difficulties in devising such a system would be to minimize the perturbing effect of the probe, but such a perturbation should not be critical in regard of the high voltages involved in the sheaths under study.
3. The existence of the sheath asymmetries which have been identified through simulations even with moderate flow energies (66% of thermal energy) should be assessed experimentally. This could be done by measuring the electron density profile using the low-voltage bias probe system described above, or, preferably, using a different measurement method that would obtain a more direct measurement of the ion density.

APPENDICES

APPENDIX A

Nomenclature

The mksA (meter–kilogram–second–Ampère) units are used throughout this work, rather than cgs (centimeter–gram–second). The following is a listing of the major symbols and variables used in this work, along with a brief description and the appropriate unit.

Nomenclature	Description (Unit)
α	Direction of particle velocity vector (rad)
α_c	Angle between successive search directions (rad)
α_c^t	Target value for α_c (rad)
β	Step size of iterative resolution procedure
α_i	Direction of particle velocity vector upon entry into the computational domain (rad)
$\gamma(n)$	Specified decay rate of the n^{th} circular harmonic of the exterior potential
$\Gamma_{e,i}$	Electron/ion particle flux ($\text{s}^{-1}\text{m}^{-2}$)
$(\Delta V)_{\max}$	Absolute mesh error tolerance on electric potential
Δx	Center-to-center spacing between two cylinders (m)
ϵ_0	Vacuum permittivity (F/m)
θ_{var}	Angular displacement (rad)
κ	Particle kinetic energy (eV)
κ_{range}	Kinetic energy integration range (in terms of temperature T)
λ	Tikhonov regularization parameter
λ_{De}	Debye length (m)
μ_b	Fraction of high-speed ions
Π	Energy functional of FEM-based Poisson solver
Π_1	Energy functional associated with Laplace fields
Π_2	Energy functional associated with exterior fields
Π_3	Energy functional associated with space charge
Π_{discrete}	Numerical approximation of Π
ρ	Net charge density (C/m^3)

Nomenclature	Description (Unit)
ρ_n	Normalized net charge density
$\vec{\rho}$	Vector containing the net charge density samples at all mesh nodes (C/m^3)
$\rho_{in}(x, y)$	Input charge density distribution (input of Poisson functional)
$\rho_{out}(x, y)$	Output charge density distribution (output of Vlasov functional)
$\vec{\rho}_{in}$	Vector form of the input charge density distribution
$\vec{\rho}_{out}$	Vector form of the output charge density distribution
σ_i	i^{th} singular value of the preconditioned system matrix \mathbf{A}'
$\vec{\sigma}$	Vector containing the singular values of the preconditioned system matrix \mathbf{A}'
τ_{rel}	Relative quadrature tolerance on number densities
$\tau_{abs,E}$	Absolute tolerance on energy-quadrature error
$\tau_{mesh,abs}$	Absolute mesh error tolerance
$\tau_{mesh,n}$	Absolute mesh error tolerance on the density distribution, relative to its total range
$\tau_{mesh,V}$	Absolute mesh error tolerance on the electric potential distribution $V(r, \theta)$, relative to its total range
$\tau_{mesh,\rho}$	Absolute mesh error tolerance on the net charge density distribution $\rho(r, \theta)$, relative to its total range
ϕ	Normalized potential
ϕ_0	Normalized bias potential
$\phi_{\text{collision boundary}}$	Normalized potential at the frontier between collisional and collision-free zones
a_{0i}, a_{ni}, b_{ni}	Quadrature coefficients used to approximate the Fourier series coefficients of the potential profile on the outer boundary
$\vec{a}_0, \vec{a}_n, \vec{b}_n$	Vector form of the quadrature coefficients a_{0i}, a_{ni}, b_{ni}
A_0	Cylinder's cross sectional area (m^2)
A_n	Normalized area (in terms of λ_{De}^2)
A_s	Effective sheath area (m^2)
$A_{s,1}$	Single-cylinder effective sheath area (m^2)
$A_{s,virtual}$	Virtual effective sheath area (m^2)
A_∞	Surface of the domain exterior to the computational zone
\mathbf{A}	System matrix
\mathbf{A}'	Preconditioned system matrix
\vec{b}	Right-hand side of the linearized system of equations
\tilde{b}	Transformed Poisson–Vlasov residual
B	Magnetic field intensity (Tesla)
\mathbf{D}_p	Diagonal right preconditioner
e	Constant ($1.6 \times 10^{-19} \text{ J/eV}$)
E	Transverse energy of a particle (J)
$E_{k_\alpha, k_E} = E_v(k_\alpha, k_E)$	Total energy of quadrature samples (eV)
E_{\min}	Minimum transverse particle energy (J)

Nomenclature	Description (Unit)
E_{nr}	Normalized radial component of the electric field under flowing conditions
$E_{nr,nf}$	Normalized radial component of the electric field for a non-flowing plasma
E_r, E_θ	Directional total energy components (eV)
E_n	n^{th} azimuthal mode of the radial electric field on the outer boundary
E_v	Total particle energy (eV)
$E_{v,min}, E_{v,max}$	Minimum and maximum total particle energies in quadrature integration (eV)
$f_E(E)$	1-D total energy distribution
$f(v_x, v_y)$	2-D velocity distribution
$f_i(v_{xi}, v_{yi})$	2-D velocity distribution at the entry point on the outer boundary of the computational domain
f_P	Poisson functional
f_{PV}	Poisson–Vlasov functional
f_V	Vlasov functional
$g(\kappa, \alpha)$	2-D directional kinetic energy distribution
$g(E_v, \alpha)$	2-D directional total energy distribution
h	Local grid size for 1-D model
h_{goal}	Target local grid size for 1-D model
H	Altitude (m)
I	Total collected current (A)
I_d	Hall thruster discharge voltage (volts)
I_e	Collected electron current (A)
I_i	Collected ion current (A)
I_{im}	Hall thruster inner magnet current (A)
I_{indep}	Current collected on a single independent cylinder (A)
I_{om}	Hall thruster outer magnet current (A)
I_n	Normalized collected current
I_{oml}	Orbital motion limited current (A)
I_{refcyl}	Current collected to the reference cylinder (A)
I_{tape}	Current collected to a thin tape (A)
I_{tether}	Current flowing along tether (A)
I_{th}	Thermal current (A)
$J_{e,i}$	Electron/ion current density (A/m^2)
J_{th}	Thermal current density (A/m^2)
\mathbf{J}_P	Jacobian matrix of the Poisson solver
\mathbf{J}_V	Jacobian matrix of the Vlasov Solver
\mathbf{J}_{PV}	Poisson–Vlasov Jacobian matrix
\mathbf{K}	Stiffness matrix of the FEM-based Poisson formulation
L	Angular momentum ($\text{kg m}^2/\text{s}$)
L_r	Special Definition given on page 52 ($\text{kg m}^2/\text{s}$)

Nomenclature	Description (Unit)
\dot{m}_a	Hall thruster anode flow rate (sccm)
\dot{m}_c	Hall thruster cathode flow rate (sccm)
$m_{e,i}$	Electron/ion mass (kg)
$m_{e,n}, m_{i,n}$	Normalized electron/ion mass
$\text{mod}()$	Modulo function
M_{orb}	Maximum angular displacement (number of multiples of 2π)
M_{rosc}	Maximum number of radial oscillations
M_{segcross}	Maximum number of intersections of any single edge
n_0	Background plasma number density (m^{-3})
$n_{e,i}$	Electron/ion number density (m^{-3})
n_{est}	Numerical estimate of number density (m^{-3})
$\vec{n}_{e,i}$	Vector containing the Electron/ion number density samples at all mesh nodes (m^{-3})
N	Number of mesh nodes (also the number of unknowns)
$N_E(k_\alpha)$	Number of energy quadrature samples for the k_α^{th} α -integral
N_{modes}	Number of azimuthal modes used to represent the outer boundary potential profile
N_{ob}	Number of potential samples on the outer boundary
N_r	Number of mesh refinement steps
$q_{e,i}$	Electron/ion charge (C)
$q_{e,n}, q_{i,n}$	Normalized electron/ion charge
\mathbf{Q}	Loading matrix of the FEM-based Poisson formulation
Q	Linear surface charge (C/m)
Q_n	Normalized surface charge
$Q_{n,1}$	Single-cylinder normalized surface charge
r_0	Round cylinder radius (m)
r_G	Gyroradius (m)
r_{GL}	Larmor gyroradius (m)
r_M	Radius of the outer boundary of the computational domain (m)
r_s	Effective sheath radius (m)
$r_{s,1}$	Effective sheath radius of a single independent cylinder (m)
R_{A_s}	Effective sheath area ratio
R_{eq}	Equal-charge equivalent circular cylinder radius (m)
S_d	Ion speed ratio
$T_{e,i}$	Ambient electron/ion temperature (eV)
$T_{e,n}, T_{i,n}$	Normalized ion/electron temperature
T_{slow}	Temperature of a low-energy, non-flowing ion population (eV)
U	Plasma flow velocity (m/s)
U_{ev}	Plasma flow energy (eV)
v_r, v_θ	Particle velocity components in cylindrical coordinates (m/s)
v_x, v_y	Particle velocity components in Cartesian coordinates (m/s)
v_{xi}, v_{yi}	Particle velocity components upon entry into the computational domain (m/s)

Nomenclature	Description (Unit)
v_{xf}, v_{yf}	Particle velocity components at the interrogation point within the computational domain (m/s)
v_{xn}, v_{yn}	Normalized particle velocity components
$v_{x\infty}, v_{y\infty}$	Particle velocity components in the background plasma, away from the perturbation as $r \rightarrow \infty$ (m/s)
V	Potential (volts)
V_0	Bias potential (volts)
\vec{V}	Vector containing the potential samples at all mesh nodes (volts)
\vec{V}_b	Vector containing the potential samples on the outer boundary (volts)
$V_{\text{avg,fit}}$	Average bias potential over which the ion saturation best fit is performed as part of the Langmuir probe data analysis
V_c	Hall thruster cathode voltage (volts)
V_d	Hall thruster discharge voltage (volts)
V_{edge}	Electric potential at the entry point of the particle on the outer boundary
V_{emf}	Potential drop along an electrodynamic tether due to the net effect of motional electromotive force combined with an on-board voltage source (volts)
V_{htr}	Hall thruster Heather voltage (volts)
V_p	Plasma potential (volts)
V_{xn}	n^{th} azimuthal mode of the electric potential on the outer boundary (volts)
\vec{x}	Linearized system unknowns
\tilde{x}	Transformed system unknowns
x_i, y_i	Particle coordinates upon entry into the computational domain (m)
x_f, y_f	Coordinates of the interrogation point within the computational domain (m)
x_n, y_n	Normalized coordinates (in terms of the Debye length)
w_k	Quadrature weights, 1-D Vlasov solver
$w_{k\alpha, k_E}$	Quadrature weights, 2-D Vlasov solver
$z(t) = z_A t^2 + z_B t + z_C$	Quadratic equation of the intersection of a sub-trajectory with a mesh segment

APPENDIX B

Acronyms

Although most of the acronyms used are defined in the text, we have listed them here for convenience.

Acronym	Description
BAMG	Bidimensional Anisotropic Mesh Generator
CAEN	Computer Aided Engineering Network
CPU	Central Processing Unit
FEM	Finite Element Method
HV	High Voltage
INRIA	Institut National de Recherche en Informatique et en Automatique
ISS	International Space Station
LIF	Laser Induced Fluorescence
LP	Langmuir Probe
LVTF	Large Vacuum Test Facility
NPACI	National Partnership for Advanced Computational Infrastructure
PEPL	Plasmadynamics and Electric Propulsion Laboratory
RHS	Right-Hand Side
KiPS-1D	Kinetic Plasma Solver, 1-D
KiPS-2D	Kinetic Plasma Solver, 2-D
OML	Orbital Motion Limit
MFP	Mean Free Path
MPMD	Multiple Processors, Multiple Data
PIC	Particle-In-Cell
PVM	Parallel Virtual Machine
SHV	Super High Voltage

APPENDIX C

2-D Poisson Solver: Detailed Expression of the Loading Matrix Elements

Section 2.3.2.2.2 includes a derivation of the 2-D finite element method used for our Poisson solver. The definite integral given by (2.63) was performed using *Matlab*TM, which allowed us to obtain an analytical expression for each of the 3 components of \mathbf{Q}_n 's matrix elements. The resulting expression is

$$\begin{aligned}
 & \left((\mathbf{Q}_n)_{ij} \right)_{i_e} = \frac{1}{96\Delta^2} \times \\
 & \{ (2b_j b_i y_0 + 2b_j b_i y_1) x_0^3 \\
 & + [(b_j c_i + c_j b_i) y_1^2 + 2(b_j a_i + b_i a_j) y_0 - 2b_j b_i x_1 y_0 + 2b_j b_i x_1 y_1 \\
 & + 2(b_j c_i + c_j b_i) y_1 y_0 + 4(b_i a_j + b_j a_i) y_1] x_0^2 \\
 & + [2c_j c_i y_1^3 - 2c_j c_i y_0^3 + 2c_j c_i y_1^2 y_0 + 2c_j c_i y_1 y_0^2 + 2b_j b_i x_1^2 y_1 + 2(b_j c_i + c_j b_i) x_1 y_1^2 \\
 & - 2(b_j c_i + c_j b_i) x_1 y_0^2 - 2b_j b_i x_1^2 y_0 - 2(c_j a_i + c_i a_j) y_0^2 + 4(c_i a_j + c_j a_i) y_1^2 \quad (C.1) \\
 & + 4(b_i a_j + b_j a_i) x_1 y_1 + 4(c_i a_j + c_j a_i) y_1 y_0 - 4(b_i a_j + b_j a_i) x_1 y_0 + 12a_j a_i y_1] x_0 \\
 & - 4(c_j a_i + c_i a_j) x_1 y_1 y_0 - 2c_j c_i x_1 y_1 y_0^2 + 2x_1 c_j c_i y_1^3 + 2(c_j a_i + c_i a_j) x_1 y_1^2 \\
 & - (b_j c_i + c_j b_i) x_1^2 y_0^2 - 2c_j c_i x_1 y_0^3 - 4(c_i a_j + c_j a_i) x_1 y_0^2 - 12a_j a_i x_1 y_0 - 2b_j b_i y_0 x_1^3 \\
 & - 4(b_j a_i + b_i a_j) y_0 x_1^2 - 2(b_j a_i + b_i a_j) x_1^2 y_1 - 2c_j c_i x_1 y_0 y_1^2 \\
 & - 2(c_j b_i + b_j c_i) x_1^2 y_1 y_0 - 2b_j b_i y_1 x_1^3 \},
 \end{aligned}$$

where the coordinates of the vertices corresponding to edge i_e are simply noted as (x_0, y_0) and (x_1, y_1) to avoid making the expression any heavier.

APPENDIX D

Adaptive Integration Using Trapezoidal Quadrature

Both the 1-D and 2-D implementations of the Vlasov solver use a common adaptive quadrature algorithm in order to numerically evaluate integrals with a given finite accuracy. We describe here the implementation of this adaptive quadrature technique.

A low-order quadrature integration scheme, the trapezoidal rule [48], was chosen instead of higher-order quadrature schemes, because it is more suitable for the integration of functions comprising discontinuities, as discussed in Section 2.4.2.3.2.

In order to adequately capture most existing discontinuities in the functions of interest, the 1-D domain of integration is first sub-divided into a set number of sub-intervals. The integral over each sub-interval is then performed using both 2-point and 3-point trapezoidal rules [48], and the difference between the two results is retained as an estimate for the local quadrature error.

The sub-intervals are then refined, in decreasing order of their respective quadrature error estimates, by doubling the number of samples and re-evaluating the sub-integral using trapezoidal quadrature applied to the new set of samples. This refinement procedure continues until the total absolute error estimate (the sum of the errors on each sub-interval) becomes smaller than a given absolute tolerance τ_{abs} , or until the total relative error estimate becomes smaller than a given relative tolerance τ_{rel} .

APPENDIX E

Linearization of the 2-D Vlasov Solver

The basic philosophy underlying the linearization of the 2-D Vlasov operator is very similar to that presented in Section 2.4.1.2 for the one-dimensional Vlasov operator. However, approximations must be made in the process that were not necessary in the 1-D case. The reason for that is that no information can be inferred regarding the potential dependence of the “shadow” boundaries of the directional-energy distribution function, i.e., the boundaries at the interface between the populated regions and the regions that are unpopulated due to obstruction (shadowing) by conductive surfaces.

Nonetheless, even partial information on the gradient can be sufficient to provide proper search directions that can be used in order to reduce the residual term and eventually lead to a self-consistent solution. Two alternative approaches have been successfully used in approximating the gradient and are described in the following. The first method, presented in section E.1, is appropriate for use with stationary plasmas, regardless of geometry. The second method, presented in section E.2, can be used for both stationary and flowing plasmas. Although the second method can provides a continuum of results from the stationary regime through high-speed regimes, the first method leads to faster convergence for stationary cases.

E.1 Gradient Approximation for Stationary Plasmas

In stationary plasmas, each sample of the directional-energy distribution function only depends on total energy. Since energy is the dependent variable in the integral given by (2.99), the total value of the integral is only a function of the bounds of the domain over which the integrand is non-zero. The α -dependence of those bounds cannot be accounted for, because no information is available on the potential dependence of the origin of each collisionless trajectory. However, the dependence of the integral on the minimum total energy E_{\min} is well defined and can be approximated as

$$\frac{\partial n_{e,i}}{\partial E_{\min}} \approx - \int_{\alpha=0}^{2\pi} g_{e,i}(E_{\min}, \alpha) d\alpha \quad (\text{E.1})$$

where E_{\min} is determined from (2.102), the directional-energy distribution $g_{e,i}$ was defined in (2.100), and we have omitted the position variables x and y for compactness. The dependence of E_{\min} on the local potential V can be determined from (2.102) to be

$$\frac{\partial E_{\min}}{\partial V} = \begin{cases} \frac{q_{e,i}}{e}, & \frac{q_{e,i}}{e}V(x,y) > \left(\sqrt{\frac{m_{e,i}}{2e}}U - \sqrt{\kappa_{\text{range}}T_{e,i}} \right)^2 \Big|_{U=0} \\ 0, & \text{otherwise} \end{cases} = \kappa_{\text{range}}T_{e,i} \quad (\text{E.2})$$

The chain rule can then be used to infer the gradient of the local density with respect to the local potential, following

$$\frac{\partial n_{e,i}}{\partial V} = \frac{\partial n_{e,i}}{\partial E_{\min}} \frac{\partial E_{\min}}{\partial V} \quad (\text{E.3})$$

In this approximation, the local density is assumed to only depend on the local potential. The Jacobian $\frac{\partial \vec{n}_{e,i}}{\partial \vec{V}}$ is therefore a diagonal matrix with diagonal entries computed according to (E.3) and all other entries set to zero.

E.2 Gradient Approximation for Flowing Plasmas

For flowing plasmas, the bulk contributions to the integral in (2.99) by the integrand given by (2.100) is no longer located near the minimum energy E_{\min} , provided that the flow

energy is a sizeable fraction of the temperature. It was determined that the best available approximation for the gradient would instead be obtained by summing the contributions of the integrand's gradient in directional-kinetic-energy space, instead of directional-energy (i.e. total energy) space. This entails re-writing the integral given by (2.99) in terms of the kinetic energy in electron-Volts, denoted here by κ :

$$n_{e,i}(x, y) = \int \int g_{e,i}(x, y, \kappa, \alpha) d\kappa d\alpha \quad (\text{E.4})$$

where $g_{e,i}(x, y, \kappa, \alpha)$ is the directional, kinetic energy distribution function defined as

$$g_{e,i}(x, y, \kappa, \alpha) = \frac{e}{m_{e,i}} f_{e,i} \left(x, y, \sqrt{\frac{2e}{m_{e,i}}} \kappa \cos(\alpha), \sqrt{\frac{2e}{m_{e,i}}} \kappa \sin(\alpha) \right) \quad (\text{E.5})$$

Consistent with (2.101), a sample of the kinetic-energy distribution $g_{e,i}(x, y, \kappa, \alpha)$ at a given location (x, y) within the computational domain is given by

$$g_{e,i}(x, y, \kappa, \alpha) = \frac{n_0}{2\pi T_{e,i}} \exp \left\{ -\frac{1}{T_{e,i}} \left(\frac{q_{e,i}}{e} V + \kappa - U \sqrt{\frac{2m_{e,i}(\frac{q_{e,i}}{e} V + \kappa)}{e}} \cos \alpha_i + \frac{m_{e,i} U^2}{2e} \right) \right\}, \quad (\text{E.6})$$

where α_i specifies the orientation of the velocity vector upon entry into the computational space. Re-writing this expression in a more suitable form, we obtain

$$g_{e,i}(x, y, \kappa, \alpha) = \frac{n_0}{2\pi T_{e,i}} \exp \left\{ -\frac{1}{T_{e,i}} \left(\underbrace{\frac{q_{e,i}}{e} V + \kappa - \frac{m_{e,i}}{e} U v_{xi}}_{\square} \underbrace{\sqrt{\frac{1}{1 - \frac{q_{e,i}}{e} V_i} + \frac{m_{e,i} U^2}{2e}}}_{\square} \right) \right\}, \quad (\text{E.7})$$

where v_{xi} is the x -component of the velocity at the entry point and V_i is the electric potential at the entry point (x_i, y_i) . It can now be seen that the value of a given sample $g_{e,i}(x, y, \kappa, \alpha)$ not only depends on the local potential V , but also depends on the entry potential V_i and on all potential samples that affect the trajectory connecting the “entry” point of the trajectory

at $(x_i, y_i, \kappa_i, \alpha_i)$ and the interrogation point (x, y, κ, α) , through the dependence on v_{xi} in the term denoted by \square .

In order to simplify the gradient expression, we recognize that the potential values on the outer boundary are very close to zero, at least upon reaching a solution. This means that the expression under the square root in (E.7) will be very close to 1 and that its dependence upon the entry potential V_i as well as the local potential V is weak, and can therefore be neglected. Furthermore, the dependence upon all the potential samples affecting the trajectory and by extension the value of v_{xi} could be computed using a chain rule combining sub-trajectory coordinate Jacobians. However, an attempt at this calculation showed that the numerical errors generated during such a lengthy chain rule can generate noise that hinders convergence under certain conditions.

In light of the above two observations, it was decided for the gradient calculation to drop any dependence upon the mesh potential samples of the term given by \square in (E.7). Extensive testing under various conditions has shown that this doesn't prevent convergence of the simulation. For the purpose of computing the gradient $\frac{\partial g_{e,i}}{\partial \vec{V}}$, the only term deemed to represent a significant dependence upon potential mesh samples is the first term within the parentheses in (E.7), which contains the local potential V . Our first-order approximation for the gradient of $g_{e,i}$ with respect to the local potential V is therefore given by

$$\frac{\partial g_{e,i}}{\partial V} \approx -\frac{q_{e,i}}{eT_{e,i}} g_{e,i}. \quad (\text{E.8})$$

Due to the simplicity of this expression, it is seen that a corresponding first-order approximation for the gradient of the local density $n_{e,i}$ as obtained from (E.4) is given by

$$\frac{\partial n_{e,i}}{\partial V} \approx -\frac{q_{e,i}}{eT_{e,i}} n_{e,i}. \quad (\text{E.9})$$

Again, as in the case of stationary plasmas, we observe that the local density only depends on the local potential in our first-order approximation of the gradient. The Jacobian $\frac{\partial \vec{n}_{e,i}}{\partial \vec{V}}$

will therefore take the form of a diagonal matrix with the diagonal entries computed according to (E.9) and all other entries set to zero.

Although the resulting Jacobian expression is only approximate, it has been shown in practice to be quite sufficient to obtain convergence to low-error self-consistent solutions. As noted above, the accuracy of the approximation improves as we get closer to the solution due to the fact that the edge potentials tend to go down to very small values, which helps providing better search directions as we get closer to a solution.

In closing, we should emphasize that the approximation used for the Jacobian only affects the intermediate search directions, not the actual specified plasma source, for which all the terms in (E.6) or (E.7) are fully accounted for. The approximations used in the gradient calculations are therefore of no consequence to the accuracy of any obtained self-consistent solution.

APPENDIX F

Langmuir Probe Analysis for the Experimental Assessment of Density, Temperature, and Flow Speed

The plasma parameter extraction is an iterative procedure that requires several iterations of the “ion saturation analysis” and “electron retardation analysis”, described below, to reach convergence. At every step, the electron retardation analysis is performed on the electron current exclusively, by removing the ion saturation best fit from the current data. Conversely, the ion saturation analysis is performed on the ion current alone by removing the latest best fit to the electron retardation region from the measured current.

F.1 Ion Saturation Analysis: Density $n_e = n_i$, Flow Energy U_{ev} , and High-Speed Fraction μ_b

The OML ion current to a cylindrical probe biased negatively, $V_0 - V_p < 0$, in a plasma flowing at a velocity U and a corresponding “flow energy” $U_{\text{ev}} = \frac{m_i U^2}{2e}$ is given by [29]

$$I_i = \sqrt{2} \frac{A_p e^{1.5}}{\pi \sqrt{m_i}} n_i \sqrt{\underbrace{\frac{1}{2} T_i + U_{\text{ev}} + V_p - V_0}_{\approx 0}} \quad (\text{F.1})$$

where $V_p - V_0 \gg U_{\text{ev}}$. The slope of the best fit to the I_i^2 -vs.- V LP data can be used to determine the plasma density $n_e = n_i$ (quasi-neutrality is strongly enforced within the plasma beam), while the offset allows one to determine an estimate for the quantity $\frac{1}{2} T_i + U_{\text{ev}}$. An example of this procedure is shown in Figure F.1. In our calculations of the flow

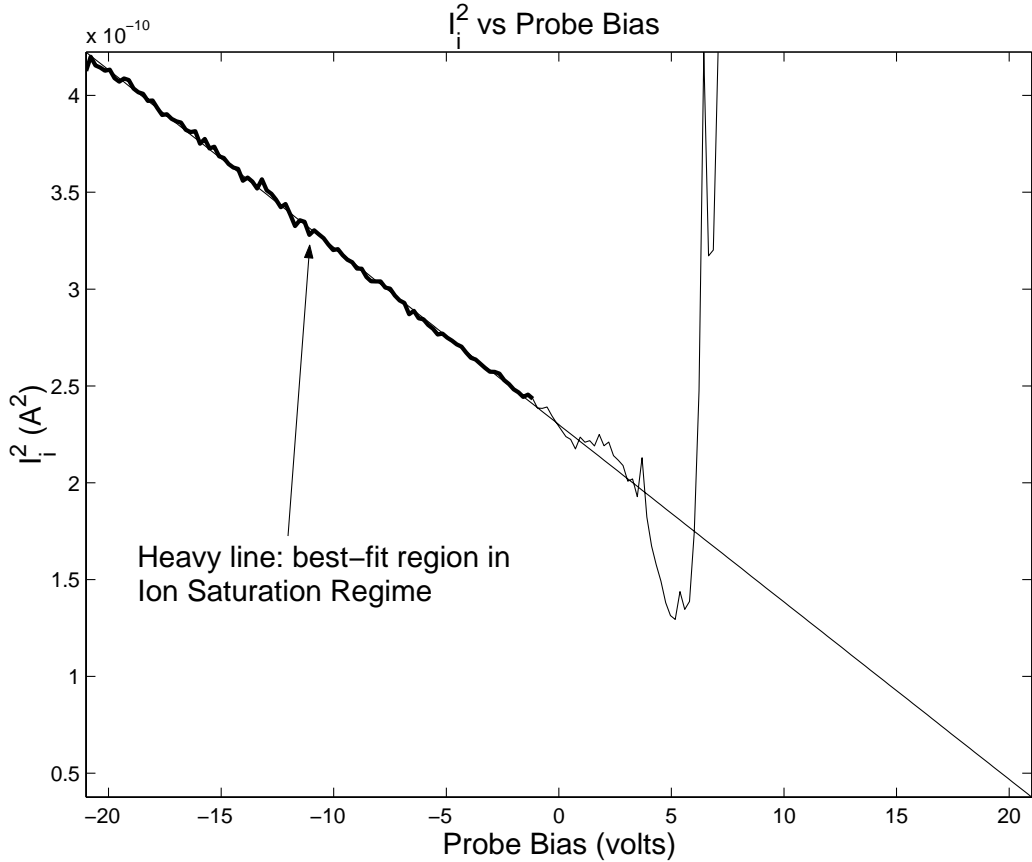


Figure F.1: Best fit of the I_i^2 -vs.- V data in the ion saturation regime. This is used to determine the density, flow energy, and fraction of beam ions.

energy U_{ev} , we have neglected the first term $\frac{1}{2}T_i$ since the ion temperature is very low (on the order of 1 eV).

An additional feature was added to the analysis in order to account for the presence of a background of low-energy ions that have only thermal energy (i.e., they are not flowing), in addition to the beam of directed ions. If we suppose that a fraction μ_b of the ions are beam ions and that the low-energy ions have a temperature T_{slow} , then the total ion current collected is given by

$$I_i = \sqrt{2} \frac{A_p e^{1.5}}{\pi \sqrt{m_i}} n_i \left\{ \mu_b \sqrt{\frac{1}{2} T_i + U_{\text{ev}} + V_p - V_0} + (1 - \mu_b) \sqrt{T_{\text{slow}} + V_p - V_0} \right\}. \quad (\text{F.2})$$

Now, the slope of the resulting I_i^2 -vs.- V graph only varies slowly, as evidenced in Figure F.1, which clearly shows the linear behavior in the ion saturation region. We may still perform

a best fit of the collected I_i^2 vs. V , and determine the “apparent” ion density $n_{i,\text{app}}$ and flow energy $U_{\text{evapp}} < U_{\text{ev}}$. Assuming the flow energy U_{ev} of the high-speed ion population is known, the actual ion density n_i and the “high-speed fraction” μ_b both can be determined accurately, using the following set of formulas that were devised based on (F.2):

$$A = \sqrt{T_{\text{slow}} + V_p - V_{\text{avg,fit}}}, \quad (\text{F.3})$$

$$B = \sqrt{U_{\text{ev}} + V_p - V_{\text{avg,fit}}}, \quad (\text{F.4})$$

$$C = U_{\text{evapp}} + V_p - V_{\text{avg,fit}}, \quad (\text{F.5})$$

$$D = \frac{1}{B} - \frac{1}{A}, \quad (\text{F.6})$$

$$\mu_b = \frac{A - C/A}{CD + A - B}, \quad (\text{F.7})$$

$$n_i = n_{i,\text{app}} \frac{\sqrt{AB}}{\sqrt{(\mu_b B + (1 - \mu_b)A)(\mu_b A + (1 - \mu_b)B)}}, \quad (\text{F.8})$$

where $V_{\text{avg,fit}}$ is the average bias potential over which the best fit was performed to obtain the values for $n_{i,\text{app}}$ and U_{evapp} . There is a one-to-one map between the apparent flow energy U_{evapp} and the actual high-speed ion fraction μ_b for a given value of the high-speed energy U_{ev} .

The value of the high-speed energy U_{ev} was selected such that the high-speed ion fraction μ_b is equal to 0.95 at the closest position to the thruster (75 cm), which is approximately in agreement with the energy distributions obtained using laser-induced fluorescence (LIF) at the same position. This procedure has yielded a beam energy of $U_{\text{ev}} = 25$ eV, which is within the bounds of the error of the LIF result (43 eV), as discussed earlier. The high-speed fractions obtained for all three positions are shown in Table 3.4: 95% at 75 cm, 53% at 160 cm, and 32% at 300 cm.

F.1.1 Evaluation of the Error on Density Estimates

Typically, the error on Langmuir probe density measurement is estimated as the discrepancy between the electron and ion densities. However, in the case of a flowing plasma, electron current collection is significantly enhanced, as is shown in chapter 3, a phenomenon that no existing model can quantitatively predict, as discussed in Section 4.6. On the other hand, the effect of flow on ion current collection is very well understood, which means that plasma flow does not cause significant errors in the ion density estimates. Thus, the quantity $|n_e - n_i|$ would merely provide a measure of the error on the electron density introduced by the plasma flow.

Given that plasma flow does not contribute a significant error to the ion density estimate, the primary source of error in the determination of plasma density estimates is the error on the Langmuir probe area estimate. We estimate the error on the length of the 4-cm Langmuir probe to be about 1 mm. As for the Langmuir probe's diameter of 0.28-mm, it is much more accurate due to precision manufacturing; it is estimated to have a 0.01-mm tolerance (actual tolerance could not be obtained from the manufacturer). Based on these two errors, the relative error on the probe area can be computed as $1/40 + 0.01/0.28 \approx 6\%$.

Now, the collected ion current is proportional to the product of the probe area and plasma density. Thus, the 6% relative error on probe area contributes a 6% relative error on our density estimates. Other, secondary sources of error, such as voltage and current measurement errors, should certainly amount to less than 2%. A conservative error estimate would thus be obtained by the sum of 6% and 2%, for a total of 8%.

F.2 Electron Retardation Analysis: Plasma Potential V_p and Electron Temperature T_e

Variations in the effective work function on the surface of our Langmuir probe (referred to as work function *patchiness* by Brace [7]) has turned out to be an area of concern in our experimental data. Our results appear to suggest a total effective work function variation of several eV. Figure F.2 illustrates that effect, which leads to a departure from exponential behavior before the plasma potential is attained. Possible explanations for this variation could include polycrystalline workfunction variations of the Tungsten probes (on the order of 1 eV, the Tungsten workfunction being on the order of 4.5 eV), and possible surface contaminants, such as adsorbed residual gases and adsorbed xenon ions. A quantitative assessment of the contamination sources is outside of the scope of the present paper, but we note here that several authors have linked effective work function variations to surface adsorbates [85–91].

A simple numerical experiment on the theoretical current collection curves was performed in order to emulate the “blurring” effect of the work function variation. Figure F.3 shows the results of this numerical experiment in the “thin sheath” and “OML” limits. The dashed curves, shown in both linear and semi-logarithmic formats, is the result of “blurring” the theoretical curves using a local averaging window of width equal to 4.8 times the electron temperature. The blurred thin sheath curve is shown to collect less than the thermal current I_{th} at the plasma potential ($V/T_e=0$ here), while on the blurred OML curve, the collected current at plasma potential is still equal to the thermal current I_{th} . It turns out that it will stay within 3% of I_{th} as long as the work function variation is under 6.7 times the thermal temperature.

We use this feature of the OML blurring in our determination of the plasma potential. In other words, we locate the plasma potential by finding the potential where the collected

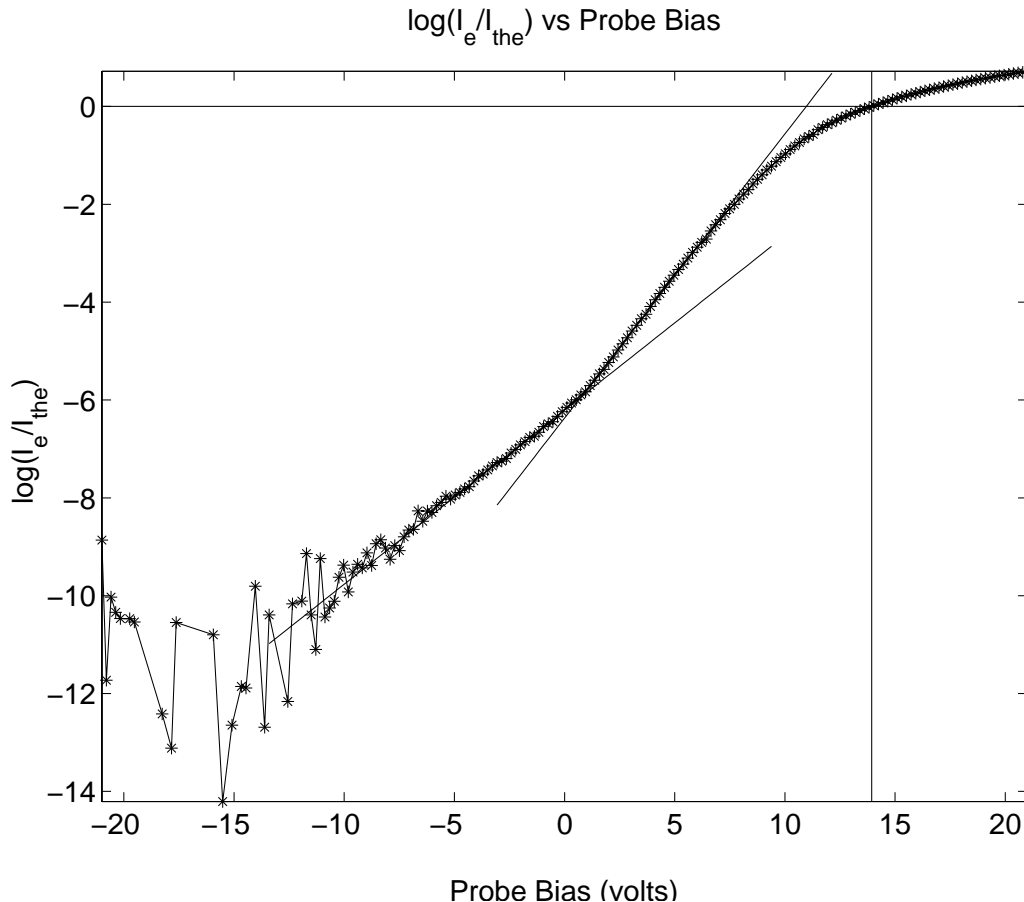


Figure F.2: Best fits in the electron retardation regime of a transverse-flow Langmuir probe. Two linear best-fits are performed on this semi-log plot. The one occurring at lower potential values corresponds to a population of warmer electrons, which account for just a few percent of the electron population.

current is equal to the electron thermal current. The cross-hair in Figure F.2 illustrates that result. As for the electron temperature, we may safely determine it based on the inverse of the slope of the retardation region *within the linear part* of Figure F.3(b), that is, beyond the reach of the blurring effect of the work function variation, as the rightmost linear fit shows in Figure F.2. The leftmost linear fit shown on the same figure is identified with a population of warmer electrons, which account for just a few percent of the total electron population.

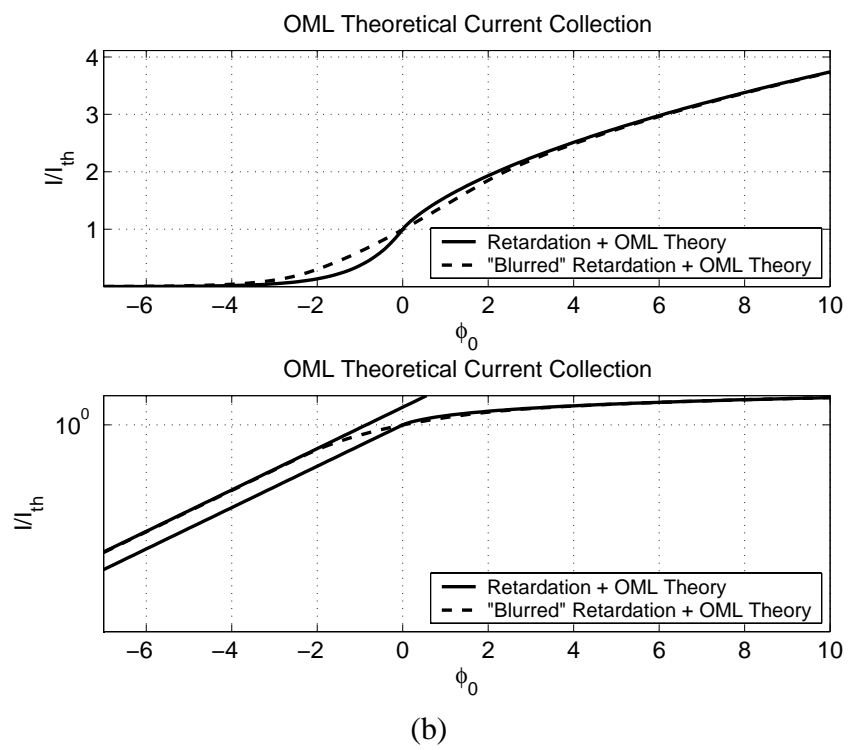
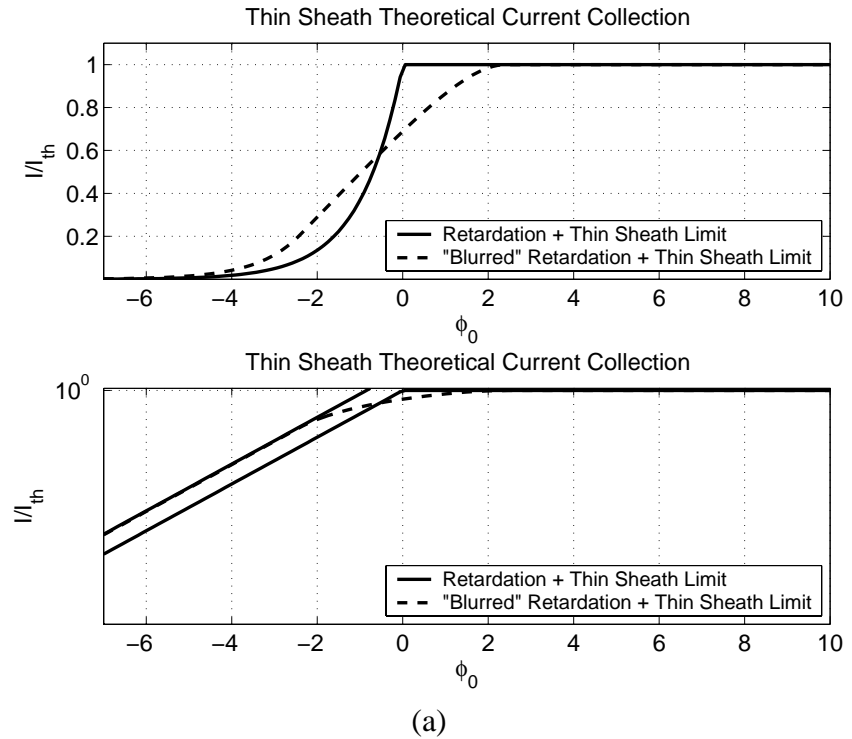


Figure F.3: Theoretical “blurring” of the current collection to probes in the (a) *thin sheath* and (b) *OML* limits.

F.2.1 Evaluation of the Error on Temperature Estimates

The temperature determination from the exponential fit of the retardation data is independent of the probe area, and as a consequence, the error on the Langmuir probe area estimate has no bearing on the accuracy of the temperature estimate. The primary sources of error in the temperature determination are thus

- the relative accuracy of the voltages measured by the Keithley 2410 sourcemeter that was used for the LP measurements, which is better than 1%; and
- the empirical process used to select the voltage range over which a best fit of the retardation regime is performed.

In order to be conservative in accounting for both of these error terms, we will assume an overall accuracy of 5% for our temperature estimates.

Because the Debye length estimate is determined based on the estimated density and temperature values through the relationship $\lambda_{\text{De}} = \sqrt{\frac{\epsilon_0 T_e}{en_0}}$, the relative accuracy on Debye length, consistent with the 5% and 8% relative accuracy estimates for temperature and density, is obtained from:

$$\frac{\Delta \lambda_{\text{De}}}{\lambda_{\text{De}}} = \frac{1}{2} \left(\frac{\Delta T_e}{T_e} + \frac{\Delta n}{n} \right) = \frac{1}{2} (5\% + 8\%) = 6.5\% \quad (\text{F.9})$$

BIBLIOGRAPHY

BIBLIOGRAPHY

- [1] J. Sanmartín, M. Martínez-Sánchez, and E. Ahedo, “Bare wire anodes for electrodynamic tethers,” *Journal of Propulsion and Power*, vol. 9, no. 3, pp. 353–360, 1993.
- [2] R. Estes, E. Lorenzini, J. Sanmartín, J. Peláez, M. Martínez-Sánchez, C. Johnson, and I. Vas, “Bare tethers for electrodynamic spacecraft propulsion,” *Journal of Spacecraft and Rockets*, vol. 37, no. 2, pp. 205–211, March–April 2000.
- [3] V. V. Danilov, V. V. Mirnov, and D. Ucer, “High-voltage space tether for enhanced particle scattering in Van Allen belts,” *Fusion Technology*, vol. 35, no. 1T, pp. 312–314, January 1999.
- [4] V. V. Danilov, B. Elgin, O. Grafodatsky, and V. Mirnov, “High-voltage satellite tethers for active experiments in space,” in *Proceedings of the 6th Spacecraft Charging Technology Conference, AFRL-VS-TR-20001578*, September 2000, pp. 165–168.
- [5] Y. V. Vasil'yev and V. V. Danilov, “Proposal for an attempt to influence the precipitation of charged particles from the Earth’s radiation belts by means of a satellite-borne high-voltage cable system,” *Transaction (Doklady) of the Russian Academy of Sciences: Earth Science Sections*, vol. 345A, no. 9, pp. 172–176, October 1996.
- [6] J. Laframboise and L. Parker, “Probe design for orbit-limited current collection,” *The Physics of Fluids*, vol. 16, no. 5, pp. 629–636, May 1973.
- [7] L. H. Brace, *Measurement Techniques in Space Plasmas: Particles*. American Geophysical Union, 1998, ch. Langmuir Probe Measurements in the Ionosphere, pp. 23–35.
- [8] J. Laframboise, “Theory of spherical and cylindrical Langmuir probes in a collisionless, Maxwellian plasma at rest,” Ph.D. dissertation, University of Toronto, June 1966.
- [9] S. G. Bilén, “Pulse propagation along conductors in low-density, cold plasmas as applied to electrodynamic tethers in the ionosphere,” Ph.D. dissertation, University of Michigan, 1998.
- [10] I. E. Vas, T. J. Kelly, and E. A. Scarl, “Space station reboost with electrodynamic tethers,” *Journal of Spacecraft and Rockets*, vol. 37, no. 2, pp. 154–164, March–April 2000.

- [11] J. Sanmartín and R. Estes, “The orbital-motion-limited regime of cylindrical Langmuir probes,” *Physics of Plasmas*, vol. 6, no. 1, pp. 395–405, 1999.
- [12] R. Estes and J. Sanmartín, “Cylindrical Langmuir probes beyond the orbital-motion-limited regime,” *Physics of Plasmas*, vol. 7, no. 10, pp. 4320–4325, October 2000.
- [13] L. Johnson, B. E. Gilchrist, R. D. Estes, E. Lorenzini, and J. Ballance, “Propulsive small expendable deployer system (ProSEDS) space experiment,” AIAA Paper AIAA-98-4035, 1998.
- [14] J. V. Noord and R. Strumfels, “Electrodynamic tether optimization for the STEP-AirSEDS mission,” AIAA Paper AIAA-2001-3980, 2001.
- [15] R. P. Hoyt and B. M. Minor, “Remediation of radiation belts using electrostatic tether structures,” 2004, Tethers Unlimited, Inc.
- [16] J. Parmentola *et al.*, “High altitude nuclear detonations against low Earth orbit satellites,” Defense Threat Reduction Agency, Advanced Systems and Concepts Office, U.S. Government,” Slides, April 2001. [Online]. Available: <http://www.fas.org/spp/military/program/asat/haleos.pdf>.
- [17] G. Z. Xu, “The interaction of a moving spacecraft with the ionosphere: Current collection and wake structure,” Ph.D. dissertation, York University, 1992.
- [18] J. Sanmartín and R. Estes, “Interference of parallel cylindrical Langmuir probes,” *Physics of Plasmas*, vol. 8, no. 9, pp. 4234–4239, September 2001.
- [19] A. S. Jursa, Ed., *Handbook of geophysics and the space environment*. Air Force Geophysics Laboratory, Air Force Systems Command, U.S. Air Force, 1985.
- [20] R. Hoyt, B. Minor, J. Slostad, and N. Voronka, “Electrodynamic/electrostatic tether performance assessment program-tether payloads concept design, appendix H (electrostatic scattering model),” September 2003, TUI Final Report on DARPA/SPO Seedling Contract.
- [21] D. Gallagher, P. Craven, and R. Comfort, “Global core plasma model,” *Journal of Geophysical Research*, vol. 105, no. A8, pp. 18 819–18 833, August 2000.
- [22] J. C. McMahon, “The interaction of infinite and finite cylindrical probes with a drifting collisionless Maxwellian plasma,” Ph.D. dissertation, York University, September 2000.
- [23] J. M. Quinn, R. J. Coleman, D. L. Shiel, and J. M. Nigro, “The joint US/UK 1995 epoch world magnetic model,” Naval Oceanographic Office, Tech. Rep., 1995.
- [24] J. M. Quinn, 1990, ”GEOMAG.for” and ”GEOMG1.for” Fortran subroutines for the calculation of geomagnetic field based on the World Magnetic Model, Naval Oceanographic Office.

- [25] M. A. Lieberman and A. J. Lichtenberg, *Principles of Plasma Discharges and Materials Processing*. Wiley Interscience, 1994.
- [26] H. Mott-Smith and I. Langmuir, “The theory of collectors in gaseous discharges,” *Physical Review*, vol. 28, pp. 727–763, 1926.
- [27] I. Bernstein and I. Rabinowitz, “Theory of electrostatic probes in a low-density plasma,” *Physics of Fluids*, vol. 2, no. 2, pp. 112–121, March-April 1959.
- [28] M. Kanal, “Theory of current collection of moving cylindrical probes,” *Journal of Applied Physics*, vol. 35, p. 1697, 1964.
- [29] W. Hoegy and L. Wharton, “Current to a moving cylindrical electrostatic probe,” *Journal of Applied Physics*, vol. 44, no. 12, pp. 5365–5371, December 1973.
- [30] R. Godard and J. Laframboise, “Total current to cylindrical collectors in collisionless plasma flow,” *Planetary and Space Science*, vol. 31, no. 3, pp. 275–283, 1983.
- [31] T. Onishi, “Numerical study of current collection by an orbiting bare tether,” Ph.D. dissertation, Massachusetts Institute of Technology, August 2002.
- [32] A. Geist, A. Beguelin, J. Dongarra, W. Jiang, R. Manchek, and V. Sunderam, *PVM 3 User’s Guide and Reference Manual*, Oak Ridge National Laboratory, September 1994.
- [33] C. Birdsall and A. B. Langdon, *Plasma Physics Via Computer Simulation*. IOP Publishing, 1991.
- [34] F. Filbet and E. Sonnendrücker, “Comparison of Eulerian Vlasov solvers,” *Comp. Phys. Comm.*, vol. 150, no. 3, pp. 247–266, 2003.
- [35] L. Parker and E. Sullivan, “Numerical solution of the Poisson-Vlasov system for a spherical electrostatic probe,” SIAM Fall Meeting, October 1970.
- [36] L. W. Parker, “Computation of collisionless steady-state plasma flow past a charged disk,” Lee W. Parker, Inc., Tech. Rep., 1976, prepared for NASA - George C. Marshall Space Flight Center.
- [37] M. Tautz, D. Cooke, A. Rubin, and G. Yates, “Preliminary documentation of the MACH code,” Hanscom Air Force Base, Tech. Rep., September 1987.
- [38] F. F. Chen, *Introduction to plasma physics and controlled fusion*, 2nd ed. Plenum Press, 1984.
- [39] P. M. Chung, L. Talbot, and K. J. Touryan, *Electric Probes in Stationary and Flowing Plasmas: Theory and Application*. Springer-Verlag, 1975.
- [40] A. V. Gurevich, “Distribution of captured particles in a potential well in the absence of collisions,” *Soviet Physics JETP*, vol. 26, no. 3, pp. 575–580, March 1968.

- [41] M. Lampe, V. Gavrishchaka, G. Ganguli, and G. Joyce, “Effect of trapped ions on shielding of a charged spherical object in a plasma,” *Physical Review Letters*, vol. 86, no. 23, pp. 5278–5281, June 2001.
- [42] F. Hecht, “Bidimensional anisotropic mesh generator,” INRIA (France), Tech. Rep., 1998.
- [43] D. K. Cheng, *Field and wave electromagnetics*. Addison-Wesley Pub. Co., 1989.
- [44] P. Tong and J. N. Rossettos, *Finite-Element Method - Basic Technique and Implementation*. The MIT Press, 1977, ch. 2: The Finite-Element Method for Poisson’s Equation, pp. 40–71.
- [45] C. Fox, *An Introduction to the Calculus of Variations*. Dover Publications Inc., 1987.
- [46] W. R. Smythe, *Static and Dynamic Electricity*, 3rd ed. McGraw-Hill Book Company, 1968.
- [47] E. Kreysig, *Advanced Engineering Mathematics*, 7th ed. John Wiley & Sons, 1993.
- [48] W. H. Press, S. A. Teukolsky, W. T. Vetterling, and B. P. Flannery, *Numerical Recipes in C*, 2nd ed. Cambridge University Press, 1992.
- [49] L. C. Evans, *Partial differential equations*. American Mathematical Society, 1998.
- [50] J. Bernstsen and T. O. Espelid, “Algorithm 706–DCUTRI: An algorithm for adaptive cubature over a collection of triangles,” *Transactions on Mathematical Software*, vol. 18, no. 3, pp. 329–342, September 1992.
- [51] T. O. Espelid, “Remark on algorithm 706: DCUTRI – An algorithm for adaptive cubature over a collection of triangles,” *Transactions on Mathematical Software*, vol. 24, no. 3, pp. 334–335, September 1998.
- [52] K. A. Sikorski, *Optimal Solution of Nonlinear Equations*. Oxford University Press, 2001.
- [53] R. L. Burden, *Numerical Analysis*, 4th ed. PWS-KENT Publishing Company, 1989.
- [54] L. N. Trefethen and I. David Bau, *Numerical Linear Algebra*. Society for Industrial and Applied Mathematics, 1997.
- [55] A. Neumaier, “Solving ill-conditioned and singular linear systems: a tutorial on regularization,” *SIAM Review*, vol. 40, no. 3, pp. 636–666, September 1998.
- [56] C. Hansen, “Regularization tools – a Matlab package for analysis and solution of discrete ill-posed problems,” *Numerical Algorithms*, vol. 6, pp. 1–35, 1994.
- [57] C. Hansen, *Regularization Tools – A Matlab Package for Analysis and Solution of Discrete Ill-Posed Problems*. Department of Mathematical Modelling, Technical University of Denmark, September 2001.

- [58] A. Tikhonov, A. Goncharsky, V. Stepanov, and A. Yagola, *Numerical Methods for the Solution of Ill-Posed Problems*. Kluwer Academic Publishers, 1995.
- [59] C. Kelley, *Iterative Methods for Linear and Nonlinear Equations*. Philadelphia: Society for Industrial and Applied Mathematics, 1995.
- [60] H. W. Engl, M. Hanke, and A. Neubauer, *Regularization of Inverse Problems*. Kluwer Academic Publishers, 1996.
- [61] S. Fridman, “Reconstruction of a three-dimensional ionosphere from backscatter and vertical ionograms measured by over-the-horizon radar,” *Radio Science*, vol. 33, no. 4, pp. 1159–1171, 1998.
- [62] B. Kaltenbacher, “Some Newton-type methods for the regularization of nonlinear ill-posed problems,” *Inverse Problems*, vol. 13, pp. 729–753, 1997.
- [63] J. Qi-Nian, “Applications of the modified discrepancy principle to Tikhonov regularization of nonlinear ill-posed problems,” *SIAM Journal of Numerical Analysis*, vol. 36, no. 2, pp. 475–490, 1999.
- [64] A. Rieder, “On the regularization of nonlinear ill-posed problems via inexact Newton iterations,” *Inverse Problems*, vol. 15, no. 1, pp. 309–327, February 1999.
- [65] E. Haber and D. Oldenburg, “A GCV based method for nonlinear ill-posed problems,” *Computational Geosciences*, vol. 4, pp. 41–63, 2000.
- [66] A. Rieder, “On convergence rates of inexact Newton regularizations,” *Numerical Mathematics*, vol. 88, pp. 347–365, 2001.
- [67] V. Morozov, *Methods for Solving Incorrectly Posed Problems*. Springer-Verlag, 1984.
- [68] F. Hecht, *BAMG: Bidimensional Anisotropic Mesh Generator*, Institut National de Recherche en Informatique et en Automatique, Rocquencourt, 75153 Le Chenay, France, October 1998, edition 0.58.
- [69] M. Castro-Díaz, F. Hecht, B. Mohammadi, and O. Pironneau, “Anisotropic unstructured mesh adaption for flow simulations,” *International Journal for Numerical Methods in Fluids*, vol. 25, pp. 475–491, 1997.
- [70] H. Borouchaki, P. L. George, F. Hecht, P. Laug, and E. Saltel, “Delaunay mesh generation governed by metric specifications. Part I. Algorithms,” *Finite Elements in Analysis and Design*, vol. 25, pp. 61–83, 1997.
- [71] É. Choinière, B. E. Gilchrist, S. G. Bilén, K. R. Furhrhop, and A. D. Gallimore, “Experimental investigation of electron collection to solid and slotted tape probes in a high-speed flowing plasma,” submitted for publication to the *IEEE Transactions on Plasma Science* in April 2004.

- [72] B. E. Gilchrist, S. G. Bilén, É. Choinière, A. D. Gallimore, and T. B. Smith, “Analysis of chamber simulations of long collecting probes in high-speed dense plasmas,” *IEEE Transactions on Plasma Science*, vol. 30, no. 5, pp. 2023–2034, October 2002.
- [73] J. M. Haas, F. S. G. II, A. D. Gallimore, G. G. Spanjers, and R. A. Spores, “Performance characteristics of a 5 kw laboratory Hall thruster,” AIAA Paper AIAA-98-3503, 1998.
- [74] B. E. Gilchrist, S. Bilén, É. Choinière, and A. D. Gallimore, “Laboratory experiments of current collection to long tape probes using a high-speed plasma relevant to bare electrodynamic tethers: Calibration and initial solid and slotted tape measurements,” University of Michigan, Tech. Rep., 2002.
- [75] G. J. J. Williams, T. B. Smith, M. T. Domonkos, K. J. Shand, A. D. Gallimore, and R. P. Drake, “Laser induced fluorescence measurement of ion velocities in the plume of a hall effect thruster,” AIAA Paper AIAA-99-2862, 1999.
- [76] T. B. Smith, D. A. Herman, A. D. Gallimore, and R. P. Drake, “Deconvolution of axial velocity distributions from Hall thruster LIF spectra,” Paper IEPC-01-0019 presented at the 27th International Electric Propulsion Conference, 1999.
- [77] É. Choinière and B. E. Gilchrist, “Modeling long probes in flowing plasmas using KiPS-2D, a novel steady-state Vlasov solver,” AIAA Paper AIAA-2003-5098, 2003.
- [78] É. Choinière and B. E. Gilchrist, “Electron collection to arbitrarily shaped electrodynamic tethers in flowing plasmas: a kinetic model – validation for circular cross-sections,” AIAA Paper AIAA-2002-4050, July 2002.
- [79] J. G. Laframboise, “Correction of one ion density data curve from [8, figure 33] for the case $r_0 = \lambda_{De}$,” 1974, private Communication.
- [80] W. J. Larson and J. R. Wertz, *Space Mission Analysis and Design*. Kluwer Academic Publishers, 1992.
- [81] D. Cooke and I. Katz, “TSS-1R electron currents: Magnetic limited collection from a heated presheath,” *Geo. Res. Let.*, vol. 25, no. 5, pp. 753–756, March 1998.
- [82] É. Choinière, “Assessment of possible space charge effects caused by secondary electron emission,” July 2004, technical Note.
- [83] J. Laframboise, D. Wallis, and H. James, “RF effects on Oedipus-C floating voltages,” in *Proceedings of the 8th Spacecraft Charging Technology Conference*, 2003.
- [84] G. E. Moore, “Cramming more components onto integrated circuits,” *Electronics*, vol. 38, no. 8, April 1965.
- [85] G. Wehner and G. Medicus, “Reliability of probe measurements in hot cathode gas diodes,” *Journal of Applied Physics*, vol. 23, no. 9, pp. 1035–1045, September 1952.

- [86] C. Winkler, D. Strele, S. Tscholl, and R. Schrittweiser, “On the contamination of Langmuir probe surfaces in a potassium plasma,” *Plasmas Physics and Controlled Fusion*, vol. 42, pp. 217–223, 2000.
- [87] B. Waclawski and L. Hughey, “Adsorption of water vapor on polychrystalline tungsten,” *Surface Science*, vol. 19, pp. 464–468, 1970.
- [88] M. J. Dresser, T. E. Madey, and J. John T. Yates, “The adsorption of xenon by W(111), and its interaction with preadsorbed oxygen,” *Surface science*, vol. 42, pp. 533–551, 1974.
- [89] H. Miki, H. Inomata, K. Kato, T. Kioka, and K. Kawasaki, “Chemisorption of NO on polychrystalline tungsten surface,” *Surface Science*, vol. 141, pp. 473–486, 1984.
- [90] T. Kioka, A. Kawana, H. Miki, S. Sugai, and K. Kawasaki, “Chemisorption of NO on W(100) and W(110) surfaces studies by AES and UPS,” *Surface Science*, vol. 182, pp. 28–40, 1987.
- [91] E. Stamate and K. Ohe, “Influence of surface condition in Langmuir probe measurements,” *Journal of Vacuum Science and Technology*, vol. 20, no. 3, pp. 661–666, 2002.